Transport Properties of II-VI Organic-Inorganic Hybrid Semiconductors

by

Wanseok Oh

A dissertation submitted to the faculty of
The University of North Carolina at Charlotte
in partial fulfillment of the requirements
for the degree of Doctor of Philosophy in
Electrical Engineering

Charlotte

2025

Approved by:

_____
Dr. Yong Zhang

_____
Dr. Abasifreke Ebong

_____
Dr. Haitao Zhang

_____
Dr. Thomas A. Schmedake

_____
Dr. M. Yasin Akhtar Raja

ABSTRACT

Wanseok Oh. Transport Properties of II-VI Organic-Inorganic Hybrid Semiconductors
(Under the direction of Dr. Yong Zhang)

β-ZnTe(en)$_{0.5}$, an organic-inorganic hybrid semiconductor, demonstrates exceptional long-term stability exceeding 15 years in ambient conditions, surpassing most hybrid semiconductors like halide perovskites. This stability arises from strong covalent-like bonds between the alternating inorganic and organic layers, forming a superlattice structure, where ZnTe inorganic layers are bonded with ethylenediamine (en). The crystalline structure exhibits various unique and interesting properties, such as strong quantum confinement effects, resulting in a large bandgap blueshift compared to bulk ZnTe and strong excitonic absorption, and anisotropic thermal expansion with a low uniaxial thermal expansion coefficient along the stacking direction. High crystallinity, evidenced by narrow X-ray diffraction and Raman line widths, makes β-ZnTe(en)$_{0.5}$ a promising candidate for optoelectronic applications.

β-ZnTe(en)$_{0.5}$ crystals were synthesized via a solvothermal method, leveraging high autogenous pressures and controlled crystallization in sealed reaction vessels at elevated temperatures. This technique, using ethylenediamine as a solvent, facilitated the formation of colorless flake-like crystals through controlled reaction parameters and purification. For device fabrication, a shadow mask approach was chosen over conventional lithography like UV photolithography and electron beam lithography (EBL), offering a resist-free, versatile, and less invasive patterning method that avoids chemical exposure and preserves material integrity. This allowed for high-quality devices with minimal artifacts, enabling reliable transport property investigation.

To explore charge transport, Space-Charge-Limited Current (SCLC) analysis, based on the Mott-Gurney law ($J \propto V^2$), was employed. While real materials deviate from ideal behavior, this

analysis established a baseline understanding of charge carrier mobilities. Two-probe electrical measurements on both vertical and lateral device configurations were conducted. Initial vertical measurements on pristine samples with metal electrodes revealed SCLC behavior, with mobilities of 8.8×10^{-3} $cm^2/(Vs)$ and 2.5 10^{-3} $cm^2/(Vs)$ for samples synthesized in 2007 and 2019, respectively. Lateral measurements, conducted along the a- and c-axes, revealed significantly higher mobilities, with values of 1.787×10^2 $cm^2/(Vs)$ along the a-axis and 1.696×10^1 $cm^2/(Vs)$ along the c-axis, demonstrating anisotropic charge transport. These results underscore the importance of SCLC measurements in characterizing the anisotropic transport properties of materials.

Complementary electronic structure analysis using X-ray photoelectron spectroscopy (XPS), ultraviolet photoelectron spectroscopy (UPS), Kelvin probe force microscopy (KPFM), and hot probe measurements were performed. XPS revealed a valence band maximum (E_v) of 0.80 eV below the Fermi level (E_F), indicating p-type conductivity, corroborated by a 3.55 eV bandgap from photoluminescence (PL). KPFM yielded work function of 4.59 ± 0.03 eV, consistent with UPS data, falls within the 4.49 eV to 4.71 eV range determined by UPS, which accounts for substrate-dependent variations in the β-$ZnTe(en)_{0.5}$ work function. The hot probe measurements indicated p-type conductivity of β-$ZnTe(en)_{0.5}$. Integrating these results produced a reliable energy band diagram, confirming p-type conductivity and establishing band alignment. This multi-technique approach emphasizes its importance for accurate electronic structure determination.

DEDICATION

Start text on this line. Insert the proper page number in lower case Roman Numerals at the top right side.

ACKNOWLEDGEMENTS

The important element in the Acknowledgements is simple courtesy in which there are usually two possible ingredients to consider. First you should acknowledge any significant help you received from any individual whether in your department or elsewhere. Specifically, you should acknowledge the source of special materials, documents, or equipment. Further, you should acknowledge the help of anyone who contributed significantly to the work or to the interpretation of the work. Second, you should acknowledge any outside source of financial assistance, such as grants, contracts, or fellowships. A word of caution is in order. Often it is wise to show the proposed wording of the Acknowledgments to the person whose help you are acknowledging. He or she might well believe that your acknowledgment is insufficient or (worse) that it is too effusive.

TABLE OF CONTENTS

LIST OF TABLES

LIST OF FIGURES

LIST OF ABBREVIATIONS

CHAPTER 1: INTRODUCTION

1.1. The Unique Properties and Potential Applications of β-ZnTe(en)$_{0.5}$

β-ZnTe(en)$_{0.5}$ stands as a compelling subject of study due to its unique properties and potential applications, distinguishing itself within the realm of organic-inorganic hybrid materials. Most hybrid materials, while offering improved processability, tailored bandgap energies, and tunable electronic properties, often suffer from poor long-term stability and structural disorder [1-2, 4-6, 9, 66]. However, β-ZnTe(en)$_{0.5}$ demonstrates exceptional long-term stability in ambient environments, exceeding 15 years, a significant advantage over materials like halide perovskites, which face substantial stability challenges [10, 66, 93]. This remarkable stability is attributed to its intrinsic strong chemical bonding with covalent-like bonds and further enhanced by conformation distortion of the organic and inorganic components [93]. Structurally, β-ZnTe(en)$_{0.5}$ is a three-dimensional (3D) hybrid single-crystal nanostructure where inorganic ZnTe layers are covalently bonded with organic ethylenediamine molecules, resulting in a quasi-two-dimensional (quasi-2D) layered architecture for the inorganic component [1, 5-6, 8-9, 66]. The meticulous layering induces strong quantum confinement effects, leading to a substantial blueshift in the bandgap energy compared to bulk ZnTe [1, 2, 6, 163]. With a bandgap energy of 3.719 eV at 1.5 K, and 3.55 eV at room temperature, the blueshift is evident when compared to bulk ZnTe's 2.3805 eV at 4 K and 2.26 eV at room temperature, showcasing temperature-dependent variations consistent with typical inorganic semiconductor behavior [1-2, 5-6, 76-81, 84-89, 142-144, 183]. Furthermore, β-ZnTe(en)$_{0.5}$ exhibits anisotropic thermal expansion, with an exceedingly small uniaxial thermal expansion coefficient along its stacking direction, making it promising for optoelectronic applications like lasers and optical cavities [8, 163]. Its high

crystallinity, evidenced by narrow Raman line widths (FWHM = 0.8 cm^{-1} at 30 K), XRD linewidths (W_{RC} = 22", $W_{2\theta}$ = 38"), and distinct vibrational modes, highlights its superior material quality [2, 6, 9, 10]. The material's orthorhombic crystal system, akin to ultrashort-period superlattice heterostructures, is synthesized via a solvothermal method, allowing for tailored cation, anion, and organic constituent manipulation [1, 2, 3, 5, 6, 10]. This method facilitates the creation of new hybrid nanostructures by enabling organic molecules to break 3D ZnTe crystal lattices into 2D ZnTe slabs [1]. The high-frequency dielectric constants of β-$ZnTe(en)_{0.5}$, ε_x = 6.06, ε_y = 5.41, and ε_z = 4.88, contrast with ZnTe's 7.28, reflecting its unique structural properties [6]. In essence, β-$ZnTe(en)_{0.5}$, while fundamentally 3D, exhibits quasi-2D characteristics due to its layered architecture, demonstrating quantum confinement effects and anisotropic properties, making it a valuable material for exploring novel electronic and optoelectronic applications [66]. These unique properties necessitate precise synthesis and fabrication methods, as discussed in the following section.

1.2. Solvothermal Synthesis and Shadow Mask Lithography for β-$ZnTe(en)_{0.5}$

β-$ZnTe(en)_{0.5}$ crystals are synthesized through a carefully controlled solvothermal method, which leverages the generation of high autogenous pressures within sealed reaction vessels at elevated temperatures. This technique facilitates precise control over the crystallization process [72, 73]. Utilizing ethylenediamine as a solvent, this approach enables the synthesis of highly crystalline, colorless flake-like crystals through a process involving meticulously controlled reaction parameters, including temperature, pressure, and reaction time, followed by a rigorous purification protocol [1]. The solvothermal method allows for the creation of materials with tailored morphologies and sizes, offering advantages such as the ability to use diverse precursors and perform high-pressure reactions at lower temperatures [73]. Careful control of the synthesis

is required to produce high quality crystals suitable for electronic testing. The samples used in this study were synthesized by our collaborators: the newest ones by my team member Mr. Yizhou Wang, and older ones by other collaborators mentioned in a previous publication [10]. For the fabrication of devices necessary to study the material's electrical properties, a shadow mask approach was selected over conventional lithographic techniques like UV photolithography and electron beam lithography (EBL). While UV photolithography and EBL are capable of high-resolution patterning, they introduce potential drawbacks when applied to delicate materials like β-$ZnTe(en)_{0.5}$. These methods involve the use of photoresists, developers, and solvents, which can lead to chemical degradation of the material [109, 110, 194]. Furthermore, UV photolithography has been observed to induce mechanical stress, resulting in cracks within the β-$ZnTe(en)_{0.5}$ crystals. In contrast, the shadow mask technique offers a resist-free, versatile, and less invasive patterning method, avoiding direct chemical exposure and preserving the material's structural integrity by eliminating exposure to UV photons and high-energy electrons [159, 189, 190, 191, 193]. This approach simplifies the fabrication process, reducing potential errors and enhancing cost-effectiveness. Specifically, successful lateral device fabrication was achieved by employing a planarizing coating as a temporary adhesive, which negated the need for harsh chemicals and UV exposure, both of which can degrade the material [192]. This method allowed for accurate alignment of electrodes along the a- or c-axis, crucial for studying the anisotropic transport properties of β-$ZnTe(en)_{0.5}$. The precision afforded by the shadow mask technique ensures the creation of high-quality devices with minimal processing artifacts, enabling reliable and accurate investigation of the material's inherent transport characteristics. The carefully fabricated devices allowed for the study of the charge transport properties of β-$ZnTe(en)_{0.5}$ via space-charge-limited current (SCLC) analysis, as detailed in the following section.

1.3. Space-Charge-Limited Current (SCLC) Analysis of β-ZnTe(en)$_{0.5}$

Understanding charge transport in organic-inorganic hybrid materials is crucial for their applications in advanced optoelectronic devices. β-ZnTe(en)$_{0.5}$, a material with exceptional long-term stability and a unique layered nanostructure, presents an intriguing case for such investigation [10]. To explore the charge transport properties of this material, this study employed Space-Charge-Limited Current (SCLC) analysis, a technique grounded in the idealized Mott-Gurney law [11]. The Mott-Gurney law predicts a direct quadratic relationship between current density and applied voltage ($J \propto V^2$), providing a fundamental framework for understanding charge transport in semiconductors and insulators under conditions where space-charge dominates [12-14]. While it is well-established that real materials often exhibit deviations from the ideal Mott-Gurney behavior due to factors such as impurities, defects, and traps, this initial analysis focused on applying the idealized model to establish a baseline understanding of charge carrier mobilities in β-ZnTe(en)$_{0.5}$. By assuming conditions that approximate the ideal, such as a dominant space-charge regime, and neglecting the immediate effects of traps and non-idealities within the initial step of this analysis, the intrinsic transport characteristics of the material were assessed. This approach provides a foundation for future investigations that may incorporate more complex models to account for non-idealities. The derived mobility values, within the context of this ideal model, serve as a starting point for further exploration into more intricate transport phenomena [16-18].

Two-probe electrical measurements were performed on both vertical and lateral device configurations to investigate the charge transport properties of β-ZnTe(en)$_{0.5}$. Initial vertical measurements on pristine samples, without metal electrodes, revealed SCLC behavior, with mobilities of 8.8×10^{-3} cm^2/(Vs) and 2.5×10^{-3} cm^2/(Vs) for samples synthesized in 2007 and

2019, respectively [10]. These values, derived using the Mott-Gurney law, are consistent with the expected reduced mobility for the transport along the inorganic-organic stacking direction (b-axis). Lateral measurements, conducted along the a- and c-axes, revealed significantly higher mobilities, with values of 1.787×10^2 $cm^2/(Vs)$ along the a-axis and 1.696×10^1 $cm^2/(Vs)$ along the c-axis, demonstrating anisotropic charge transport, as suggested by the biaxial crystal symmetry [66]. These results emphasize the importance of SCLC measurements in characterizing the anisotropic transport properties of materials, particularly in layered hybrid nanostructures like β-$ZnTe(en)_{0.5}$, whose anisotropic crystal structure directly contributes to the observed directionality in charge carrier mobility.

1.4. Complementary Electronic Structure Investigation of β-$ZnTe(en)_{0.5}$

To thoroughly characterize the electronic structure of β-$ZnTe(en)_{0.5}$, a complementary investigation employing a combination of surface-sensitive and bulk-probing techniques was conducted. X-ray photoelectron spectroscopy (XPS) was utilized to probe the valence band electronic structure, revealing a valence band maximum (E_v) located approximately 0.80 eV below the Fermi level (E_F), a key indicator of p-type conductivity. This observation was further supported by room-temperature photoluminescence (PL) measurements, which independently determined a bandgap of 3.55 eV, providing crucial information about the material's optical properties and electronic transitions.

Ultraviolet photoelectron spectroscopy (UPS) measurements were performed to determine the secondary electron cutoff (E_{SECO}) and the Fermi level, aiming to understand the surface electronic properties and work function (∅). The UPS measurements estimated the work function to be within the range of 4.49 eV to 4.71 eV. However, due to the inherent surface sensitivity of UPS and potential interference from the substrate, challenges were encountered in accurately

identifying the valence band maximum. Nonetheless, the UPS data provided valuable insights into the material's surface electronic structure.

Kelvin probe force microscopy (KPFM) was employed to directly measure the work function of β-$ZnTe(en)_{0.5}$, yielding an average value of 4.59 ± 0.03 eV. This result was consistent with the range of 4.49 eV to 4.71 eV estimated from the UPS data, reinforcing the reliability of the work function determination. Additionally, hot probe measurements were conducted to independently verify the p-type conductivity of β-$ZnTe(en)_{0.5}$, confirming the nature of the majority charge carriers.

By integrating the data obtained from XPS, UPS, KPFM, and hot probe measurements, a comprehensive and reliable energy band diagram of β-$ZnTe(en)_{0.5}$ was constructed. This energy diagram confirmed the p-type conductivity of the material and accurately established its work function and band alignments, providing a solid foundation for understanding its electronic behaviors. This multi-technique approach underscores the critical importance of utilizing a combination of spectroscopic and electrical characterization methods to accurately elucidate the electronic structure of complex materials like β-$ZnTe(en)_{0.5}$, ensuring a more complete and accurate understanding of their properties.

CHAPTER 2: MATERIAL PROPERTIES OF β-ZnTe(en)$_{0.5}$

Organic-inorganic hybrid materials offer unique properties and several advantages that are not found in either organic or inorganic materials alone, such as improved processability, tailoring bandgap energy, lattice-matching flexibility, and tunable optical and electronic properties, while often demonstrating cost-effectiveness; however, they frequently suffer from poor long-term stability and crystal structural disorder [1, 2, 4, 5, 6, 9, 36, 66]. These materials are synthesized through the incorporation of organic components into inorganic constituents via various chemical bonds, including ionic, covalent, hydrogen bonds, coordinate bonds, and van der Waals interactions [1, 2]. Moreover, many hybrid materials exhibit non-crystalline structures due to the lack of translational symmetry, as defined by strict crystallographic classifications [58, 66]. α-ZnTe(en)$_{0.5}$, β-ZnTe(en)$_{0.5}$, and ZnTe(pda)$_{0.5}$ represent the first examples of chalcogenide-based organic-inorganic hybrid nanostructures, distinguished by uniform and fully ordered short-period superlattice structures devoid of physical and chemical fluctuations [1, 5, 6, 8, 9, 10]. Notably, β-ZnTe(en)$_{0.5}$ exhibits exceptional stability within ambient environments over an extended period, exceeding 15 years [10]. These materials are three-dimensional (3D) hybrid single-crystal nanostructures where the inorganic host II-VI semiconductors (ZnTe) are covalently bonded with the organic molecules (en: ethylenediamine, $C_2H_8N_2$ or pda: propanediamine, $C_3H_{10}N_2$); however, the organic materials and inorganic materials are perfectly stacked, resulting in a quasi-2D nanostructures [1, 5, 6, 8, 9, 66]. Additionally, one-dimensional (1D) and two-dimensional (2D) chalcogenide-based organic-inorganic hybrid nanostructures can be designed and synthesized [2].

II-VI compound semiconductors are direct bandgap material with wide-bandgap energies, and

ZnTe (Zinc Telluride), a prominent member of this family, has found widespread applications in optoelectronic devices such as detectors, green LEDs, and multi-junction tandem solar cells owing to its size-dependent characteristics, low resistivity, optical tunability, and dopability [80-82, 84-87]. The ethylenediamine, $C_2H_8N_2$, which serves as a spacer in α-ZnTe$(en)_{0.5}$ and β-ZnTe$(en)_{0.5}$, is an organic solvent at room temperature with a bandgap energy of 5.27 eV (± 0.03 eV), transitioning into a molecular crystal at temperatures below 10℃ [6]. Notably, while organic-inorganic halide perovskites are among the most extensively researched organic-inorganic hybrid materials, they face significant stability challenges; in contrast, the exceptional long-term stability demonstrated by β-ZnTe$(en)_{0.5}$ strongly suggests its potential as a promising candidate for (opto-)electronic applications [10, 66, 93]. The impressive long-term stability of β-ZnTe$(en)_{0.5}$ is primarily attributed to its intrinsic relatively large formation energy and conformation distortion induced sizable kinetic barrier, despite that the influence of oxygen, the most significant external factor, accelerates the degradation of the material in ambient conditions by lowering the thermal activation barrier and forming oxidation products [93].

Single crystal X-ray diffraction (XRD) reveals that these chalcogenide-based hybrid nanostructures possess orthorhombic crystal systems ($a \neq b \neq c$), and their atomic structures exhibit a striking resemblance to the ultrashort-period superlattice heterostructure $(GaAs)_n/(AlAs)_n$, the most extensively studied semiconductor superlattice examples grown by molecular beam epitaxy (MBE) [3, 10]. The solvothermal synthesis approach enables the creation of new hybrid nanostructures by tailoring the cation, anion, and length of the organic constituents where the organic compounds serve as effective spacers, solvents, reagents, and ligands within the synthesis process [1, 2, 5, 6]. Specifically, the formation of hybrid nanostructures is facilitated by the ability of organic molecules to be strong enough to break

three-dimensional ZnTe crystal lattices into two-dimensional ZnTe slabs [1]. Furthermore, the conversion of hybrid nanostructures can be achieved under mild conditions (e.g., α-$ZnTe(en)_{0.5}$↔ $ZnTe(pda)_{0.5}$ or β-$ZnTe(en)_{0.5}$↔ β-$ZnTe(pda)_{0.5}$), while high temperature can induce the reversion of these hybrid materials to their original state (e.g., β-$ZnTe(en)_{0.5}$ into ZnTe and en, and vice versa) [1].

The high-frequency dielectric constants, calculated using the Projected Augmented Wave (PAW) method are, $\varepsilon_x = 6.06$, $\varepsilon_y = 5.41$, and $\varepsilon_z = 4.88$, contrasting with the dielectric constant of ZnTe, which is 7.28 [6]. Materials exhibiting uniaxial or biaxial zero thermal expansion (ZTE) coefficients are often considered viable alternatives when isotropic ZTE material is unavailable; however, their anisotropic TE coefficients, despite isotropic volumetric ZTE coefficient, significantly degrade the conductivity due to grain boundary effects and the potential for the internal cracking induced by this anisotropy [8, 58, 163]. β-$ZnTe(en)_{0.5}$ shows exceedingly small uniaxial TE along the stacking direction (i.e., b-axis) between 4 K and 400 K, which can be attributed to the fact that organic materials typically exhibit negative TE coefficients (contraction upon heating), while inorganic materials typically exhibit positive TE coefficients (expansion upon heating) [8, 163]. Consequently, this opposing behavior effectively compensates for the TE of β-$ZnTe(en)_{0.5}$ along the stacking axis, making β-$ZnTe(en)_{0.5}$ a promising candidate for applications in high-efficiency semiconductor lasers, ultrathin window or transport layer for solar cells, and light-emitting and detecting devices [8, 163].

Figure 1 illustrates α-$ZnTe(en)_{0.5}$, which exhibits a wurtzite structure in the inorganic layer with some distortion and belongs to the space group of Pbca (No. 61) where two-dimensional ZnTe slabs are arranged along the stacking axis (i.e., c-axis) [1]. Specifically, the nitrogen atom is repeatedly connected to the zinc atom along the c-axis, resulting in the formation of a stable

tetrahedral coordination [1]. The ZnTe slab comprises a puckered 6^3 (honeycomb) net constructed from alternating, three-coordinated Zn and Te atoms [1]. These slabs are interconnected by bridging a nitrogen atom from organic spacers, positioned at the center of the Zn atom within the ZnTe slabs along the c-axis, forming (coordinate) covalent bonds in α-$ZnTe(en)_{0.5}$ [1, 2].

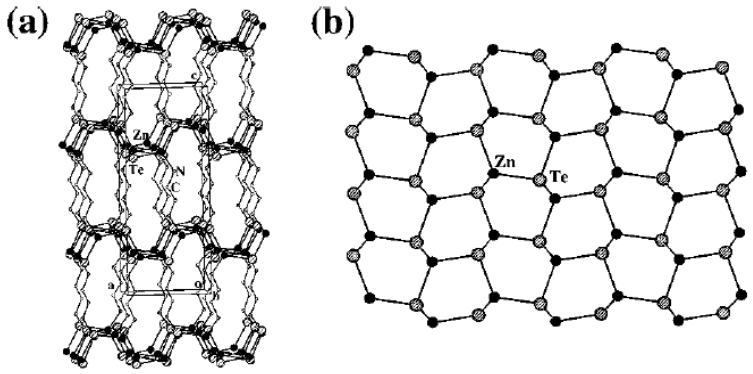

Figure 1: (a) Side view of α-$ZnTe(en)_{0.5}$ structure shown along the b-axis with the unit cell outlined. The large solid circles are Zn, shaded circles Te, and small open and singly shaded circles C and N, respectively. (b) The 2D (ZnTe) slab is projected along the c-axis [1].

Figure 2 illustrates β-$ZnTe(en)_{0.5}$, a polymorph of α-$ZnTe(en)_{0.5}$, where it grows normal to the (110) ZnTe slab, but the stacking axis (i.e., b-axis), topology of ZnTe slabs, and connectivity between zinc and nitrogen atoms differ from those in α-$ZnTe(en)_{0.5}$ [1, 5, 9]. β-$ZnTe(en)_{0.5}$ exhibits a zinc-blende structure in the ZnTe slab with some distortion and belongs to the space group of Pnnm (No. 58) where the zinc atoms from two (110) monolayers of ZnTe are connected to the nitrogen atoms from organic spacers, enabling the formation of stable tetrahedral coordination along the b-axis [1, 10, 66].

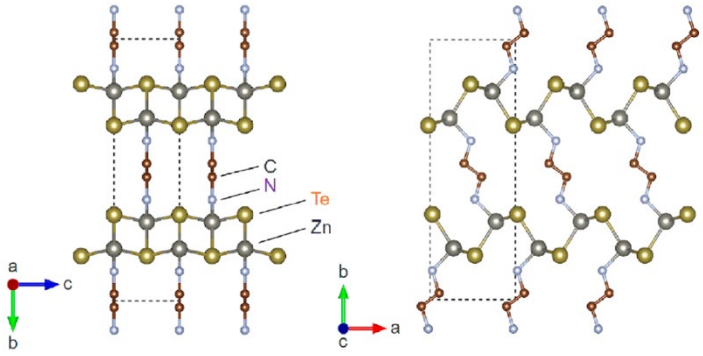

Figure 2: Crystal structure of β-ZnTe(en)$_{0.5}$ viewed along the a-axis and c-axis [10].

ZnTe(pda)$_{0.5}$ exhibits a wurtzite structure with some distortion and belongs to the space group of Cmc2$_1$ (No. 36), displaying a topology similar to α-ZnTe(en)$_{0.5}$, although the relative orientation of ZnTe slabs and connectivity of host materials (ZnTe) and organic spacer (pda) differ [1]. Carbon and nitrogen are observed in the crystal structure of II-VI-based organic-inorganic hybrid nanostructures, but hydrogen atoms are absent for clarity.

Strong quantum confinement effects (QCEs) are achieved when three-dimensional ZnTe crystal lattices are segmented into two-dimensional ZnTe slabs, resulting in an observed increase in the bandgap energy of ZnTe slabs compared to bulk ZnTe [1, 2, 6, 163]. QCE, a size-dependent effect and an inherent structural property of hybrid materials, qualitatively explains the substantial blueshifts observed in the absorption edge relative to bulk ZnTe; however, the extent of this blueshift is also affected by the property of organic spacers [2]. Low-temperature absorption and photoluminescence (PL) experiments can be employed to investigate changes in electronic properties of hybrid nanostructures, providing valuable insights into the emergence of additional absorption peaks, shifts in the bandgap energy, and the allowed energy transitions near the absorption edge [1, 5, 6, 92].

The bandgap energy of β-ZnTe$(en)_{0.5}$ is 3.719 eV (determined from the free exciton absorption peak at 1.5 K), exhibiting a large blueshift compared to the bandgap energy of bulk ZnTe (2.3805 eV), as determined from the free exciton transition energy [6]. Similar large blueshifts are also observed in other hybrid nanostructures (e.g., α-ZnTe$(en)_{0.5}$ and ZnTe$(pda)_{0.5}$) [1-2, 5]. The bandgap energy of β-ZnTe$(en)_{0.5}$ was found to be 3.55 eV based on room-temperature photoluminescence (PL) measurements. This temperature dependence is consistent with the observed bandgap energy of ZnTe (E_g = 2.39 eV at 4 K) is greater than the typically reported value of 2.26 eV at room temperature [6, 76-81, 84-89]. Specifically, this aligns with the expected behavior of semiconductors, where the bandgap energy generally increases at lower temperatures and decreases at higher temperatures, as described by the Varshni equation [142-144, 183].

Indeed, temperature-dependent variations in bandgap energy arise from thermal energy-induced intensification of atomic vibrations and lattice expansion at higher temperatures, resulting in enhanced electron-phonon interactions and bandgap reduction, in contrast, diminished lattice vibrations and slight atomic spacing contraction at lower temperatures lead to bandgap widening [141].

Beyond temperature effects, the observed attenuation of bandgap state intensity upon surface oxidation is a consequence of defect passivation, charge state modulation, and the formation of insulating oxide layers, all of which contribute to modifications in the material's electronic structure [138]. Additionally, variations in experimental methods and setups can also contribute to minor discrepancies in measured bandgap values [89].

The density of states (DOS) analysis reveals that the ZnTe slab plays a dominant role in the optical absorption of the band edge states, and these states can be engineered by manipulating the

dimensionality of the hybrid nanostructures [2, 5]. Electronic states near the band edge typically appear in pairs due to the presence of two ZnTe slabs within each period, and the splitting observed between these complementary states reflects the coupling strength between the two ZnTe slabs [6].

Furthermore, strong absorption peaks exhibit anisotropic even within the ZnTe plane, and additional absorption peaks are observed in the hybrid nanostructure that are not observed in bulk ZnTe [5, 6]. Although QCE leads to bandgap energy blueshifts in many nanostructures, the magnitudes are typically smaller in inorganic quantum wells and quantum dots than in these hybrid materials ($\Delta E_g \approx 1.0$ eV) [1-2, 4-6].

One of the major drawbacks of most organic-inorganic hybrid materials is their inherent instability under chemical and thermal stresses; however, β-ZnTe$(en)_{0.5}$ exhibits remarkable stability in ambient conditions, even under exposure to UV radiation and elevated temperature (up to 200 ℃), with no noticeable changes in its crystal structures, electronic, and optical properties. This exceptional stability is attributed to the presence of a strong covalent-like bond within the material [1, 8, 9]. Moreover, while high formation energy is generally considered a contributing factor to the long-term stability of hybrid materials, the presence of defects can still degrade their stability, even under ambient conditions [9, 10].

Figure 3 presents in situ Raman spectroscopy data of freshly made pristine β-ZnTe$(en)_{0.5}$ with N_2 flow [10]. A characteristic hybrid Raman peak at 133 cm^{-1} disappears above 240 ℃ [10].

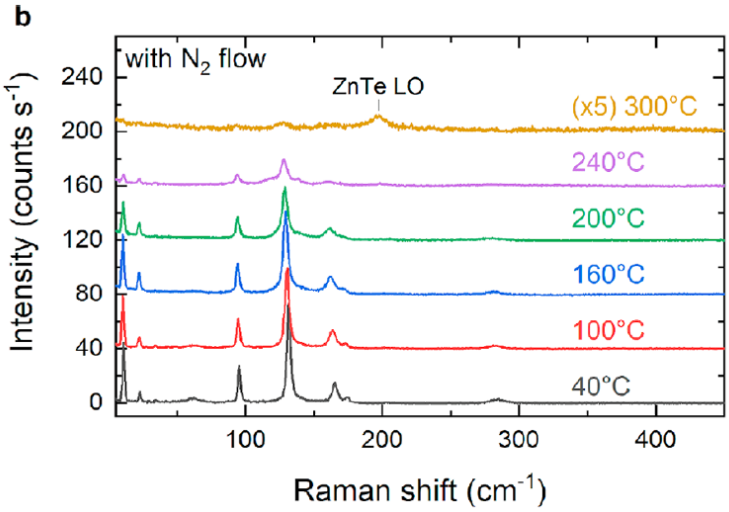

Figure 3: Thermal degradation of freshly prepared pristine β-ZnTe(en)$_{0.5}$ by in situ Raman spectroscopy with N_2 flow [10]

Figure 4 shows Raman spectra for hybrid nanostructures and bulk ZnTe [2]. The narrow Raman line width (FWHM = 0.8 cm^{-1} for β-ZnTe(en)$_{0.5}$) at low temperature (30 K) in high-resolution Raman spectra indicates a high degree of crystallinity comparable to high-quality elemental or compound semiconductors with superior surface quality, with distinct vibrational modes observed in these hybrid nanostructures that are absent in bulk ZnTe [2, 6, 9]. These newly observed phonon features can be explained by the band folding of the semiconductor-related modes (analogous to superlattices) and coupling between the organic and inorganic constitutes, while Raman studies on the same nanostructures with varying dimensionality and topology reveal distinct spectral signatures [2].

Although typical Raman peaks exhibit a redshift with increasing temperatures, a significant blueshift (56.0 cm^{-1} at 30 K vs. 63.2 cm^{-1} at 300 K) and several modes with weak temperature dependence are observed in β-ZnTe(en)$_{0.5}$ [8].

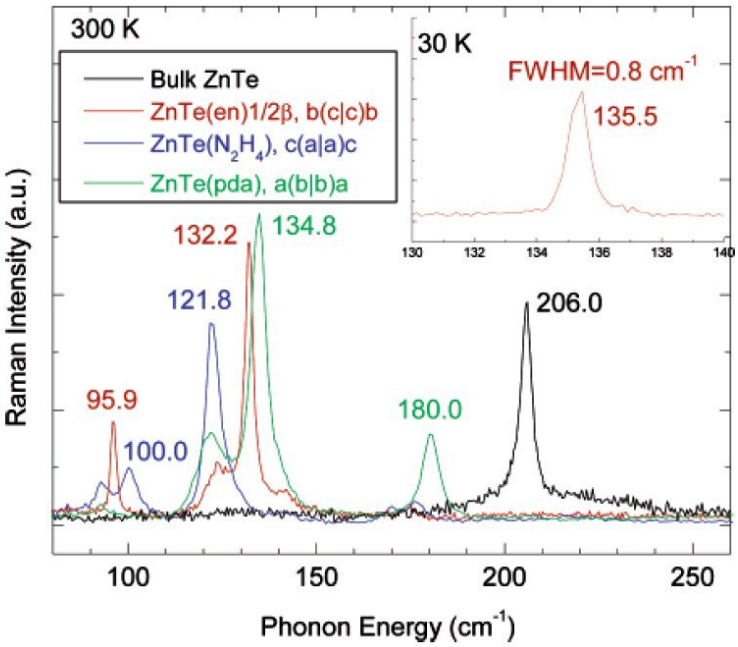

Figure 4: Raman Spectra for Bulk ZnTe, 3D β-ZnTe(en)$_{0.5}$, 2D ZnTe(N_2H_4), and 1D ZnTe(pda) measured at 300K. The insertion is a hybrid peak of β-ZnTe(en)$_{0.5}$ measured at 30K [2].

Figure 5 shows the Raman spectrum of β-ZnTe(en)$_{0.5}$ acquired using a 532 nm laser with a backscattering geometry along the b-axis, demonstrating the material's long-term stability through the persistent presence of the hybrid Raman peak at 133 cm^{-1} under ambient conditions; however, partially degraded β-ZnTe(en)$_{0.5}$ exhibits tellurium Raman peaks at 124 cm^{-1} and 142 cm^{-1}, with the hybrid Raman peak vanishing in severely degraded β-ZnTe(en)$_{0.5}$ [10, 80].

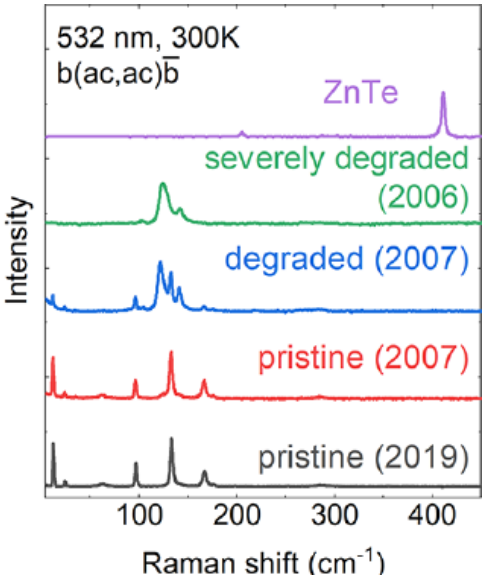

Figure 5: Raman spectra of β-ZnTe(en)$_{0.5}$ [10].

For over two decades, the scientific community has actively researched 2D materials, a category of low-dimensional nanostructures defined by their ultra-thin, nanometer or single-atom layer structure, electron confinement to two dimensions, and resulting markedly different and exceptional properties compared to bulk materials, where one axis is limited to a single or few monolayers (not exceeding a few nanometers) [100, 101]. Although these materials manifesting an atomically thin, sheet-like structure, exhibit unrestricted lateral dimensions and encompass a diverse range of properties, from insulating to highly conductive and from soft to extremely strong [102].

Indeed, the exceptional properties of 2D materials, stemming from their ultra-thin nature, including novel physical phenomena such as high carrier mobility, a high switching speed, low power dissipation, high surface area, quantum confinement effects, strong in-plane bonds (high mechanical strength and stability), van der Waals layer stacking for heterostructure creation

(easy exfoliation of single layers), and thickness-dependent tunable properties, making them versatile for diverse applications [100, 102].

The advent of mechanical exfoliation revolutionized 2D material studies by offering a simple and cost-effective method to obtain exceptionally high-quality and pure crystal samples, replacing the need for complex, cost-intensive growth processes and enabling wider exploration of fundamental physics [108, 109]. This breakthrough, coupled with the inherent properties of 2D materials, such as scalability, integrability, high surface-to-volume ratio, mechanical flexibility, chemical stability, tunable bandgaps, ultra-flat surfaces, strong spin-orbit coupling, and quantum confinement-induced direct-indirect bandgap transitions, has propelled their exploration [103].

Graphene, as the most widely researched 2D material, exemplifies these unique properties, exhibiting 2D semimetal behavior, high room-temperature charge carrier mobility, superior electrothermal conductivity, high specific surface area, exceptional optical transparency, large Young's modulus, quantum transport phenomena, a strong ambipolar electric field effect, and remarkable stability [55, 101, 102, 110]. Graphene's charge carrier mobility, minimally affected by temperature and thus limited by impurities or defects, can be improved through enhanced fabrication, while its low-noise nature and long electron mean free path, due to weak electron-electron interactions, contribute to its high environmental sensitivity [110].

However, despite these advantages, 2D materials, including graphene, face challenges. For example, although bandgap engineering in graphene has been demonstrated, the resulting reduction in carrier mobility compromises its practical efficacy, and its low light absorption limits optoelectronic applications [102, 103]. Furthermore, while 2D materials, with their atomically flat surfaces, were expected to form ideal ohmic contacts, interfacial Fermi-level

pinning commonly leads to large Schottky barriers and deviations from the Schottky-Mott rule, impeding efficient charge carrier injection [90, 97, 106]. Moreover, despite their atomically flat, dangling bond-free surfaces, which suggest promise for ohmic metal contacts, 2D materials present challenges due to the inapplicability of traditional doping methods and their extreme sensitivity to surface adsorbates, leading to complex interfacial states [106].

Graphene's success has spurred the discovery of diverse 2D materials like Group IV-V monolayers, layered double hydroxides (LDHs), transition metal oxides (TMOs), transition metal dichalcogenides (TMDs), MXenes, phosphorene, silicene, antimonene, and hexagonal boron nitride (h-BN), each exhibiting unique physicochemical properties and superior performance compared to their bulk counterparts [100, 102]. 2D materials generally offer high device performance due to their unique properties; however, graphene and h-BN suffer from unsuitable bandgaps, and though tunable, their control is difficult [107]. In contrast, TMDs provide a wide range of easily tunable bandgaps, making them superior alternatives for field-effect transistors (FETs) applications [103].

As Moore's Law nears its limits, necessitating alternative materials for continued circuit performance advancements, these newly discovered atomically thin 2D materials have emerged as a prominent focus for post-silicon era electronics [104, 109]. The inherent physicochemical properties of these 2D materials suggest diverse fabrication methodologies for 2D structures; consequently, a strategic selection of synthetic routes, informed by the properties of constituent materials, enables the construction of 2D superlattice materials, thereby facilitating enhanced performance [100].

To address the limitations of individual 2D materials, heterostructures formed by van der Waals stacking have emerged. By integrating varied 2D materials, researchers can broaden their

physicochemical properties, design novel device architectures, and generate new functionalities [100, 103]. 2D superlattice heterostructures, created by controlled alternating or periodic stacking of distinct 2D monolayers, further expand the possibilities, offering tunable (opto-)electronic properties, ultrafast charge transfer, and tailored physicochemical attributes [100]. Fabricating devices from mechanically exfoliated 2D materials is challenging due to their micron-scale size, random distribution, and irregular shapes, hindering precise patterning and metal contact alignment; while EBL is slow and defect-inducing, optical lithography, enhanced by innovative alignment mark designs, offers a solution to these limitations, enabling channel fabrication on graphene with a 2 μm width [109]. The synergistic combination of EBL for metal contact patterning and helium ion beam milling for sub-nanometer graphene carving by sputtering enables unprecedented precision and yield in fabricating advanced nanoelectronic devices, crucial for exploring quantum effects and developing next-generation technologies [110].

Efficient 2D material device operation crucially depends on electrical contacts, as high contact resistance, especially in top contacts limits performance; therefore, edge contacts, offering superior orbital overlap and reduced tunneling barriers, are preferred for optimal carrier injection [105]. Despite TMDs' potential for FET applications, high contact resistance due to interfacial charge transfer remains a challenge, mitigated by selecting TMD-metal combinations based on lattice mismatch to induce phase transitions for enhanced charge transfer and ohmic contact formation [102-103, 105-107].

2D materials promise transformative advancements in sensing, MEMS/NEMS, optoelectronics/photonics, neuromorphic computing, and quantum technologies [104]. Notably, 2D heterostructures are poised to revolutionize topological quantum computing [104]. The

fabrication of superlattice structures composed of organic/inorganic hybrid materials necessitates the strategic molecular integration (intercalation and polymerization) of organic molecules within the interlayer regions of the inorganic 2D components [100]. This approach, by enabling controlled defect engineering and offering tunable properties through the strategic combination and interfacial modification of distinct materials, provides a versatile platform for designing high-performance electronic devices and gaining insights into interfacial interactions, thereby guiding optimal material selection [103]. Furthermore, organic-inorganic heterostructures, by combining the low-cost, scalable synthesis, tunable functionalities, and high light absorption of organic materials with the high quality, mobility, and structural integrity of 2D van der Waals inorganic materials, offer a versatile, flexible, and adaptable platform for creating customized advanced optoelectronic devices and expanding application spaces by mitigating the limitations of each component through their complementary strengths [103].

Despite progress, challenges remain in synthesis, application, and understanding interfacial interactions [100, 102, 103]. The widespread adoption of 2D materials requires addressing challenges in wafer-scale deposition, bonding, controlled interfaces, etching, and doping [104]. Future research should focus on exploring novel material combinations and utilizing advanced in situ/operando techniques to enhance performance [100].

A lithography-free method using carbon fiber microprobes ($d = 7\ \mu m$), as an alternative to metal electrodes, enables non-destructive electrical measurements on 2D materials, demonstrating comparable results to lithography-based methods while emphasizing that the probes' flexibility allows for placement on materials without surface damage, with a minimum placement separation of approximately 10 μm [108]. This highlights the ongoing development of innovative techniques to overcome fabrication and characterization challenges. The principles governing the

behavior of 2D materials are also observed within organic-inorganic hybrid nanostructures, as exemplified by the unique properties of β-ZnTe$(en)_{0.5}$.

The β-ZnTe$(en)_{0.5}$, while fundamentally a three-dimensional (3D) superlattice nanostructure, exhibits characteristics of a quasi-two-dimensional (quasi-2D) material [66]. This apparent contradiction stems from its unique architecture: a precisely layered heterogeneous structure wherein two ZnTe monolayers are interconnected by ethylenediamine (en) molecules, forming an alternating stack. This meticulous layering of inorganic (ZnTe) and organic (en) ligand creates a highly anisotropic environment, effectively confining electronic states within the ZnTe layers. Consequently, despite its 3D nature, the structure manifests quantum confinement effects, a phenomenon typically observed only in low-dimensional materials [6]. This behavior emphasizes the importance of considering not just the dimensionality of the constituent building blocks, but also the overall architectural arrangement in determining the electronic properties of complex nanostructures.

CHAPTER 3: SPACE-CHARGE-LIMITED CURRENT (SCLC)

3.1. Fundamentals of Space-Charge-Limited Current (SCLC)

The space-charge effect, which describes the phenomenon wherein the electromagnetic interactions between a charge particle flow and its surrounding structures exert a substantial influence on the flow's dynamics, was first observed by Thomas Edison, and has tremendously impacted vacuum and solid-state electronics applications [21, 60]. Understanding charge transport and its limitations is vital for advancements in device performance, circuit design, and material development [40, 49]. Early band theory models for solids like semiconductors or insulators suggest that as long as charge carriers are injected through either the conduction band or the valence band, they can move freely through an interface (i.e., metal-semiconductor or metal-insulator) with ohmic contact, where the currents are only limited by the charge carriers, which is analogous to a Space-Charge-Limited Current (SCLC) in a vacuum diode [13, 16-19, 21, 32, 48]. SCLC is the upper limit of steady-state current density that can be transported through a material [60]. For simplicity and to avoid confusion, the term 'semiconductor' will be used, even though many studies specifically refer to 'insulator' in their papers, because the classification of materials as either semiconductors or insulators is often roughly determined by their bandgap energy, with a somewhat arbitrary boundary [32, 123]. While electrons and holes are considered as the charge carriers, ions are also charge carriers in semiconductors; however, electrons are the only charge carriers in the vacuum diode. Although the contributions of both electrons and holes are evident, with some distinctions in SCLC, the term ‘electrons’ is often used to encompass both for brevity, with specific distinctions made when necessary [15].

Although SCLC originated in the 1930s as a semiclassical transport model for solid diodes, it persists as a significant research area for material scientists and device engineers, particularly in the experimental analysis of charge transport and trapping mechanisms [60]. Linear currents in SCLC current density-voltage (J-V) characteristics arise from equilibrium charge carrier flow at low voltages, doping-induced carrier density increases, or bulk charge carrier saturation at high bias or with large injection barriers, excluding trap and doping effects [121]. Despite the theoretical significance of the SCLC model, experimental evidence supporting its validity in semiconductors remained limited until the 1950s [16-17, 19, 34]. SCLC measurement, a convenient, simple, and powerful two-probe electrical technique, involves applying sequential voltage steps and recording the corresponding current [49-50, 52, 55, 91]. The interpretation of J-V characteristics of single-carrier devices is essential for SCLC measurements [52, 122]. Moreover, SCLC measurements do not require light illumination for charge carrier generation; instead, the injected charge carriers are responsible for the charge transport property [54]. This allows for the extraction of crucial charge carrier transport properties, including mobility, surface potential, electronic trap density, capture cross-section, and energy distribution of carrier trapping states in semiconductors; furthermore, direct data interpretation is possible on functioning optoelectronic devices [16-19, 22-24, 32, 34, 37, 41, 43-45, 49-50, 52, 54-56, 60, 91, 121-122]. The direct dependence of the SCLC model on mobility and trap carrier density reveals its inherent connection to the electronic properties, charge traps, and dopants of solids, and its functional relationship with applied field, temperature, and carrier density [60, 121-122]. While numerical models can describe mobility independent of field, temperature, and charge-carrier density, analytical approximations of mobility necessitate incorporating temperature dependence [121]. Furthermore, SCLC measurements offer the advantage that their measurement conditions

are similar to those of optoelectronic devices, and their low material demand is crucial for devices made from rare or expensive substances [55]. It is noteworthy that SCLC is one of the most sensitive methods to measure the presence of traps in semiconductors with a high degree of crystallinity and SCLC behavior with the trap presence can qualitatively explain the most observed current phenomena in devices with ohmic contacts [16-18, 58, 122]. SCLC measurements on single-carrier devices are a common technique for investigating charge carrier transport, particularly in organic semiconductors [43, 122]. In high-mobility inorganic semiconductors, while the rapid accumulation of injected charge carriers is fundamental to SCLC, the very high mobility can hinder the effective formation of a stable space charge region at lower voltages, making it challenging to achieve the ideal SCLC regime due to the potential for non-ideal injection (where transport could be limited by the rate at which charge carriers overcome a barrier, rather than the density of injected charge carriers itself due to barrier formation), the need to overcome the influence of intrinsic carriers, and the rapid transit of injected charges before a significant space charge can build up, whereas organic semiconductors, with their lower mobilities and significantly higher trap densities, readily exhibit space-charge-limited current behavior, though this is typically a trap-limited regime characterized by distinct current-voltage (I-V) characteristics that reflect the trapping and detrapping of charge carriers [36, 44].

Originally, proposed by Clement Child in 1911 to describe electron conduction in vacuum diodes (Child-Langmuir Law, $J \propto V^{1.5}$), the SCLC concept has been effectively adapted to describe charge carrier transport in semiconductors using Mott-Gurney law ($J \propto V^2$) [11-13, 19, 21-22, 29, 32, 47, 60, 62-63, 123, 196]. In addition, the Child-Langmuir law has been extensively modified to accommodate considerations like non-standard geometries, relativistic electron

energies, initial electron velocities, quantum effects, cathode surface electric fields, and slowly varying charge densities [63, 47]. SCLC mechanism has been extensively employed to investigate the electrical properties of semiconductors (≤ 300 K) due to their typically low free charge carrier densities, which facilitate the creation of charge imbalances under applied voltages, and in this regime, both charge carrier mobility and space-charge density, influenced by the semiconductor's permittivity, significantly contribute to SCLC [48, 53, 56]. The Mott-Gurney law provides a framework for interpreting SCLC behavior in devices with two symmetrical, ohmic contacts, enabling the study of charge carrier mobility through drift current in the intermediate voltage regime, specifically within the SCLC or Mott-Gurney regime, in trap-free and undoped single-carrier devices [11, 17-18, 23, 26, 30, 34, 36, 42-45, 52, 58, 62-63, 65, 91, 119, 122, 124]. A single charge carrier device (unipolar device) refers to a device in which only one charge carrier (i.e., electron-only devices or hole-only devices) is responsible for the current flow through the ohmic contact, with the maximum current limited by the space-charge density, encompassing both equilibrium charge carriers and injected charge carriers [23, 44, 50, 52-55, 121-122]. In single charge carrier devices, where current-voltage behavior is governed by the mobility and concentration of injected charge carriers and the electric field, rather than electron-hole recombination, the current density in an undoped electron-only device with optimal contact injection becomes primarily determined by the Mott-Gurney law, independent of the equilibrium electron concentration [43, 50, 52, 121-122, 124]. Ideal ohmic contacts, characterized by zero barrier height, eliminate injection barriers at the metal-semiconductor interface, enabling efficient charge carrier injection into the semiconductor, and enhancing the SCLC mechanism [30, 50, 56, 121-122, 124]. In an ideal single charge carrier device with an ohmic contact, charge carrier injection is unrestricted, and the resulting current flow becomes limited solely by the

accumulated space-charge, which can ultimately diminish the electric field at the injection contact to zero [30, 50, 52, 119-120, 122, 124]. To ensure current continuity when the electric field at the injecting contact is zero, an infinite carrier concentration at the boundary is required [119]. In contrast, under non-ohmic contact conditions, the total barrier height, which influences the charge transport property, is the sum of the internal diffusion barrier height (V_{bi}) and the injection barrier height ($\emptyset_{Bn}^{SM}$) [49-50, 121, 131]. The injection barrier height is the same as the Schottky barrier height in ideal cases where interface states or dipoles are ignored, whereas, in real devices, the interface plays an important role in charge carrier transport [39, 90, 121]. Herein, this ideal condition is applied. It is important to note that, for SCLC analysis of single charge carrier electron device only, the terms 'injection barrier height' and 'Schottky barrier height' are synonymous and will be used interchangeably without loss of ambiguity. However, these terms differ from the conventional built-in voltage (diffusion barrier height) found in most metal-semiconductor (MS) junctions, which is defined as the difference between the work function ($\emptyset$) of the metal and the semiconductor [43, 57, 70-71, 96, 124, 133]. Furthermore, the injection barrier height for electrons differs from that for holes. The equilibrium charge carriers exist within the semiconductor under thermal equilibrium conditions without applied bias, while injected charge carriers originate from the metal to the semiconductor or vice versa under an applied voltage. In an ideal single charge carrier device, all injected charge carriers remain free, and they all contribute to the space-charge carriers, resulting in SCLC at the Mott-Gurney regime [34, 50, 52, 56, 122-123]. The current-voltage (I-V) characteristics of a metal-semiconductor-metal (MSM) junction are expected to be highly asymmetric when Schottky barrier effects are dominant [41].

The space-charge carriers are typically observed in the depletion region (space-charge region) of pn-junction, metal-semiconductor junction, and the near cathode region of the vacuum diode. In the space-charge region of the pn junction, recombination occurs due to the diffusion of excessive majority charge carriers driven by the carrier concentration gradient across pn junction interface, leading to charge carriers depletion near the junction interface. In contrast to the pn junction, where electron-hole recombination occurs, electron liberation from the cathode in a vacuum diode leads to the accumulation of electrons near the cathode, forming an electron cloud, since the electron emission occurs more rapidly than the time required for the emitted electrons, accelerated by the electric field, to reach the anode. It's important to note that the physical properties of a semiconductor influence the behavior of injected charge carriers flowing through an ohmic contact, which introduces complexities not accounted for in the ideal model [32].

The Mott-Gurney law provides a foundational description of SCLC behavior in ideal devices. While the Mott-Gurney law is the standard for SCLC analysis, it's crucial to acknowledge its inadequacy in describing semiconductors with doping or trap states [55, 121]. However, real materials exhibit non-ideal characteristics, such as disorder and impurities, which introduce trap sites and necessitate corrections to the Mott-Gurney law [11, 19, 23-24, 26, 44, 91, 121- 122]. Charge carrier mobility, influenced by temperature, electric field, and carrier density, reflects the broad density of states (DOS) in these materials, which modifies the current-voltage relationship due to trap-like tail states, often modeled as an exponential distribution rather than a Gaussian broadening [45, 58, 121]. Shallow traps are often attributed to localized tail states within the band gap [58]. In a single charge carrier device, carrier mobility and SCLC are functions of temperature, carrier density, and electric field at high bias voltages, whereas mobility is generally constant at low bias voltages and room temperature [40, 121]. SCLC measurements have been

proven valuable for investigating mobility, trap density, and trapping sites in complex materials like hybrid halide perovskites, which exhibit mixed ionic-electronic conduction mechanisms [46, 53-54, 158]. Yet, the interpretation of SCLC measurements in the perovskites is complicated by significant variability in reported mobility values, influenced by experimental techniques, sample conditions (chemical composition and morphology), and other factors [53]. Time-of-flight (TOF) spectroscopy minimizes the influence of contact barriers by using one blocking contact and surface effects, making it useful for studying the charge carrier mobility [38, 46, 49]. A significant drawback of the TOF technique is that it necessitates films thicker than 1 μm and with low conductivity [44, 49-50]. In contrast, when comparing SCLC and TOF techniques in organic semiconductors, a small discrepancy in electron mobility values is observed, which is readily explained by differing measurement conditions [30, 46]. In organic semiconductors, where systematic charge transport studies were conducted, SCLC analysis was proved to be the sole technique capable of consistently extracting mobility values across all devices [44]. Furthermore, when comparing different materials, it is noteworthy that while SCLC, TOF, and Hall effect measurements yield a wide range of mobility values for the perovskites ($\mu_{perovskite}$ = $1\times10^{0} \sim 1\times10^{2}$ $cm^2/(Vs)$), the electron mobility values of β-$ZnTe(en)_{0.5}$ along the a-axis and c-axis are within the mobility range of the perovskite, despite its significantly lower mobility along the stacking b-axis ($\mu \approx 10^{-3}$ $cm^2/(Vs)$) [10, 46, 53, 59].

A strategic methodology is necessitated to achieve the first critical condition for two-carrier SCLC, which requires symmetrical electrodes with metal's work functions closely aligned to the semiconductor's electron affinity and ionization energy. Achieving ohmic contact formation for two-carrier SCLC is complex, requiring precise execution beyond mere metal selections, as any deviation could disrupt essential conditions, complicating the process beyond the challenges of

single-carrier ohmic contact formation [57, 70-71, 96, 133, 136]. To ensure the perfect injection of both electrons and holes, the introduction of unintended consequences, such as the creation of new traps within the semiconductor that would impede carrier flow, must be prevented during the contact formation process. The objective is to create contacts that enable balanced injection while protecting the integrity of the semiconductor material and maintaining the ideal conditions necessary for accurate two-carrier SCLC measurements.

Despite the simplification of a trap-free semiconductor and idealized boundary conditions, the theoretical framework developed for two-carrier SCLC provides valuable fundamental insights into charge transport [20].

Figure 6 depicts a simplified scenario illustrating SCLC behavior where a semiconductor has two symmetrical ohmic contacts. When the work function ($\emptyset$) of the metal electrode is closely aligned with the electron affinity (χ) of the semiconductor, injected electrons from the electrode connected to the negative terminal can readily inject and transfer into the conduction band of the semiconductor, accumulating near the electrode region of the semiconductor [16, 19, 44, 51, 57-58, 121-122]. This region of accumulated free electrons (i.e., space-charge electrons) is termed the space-charge region, and these space-charge electrons are rapidly transported toward the other side of the electrode when an electric field is applied [16, 44]. Once the space-charge sufficiently reduces the electric field at the injecting contact, the device reaches charge saturation, with new charge injected solely to replenish that extracted at the opposing electrode [44]. This flow of charge carriers significantly enhances the conductivity of the semiconductors within Mott-Gurney regime, leading to a maximum steady current when the injection of charge carriers, and consequently the space-charge density, remains constant [17].

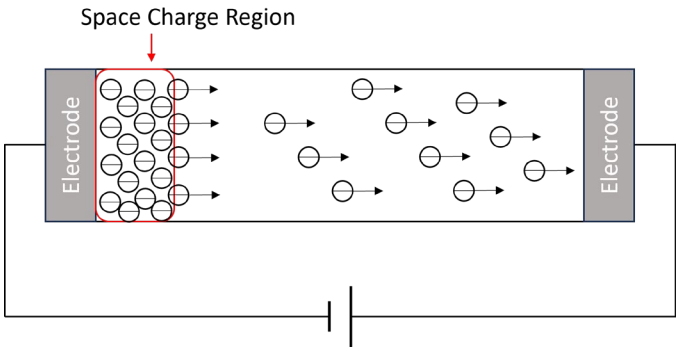

Figure 6: Simplified schematic drawing to explain SCLC in the semiconductor with two symmetric electrodes

Although ideal SCLC models emphasize the injecting contact's role in determining current flow through efficient carrier injection and space-charge formation, treating the collecting contact as a passive sink, real devices demonstrate that the collecting contact's properties can significantly influence SCLC behavior by affecting extraction, recombination, and field distribution, particularly in non-ideal conditions [119-120, 123]. In analyzing these real devices, particularly within the Mott-Gurney regime, it's crucial to understand the conditions under which the theoretical assumptions hold. While precise voltage thresholds for Mott-Gurney regime are not explicitly defined, the mobility value is expected to remain independent of the applied voltage as long as the electron temperature remains comparable to the semiconductor temperature ($T_{electron}$ is not always the same as $T_{semiconductor}$), ensuring the validity of the Einstein relation $\left(\frac{D}{\mu} = \frac{K_B T}{q}\right)$ [16, 43, 45, 92, 122].

Furthermore, the applied electric field should be moderate to avoid several critical effects, including the excitation of electrons from high-lying trap states into the conduction band, the

removal of electrons from ionized traps, and the capture of electrons by ionized trap states within the semiconductor [16].

The current-voltage (I-V) characteristics of semiconductors can exhibit various features, including a rapid current rise at a certain voltage, and several plausible explanations contribute to this behavior, such as poor contact, barriers, heating effects, collision ionization of trapped or valence electrons, and field emission from electrodes, traps, or valence band [16, 24, 32]. Collision ionization (impact ionization) occurs when a high-energy particle (typically an electron) collides with an atom or molecule, transferring enough energy to eject an electron and create an ion-electron pair; this process is important in semiconductor physics, especially in high-field regions, and can cause avalanche multiplication of carriers. Although ohmic contacts mitigate poor contact and field emission from the electrodes, complete elimination of all barriers is not always achievable [16, 57, 71]. The low currents and linear I-V characteristics under steady illumination, along with the use of a moderate field, help prevent heating effects, rule out collision ionization, and minimize field emission from traps or the valence band, thereby limiting their impact on electron temperature [16, 17].

Deviations from the ideal Mott-Gurney law can arise from non-ideal conditions, such as the non-ohmic contact, oxidation of metal contact, and neglecting the diffusion contributions, which are primarily caused by the concentration gradients but can be weakened by traps and disorder [22, 24, 44, 50, 91, 122]. Due to inherently weak intermolecular interactions in organic semiconductors, defect-induced localized bandgap states emerge, trapping charge carriers at varying timescales [58]. Consequently, these traps significantly impact diffusion currents and overall device performance, necessitating their careful consideration in SCLC analysis [45]. Furthermore, experimental and drift-diffusion simulation results have demonstrated that minor

deviations from the ideal SCLC model occur when a small injection barrier height (a few tenths of K_BT) exists [44, 50, 54, 97, 131]. In contrast, organic semiconductors exhibiting a moderate injection barrier height display well-defined SCLC characteristics, enabling accurate determination of charge carrier mobility, a result corroborated by other techniques such as the Time-of-flight (TOF) method and the field-effect-transistor (FET) method [30, 49-50]. The introduction of shallow traps enhances SCLC analysis by creating characteristic features in the I-V characteristics, which, when analyzed using appropriate theoretical models that also account for the influence of high electric fields on trap occupancy and detrapping rates, enable the determination of the energy distribution and density of these traps and provide insights into multiple trapping and release transport mechanisms [24, 26, 56].

The conductivity of semiconductors is directly proportional to charge carrier mobility ($\sigma \propto \mu$) and exhibits strong sensitivity to the temperature, pressure, and the presence of the impurities within the bandgap, where the energy required to excite an electron from the center of the impurities is less than that of intrinsic bandgap transitions [11, 53, 56]. Consequently, conduction in such materials is primarily dominated by impurity-mediated processes rather than intrinsic bandgap transitions in pure semiconductors with uniform properties, and in these semiconductors, such as compound semiconductors, deviations from perfect stoichiometry can lead to imperfection (impurities or defects), which can significantly influence the electrical properties [53, 56].

Furthermore, in highly doped semiconductors, charge carriers can tunnel through the thin potential barrier at the semiconductor-metal interface, contributing to the overall conduction mechanism, and this tunneling phenomenon results in low-resistance, non-rectifying (ohmic) contact behavior [56-57]. Increased semiconductor doping causes the current to become more

ohmic and less space-charge limited across the voltage range, diminishing the applicability of the Mott-Gurney law in the drift regime [55].

An analytical model, confirmed by simulations, supports the observation that thin film devices exhibit higher current levels than bulk materials due to injected electrons spreading beyond the film, resulting in a higher injection rate exceeding the Mott-Gurney law for bulk materials [28]. Charge carriers can also be trapped and stored in equilibrium states, with the occupancy of localized states directly impacting the magnitude of SCLC [58, 122]. Analysis of SCLC characteristics yields valuable information regarding the trap density (N_t), capture cross-section of traps (σ_n), and trap locations in the energy band diagram (E_t) [56, 122]. The capture cross-section of traps, given below, serves as a measure of the effectiveness of charge carriers to the center of defects or impurities, indicating the efficacy of the capture process,

$$\sigma_n = (\tau_t v_{th} N_t)^{-1} \quad \text{Eq. 1}$$

where τ_t is the trapping time, v_{th} is the thermal velocity, and N_t is the total number of traps [16, 27, 33, 57].

The probability of electron capture, which can be visualized as the volume swept per unit of time by electrons moving at thermal velocity, where an electron is captured when a trap state resides within this volume, highlighting the interplay between thermal motion and capture efficiency, is given below [195].

$$C_n = \sigma_n v_{th} \quad \text{Eq. 2}$$

Furthermore, the frequency of escape (f) represents the rate at which charge carriers (electrons or holes) are released from traps within a semiconductor, and is defined by,

$$f = \frac{\theta}{\tau_t} exp\left(\frac{E_c - E_t}{K_B T}\right) \quad \text{Eq. 3}$$

where θ is the free to trapped charge carrier ratio, influenced by the number and depth of traps, E_c is the conduction band edge, E_t is the trap energy level, K_B is the Boltzmann's constant, and T is the absolute temperature [27, 33, 51, 54].

Recent advancements in nanoscale fabrication techniques have spurred renewed interest in applying the Mott-Gurney law to analyze SCLC behavior in diverse optoelectronic devices across various size scales [31, 36, 39-41]. Driven by rapid progress in nanoscale technology, the successful fabrication of nanosized gaps between metallic electrodes, where spacing is comparable to the electron de Broglie wavelength $\left(\lambda_B = \frac{h}{p}\right)$, has propelled a renewed interest in exploring and applying the quantum analysis of the Mott-Gurney law, which predicts a linear current-voltage relationship in the quantum regime [47].

While SCLC analysis was initially focused on vertical device structures with two terminals, such as solar cells and LEDs, similar charge carrier transport behaviors are observed in lateral device structures with two or three terminals, for example, field-effect transistors (FETs), despite the differing device configuration [25, 28, 34, 36, 41-42, 49, 115-117, 125, 157, 192]. An analytical model developed for a thin semiconductor film with coplanar contacts, where film thickness and electrode dimensions are negligible relative to electrode spacing (10^2 μm ~ 10^3 μm), reveals two key observations: the transverse electric field's control over mobile charge density and the transition from ohmic to SCLC in lateral configuration [25]. Furthermore, fabricated FET arrays, with channel lengths from 500 nm to 50 μm, demonstrated stable, low-resistance contacts, revealing scaling effects, attributing observed channel length-dependent mobility and hysteresis

behaviors to SCLC dominance in shorter channels, with peak mobility at 5 μm [192]. To further understand these lateral devices, rigorous analytical work has been introduced to address the crucial role of contact configuration [25, 28]. The electrical conductivity of reduced graphene oxide FETs changed from ohmic to SCLC, with the transition occurring at progressively lower voltages as temperature decreased; at higher voltages, the SCLC exponent increased from 2 to 3 with decreasing temperature, indicating a transition from negligible to exponentially distributed traps [41, 58]. This observation can be explained by the temperature-dependent changes in charge carriers and trap densities: at room temperature, the free charge carrier concentration exceeds the trap state density, allowing for ohmic conduction. However, upon temperature reduction, the free carrier concentration decreases, resulting in the dominance of trap states through charge carrier localization, thus leading to the observed SCLC behavior and the shift of the ohmic-SCLC transition to lower voltages [41].

In addition to these structural considerations, SCLC devices with semiconductor thin films, exceptionally high currents occur, exceeding bulk property expectations. This phenomenon can be attributed to various factors, including quantum confinement effects, trap-assisted transport, surface states and interfaces, mobility enhancement, and field enhancement, all unique to thin films and localized charge carriers [28, 56]. By decreasing semiconductor thickness, the resulting increase in background charge carrier density, influenced by device geometry and electrostatics and capable of neutralizing traps or being replaced by the free charge carriers introduced through doping, allows to neglect the effects of traps and doping, but simultaneously makes the device more susceptible to injection barrier effects, which become negligible only in significantly thicker devices where the background charge carrier density is less affected by the barrier and injection from non-Ohmic contacts [122]. With all other conditions constant except for thickness,

as film thickness reaches a sufficiently small value, the total current remains constant, a result of a dynamic equilibrium where the expected current decrease from reduced film volume is precisely compensated by an increase in charge carrier injection, maintaining a constant current density [28].

Figure 7 provides a simplified schematic illustration of the lateral device configuration under study, depicting the transport mechanism of injected charge carriers based on established models (FETs) [116, 117]. While the real transport mechanism is more complex, this diagram highlights the existence of both vertical and lateral charge transport with distinct mobility components experienced by these carriers as they traverse the device [64-65, 57, 70-71, 96, 133]. Specifically, vertical transport from the injecting and collecting electrodes is associated with a vertical mobility $\mu_{\perp}$ (indicated by red arrows), while horizontal transport across the active region is characterized by a horizontal mobility $\mu_{\parallel}$ (indicated by blue arrows). This visual representation serves as a fundamental illustration to aid in understanding the anisotropic nature of charge transport within the lateral device structure.

Given that Figure 7 is based on FET models, it is important to note that while Shockley's equation is used to evaluate the charge carrier transport property, such as charge carrier mobility, in FETs, accurate charge carrier mobility values can be challenging to obtain due to factors like carrier concentration, disorder, charge trapping in the gate dielectric, contact effects at low gate voltage, and Coulombic interactions between charges at high concentrations [117].

The optimal performance of a single charge carrier device requires precise electrode dimension specifications, particularly ensuring that the transverse dimensions of the parallel electrodes exceed the interelectrode spacing to prioritize the injected charge carriers over thermally generated ones, a critical factor in achieving superior SCLC behaviors [25, 47]. Furthermore, it

is relevant to consider that while the fundamental SCLC mechanism persists in both two- and three-terminal devices when charge injection dominates, the gate voltage in three-terminal devices introduces additional control over charge transport, leading to distinct transport characteristics [28]. As expected, the longer interelectrode distance resulted in lower current values at the same voltage, corresponding to a higher observed resistance [116].

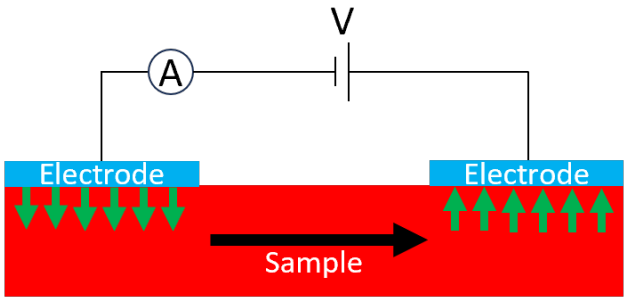

Figure 7: Simplified schematic diagram of lateral device configuration, illustrating the transport mechanism (based on [116] and [117]) of injected charge carriers: vertical transport from the injecting electrode ($\mu_{\perp}$, vertical mobility, green arrow), horizontal transport across the sample ($\mu_{\parallel}$, horizontal mobility, black arrow), and vertical transport into the collecting electrode ($\mu_{\perp}$, vertical mobility, green arrow).

Although the material thickness in lateral devices affects the available volume for charge transport and potentially the electric field profile to some degree, it is the interelectrode distance that serves as the primary parameter for mobility determination via SCLC, as it dictates the charge carrier transit length and governs the electric field and current flow [116]. Under the condition that the interelectrode distance is less than the electrode width, a two-dimensional theoretical framework becomes applicable, enabling the modeling of current flow within thin semiconductor layers as confined to an idealized, infinitely thin plane [25].

Although an energy distribution of defect states is commonly assumed to fit SCLC data, this simplification neglects the crucial roles of interactions between dopants and deep traps, as well as the Frenkel effect, which ultimately determines the current-voltage (I-V) characteristics and the capacity of SCLC to analyze deep trap levels [42].

Finally, it is noted that following its initial discovery, SCLC theory has been significantly expanded by refinements that address limitations in the basic scaling laws, including considerations of finite initial velocity, relativistic applied voltage, and quantum mechanical effects [29].

3.2. Assumptions, Requirements, and Limitations of Mott-Gurney Law on SCLC Analysis

The reliable interpretation of Mott-Gurney law regarding space-charge-limited current (SCLC) behavior relies on an idealized single charge carrier device (unipolar device), necessitating four conditions: 1) the material must be undoped and trap-free; 2) ideal ohmic contacts must exist at the metal-semiconductor junctions; 3) current flow must be dominated by space-charges rather than intrinsic charge carriers; and 4) only drift current, and not diffusion current, should be present within the Mott-Gurney regime, even in devices satisfying the first two conditions [16-17, 19, 26, 34, 43-44, 47-50, 52, 56, 58, 123]. Although weakly doped semiconductors violate the ideal conditions, their SCLC behaviors are used for analysis [52]. Furthermore, to achieve the second critical condition for single charge carrier SCLC, ensuring low contact resistance, a strategic methodology is mandated, requiring symmetrical electrodes with metal work functions closely aligned to the semiconductor's electron affinity (for electron-only devices) and ionization energy (for hole-only devices), and necessitating that one electrode facilitates efficient charge carrier injection while the other effectively blocks opposite polarity injection [44, 52, 121-122].

Additionally, to ensure unipolar charge transport for accurate SCLC mobility measurements, electron injection must be blocked in hole-only devices and vice versa, verifiable by comparing electrode combinations, while light emission testing can indicate bipolar transport through electron-hole recombination, though its absence does not confirm unipolarity [44]. While the effects stemming from doping or defects conflict with the third assumption, they must be low so that their contribution is negligible compared to the injected charge carrier density [52].

An ideal single charge carrier device fulfills these conditions, with only one type of charge carrier contributing to SCLC behavior [122]. Current flow is exclusively limited by space-charge carriers, primarily injected carriers, assuming the thermodynamically equilibrated carrier concentration is negligible [23, 34, 49-50, 52-53]. Injected charge carriers remain free within the space-charge region, thereby contributing to SCLC behavior [34, 50, 56]. This current flow mechanism closely resembles the conduction mechanism seen in vacuum diodes [13, 16-17, 19, 21, 32]. However, the Mott-Gurney law, derived using assumptions, all of which are frequently invalid in organic semiconductors (particularly the absence of charged defects) faces limitations in accurately modeling these materials, as while numerous trap-inclusive models exist that still rely on drift-only transport, trap presence often necessitates considering diffusion currents, hindering analytical approximations [43, 45]. Trap-assisted space-charge limited conduction is the primary source of electrical leakage in thin films (Cr_2O_2), where the density and distribution of charge traps are highly dependent on the underlying substrate [51].

In practice, the agreement between SCLC measurements and theoretical predictions is often inadequate, especially in experiments involving high-quality materials with low defect densities. First, the interpretation of I-V characteristics is challenging due to the inability to independently validate ideal conditions, leading to ambiguities, and even when theory aligns with experiments,

detailed analysis often reveals inconsistencies; second, significant variations in I-V curves among nominally identical samples make it difficult to compare experimental data with theory, highlighting potential gaps in understanding of SCLC transport [34]. Moreover, the presence of external series resistances, arising from thin film electrode materials, attenuates the voltage potential across the semiconductor film at elevated current levels, manifesting as a linear current-voltage characteristic and presenting a significant challenge in the characterization of high-mobility thin film materials [44].

Accurate interpretation of mobility values derived from the Mott-Gurney law is crucial, as these values derived from SCLC measurements differ significantly from those obtained in the ohmic regime due to differences in the dominant charge carrier species. Therefore, using mobility values extracted from SCLC analysis within the framework of Mott-Gurney law to subsequently calculate charge carrier density within the ohmic regime using Ohm's law can lead to erroneous results [49-50].

The applicability of the Mott-Gurney law, while SCLC occurs in various materials with impurities or defects provided ideal ohmic contacts are present, is limited to the intermediate voltage regimes due to two primary factors: 1) the theoretical derivation of the Mott-Gurney law assumes a zero electric field at the injecting contact, which may not accurately reflect experimental reality, where diffusion dominates near the injecting electrode, leading to inadequate boundary condition application; and 2) saturation current regimes at higher voltages, limited by the maximum achievable space-charge density, causing deviations from the expected current-voltage behavior [23, 28-30, 26, 50, 56].

It is important to understand that the behavior of charge carriers near contacts plays a significant role in these observations. When diffusion from Ohmic contacts significantly alters current-

voltage characteristics in thin organic single charge carrier devices, the drift-only approximation of trap-limited currents (shallow-trap SCLC) with an exponential trap distribution becomes unreliable for trap distribution analysis [45, 58, 60]. The inevitable presence of carrier-concentration gradients and space-charge near any contact indicates that current transport is predominantly governed by carrier diffusion in the vicinity of ohmic contacts, thus providing qualitative insights into metal-semiconductor contact behavior, and also influences the boundary condition for the Mott-Gurney law [22].

Non-ideal features of semiconductors, such as traps, energetic disorder, defects, impurities such as unintentional doping, and non-idealities within the charge carrier device, including injection barrier heights due to non-ohmic contacts, further complicate the analysis and cause discrepancies between the experimental results and theoretical predictions [19, 23-24, 43-44, 50, 91, 121-122]. Although significant efforts have incorporated non-ideal features such as traps into Mott-Gurney law, a direct assessment of its suitability for analyzing the behavior of ideal devices, particularly regarding the impact of the metal-semiconductor contact, has not been adequately addressed. This is crucial because an accurate description of charge carrier injections beyond equilibrium charge carrier density, especially at low and high applied voltages, is dependent on a realistic contact behavior [50].

Although the initial analysis of SCLC with a shallow trap neglected diffusion currents arising from the zero electric fields at the metal-semiconductor interface, Mott-Gurney law nonetheless remains a valuable qualitative analytical tool [23, 30, 45, 50, 56, 119-120]. However, its inability to fully elucidate charge transport in single-carrier devices emphasizes the necessity for a more comprehensive approach that considers the limitations and assumptions inherent in the Mott-Gurney law model [43, 50, 121]. Ultimately, understanding the requirements and limitations of

Mott-Gurney law in both ideal and non-ideal conditions is crucial for accurate analysis of charge carrier transport mechanism, especially given the growing interest in new applications of organic-inorganic hybrid materials and micro/nano-scale structures [23, 31, 36, 39, 40-41, 53]. Rigorous standardization of SCLC measurement protocols, encompassing data analysis and device fabrication, is essential to overcome inherent variability, particularly from thickness uncertainties and injection limitations, thereby ensuring reliable material benchmarking [44].

3.3. Mott-Gurney Law Derivation for SCLC

The derivation of Mott-Gurney law to describe space-charge-limited current (SCLC) behavior in an ideal scenario proceeds as follows. It is important to note that SCLC is one of the distinct regimes within a semiconductor device, occurring at intermediate voltages. In order to establish a comprehensive understanding of SCLC, a brief analysis of other relevant charge transport mechanisms is required. At very low voltages, thermal injection results in a pure diffusion regime, where carrier diffusion dominates. As voltage increases, a drift-diffusion regime prevails in the ohmic region, where both drift and diffusion contribute to current flow. At intermediate voltages, SCLC becomes the primary transport mechanism, as described by the Mott-Gurney law. Understanding these regimes provides a comprehensive picture of charge transport, highlighting the specific conditions under which SCLC becomes dominant.

In the pure diffusion regime, current transport is governed by carrier diffusion, described by Fick's law, yielding an approximately exponential relationship with applied voltage in the diode and a high degree of thermal sensitivity, as follows,

$$J_{diff} = J_n + J_p = \left(qD_n \frac{dn}{dx} - qD_p \frac{dp}{dx}\right) \quad \text{Eq. 4}$$

where q is the electric charge, D_n is the electron diffusivity, D_p is the hole diffusivity, n is the electron concentration in the conduction band, and p is the hole concentration in the valence band [22, 43, 70, 133]. It is important to note that the current expressed in this regime accounts for ideal ohmic contact formation, and the diffusion current deviates from Eq. 4 in the presence of a barrier height [52].

The diode diffusion current density is given by,

$$J_{diff} = \left(exp\left(\frac{qV}{K_B T}\right) - 1\right) \quad \text{Eq. 5}$$

where V is the applied voltage, K_B is the Boltzmann's constant, and T is the absolute temperature [32, 57, 65, 71].

As voltage increases, the total current density for two charge carriers is determined by the drift-diffusion equations, which are essential for providing the current density terms needed to fully describe carrier dynamics within the continuity equation, thus allowing for a comprehensive understanding of charge transport in semiconductor devices

$$J = \sigma E + \left(qD_n \frac{dn}{dx} - qD_p \frac{dp}{dx}\right) = q\left(n\mu_n + p\mu_p\right)E + \left(qD_n \frac{dn}{dx} - qD_p \frac{dp}{dx}\right) \quad \text{Eq. 6}$$

where σ is the conductivity, E is the electric field, μ_n is the electron mobility, and μ_p is the hole mobility [13, 22, 43, 45, 47, 52, 55-57, 65, 71, 119-120, 122, 133]. Mobility and the diffusion constant are related by the Einstein relation $\left(\frac{D}{\mu} = \frac{K_B T}{q}\right)$ [43, 45, 122]. While Einstein's

relationship strictly applies only to small concentration gradients, experimental data suggests its validity extends to conditions with moderate current densities [118].

At intermediate applied bias, where diffusion currents are negligible and total current density is dominated by drift, the current increases steadily and smoothly with voltage, albeit less rapidly than the exponential increase observed in the pure diffusion regime [22].

Conductivity, a measure of a material's ability to conduct electricity, is given by,

$$\sigma = q(n\mu_n + p\mu_p) \qquad \text{Eq. 7}$$

where all n and p have the same μ_n and μ_p, respectively, a constant mobility approximation was employed in the current density [11, 22, 28, 57]. The average mobility values are employed when it has the dependency on the electron energy where the electron energies are distributed within the range of the order of K_BT ($\approx 0.0259\ eV$ at room temperature T, K_B is Boltzmann constant) [11].

Conventional Ohm's law exhibits linear I-V characteristics, while ideal SCLC exhibits a quadratic I-V characteristics. Despite potential linear behavior at very low voltages within the SCLC regime, their underlying charge carrier dynamics differ significantly. Conventional Ohm's law has negligible space-charge carriers compared to the majority charge carriers, while SCLC is dominated by space-charge carriers [49, 122]. In complex materials where space-charge and majority carriers can exhibit differing polarities, such as in a pn junction, relying solely on photoconductive measurements to identify majority carriers is insufficient, necessitating the application of complementary analytical techniques [164].

In electron-only devices, unlike conventional Ohm's Law describing drift current, injected electrons from the metal contact into the semiconductor's conduction band, driven by an applied field, create space-charges and a current density deviating from Ohm's Law, similar to the behavior of a vacuum diode,

$$J = qn\mu E = \sigma E = \rho\mu E = \rho\mu\frac{V}{L} \quad \text{Eq. 8}$$

where ρ is the total carrier density, including both equilibrium charge carriers (n_0) and injected charge carriers (n), but with the equilibrium charge carrier density exceeding the injected charge carriers ($n_0 >> n$) [13, 18, 22, 26-27, 33, 35, 39-40, 47-51, 55-57, 91, 121, 123].

The drift velocity of the charge carriers, which depends linearly on the electric field, is given by [25].

$$v_d = \mu E \quad \text{Eq. 9}$$

Poisson's equation derived from Gauss's law is,

$$\frac{dE}{dx} = \frac{\rho}{\varepsilon} \quad \text{Eq. 10}$$

where ε is the permittivity ($\varepsilon = \varepsilon_o \varepsilon_r$), ε_o is the vacuum permittivity, and ε_r is the relative permittivity [22, 26, 34, 40, 43, 45, 47, 52, 54-56, 91, 119-120, 123, 196]. Substituting Eq. 10 into Eq. 8 yields current density below [34, 47, 54, 123].

$$J = \rho\mu E = \mu\varepsilon E\frac{dE}{dx} \quad \text{Eq. 11}$$

The electric field distribution within the device can be obtained by integrating Eq. 11 under steady-state current conditions, applying the boundary condition *E(0) = 0* [47, 123].

$$\int_0^x \frac{J}{\mu\varepsilon}dx = \int_0^x E\,dE \quad \text{Eq. 12}$$

$$\frac{Jx}{\mu\varepsilon} = \frac{1}{2}E^2 \quad \text{Eq. 13}$$

$$E(x) = \sqrt{\frac{2Jx}{\mu\varepsilon}} \quad \text{Eq. 14}$$

The magnitude of the electric field under uniform conditions is expressed.

$$E(x) = -\frac{dV}{dx} \quad \text{Eq. 15}$$

The electric potential is determined by integrating *E(x)* [47, 123].

$$V = \int_0^x E\,dx = \int_0^x \sqrt{\frac{2Jx}{\mu\varepsilon}}\,dx \quad \text{Eq. 16}$$

$$V(x) = \frac{2}{3}\sqrt{\frac{2J}{\mu\varepsilon}}x^{\frac{3}{2}} \quad \text{Eq. 17}$$

The current density is derived by substituting the length of the sample, L, for x, in Eq. 17 and then squaring both sides of the resulting equation. This process yields the well-known Mott-Gurney law as expressed below,

$$J = \frac{9}{8}\mu\varepsilon\frac{V^2}{L^3} \quad \text{Eq. 18}$$

where μ is the mobility in the SCLC regime [13-14, 17, 19, 24, 26-27, 30, 33, 38, 44, 47-50, 52-55, 60, 65, 91, 121-123, 186, 196]. Within the intermediate voltage regime, characterized by steady-state current where charge carrier injection and transport reach a stable condition under applied voltage, current transport is dominated by drift under applied bias and exhibits minimal temperature-dependence [22, 30, 35]. The L term in the denominator of Eq. 18 exhibits an inverse third-power dependency compared to the current density [119]. Both analytical and experimental results reveal this inverse third-power relationship for bulk materials ($J \propto L^{-3}$), whereas in thin films, specifically 2D lateral devices, the current density is inversely proportional to the square of the electrode length ($J \propto L^{-2}$) [25, 28, 48, 124]. Furthermore, while current density in 1D materials exhibits an inverse proportionality to material length, the geometry of both 1D and 2D materials plays a significant role in maintaining current density units consistent with those of bulk materials [48]. These dimensionality and geometrical factors result in a clear correlation between material thickness and the observed current-voltage (I-V) characteristics.

While the Mott-Gurney law neglects lateral effects, an analytical model shows that in lateral electrode configurations, lateral charge redistributions significantly influence SCLC in thin semiconductor layers due to a strong transverse electric field, which controls mobile charge density and is comparable to the longitudinal field [25].

Understanding the relationship between voltage regimes, material thickness, and charge carrier mobility is critical for understanding the charge transport property of devices. To further understand charge transport, consider charge carrier mobility, which refers to the capability of how quickly the charge carrier moves in a material in response to external fields, and high charge carrier mobility values are important in electronic and optoelectronic devices to achieve high switching speed and low power dissipation [102]. The Mott-Gurney law is predicated on the assumption of constant mobility; however, temperature-dependent mobility, governed by scattering mechanisms, is subject to complications arising from deep traps, dopants, and the Frenkel effect [42, 58]. This deviation from constant mobility, particularly in organic semiconductors, manifests in complex temperature-dependence of charge carrier mobility, ranging from band-like transport (mobility increasing with cooling) in high-quality crystals to thermally-activated hopping (mobility decreasing with cooling, Arrhenius relation, $\mu \propto exp(-1/T)$) in materials with higher trap densities, with transitions between these regimes influenced by factors such as drain-source voltage, semiconductor/dielectric interface strain, and ferroelectric dielectric polarization [58]. Although often assumed constant and field-independent, charge carrier mobility can exhibit field-dependent behavior, particularly in organic semiconductors and disordered materials where trap states significantly influence it, and this field-dependent charge carrier mobility is given below,

$$\mu(E) = \mu_0 exp\left(\gamma\sqrt{E}\right) \quad \text{Eq. 19}$$

where, is the μ_0 field-independent charge carrier mobility and γ is the field activation of the mobility [30, 43-44, 57, 60]. While the parameter γ is intended to represent the Poole–Frenkel effect's field dependence on current, its actual value is often influenced by traps and trap-induced diffusion currents [43-44]. The Einstein relation retains its applicability in disordered semiconductors, given that continuity equations are defined in terms of free carriers [43]. Substituting Eq. 19 into Eq. 18 results in the field-dependent SCLC,

$$J = \frac{9}{8}\varepsilon\frac{V^2}{L^3}\mu_0 exp\left(0.89\gamma\sqrt{E}\right) \quad \text{Eq. 20}$$

where the inclusion of 0.89 originates from the analytical model [26, 30, 43-44, 57, 60]. However, inherent limitations exist in models that assume uniform current density, necessitating the consideration of nonuniform current density for a more complete understanding of charge transport [29].

Mott-Gurney law, as presented in Eq. 18, predicts a square-law voltage dependence for charge carrier devices under space-charge-limited conditions, assuming a nearly constant Fermi level throughout the semiconductor, except in the vicinity of the electrodes [11, 15-17, 22, 48, 65, 119].

The region where Ohm's law is applicable exhibits linear transport characteristics, while non-linear transport characteristics emerge at a transition voltage when the injected charge carriers surpass the equilibrium charge carriers, leading to non-uniform electric fields and charge distributions dependent on sample geometry [65]. The transition between Ohm's law and Mott-Gurney regime occurs at transition voltage, $V_{Tr,\ Ohm\text{-}Mott\text{-}Gurney}$, where the current densities in both

regimes are equal. This transition voltage can be determined by equating the current density expressions from Eq. 8 and Eq. 18.

$$J_{Ohm's\ law} = J_{MG-law} \quad \text{Eq. 21}$$

Substituting the expressions for current density from Eq. 8 and Eq. 18 into Eq. 21 yields the following result.

$$qn\mu\frac{V}{L} = \frac{9}{8}\mu\varepsilon\frac{V^2}{L^3} \quad \text{Eq. 22}$$

This yields the transition voltage, $V_{Tr,\ Ohm\text{-}Mott\text{-}Gurney}$, from ohmic to Mott-Gurney regime [49, 51, 56, 56].

$$V_{Tr,Ohm-MG} = \frac{8qnL^2}{9\varepsilon} \quad \text{Eq. 23}$$

Eq. 21, Eq. 22, and Eq. 23 are only valid when the current flow is exclusively governed by space-charge carriers under the applied bias; however, significant variations in transition voltage are observed among samples, limiting the practical utility of Eq. 23 for predicting the transition voltage in charge carrier devices [49, 123].

Figure 8 depicts simplified schematic representations illustrating the conceptual difference between the formation of a virtual electrode and the progression of a moving electrode within a single charge carrier device, crucial for SCLC analysis. The virtual electrode effect, occurring during the ohmic-to-SCLC transition in semiconductors, is characterized by charge accumulation near the injecting contact [22]. Initially, ohmic conduction driven by drift and diffusion

transitions to SCLC, where space-charge dominates, exhibiting a quadratic voltage dependence (Mott-Gurney law). This virtual electrode formation, resulting from the enhanced injection, screens the real electrode and explains nonlinear current-voltage transitions [22, 28].

Virtual electrode formation is illustrated in Figure 8 (a). In the initial stages following voltage application to a semiconductor thin film with injecting and collecting electrodes, charge carriers are injected from the injecting terminal and begin to drift across the material under the influence of the electric field. However, as injection continues, a space-charge accumulates near the injecting contact, particularly pronounced in materials with lower mobility or a significant presence of traps. This localized charge buildup creates a region where the electric field is strong near the injecting contact but is effectively screened and weakened further into the bulk of the semiconductor. The boundary separating the charge-rich region near the injector from the relatively charge-neutral region deeper within the material constitutes the virtual electrode: a dynamic, voltage- and space-charge-dependent, non-physical region within a semiconductor, formed by charge distribution, acting as a shifting boundary for carrier injection [50].

Moving electrode progression from virtual electrode formation is illustrated in Figure 8 (b). With continued charge carrier injection over time, the space charge region occupied by the injected space-charge carriers expands further into the semiconductor film. Consequently, the virtual electrode, the boundary of this charge-filled region, propagates from the injecting contact towards the collecting contact. The moving electrode model specifically describes the SCLC resulting from this voltage-driven shift of the virtual electrode towards a physical electrode, typically under conditions of low injection barriers or equilibrium charge-carrier densities, yielding a unique current flow characteristic [50]. Behind the moving electrode (towards the injecting contact), the material exhibits a high concentration of injected charge carriers, while

ahead of it, the material remains relatively depleted. This dynamic boundary effectively acts like a mobile electrode, separating the portion of the device actively contributing to SCLC from the region yet to be significantly influenced by the injected space charge.

These simplified illustrations in Figure 8 aim to provide a fundamental understanding of these non-physical electrode concepts that are crucial in comprehending the spatial and temporal dynamics of charge transport under SCLC conditions. The virtual electrode can approach a physical electrode at high voltages [50].

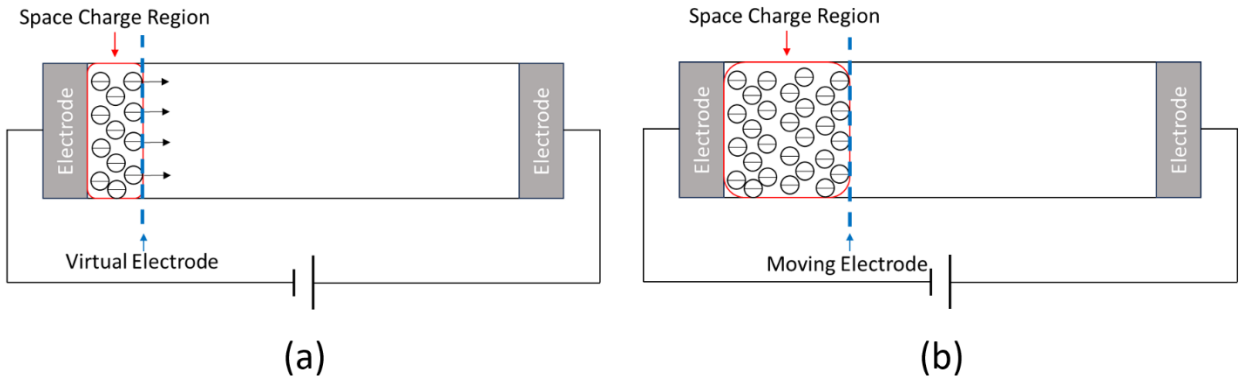

Figure 8: Simplified schematic representations illustrating the conceptual difference between (a) the formation of a virtual electrode and (b) the progression of a moving electrode within a single charge carrier device for SCLC analysis.

Typically, free electron density at the thermal equilibrium state, n_0, is generally less than the injected charge carrier density for SCLC devices [23, 34, 41, 56, 57]. However, under certain conditions, such as a low voltage regime at certain temperatures ($T > 0$), the free electron density at the thermal equilibrium state, n_0, can exceed the injected carrier density. As a result, Ohm's law might be used instead of the Mott-Gurney law. However, the observed linear I-V

characteristic is not a true ohmic current, as the behavior is not derived from the intrinsic charge carrier density but rather from space-charge carriers in the middle of the single charge carrier device [50-51, 56].

Some literature mistakenly utilized the intrinsic charge carrier density for ohmic conduction behavior at low voltage regimes in SCLC measurements, but the current flow is completely governed by the space-charge carriers; employing either the intrinsic charge carrier density or the doping concentration for analysis introduces significant deviations from ideal SCLC analysis [49].

In an ideal trap-free SCLC regime, carrier injection from the metal contact into the semiconductor is initially limited. However, as the applied voltage increases, a greater number of charge carriers are injected [124]. These injected charge carriers accumulate within the semiconductor, forming a space-charge region that significantly alters the internal electric field. Instead of immediately recombining or leaving the material, these injected carriers redistribute, creating a non-uniform charge density within the device. This redistribution leads to a non-linear electric field profile, which ultimately results in an increased current flow that follows the characteristic square-law voltage dependence described by the Mott-Gurney law (11, 15-17, 22). In the intermediate voltage regime (Mott-Gurney regime), the internal diffusion barrier (V_{bi}) becomes negligible, and the injected charge carriers accumulate in the space-charge regions, allowing the Mott-Gurney law to accurately describe the current behavior [17, 49-50, 123]. Under the ideal condition, the double logarithmic I-V characteristic of SCLC measurement exhibits a slope of 2, allowing for direct calculation of the mobility of the charge carrier (e.g., electrons or holes) using the Mott-Gurney law [18, 23, 49-51]. The intrinsic charge carrier

concentration is negligible, and the space-charge carriers dominate, contributing primarily to the drift current [50, 122].

In high voltage regime, a large number of injected charge carriers results in a uniform distribution of charge carriers within the device, and the absence of an injection barrier (effectively a zero injection barrier height) contributes to these uniform charge carriers across the single charge carrier device [50]. Furthermore, the condition where the density of states (DOS) is saturated, quantifying how many electronic states exist at each energy level within a material's energy bands, and the internal diffusion barrier height ($\underline{V_{bi}}$) is zero, is referred to as the charge carrier saturation limit or injection limit [23, 50-51, 56, 58]. Consequently, the semiconductor behaves like a metal, exhibiting a negligible internal electric field, while the electric field across the semiconductor is determined solely by the applied voltage due to the charge accumulation at the contacts [50]. The saturation limit, incorporating the injection barrier height, is given, along with the corresponding saturation current,

$$J = q\mu_n N_0 \frac{V}{L} exp\left(-\frac{q\emptyset_{Bn}^{SM}}{K_B T}\right) \quad \text{Eq. 24}$$

where N_0 is the effective density of states (DOS) for space-charge electron in the semiconductor at the surface in contact with the electrode and $\emptyset_{Bn}^{SM}$ is the Schottky barrier height for electrons [19, 22, 50, 90, 97, 122]. Eq. 24 is valid when the injection barrier height is greater than twice of $K_B T$ [23, 50, 57].

The approximate transition voltage between SCLC and saturation voltage is expressed as [19, 23, 122].

$$V_s = \frac{8qL^2N_0}{9\varepsilon} exp\left(-\frac{q\emptyset_{Bn}^{SM}}{K_BT}\right) \quad \text{Eq. 25}$$

While this transition voltage bears similarity to Eq. 23, the numerator of the expressions utilizes distinct charge carrier densities (*n* vs. N_0).

Pulsed I-V measurements are encouraged in SCLC measurement because, despite instrument resolution limitations causing some charge carriers to remain trapped before pulsed I-V measurements, using a small amount of light allows these measurements to approximate the theoretical trap-free SCLC behavior, revealing higher current values than steady-state measurements (AC or DC) and showing how trap presence deforms I-V characteristics in steady-state [16].

In single charge carrier devices, particularly in the low voltage regime, the moving electrode (ME) equation provides a more accurate interpretation of current flow than Ohm's law, as it incorporates both drift and diffusion, crucial for describing linear current flow [17, 18, 49-50, 55-56, 121]. This is because injected space-charge carriers from contacts, rather than intrinsic charge carriers (n_0), are the primary influence on linear current flows [49, 55]. In contrast, ohmic conduction, which is described by Ohm's law, assumes negligible space-charge region formation. Based on the principles of charge transport and electrostatics, the moving electrode model describes SCLC behavior by considering the redistribution of charge carriers due to the moving electrode, a conceptual representation of charge carrier injection or extraction at the device electrode, rather than physical movement of the electrode itself [49-50, 55]. Consequently, space-charge regions form, and the applied bias influences current flow by modulating charge carrier transport within the device.

The moving electrode equation for the charge carrier device is given below [50, 55, 121-122].

$$J = 4\pi^2 \frac{K_B T}{q} \mu_n \varepsilon \frac{V}{L^3} \quad \text{Eq. 26}$$

In contrast, the current density at high voltage regime (Eq. 24) shows the linear dependence on the applied voltage, which is similar to Ohm's law (Eq. 8) and ME equation (Eq. 26) in terms of linearity with voltage, but the current density in this high voltage regime is proportional to L^{-1} like Ohm's law (Eq. 8). This linear increase in current with applied voltage in the high voltage regime can be explained by the fact that the electron drift velocity (v_d) increases linearly with applied voltage, resulting in a linearly increasing current [19, 25].

Both the Mott-Gurney law (Eq. 18) and the moving electrode equation predicts a current density proportional to L^{-3}, indicating that the system is not injection-limited, and the thickness parameter dependence allows for distinguishing the linear I-V characteristic behavior predicted by Ohm's law (L^{-1}) from that predicted by the moving electrode equation (L^{-3}) [49, 119, 124]. However, even with this theoretical distinction, to accurately measure SCLC and avoid false mobility readings due to similar characteristics with injection-limited behavior, at least one ohmic contact condition must be satisfied, a condition difficult to verify experimentally, particularly in thinner films where poor charge injection becomes more problematic and necessitates a minimum film thickness for successful SCLC measurements [44].

The transition voltage, $V_{Tr\text{-ME-Mott-Gurney}}$, from the moving electrode equation to Mott-Gurney law can be determined by equating Mott-Gurney law (Eq. 18) and ME equation (Eq. 26).

$$J_{ME\ equation} = J_{Mott-Gurney\ law} \quad \text{Eq. 27}$$

Substitution of Eq. 18 and Eq. 26 into Eq. 27 gives the following.

$$4\pi^2 \frac{K_B T}{q} \mu\varepsilon \frac{V}{L^3} = \frac{9}{8} \mu\varepsilon \frac{V^2}{L^3} \quad \text{Eq. 28}$$

The transition voltage, $V_{Tr\text{-ME-Mott-Gurney}}$, is given below [49-50, 122, 131].

$$V_{Tr,ME-Mott-Gurney} = \frac{32\pi^2}{9} \frac{K_B T}{q} \quad \text{Eq. 29}$$

Eq. 29 demonstrates that the temperature is the only variable influencing $V_{Tr\text{-}ME\text{-}Mott\text{-}Gurney}$, and this transition voltage is typically around 0.9 V at room temperature ($V_{Tr\theta,ME\text{-}Mott\text{-}Gurney} \approx 0.9\ V$). For the single charge carrier devices, $V_{Tr\text{-}ME\text{-}Mott\text{-}Gurney}$ (Eq. 29) provides a more accurate transition voltage than $V_{Tr\text{-}Ohm\text{-}Mott\text{-}Gurney}$ (Eq. 23), as both the Mott-Gurney law (Eq. 18) and the moving electrode equation (Eq. 26), used to derive, $V_{Tr\text{-}ME\text{-}Mott\text{-}Gurney}$ (Eq. 29) are based on space-charge carriers, the relevant charge carriers for SCLC analysis.

The total drift current density, obtained by summing Eq. 18 and Eq. 26, can be used to fit the entire J-V curve, enabling the extraction of charge carrier mobility in intrinsic and single charge carrier devices with ideal ohmic contacts, as described below [55, 121].

$$J = 4\pi^2 \frac{K_B T}{q} \mu\varepsilon \frac{V}{L^3} + \frac{9}{8} \mu\varepsilon \frac{V^2}{L^3} \quad \text{Eq. 30}$$

It is noteworthy that Eq. 30 overlooks the significant impact of traps, which are commonly found in organic semiconductors [121].

As a consequence of the fourth assumption of the Mott-Gurney law (only drift current), the electric field within the charge carrier device increases, as detailed below,

$$E(x) = -\sqrt{\frac{2Jx}{\mu_n \varepsilon_0 \varepsilon_r}} \quad \text{Eq. 31}$$

where J is the current density in x direction and x is the spatial distance from the injecting contact [50]. The charge carrier density for electrons can be derived using Gauss's law, as shown below [50].

$$n(x) = \frac{1}{q}\sqrt{\frac{J_x \varepsilon_0 \varepsilon_r}{2\mu_n x}} \quad \text{Eq. 32}$$

In the SCLC regime, the electron density *n(x)* diverges near the injecting electrode ($x \rightarrow 0$) due to significant charge accumulation, decreasing proportionally to x^{-1} with increasing distance from the contact, a behavior precisely characteristic of SCLC where 'diverge' signifies an extremely high, idealized as infinite, electron density indicative of strong space charge effects at the injecting contact.

Incorporating the injection barrier height into the Mott-Gurney law modifies the expression, introducing a Schottky barrier height for electrons, and resulting in lower current density values compared to the ideal condition (Eq. 23),

$$J = \frac{9}{8}\mu\varepsilon\frac{(V - \emptyset_{Bn}^{SM})^2}{L^3} \quad \text{Eq. 33}$$

where $\emptyset_{Bn}^{SM}$ is the Schottky barrier height for electrons [38, 52, 90-91, 97, 121, 131, 158]. The manifestation of SCLC behavior in the presence of a Schottky barrier height necessitates the application of an external voltage exceeding the magnitude of the injection barrier height, provided that other confounding variables are not considered [19]. Similar to ideal SCLC, the intermediate voltage regime features drift-dominated transport and minimal temperature-dependence under steady-state conditions, with the key difference being a Schottky barrier height stemming from non-ohmic contacts [22, 30, 35]. Due to the challenges in obtaining suitable contact materials, SCLC measurements are commonly performed on asymmetric single-carrier devices, which are easier to fabricate than symmetric ones, and in these devices, the barrier height significantly influences the current density-voltage (J-V) characteristics at low and intermediate bias voltages until the barrier height is overcome [121].

In SCLC analysis, the ohmic contact condition is satisfied when the electron affinity of the semiconductor (χ) is identical to the work function of the metal [121-122]. Therefore, the Schottky barrier height in Eq. 33 differs from the diffusion barrier height (V_{bi}) found in most metal-semiconductor junctions, which is defined as the difference between the work function of the metal and the semiconductor [57, 70-71, 96, 133]. The Schottky barrier height for electron SCLC, as defined by the Schottky-Mott rule, is given below,

$$\emptyset_{Bn}^{SM} = \frac{\chi - \emptyset_m}{q} \qquad \text{Eq. 34}$$

where χ is the electron affinity of the semiconductor and $\emptyset_m$ is the work function of the metal [50, 52, 90-91, 97, 121-122]. While Eq. 34 can, in principle, account for barrier height alongside applied voltage, similarly to Eq. 33, this approach is unreliable due to dissimilar band diagrams

between symmetric and asymmetric devices (in which applied voltage is zero and equal to barrier height, respectively) and because the barrier height is rarely known precisely and is often approximated by shifting the voltage axis to a square-law regime, potentially causing misinterpretations of carrier mobility, especially with traps present [121]. An analytical expression describing the Schottky barrier height in an asymmetric single-carrier device from the ratio of the currents in the forward and reverse bias allows for easy and direct determination of the $\emptyset_{Bn}^{SM}$ without prior knowledge of charge-carrier mobility, benefiting SCLC measurements by eliminating the need for complementary barrier height measurements [52]. While this analysis simplifies barrier height determination, it's important to note that the presence of traps in actual devices introduces detailed energy and concentration contours, as most real devices include a certain degree of traps [118-120].

The ideal Mott-Gurney equation (Eq. 18) is derived from Eq. 33 when the electron affinity of the semiconductor and the work function of the metal within Eq. 34 are set to be equal, representing ideal ohmic contact for SCLC analysis. While this ideal condition is a simplification, SCLC behavior is observed, and the charge carrier mobility can be successfully determined using the ideal Mott-Gurney law equation in organic semiconductors with a moderate barrier height, as obtained from temperature-dependent SCLC measurements. [30].

3.4. The Effects of Impurity, Doping, Defects, and Device Thickness in SCLC Analysis

Impurities and defects can all give rise to traps that influence a material's electrical properties and cause deviations from ideal Mott-Gurney law predictions in SCLC analysis [13, 14, 18-19, 22, 24, 44, 49, 55-56, 61, 64, 67, 71, 122]. The temporary capture and subsequent release of charge carriers by traps, facilitated by external stimuli like electric fields, thermal energy, or

photons, occurs through models such as multiple-trap and release, band-like transport, or hopping/tunneling [58]. Impurities, encompassing both intentionally introduced dopants and unintentionally present foreign atoms within the semiconductor crystal lattice, can alter the material's electrical, optical, and structural properties, with doping, the deliberate addition of specific impurities (dopants), controlling conductivity by modifying free charge carrier concentration and consequently influencing both the transition voltage (V_{Tr}) and the magnitude of SCLC [44, 49, 57, 61, 64, 122]. Proper doping elevates low-field conductivity, whereas improper doping creates deep traps that effectively raise the built-in voltage, altering the current-voltage behavior [44, 122]. While both impurities and dopants are foreign atoms within the semiconductor lattice, the key difference is the intent behind their introduction. Defects, on the other hand, are imperfections in the crystal lattice structure itself, frequently caused by chemical impurities, and significantly alter the injection mechanism [19, 35, 37, 39, 44, 61, 64, 67]. Both defects and impurities can introduce traps or alter carrier mobility, indirectly influencing SCLC behavior [19, 24, 37, 44]. Numerical simulations reveal that charged acceptor-like defects in electron-only devices create barriers, reducing current and distorting mobility and band tail slope estimations from analytical models, but correcting for these barriers can yield accurate mobility values despite the inherent neglect of diffusion currents in such analyses [43]. Static disorder, the source of intrinsic traps, introduces localized in-gap states through two primary mechanisms: structural defects, which are crystal lattice perturbations that break symmetry and cause energetic disorder by varying electronic coupling and site energy, and chemical impurities, where foreign molecules alter the host's energy levels, distinctly different from dynamic disorder's transient localization caused by thermal motion [58].

Finally, traps are energy states within a semiconductor's bandgap caused by imperfections like impurities, dopants, or defects, creating localized electronic states spatially and energetically distributed around these imperfections; shallow traps reside close to the band edges (a few K_BT), whereas deep traps are situated deeper within the bandgap (several K_BT) [11, 13, 15, 17, 44, 58, 122]. Inherent impurities presence in all materials can act as donor or acceptor centers, thereby providing mobile charge carriers within the semiconductor, supplementing those introduced by external space-charge injection [22]. Impurities, doping, and defects create these trap states, which then affect carrier transport and lead to deviations from the ideal Mott-Gurney law in SCLC [13-14, 17-19, 37, 44, 121-122]. Theoretical solutions of the Frenkel and Hartke models demonstrate enhanced SCLC compared to the Mott-Gurney law under high electric fields and specific trap conditions; Schottky defects (paired anion and cation vacancies) maintain charge neutrality and, being mobile, contribute to ionic conductivity under electric fields; the interplay between defects, electric fields, and charge transport significantly influences semiconductor device behavior, especially in high-field regimes [11, 26]. Although the Frenkel effect accounts for field-induced trap depth reduction, leading to higher SCLC current values than the Mott-Gurney law, it overestimates the effective reduction by assuming a one-dimensional mechanism, whereas Hartke's calculation, which averages emission probability across all directions, provides a more accurate, three-dimensional representation, resulting in current values intermediate to those predicted by the Frenkel and Mott-Gurney models [26]. A complete and accurate theoretical model for observed SCLC behavior necessitates a self-consistent solution of coupled equations governing dopant and trap occupancy, explicitly incorporating the crucial Frenkel effect, particularly on Coulombic dopants, and accounting for multiple occupancies, as the Frenkel effect is not optional for accurately capturing the interplay between these factors [42].

For accurate device characterization of organic semiconductors, especially those containing traps, the significance of diffusion currents cannot be overlooked due to their influence on device performance [45]. In order for SCLC to occur, where dopant densities are lower than deep trap densities, dopant electrons, despite occupying higher energy levels, primarily fill deep traps, resulting in an ohmic behavior controlled by thermal excitation from these traps [42]. Furthermore, charge carrier traps, which significantly impact the performance of organic electronic devices, are introduced at interfaces like metal-semiconductor due to interfacial effects stemming from dissimilar materials, manifesting as surface roughness, impurity adsorption, thermal expansion mismatch, and metal-induced surface states, and consequently affecting charge injection, transport, and efficiency [58].

By way of contrast, for a trap-free semiconductor the current should increase only as the square of the applied voltage [11, 15-17, 48]. Assuming a relatively uniform trap distribution in energy within the bandgap, equal voltage increments will result in equal shifts in the Fermi level position. Because the free electron density depends exponentially on the Fermi level position, it will increase exponentially, or at least by a higher power, with increasing applied voltage. This explains the observed strong dependence of current on voltage. Finally, it is reasonable to expect that, under illumination, the density of photo-generated charge carriers would surpass the density of injected space-charges, thus dominating thesemiconductor's behavior and resulting in ohmic conduction.

Ideal semiconductors at absolute zero temperature exhibit low conductivity due to filled valence bands and empty conduction bands, but conductivity increases with temperature as thermal excitation promotes electrons to the conduction band (band to band transition) [11, 57]. However, the presence of impurities in most semiconductors introduces energy levels within the

bandgap, requiring less energy for electron excitation to the conduction band than a band-to-band transition, thereby enhancing conductivity [71]. While the Mott-Gurney law describes the SCLC behavior of ideal devices, experimental data often deviates from these predictions due to the difficulty in achieving ideal device conditions [11, 17, 18, 54, 56]. Ideal SCLC conditions are difficult to achieve due to challenges in forming ohmic contacts with electrodes; therefore, removing the electrodes can help realize these conditions, provided that trapped charges do not remain in trap states long enough to influence measurements using internal polarization techniques [16, 23]. Surface traps, exceeding bulk traps in pure semiconductors with low bulk trap densities (even in thick samples), cause significant variations in I-V characteristics of SCLC among nominally identical samples due to surface quality, a phenomenon confirmed experimentally [34]. In equilibrium state, localized states within the bandgap, capable of trapping charge carriers that would otherwise contribute to SCLC, are unavoidable, thus the conduction mechanism is not purely SCLC [17, 18, 50, 56, 58].

In a single charge carrier device (e.g., an electron-only device), the presence of traps and recombination centers alter the lifetime of charge carriers under applied voltage, which in turn influences the observed SCLC behavior [56]. The Hecht relation allows for the measurement of the mobility-lifetime product ($\mu\tau$) in semiconductors, a key material property, but it does not provide individual values for mobility (μ) or lifetime (τ) [152].

While exponential tail states from shallow traps can significantly influence I-V characteristics, their voltage dependence is not always stronger than that predicted by the Mott-Gurney law; the observed behavior is more complex and depends on several factors such as trap density, energy distribution, and the applied voltage range [23, 42, 45, 58].

In thermodynamic equilibrium, both electrons and holes populate available energy states according to Fermi-Dirac statistics; deeper states within the bandgap are localized (bound states), while intermediate states may be free but are fully occupied, and higher-lying states are free and unoccupied [15].

Figure 9 illustrates the distribution of injected charge carriers under an applied voltage across three energy levels: free carriers in the conduction band, trapped carriers above the shifted Fermi level, and trapped carriers condensed between the original (zero-field) and shifted (finite-field) Fermi levels [17]. Traps significantly alter charge carrier distribution in a semiconductor, shifting the Fermi level closer to trap energy levels and trapping a large portion of carriers near this new Fermi level, especially when trap density exceeds free carrier density in the space-charge region, leaving only a small fraction mobile; this trapping, affecting both electrons and holes depending on trap type, significantly influences effective mobility (μ_{eff}) and charge transport, with the spatial distribution of traps further impacting electrical and optoelectronic properties [16, 17, 24, 51, 54, 58, 121-122].

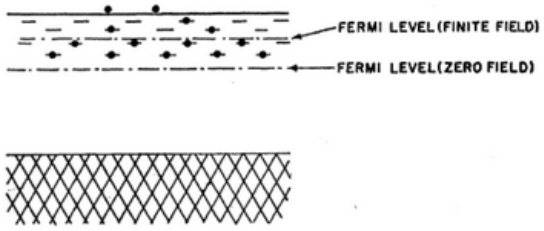

Figure 9: A simplified energy band diagram of a semiconductor showing trap distributions within the bandgap and the Fermi level shift induced by an applied electric field [17].

To understand current noise in semiconductors during operation, a trapping-detrapping model was developed. This model demonstrates the correlation between ionized trap levels and relative

current noise spectral density, which was validated by experiments, and provides a method for estimating material properties such as deep trap energy level (E_t) and concentration (N_t) [39]. Shallow traps, with their low trap depths, facilitate the thermal detrapping of charge carriers, whereas deep traps, requiring significantly higher energy for detrapping, often act as recombination centers, reducing charge carrier lifetime [58]. The trapping-detrapping model is applied to explain the situation where in a semiconductor with a uniform distribution of shallow traps near the initial Fermi level, applied electric fields cause injected charge carriers to be trapped between the initial and final Fermi levels (trap filling), shifting the Fermi level towards the trap levels and contributing to space-charge formation; while trapping dominates, thermal detrapping can also occur, significantly influencing conductivity and charge transport. [17, 24, 39, 56].

When injected charge carriers raise the Fermi level (E_F) above the trap energy level (E_t), while keeping it well below the conduction band (E_c), the Fermi level moves through a bandgap region where the trap density is much less than the free charge carriers (n) [24, 122].

Although the same number of charge carriers are injected into a semiconductor with shallow traps as in the trap-free SCLC, only a fraction remains free, resulting in a reduced effective mobility (μ_{eff}); because this fraction is voltage-independent and determined by trap density and depth, SCLC retains the same square-law voltage dependence as the ideal trap-free SCLC [16-17, 44-45, 51, 54, 58, 122]. The SCLC method can still be used to determine mobility in systems with charge traps, by employing an effective mobility that reflects both free and trapped carriers, as long as the free-to-trapped carrier ratio is voltage-independent [44-45].

In contrast, deep traps within the SCLC regime reduce the effective carrier concentration and act as recombination centers, leading to lower current and increased deviation from the Mott-Gurney

law [22, 124]. Shallow traps induce sublinear voltage dependence by reducing effective carrier mobility, and the combined presence of both shallow and deep traps results in complex, nonlinear current-voltage behavior that significantly impacts device performance through its effect on charge carrier transport [17, 22, 35]. Dangling bonds or damaged molecules lead to a higher deep trap density (N_t) near the surface in real materials, contrary to the typical assumption of uniformity in the bulk [34]. In materials with high defect and dopant concentrations, where conventional tunneling between widely spaced traps is negligible, thermally activated tunneling between deep traps and shallower dopant levels, as well as tunneling from shallow dopants to deep traps, becomes significant, contributing to the overall current [42].

In materials with high trap densities, injected charge carriers are predominantly trapped, resulting in a small Fermi level shift towards the relevant band edge, which, despite increasing free carrier density, remains minimal due to the large disparity between trap and free charge carrier densities, creating distinct quasi-Fermi levels [16]. This trapping significantly impacts charge transport and conductivity by reducing mobile carrier density, with the balance between trapped and free charge carriers, and thus the Fermi level shift, influenced by factors like temperature [16, 24, 27, 122]. Consequently, when trap density exceeds the density of injected space-charges, the magnitude of SCLC is significantly reduced, as only a small fraction of injected carriers contributes to current flow due to the reduced drift mobility [16-17, 58, 122, 124].

While ideal conditions predict a transient current enhancement upon charge carrier injection into the conduction band, real devices contain traps where injected charge carriers are captured, resulting in a small initial current followed by a transient current whose rate is governed by the trap capture cross-section (σ_n) [16, 17]. In these devices, a quasi-equilibrium state, defined by the Electron Steady-State Fermi Level (ESSFL) and influenced by bias or illumination, establishes a

dynamic balance between trapped and free charge carriers (distinct from thermal equilibrium) dictating free carrier density and trap occupancy, with shallow traps shifting the ESSFL towards the conduction band based on trap density, energy level, and injection conditions [56].

In semiconductors with disorders, the current-voltage relationship often deviates from the ideal Mott-Gurney law ($J \propto V^2$) and follows a $J \propto V^m$ relationship where m > 2; this complex voltage dependence varies significantly with disorder, carrier density, electric field, and device parameters, and can be further influenced by measurement conditions, grain-doping density, and defect state distribution, with light intensity sometimes decreasing the voltage dependence [14, 16, 43]. While measurement timing and illumination influence current-voltage characteristics, specific relationships are complex and material-dependent, highlighting the intricate nature of charge transport in disordered semiconductors [16].

The analytical expressions describing behavior in the presence of traps are presented below. The free electron density at the thermal equilibrium state, n_0, is given by,

$$n_0 = N_c e^{\left[\frac{(E_F - E_c)}{K_B T}\right]} \quad \text{Eq. 35}$$

where E_F is the Fermi level, E_c is the conduction band edge, and N_c is the effective density of states [13, 56, 57, 71, 121, 123].

The trap density at the trap energy level (E_t) under the thermal equilibrium states (n_{to}) is given by,

$$n_{t0} = \frac{N_t}{1 + \frac{1}{g} \cdot e^{\left[\frac{(E_t - E_F)}{K_B T}\right]}} \quad \text{Eq. 36}$$

where N_t is the trap density of states, E_t is the trap energy level, and g is the degeneracy factor for traps [17, 39, 56, 57, 123]. The equilibrium trap density (n_{to}), resulting from the balance of

electron capture and thermal re-emission from the traps in the absence of an applied field, can be altered by a moderate applied field due to the change in free electron density caused by varying injection levels [56].

The free electron density under a moderate applied field, *n(x)*, is given below [27, 33, 50, 54, 57, 71].

$$n(x) = N_c e^{\left[\frac{(E_{Fn}(x)-E_c)}{K_B T}\right]} \quad \text{Eq. 37}$$

The trap density under a moderately applied field (n_t) is given below,

$$n_t = \frac{N_t}{1 + \frac{1}{g} \cdot e^{\left[\frac{(E_t - E_{Fn}(x))}{K_B T}\right]}} \quad \text{Eq. 38}$$

where, E_{Fn} is the quasi-Fermi level [27, 56].

The trap density in the quasi-thermal equilibrium state is obtained by substituting Eq. 37 into Eq. 38,

$$n_t(x) = \frac{N_t}{1 + \frac{1}{g}\frac{N}{n(x)}} \quad \text{Eq. 39}$$

where $N = N_c exp\left[\frac{(E_t - E_c)}{K_B T}\right]$ is the effective density of the traps and the free charge carriers in the quasi-thermal equilibrium state [18, 56].

If *N* is much greater than $n(x)$, then the denominator in Eq. 39 can be simplified using the assumption below.

$$n_t(x) = \frac{N_t}{1 + \frac{1}{g}\frac{N}{n(x)}} \cong \frac{N_t}{\frac{1}{g}\frac{N}{n(x)}} \quad \text{Eq. 40}$$

For shallow trap conditions, the free to trapped charge carrier ratio, θ, is given by,

$$\theta = \frac{n(x)}{n(x) + n_t(x)} \approx \frac{n(x)}{n_t(x)} = \frac{N}{gN_t} = \frac{N_c}{gN_t} exp\left[\frac{(E_t - E_c)}{K_B T}\right] \quad \text{Eq. 41}$$

where θ is the ratio of the free charge carriers to total charge carriers, which is a constant value (independent of voltage), and it can be as low as 10^{-7} [13, 15, 17, 24, 26-27, 33, 39, 51, 54, 56, 58, 60, 119]. Eq. 41 describes n-type transport; for p-type transport, the density of states in the valence band (N_v) should be used instead, maintaining continuity [39]. It is noteworthy that the trap density is assumed to be much greater than the free electron density ($n(x) << n_t(x)$), so the free electron density is negligible in the denominator.

As previously noted, traps lead to a higher-power voltage dependence of current compared to the trap-free SCLC, but the current magnitude is several orders of magnitude lower than the theoretical ideal SCLC due to the exponential dependency of the free electron density on the Fermi level in Eq. 35 and the free to trapped charge carrier ratio, θ, in Eq. 41 [13-14, 16-17, 19, 38, 43, 54].

Figure 10 depicts a typical space-charge-limited current (SCLC) density-voltage characteristic on a double logarithmic scale, contrasting idealized trap-free SCLC with the realistic scenario of a single trap level, which introduces four distinct regions in the I-V characteristic [51, 56, 58]. Assuming a single discrete energy level for all traps is an oversimplification, given that trapping sites are known to be widely distributed in energy due to variations in their local environments [32, 58].

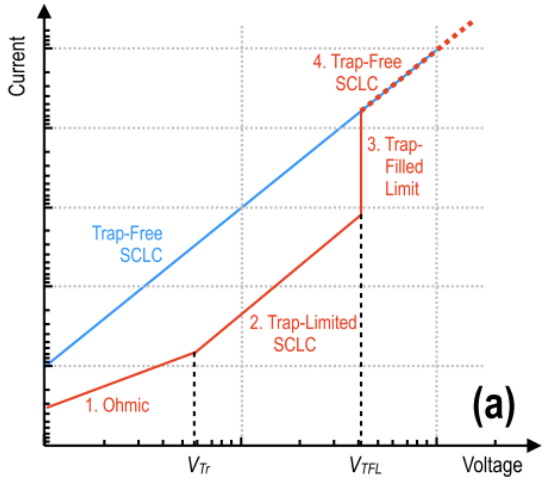

Figure 10: Double logarithmic plot of the space-charge-limited current (SCLC) density-voltage characteristic, illustrating the difference between idealized trap-free SCLC and the behavior observed with a single trap level [56]. Note the four distinct regions in the I-V characteristic that emerge due to the presence of traps [51]. V_{Tr} represents the transition voltage from ohmic to trap-limited SCLC (shallow-trap SCLC), while V_{TFL} denotes the trap-filled limit voltage [60].

While trap-free SCLC represents an idealized scenario, the presence of traps in non-ideal conditions leads to the emergence of four distinct regions in the I-V characteristic, as illustrated in Figure 10 [51]. Therefore, these four regions are examples of behaviors indicative of SCLC in semiconductors containing both shallow and deep traps, as well as thermally generated carriers [32]. Although trap-free SCLC results in higher current compared to dark ohmic conduction, the presence of traps significantly reduces the SCLC magnitude by altering the voltage dependence (from V^1 to V^2) as they capture injected space-charges; however, at higher voltages, trap filling occurs, restoring trap-free SCLC behavior [13, 14, 17-18, 24, 51, 56, 124]. Despite not being depicted in Figure 10, the intersection of ohmic and trap-free SCLC occurs at a lower voltage,

where the injected charge carrier density, calculated using square-law, equals the dark carrier density [18].

To facilitate a comprehensive understanding of the physical phenomena underlying the distinct regions observed in SCLC plots (Figure 10), a preliminary introduction to carrier transit time (τ_c) and dielectric relaxation time (τ_d) is necessary. Carrier transit time, defined as the time required for charge carriers to traverse between electrodes, is given by,

$$\tau_c = \frac{qn_tL^2}{\mu\theta V_{tr}} \quad \text{Eq. 42}$$

where q is the electric charge, n_t is the effective trap density, L is the distance between two electrodes, μ is the charge carrier mobility, θ is the ratio between the free charge carrier and the trapped charge carrier, and V_{Tr} is the transition voltage from ohmic to trap-limited SCLC regime [13-14, 17-18, 27, 33, 37, 44].

Dielectric relaxation is the process of charge redistribution within a material in response to an applied electric field, leading to a new equilibrium [33]. Dielectric relaxation time, defined as the time between charge carrier collisions, is given by,

$$\tau_d = \frac{\varepsilon}{qn\mu\theta} \quad \text{Eq. 43}$$

where ε is the dielectric constant of the semiconductor [13, 27, 33].

For intrinsic or weakly doped single charge carrier devices, space-charge influences the charge carrier density (making the Mott-Gurney law applicable) because the semiconductor thickness is usually less than twice the Debye length, thus invalidating Ohm's law and causing current to be space-charge-limited, even at low voltages [49, 55]. However, in the presence of traps, the

following behaviors are observed. In region 1 ($0 < V < V_{Tr}$), the Ohmic region, where the injected carrier density (n) is significantly lower than the free carrier density (n_0), a linear I-V characteristic consistent with Ohm's law is observed; this arises from mobile electron and hole movement and reflects ohmic conduction, which dominates when other conduction mechanisms are negligible [13, 14, 17, 27, 32-33, 37, 46-51, 54, 56, 58, 119-120, 123]. Besides trap density, injecting contact charge carrier concentration and thickness also play a vital role in transport [119]. Even within the ohmic region, where weak injection ($n < n_0$) causes partial trap filling, allowing injected carriers to begin filling traps and establish an ohmic mode within an electrically quasi-neutral state; below the transition voltage ($V < V_{Tr}$) when carrier transit time exceeds dielectric relaxation time ($\tau_c > \tau_d$), injected carriers rapidly redistribute to maintain charge neutrality, preventing transport across the semiconductor and leading to ohmic behavior upon trapping [13, 14, 27, 33]. While the moving electrode (ME) equation offers a more precise representation of current flow in trap- and doping-free semiconductors, Ohm's Law is employed here for clarity, given its established familiarity and effectiveness in basic charge transport analysis, particularly in the presence of traps [49-50, 55]. Trapping of space-charge carriers is essential for the observation of ohmic behavior [33]. Transient SCLC can dominate the initial behavior even within the steady-state ohmic regime, as a temporary surge of injected carriers exceeds volume-generated carriers before trapping reduces space-charge-carrier density, allowing the volume-generated carriers to establish steady-state ohmic currents [17].
Linear transport characteristics are exhibited within the region of Ohm's law applicability, whereas non-linear transport characteristics arise upon the injected charge surpassing the equilibrium charge, resulting in non-uniform electric fields and charge distributions that are dependent on the sample geometry [48]. In region 2 ($V_{Tr} < V < V_{TFL}$), trap-limited SCLC, where

the injected charge carrier density exceeds the thermally generated free charge carrier density, the transition from ohmic to SCLC behavior occurs ($V^1 \rightarrow V^2$), resulting in I-V characteristic modified by the presence of traps, yet still valid for Mott-Gurney law analysis [17, 19, 24, 32-35, 37, 41-42, 47-51, 54, 56, 58, 60, 120, 122-123]. Due to deep and distributed traps, the current-voltage relationship shifts from the ideal square law ($J \propto V^2$) to a power-law ($J \propto V^n$, n > 2), where n is affected by trap density, injecting contact charge carrier concentration, and material thickness, revealing a complex interplay [58, 119-120]. The voltage required to initiate trap filling (V_{Tr}) is determined by the concentration (N_t) and depth of the traps (shallow or deep traps) [119]. The transition from linear ohmic conduction to quadratically or higher-power SCLC, occurring at a voltage that rises with volume-generated conductivity, is straightforward for distinct current pathways but complex with coexisting currents and varied potential distributions, requiring higher voltages for SCLC dominance with increased volume-generated carrier density [17, 27, 34]. Under these conditions, the current is limited by the bulk of the material, not the interface [44].

Traps immobilize charge carriers, significantly reducing the mobile charge carrier density in the conduction (or valence band when holes are the majority charge carriers), resulting in lower current compared to a trap-free SCLC [119, 124]. In this regime, the current is often described by a modified SCLC equation that accounts for trapping effects and may deviate from the ideal SCLC equation (Eq. 18) [54]. Furthermore, shallow traps, while still capturing charge carriers, have a smaller impact than deep traps [19]. Charge carriers trapped in shallow states can be thermally re-emitted back into the conduction band relatively easily. This leads to increased recombination, as trapped carriers can recombine with opposite charge carriers, and a moderate delay in the onset of SCLC (V_{Tr}). The presence of traps also influences the recombination rate of

charge carriers within the device; however, shallow traps do not impede current flow as severely as deep traps.

When the electron quasi-Fermi level, influenced by injected charge carriers, remains below the shallow trap energy level, most injected charge occupies traps and does not contribute to current, maintaining a constant ratio of free to total charge (θ) regardless of applied voltage [14, 18, 27]. During intermediate injection ($V > V_{Tr}$, $\tau_c \leq \tau_d$), injected charge carriers dominate due to their rapid transit, filling traps and creating space-charge; unlike weak injection ($V < V_{tr}$), where τ_c increases inversely with voltage and τ_d remains constant, both τ_c and τ_d decrease with increasing voltage due to rising free charge carrier density, potentially raising the quasi-Fermi level (E_{Fn}) above the trapping energy level (E_t) [13, 27, 33, 35, 39, 44, 51]. The accumulated space-charge reduces the electric field at the injecting contact to a negligible level, leading to charge saturation within the device, where charge injection is limited to replacing the charge removed at the opposing electrode [44]. The injected charge carrier density is governed by electrostatics [34]. As the voltage increases, traps start to fill, beginning with the shallow ones. However, deep traps require higher energy to fill and dominate the transition to the trap-filled limit. Once the applied voltage reaches a critical value, often referred to as the trap-filled limit voltage (V_{TFL}), virtually all the traps are filled [24, 37, 41, 46, 119, 124]. There is a direct linear proportionality between V_{TFL} and the concentration of traps (N_t) [46, 58]. The slope of the I-V curve in the V_{TFL} region is directly influenced by dopant concentration, where increased dopant levels cause a reduction in the turn-on voltage [42]. This transition is characterized by a rapid increase in current with increasing voltage ($V^2 \rightarrow V^n$), where value of n is influenced by both the injection level and the distribution of trapping centers [18, 32, 34]. After the initial sharp current increase due to deep trap filling, influenced by local thermal equilibrium, the subsequent power-law current rise,

governed by dopant energy levels and the Frenkel effect (electric field-induced ionization energy reduction shielded by free carriers), ends when all traps and dopants are filled, leading to the Mott-Gurney regime [42]. Before all traps are filled, theoretically, if electrons recombine with deep-lying holes, low current values (trap-limited SCLC) are observed; however, the increment of electron density contributes to high current values (trap-free SCLC) as the field increases prior to electrons recombining with deep-lying holes, a phenomenon that can be recorded by a pulsed I-V measurement [16, 24, 60]. With the inclusion of both shallow and deep traps, the I-V curve exhibits a trap-filled limit region characterized by an abrupt current increase as the proportion of free carriers rises with voltage, rendering the ideal field-independent Mott-Gurney law inapplicable, though field-dependent mobility within the equation can account for shallow trap effects where electric fields lower the transport barrier [44, 121].

It is noteworthy that the transition from trap-limited to trap-free SCLC and the influence of recombination are observed even in the presence of ion inclusions, indicating a robustness of these processes across varying material compositions [53-54, 158].

The transition from trap-filled SCLC in Region 3 to trap-free SCLC in Region 4 is marked by a rapid increase in current. This transition occurs at the trap-filled limit voltage (V_{TFL}), which signifies the shift from trap-limited to trap-free SCLC, where the I-V characteristic exhibits ideal trap-free SCLC behavior due to complete trap filling at high injection levels [14, 18, 24, 27, 33, 37, 42, 46, 51, 56, 58, 60, 119, 124]. Specifically, at V_{TFL}, traps become saturated, the quasi-Fermi level rises above the trapping energy level, and the current sharply increases as injected charge carriers move freely, transitioning to SCLC behavior ($V^n \rightarrow V^2$) under strong injection, where the electric field is no longer constant [13, 27, 39, 46, 58]. This trap saturation is directly related to the electron quasi-Fermi level (E_{Fn}). As applied voltage increases, E_{Fn} rises, and when

it surpasses the shallow trap energy level (E_t) at V_{TFL}, traps become filled, defining V_{TFL} as the threshold voltage for trap saturation [14, 27, 39, 51, 58]. The presence of unneutralized charge carriers in trap states prior to voltage application establishes a Coulombic repulsion that impedes electron injection, necessitating the application of the trap-filled limit voltage to mitigate this effect [18].

The simple assumption of a rapid current rise toward trap-free regions upon trap filling, used to determine trap depth and density via thermally stimulated currents and photocurrent response time, can lead to deviations due to potential contributions from field ionization or double injection [24].

Beyond V_{TFL} (region 4), where injected carriers are no longer significantly trapped, the current dramatically increases and is fully controlled by space-charge carriers, which limits further free charge carrier injection into the semiconductor [13, 27, 42]. In this idealized scenario, once traps are fully saturated, they cease to impede charge injections, and all subsequent injected charge carriers contribute to ideal SCLC [14, 58]. However, real semiconductors deviate from this ideal case because traps in real semiconductors are distributed in energy, typically following exponential or Gaussian distributions within the bandgap rather than existing at a single discrete level; consequently, the transition from trap-limited to trap-free SCLC is gradual [13-14, 37, 41, 43, 54, 58]. Hopping charge transport in such a Gaussian DOS leads to a dependence of the (effective) mobility on the temperature, electric field, and charge-carrier density [121]. To elaborate, with increasing applied potential, trap states at progressively elevated energy levels become occupied, resulting in a gradual saturation of trap occupancy and a corresponding gradual increase in current, thereby inducing an energetic shift of the quasi-Fermi level towards the conduction band edge [13, 27].

Under trap-limited SCLC conditions, the double logarithmic current density-voltage (J-V) characteristics exhibit three distinct general properties: 1) Ohm's law represents a lower limit for the J-V characteristic, as electron injection can only increase the pre-existing thermal charge carriers, thereby establishing ohmic conduction as the baseline for minimum current values; 2) Under conditions of significant charge carrier injection, the J-V characteristic is constrained by the SCLC line, which indicates the theoretical maximum current achievable when injected charge carriers exist exclusively within the conduction band; and 3) The V_{TFL} line delineates the lower limit of the J-V characteristic, as it corresponds to the condition wherein the maximum proportion of injected charge carriers are localized in trap states, thereby minimizing the free charge carrier concentration available for conduction current [18].

It is well-established that charge carrier trapping-detrapping contributes to current instability and degradation in organic FETs [39]. Beyond trapping and detrapping, charge carrier redistribution also occurs due to dielectric relaxation, similar to ideal SCLC. This redistribution influences conductivity, especially when the carrier transit time (τ_c) is shorter than the dielectric relaxation time (τ_d) [44, 57]. In this scenario, injected charge carriers have sufficient time to redistribute within the semiconductor before reaching the opposite electrode. This effect is less prominent in the ohmic regime, where the charge carrier density is dominated by thermally generated charge carriers and the influence of injected charge carriers is relatively small.

Shallow traps in semiconductors alter I-V characteristics by delaying the transition to the SCLC regime, introducing a trap-limited region with a higher than square-law voltage dependence between the Ohmic and trap-free SCLC regimes; while extending the Ohmic region, they do not eliminate Mott-Gurney behavior but rather modify the SCLC regime, requiring higher injection

levels to overcome the thermally excited carrier density due to significant trapping [17, 18, 51, 56, 60].

The current density influenced only by drift is given by.

$$J = \mu n(x) E \qquad \text{Eq. 44}$$

Substituting Poisson's equation (Eq. 10) and the free to trapped charge carrier ratio (Eq. 41) into Eq. 44 gives.

$$J = \mu \theta \varepsilon E \frac{dE}{dx} \qquad \text{Eq. 45}$$

Rearrangement of Eq. 45 and subsequent integration over E, using the SCLC assumption that the electric field at the electrode (x=0) is zero, yields [8].

$$E(x) = \sqrt{\frac{2Jx}{\mu \theta \varepsilon}} \qquad \text{Eq. 46}$$

At high bias voltages, carrier mobility and SCLC are functions of temperature, carrier density, and electric field in a single charge carrier device; however, mobility is generally constant at low bias voltages and room temperature [40, 121]. The modified Mott-Gurney equation, which accounts for trap states, is analytically derived through the sequential application of the relationships presented in Eq. 15 through Eq. 17,

$$J_\theta = \frac{9}{8} \theta \mu \varepsilon \frac{V^2}{L^3} \qquad \text{Eq. 47}$$

where J_θ is the current density in the presence of traps, which is related to the trap-free current density (J) by the free to trapped charge carrier ratio, θ; this factor differentiates the current density with traps (J_θ) from the current density without traps (J) and [13-14, 17, 24, 26-27, 35,

39, 51, 54, 56, 58, 60, 119, 157]. The term μ_{eff}, known as the effective mobility, represents the product $\theta\mu$ as shown in Eq. 47 [39, 44-45, 51, 54, 121]. It is essential that Eq. 47 must reduce to the ideal Mott-Gurney law (Eq. 18) when the free to trapped charge carrier ratio (θ) equals 1, as this confirms the validity under ideal conditions; the voltage-dependent nature of the ratio is critical, as its progression to unity, achieved once all traps are filled, indicates the transition from trap-SCLC to trap-free SCLC [51, 58]. Similar to ideal SCLC, but accounting for traps, the intermediate voltage regime features steady-state current, drift-dominated transport, and minimal temperature dependence [22, 30, 35]. When traps are considered in SCLC analysis, the models often rely on the assumption of discrete, monoenergetic trapping levels [13, 60]. These traps reduce the effective mobility ($\mu_{SCLC} = \theta\mu$), effectively limiting free carrier transport and higher trap densities behave similarly to lower doping levels [17, 44-45, 51, 54, 121, 157]. Indeed, the presence of trap states can contribute to field-dependent charge carrier mobility, which is contrary to the common assumption of constant mobility, particularly in organic semiconductors and disordered materials [30, 60]. The field-dependent SCLC with trap presence is given below [26, 30].

$$J_\theta = \frac{9}{8}\theta\varepsilon\frac{V^2}{L^3}\mu_0 exp\left(0.89\gamma\sqrt{E}\right) \quad \text{Eq. 48}$$

It is noteworthy that the intended representation of the Poole-Frenkel effect's field dependence by γ is often compromised in practice due to traps and trap-induced diffusion currents [43]. In single charge carrier devices, free charge carrier density in Ohm's law (Eq. 8) is influenced by the doping due to added either donor (N_D) or acceptor (N_A) and the total current density, a summation of Eq. 8 (Ohm's law) and Eq. 47, includes doping effects on charge carrier transport;

here, Ohm's law (Eq. 8), modified by the new free charge carrier density (N_D or N_A), dominates and applies in heavily doped single charge carrier devices, but not lightly doped ones [55].

The transition voltage, $V_{Tr\theta,Ohm\text{-}Mott\text{-}GurneyY}$, marking the shift from the Ohmic to Trap-Filled Mott-Gurney law regime in the presence of shallow traps, is derived by combining Eq. 8 and Eq. 47 [13, 14, 24, 27, 29, 33].

$$J_{Ohm's\ law} = J_{\theta,MG-law} \quad \text{Eq. 49}$$

$$V_{Tr\theta,Ohm-MG} = \frac{8qn_0L^2}{9\theta\varepsilon} \quad \text{Eq. 50}$$

A transition regime at intermediate voltages, where both Ohmic and SCLC behaviors contribute to the total current, is broadened in real semiconductor and organic electronic devices by factors like contact resistance, trap states, and inhomogeneous charge injection,

$$J = \alpha V + \beta V^2 \quad \text{Eq. 51}$$

where α and β are the parameters from Eq. 8 and Eq. 47, excluding voltage terms [51].

Similarly, the transition voltage, $V_{Tr\theta,ME\text{-}Mott\text{-}Gurney}$, from the moving electrode (ME) equation regime to the Mott-Gurney law regime in the presence of shallow traps, is derived by combining Eq. 26 and Eq. 47.

$$J_{ME\ equation} = J_{\theta,MG-law} \quad \text{Eq. 52}$$

$$V_{Tr\theta,ME-MG} = \frac{32\pi^2}{9}\frac{K_BT}{q\theta} \quad \text{Eq. 53}$$

Although the moving electrode equation is used in both Eq. 52 and Eq. 53, the standard moving electrode equation for SCLC fails to accurately describe charge transport in the presence of traps; therefore, a more comprehensive model that incorporates trapping and release dynamics is necessary [121]. The impact of shallow traps on SCLC is substantial, as θ can be as low as 10^{-7},

significantly reducing SCLC magnitude, especially considering that traps are not typically confined solely to shallow energy levels [17, 56]. It is expected that the presence of traps will shift the ohmic to SCLC transition to a higher voltage compared to the ideal case outlined in Eq. 23. In addition, higher light intensity increases $V_{Tr\theta,Ohm\text{-}Mott\text{-}Gurney}$ from the Ohmic to the trap-limited SCLC regime because the increased volume-generated charge carrier density (which differs from the charge carrier density) extends the Ohmic regime to higher voltages, thus delaying the onset of the trap-limited SCLC regime where injected charge carriers dominate; beyond $V_{Tr\theta,Ohm\text{-}Mott\text{-}Gurney}$, I-V characteristics are governed by the interaction of injected charge carrier density with trap states [16, 153]. This behavior highlights the complex interplay between light-generated carriers, traps, and injected charge carriers in determining the electrical characteristics of illuminated semiconductors, demonstrating how photogenerated carriers can significantly modify charge transport regimes [153].

For deep traps, the trap density in the quasi-thermal equilibrium state ($n_t(x)$) can be simplified using the assumption that the density of the traps and the free charge carriers in the quasi-thermal equilibrium state (N) is approximately equal to the free electron density under a moderate applied field, $n(x)$ [56].

$$n_t(x) = \frac{N_t}{1 + \frac{1}{g}\frac{N}{n(x)}} \cong N_t \qquad \text{Eq. 54}$$

Deep trap states in semiconductors, which are not always fully occupied, significantly influence free carrier density by capturing carriers for extended periods, thus reducing the mobile carrier concentration; their occupancy depends on temperature, applied field, and energy level relative to the Fermi level, and their presence can substantially alter electrical properties through dopant compensation, non-radiative recombination, and modified charge transport [42, 56]. Deep traps

are typically located well below the ESSFL (often by more than K_BT), their occupancy, which is not always complete, varies with temperature, field, and energy level relative to the Fermi level; both trap types influence the ESSFL and carrier dynamics, with deep traps potentially having a greater impact on free charge carrier density, and the overall trap behavior depending on their energy distribution, density, and operating conditions [56]. While deep traps do not directly contribute to current flow, they significantly impact semiconductor behavior by capturing carriers for extended periods, reducing free carrier concentration and thus altering electrical characteristics; their influence on carrier dynamics and device performance can be substantial, particularly regarding compensation effects and recombination processes [51, 56, 154]. Analytical analyses demonstrate that deep traps significantly alter the material's bulk electrostatic profile and are essential for accurately interpreting SCLC current-voltage (I-V) curves, enabling the reproduction of experimental results that conventional theory fails to capture [34]. As injection level increases, the ESSFL rises, progressively filling traps; at the trap-filled limit voltage regime (V_{TFL}), most traps are occupied, causing a rapid current increase, followed by a gradual transition towards the trap-free SCLC regime, eventually approaching the Mott-Gurney law ($J \propto V^2$), though this transition depends on trap distribution and energy levels, with deep traps potentially influencing carrier dynamics even at high injection levels, as illustrated in Figure 10 [13, 14, 24, 27, 37, 51, 56]. The trap-filled limit voltage (V_{TFL}), which corresponds to the voltage necessary for complete trap filling or the point at which the quasi-Fermi level (E_{Fn}) crosses the trap energy level (E_t) is given below in this case [33, 39, 46, 56].

$$V_{TFL} \cong \frac{(qN_tL^2)}{\varepsilon} \qquad \text{Eq. 55}$$

Although 'ε' appears in the denominator of Eq. 55, '2ε' is also reported as a denominator, which can be explained by the degeneracy factor (g): 'ε' for discrete traps and '2ε' for an exponential trap distribution due to integration over the trap states. [13-14, 18-19, 23, 27, 33, 41-42, 51, 54, 56, 58]. Understanding these factors is crucial, as they are essential for estimating deep trap density from Eq. 55 [34]. The interplay between dopants and deep traps is theorized to be significant in SCLC, and including doping concentration (N_D or N_A) in V_{TFL} (Eq. 55) explains the early trap-filled limit voltage onset, as injected carriers fill dopant sites, resulting in a gradual current density increase [42]. It is observed that the V_{TFL} decreases with increasing temperature, attributed to higher temperatures facilitating thermal carrier generation and thus requiring a lower voltage to fill all trap levels [24, 27]. In the presence of energetically distributed charge traps, these traps are gradually filled with increasing electric field, irrespective of temperature, until the trap-filled limit voltage is reached, at which point all trap states are filled [41].

While the trap energy level (E_t) can be calculated by noting that the Fermi level (E_F) aligns E_t at *2/3* of V_{TFL} (the point of significant trap filling), and performing bandgap integration of the trap-filling equation; however, this method is inherently linked to the accuracy of V_{TFL} determination [24]. Therefore, to address this limitation, temperature-dependent SCLC measurements with the presence of traps (Eq. 34) provide a distinct advantage: the independent determination of both E_t and trap density (N_t) through V_{TFL} (Eq. 55), thereby enhancing the reliability of the results without requiring V_{TFL} interpretation [24, 27, 33, 41, 45]. It should be noted that the V_{TFL} region exhibits temperature-dependent characteristics [42]. As a result, higher temperatures reduce V_{TFL} due to increased thermal carrier generation, making it easier to fill traps [33].

The shifts in the Fermi level, ΔE_F, due to the injected charges under an applied field is given by,

$$\Delta E_F = \frac{Q}{(qN_tL)} \cong \frac{CV}{(qN_tL)} \quad \text{Eq. 56}$$

where V is the applied voltage, C is the capacitance, and $Q(= CV)$ is the injected charge carrier, which is approximately equal to the trapped charge carrier density [17, 56]. The assumption of uniform charge carrier distribution throughout the semiconductor introduces a maximum error of a factor of 2 [56].

The free charge carrier density, n_c, which includes ΔE_F is given by,

$$n_c = N_c e^{\left[\frac{(E_F - E_c)}{K_B T}\right]} e^{\left[\frac{\Delta E_F}{K_B T}\right]} = n_0 e^{\left[\frac{\Delta E_F}{K_B T}\right]} \quad \text{Eq. 57}$$

where n_0 is the initial free charge carrier concentration at thermal equilibrium states [17, 56].

Substituting Eq. 56 into Eq. 57 gives,

$$n_c = n_0 e^{\left[\frac{\Delta E_F}{K_B T}\right]} = n_0 e^{\left[\frac{CV}{qN_t L K_B T}\right]} = n_{c0} e^{\alpha V} \quad \text{Eq. 58}$$

where $n_{c0}(=n_0)$ is the free charge carriers at the initial thermal equilibrium states, and $\alpha = \frac{C}{qN_tLK_BT}$ is a constant [17, 56].

Assuming that all the injected charge carriers are trapped, and that the density of the trapped charge carrier is approximately equal to the injected charge carrier density, as given below [17, 56].

$$n_t = \frac{Q}{qL} = \frac{CV}{qL} \quad \text{Eq. 59}$$

Substituting Eq. 58 and Eq. 59 into Eq. 41 gives the free to trapped charge carrier ratio (θ) for shallow traps with a uniform energy distribution; however, unlike the previous shallow trap model (Eq. 41), this ratio is not constant [17, 56].

$$\theta = \frac{n_c}{n_t} = \frac{n_0 e^{\left[\frac{\Delta E_F}{K_B T}\right]}}{\frac{CV}{qL}} = \frac{n_{c0} e^{\alpha V}}{\frac{CV}{qL}} = \left(\frac{n_{c0} qL}{CV}\right) e^{\alpha V} \quad \text{Eq. 60}$$

A notable distinction exists in the behavior of the free-to-trapped charge carrier ratio (θ). Eq. 41 shows voltage independence in trap-limited regimes, which aligns with the behavior of discrete (shallow) traps [58]. However, Eq. 60 demonstrates a clear voltage dependence [14, 18]. This voltage dependence is attributed to deep and distributed traps, which introduce a voltage-dependent ratio and subsequently alter the current's power-law ($J \propto V^n$, $n > 2$) from a square-law relationship ($J \propto V^2$) [58]. Furthermore, charge transport is significantly influenced not only by trap density, but also by the injecting contact's charge carrier concentration and the material's thickness, suggesting a complex interplay of factors contributing to the observed current-voltage characteristics [119].

Substituting Eq. 60 into Eq. 47 gives the SCLC equation for a uniform distribution of shallow traps, as shown in Eq. 61,

$$J = \frac{9}{8}\theta\mu\varepsilon\frac{V^2}{L^3} = \frac{9}{8}\left(\frac{n_{c0} qL}{CV} e^{\alpha V}\right)\mu\varepsilon\frac{V^2}{L^2} = \left(\frac{9}{8}\frac{n_{c0} q\mu\varepsilon}{CL^2}\right) V e^{\alpha V} \quad \text{Eq. 61}$$

where $\left(\frac{9}{8}\frac{n_0 q\mu\varepsilon}{CL^2}\right)$ is a constant [17, 56].

As previously discussed, the voltage dependence of SCLC is strongly influenced by the characteristics and distribution of traps. In the absence of traps, SCLC follows the Mott-Gurney law with $J \propto V^2$. When shallow traps are present, they generally maintain the $J \propto V^2$ dependence, but with reduced current magnitude. However, in the case of an exponential trap distribution, where trap density decreases with distance from the conduction band edge, the relationship typically leads to a power-law dependence [16, 41, 56, 58, 155]. This progression illustrates how

different trap configurations can significantly alter the I-V characteristics in semiconductor devices.

Eq. 61 can be modified by using Eq. 58 and converting the current density to the current without loss of continuity, as shown below.

$$I = \left(\frac{9}{8}\frac{n_0 q\mu\varepsilon}{CL^2}\right) V e^{\left[\frac{\Delta E_F}{K_B T}\right]} \quad \text{Eq. 62}$$

The trap distribution can be determined by differentiating Eq. 62 with respect to voltage [17, 56].

$$\frac{dI}{dV} = \frac{I}{V}\left(1 + \frac{V}{K_B T}\frac{d(\Delta E_F)}{dV}\right) \quad \text{Eq. 63}$$

Eq. 63 is modified to form Eq. 64.

$$\frac{d(\Delta E_F)}{dV} = \left(\frac{V}{I}\frac{dI}{dV} - 1\right)\frac{K_B T}{V} \quad \text{Eq. 64}$$

Eq. 64 is rewritten by substituting the fundamental capacitance formula (Q = CV), assuming the charge carriers are localized in trap energy states [17, 48, 56].

$$C\frac{d(\Delta E_F)}{dQ} = \left(\frac{V}{I}\frac{dI}{dV} - 1\right)\frac{K_B T}{V} \quad \text{Eq. 65}$$

The trap density per unit energy, which can be derived from the experimental I-V characteristic, is given by [17, 56].

$$\frac{dQ}{d(\Delta E_F)} = \left\{\left(\frac{V}{I}\frac{dI}{dV} - 1\right)\frac{K_B T}{CV}\right\}^{-1} \quad \text{Eq. 66}$$

If the constant, $\left(\frac{9}{8}\frac{n_0 q\mu\varepsilon}{CL^2}\right)$, from Eq. 61 and a suitable voltage (E = QV) are chosen such that the current doubles compared to its value under the applied field, then the number of injected charge carriers (which corresponds to the number of traps within an energy range $K_B T$ near the Fermi level) can be determined [17].

The trap density of states ($N_t(E_t)$), assumed to be an exponential distribution of traps, is approximated by the temperature, as shown below,

$$N_t(E_t) = A\exp\left(-\frac{E_t}{K_B T_c}\right) \quad \text{Eq. 67}$$

where $A\left(=\frac{H}{K_B T_c}\right)$ is a constant, H is the total trap density (assuming the distribution applies across all energy levels below the conduction band or above the valence band), E_t is the trap energy level (measured from the conduction band minimum or the valence band maximum), h is Planck's constant, v is the frequency of longitudinal polarization waves of long wavelength, and $T_c(=\frac{hv}{K_B})$ is the characteristic temperature influencing the energy-dependent trap distributions (exponential distribution of trap DOS) and is greater than the measuring temperature (T) [11, 16-17, 23, 26, 58, 60]. Traps arising from surface defects and structural disorders typically exhibit an exponential energy distribution [41, 58].

The temperature-dependent voltage dependence of SCLC for $T_c > T$ condition is given below,

$$I \propto V^{\left(\frac{T_c}{T}\right)+1} \quad \text{Eq. 68}$$

where, $\frac{T_c}{T}$ is related to the width of the distribution of traps [16, 50-51, 58, 60]. Small T_c values correspond to trap distributions that vary rapidly with energy, while large T_c values correlate with the slowly varying trap distribution [17]. When $T_c < T$, the current exhibits a square-law voltage dependence ($J \propto V^2$), similar to the trap-free and shallow trap SCLC; in contrast, an exponential voltage dependence is observed for large T_c values, indicative of a uniform trap distribution [16-17].

The temperature-dependence of the mobility ($J \propto \sigma \propto \mu$) is important where the μ is not changing rapidly with the temperature above T_c, but the mobility has exponential dependence at low temperatures ($\sigma \propto e^{\frac{h\nu}{T}}$) in the case of $h\nu < \frac{1}{2}E$ [11].

While the total space-charge in a semiconductor may vary with temperature due to factors such as thermal carrier generation and dopant ionization, the fraction of mobile space-charge electrons typically increases exponentially with temperature, primarily due to thermal activation of trapped charges and enhanced carrier mobility (despite increased phonon scattering), thus significantly influencing the electrical properties and charge transport mechanisms in semiconductor devices [16, 156]. Semiconductor conductivity generally increases with temperature, primarily due to the exponential increase in charge carrier concentration, which outweighs the decrease in carrier mobility from increased phonon scattering; however, the specific temperature-dependence varies with material, doping, and temperature range [57, 71]. Though conductivity increases with temperature in semiconductors, its temperature-dependence is dictated by trap distribution, not just conductivity, as temperature increases the conduction band's proportion of constant total space-charge carriers [17].

Undoped devices are ideal for SCLC analysis; typically exhibiting a square-law voltage dependence ($J \propto V^2$); however, doping (intentional or unintentional), which is inevitable during the synthesis and fabrication process, introduces additional charge carriers, altering the equilibrium charge carrier density and disrupting the ideal SCLC regime, leading to deviations from the ideal square-law dependence, particularly at low and intermediate voltages [17, 49, 53, 55].

Experimental conditions, including applied bias and device thickness, can significantly affect SCLC behavior, influencing the measured mobility [44]. Because of the difficulty of extracting accurate mobility data in real devices, drift-diffusion simulations are used to validate the use of ohm's law, and the Mott-Gurney law. The drift-diffusion simulation proves the validity of Ohm's law by incorporating both Mott-Gurney law and Ohm's law as a function of the thickness and the doping concentrations of single charge carrier devices, where the mobility from Mott-Gurney law can be applied to find the charge carrier density using Ohm's law; however, the valid regimes are small, existing only under extreme conditions, such as thin devices or high doping concentration devices, which are physically unfavorable and impractical in most situations, at the cost of violation of SCLC assumptions [49-50]. Analyzing the thickness dependence of SCLC in the J-V characteristics of organic single-carrier devices enables the differentiation between field-dependent and charge carrier density-dependent mobility in drift-limited transport [45]. The thickness of the material, in conjunction with trap density and injecting contact charge carrier concentrations, influences a substantial influence on charge transport within both the ohmic and SCLC regimes [119]. The valid regimes, where both Ohm's law and the Mott-Gurney law are applicable, can be determined by equating Eq. 23 and Eq. 29, and substituting n with N_D (doping concentration), as shown below [49].

$$V_{Tr,Ohm-MG} = V_{Tr,ME-MG} \quad \text{Eq. 69}$$

$$N_D L^2 = \frac{4\pi^2 K_B T}{q^2}\varepsilon \quad \text{Eq. 70}$$

While Eq. 70 provides some intuitions regarding doping concentration and thickness, where Ohm's law is used in conjunction with Mott-Gurney law, the analytical expression conflicts with the drift-diffusion simulation [49]. However, doped and intrinsic charge carrier devices can be

distinguished above a threshold doping concentration by differences in charge carrier concentrations, the energy level (E_c and E_v), conductivity, Fermi level position, and the slope of the SCLC region in a double logarithmic I-V characteristic [49-50].

The presence of dopants strongly influences SCLCs by filling deep traps with electrons, thereby controlling the power-law rise and eliminating the need to postulate an exponential or Gaussian defect density of states [42, 58]. This mechanism subsequently impacts I-V characteristics through its influence on space-charge accumulation, leading to two competing phenomena involving the rapid dynamics of localized charge carriers (e.g., ionization or trap filling): the introduction of additional charge carriers, which diminishes the space-charge effect, and the capture of charge carriers by ionized dopants, which enhances it [50, 116]. Therefore, doping significantly influences both the Mott-Gurney regime (via space-charge effects) and hysteresis in semiconductors, as the interplay between introduced charge carriers and ionized dopants alters space-charge distributions and localized carrier dynamics, thus modulating both SCLC current-voltage characteristics and transient/memory behaviors, which is crucial for optimizing device performance [116].

In semiconductors, the Debye length (electric field screening length) refers to the characteristic length scale that screens out electric fields due to the presence of charge carriers and sets a limit on the potential change in response to an abrupt doping profile change, as shown below [49, 71].

$$L_D \equiv \sqrt{\frac{\varepsilon K_B T}{q^2 n}} \qquad \text{Eq. 71}$$

For a valid Mott-Gurney law analysis, the single charge carrier device thickness should be significantly larger than the Debye length, not less than twice the Debye length [49, 71].

While space-charge effects are significant in thin devices, especially those with thicknesses comparable to the Debye length, the charge carrier density is not solely determined by space-charge; intrinsic carrier density, doping, temperature, and contact effects also play substantial roles, even at low voltages [49, 64]. While the Debye length can be a useful approximation for lightly doped or intrinsic semiconductors, especially at higher temperatures, the Thomas-Fermi screening length more accurately describes electric field screening by electrons in moderately to heavily doped semiconductors [64].

Device thickness, without directly altering doping concentration, influences the impact of doping and space-charge regions; the interplay of doping, device geometry, and electric fields determines carrier distribution and device behavior, with space-charge regions in thin devices occupying a larger fraction of the total thickness and thus more significantly affecting carrier distribution [49-50]. As doping concentration increases in a single charge carrier device, the equilibrium charge carrier density becomes negligible compared to the space-charge density, and the space-charge regions at the metal-semiconductor (MS) junction shrink, resulting in a non-uniform space-charge distribution [49, 57, 71]. In single-carrier devices, the carrier density, except within space-charge regions, approximates the doping concentration, leading to SCLC behavior (governed by the Mott-Gurney law) up to a threshold doping level, above which ohmic conduction dominates, even though space-charges remain the primary carriers, with SCLC ($J \propto V^2$) behavior only occurring under specific conditions [49-50, 116]. In contrast to trap-free metal-insulator-metal (MIM) barriers (similar to single charge carrier device with asymmetric contact), which exhibit a convex energy profile at zero current, the presence of traps significantly alters the energy and concentration contours, leading to increased curvature (potentially causing a canceled or reversed resident field and an energy maximum within the barrier) and ultimately

resulting in deterioration of the rectification ratio and altered current-voltage characteristics [118]. For example, in a highly doped single-carrier device where current behavior is initially governed by Ohm's law (Eq. 8), the transition from linear to square-law voltage dependence occurs above 0.9 V; therefore, the transition voltage for ohmic to Mott-Gurney conduction (Eq. 23), $V_{Tr\theta,Ohm\text{-}Mott\text{-}Gurney}$, should be used to define this transition [49, 131].

Furthermore, the mean free path, a key parameter, influences the charge carrier mobility,

$$\mu = \frac{q\lambda^*}{m^*\bar{\upsilon}} \quad \text{Eq. 72}$$

where λ^* is the mean free path, m^* is the effective mass, and $\bar{\upsilon}$ is the mean velocity [11].

The average kinetic energy is given below.

$$E_{kin,avg} = \frac{1}{2}m^*\bar{\upsilon}^2 = \frac{2}{3}K_BT \quad \text{Eq. 73}$$

The average velocity can be obtained by rearranging Eq. 73.

$$\bar{\upsilon} = \sqrt{\frac{3K_BT}{m^*}} \quad \text{Eq. 74}$$

Substituting Eq. 74 into Eq. 72 gives the relationship between the mobility and the mean free path based, assuming the effective mass of the charge carrier (electron or hole) equals the electronic mass [11].

$$\mu = \frac{q\lambda^*}{m^*\bar{\upsilon}} = \frac{q\lambda^*}{m^*}\sqrt{\frac{3K_BT}{m^*}} = q\lambda^*\left(\frac{3K_BT}{m^{*3}}\right)^{1/2} \quad \text{Eq. 75}$$

CHAPTER 4: SAMPLE AND DEVICE PREPARATIONS

4.1. Solvothermal Method for Synthesis of β-ZnTe(en)$_{0.5}$

A primary mechanism of solvothermal synthesis lies in its ability to generate high autogenous pressures within sealed reaction vessels by operating at temperatures above the boiling points of the reactants, thereby facilitating the controlled crystallization of materials [72, 73]. This technique encompasses diverse variations like hydrothermal, ammonothermal, and saccharothermal methods, relying on solubility differences induced by temperature gradients [72, 73]. Solvent selection plays a critical role in solvothermal synthesis; while aqueous hydrothermal methods are predominantly employed for oxide formation, non-aqueous solvents are indispensable for non-oxide synthesis, and advanced techniques such as microwave-hydrothermal processing provide diverse routes to nanomaterials with precisely controlled attributes [72].

Solvothermal reactions are governed by both chemical (reagent and solvent nature) and thermodynamic parameters (temperature, pressure, reaction time), all of which are carefully controlled to optimize crystal growth [72, 73]. These reactions encompass diverse chemical processes, including redox, hydrolysis, thermolysis, complexation, and metathesis, enabling applications in material synthesis, functional material processing, low-temperature crystal growth, controlled micro/nanocrystal formation, low-temperature sintering, and thin film deposition [72].

Solvothermal synthesis enables the creation of a wide range of novel materials. For instance, employing non-aqueous solvents expands beyond traditional hydrothermal methods, allowing the fabrication of materials with tailored morphologies, such as zeolites, low-temperature diamond,

and diverse carbon nanostructures [73]. This approach facilitates the synthesis of geo-inspired compounds, light element materials, hydrothermal diamond, cubic boron nitride (c-BN), C_3N_4, MoS_2 nanosheets, organic-inorganic hybrids, and nanotube-structured nanocrystallites like carbon, bismuth, tellurium, and intermetallic nanowires such as FePt, all driven by their application potential [1, 72, 74].

Key advantages of solvothermal synthesis include precise control over morphology and size, the ability to utilize diverse precursors, the feasibility of high-pressure reactions at lower temperatures, and the potential for one-step heteroatom doping [73]. However, the process also presents challenges, such as the necessity for specialized high-pressure equipment, waste management issues, limitations in achieving ideal morphologies, and difficulties in observing reaction mechanisms [73].

The utilization of heated organic solvents under pressure in solvothermal methods offers a tunable, cost-effective, and environmentally benign strategy for the synthesis of highly crystalline micro/nanocarbons with precisely controlled properties [73]. Solvothermal methods facilitate the synthesis of II-VI based nanomaterials across diverse dimensionalities, including one-dimensional, two-dimensional, and three-dimensional structures.

β-$ZnTe(en)_{0.5}$ is synthesized by solvothermal method [1]. Two millimoles (0.595 g) of zinc nitrate hexahydrate ($Zn(NO_3)_2{\cdot}6H_20$, Strem Chemicals, Inc., CAS 10196-18-6) and one millimole (0.128 g) of tellurium (Te, Strem Chemicals, Inc., CAS 13494-80-9) were precisely measured by a laboratory scale (Fisher Scientific International, Inc., ACCU-224). These reactants were then transferred to a Teflon-lined stainless steel high-pressure acid digestion vessel (Parr Acid Digestion Bombs, 23 mL volume). Subsequently, 6 mL of ethylenediamine (EMD Millipore Corp., CAS 107-15-3) was poured into the vessel, which was then sealed with

the lid. The vessel was placed in a muffle furnace (Tabletop Furnace Company, LLC., Rapidfire Programmable Pro-LP) and heated to 200 ℃ for three days. Following this, the temperature was naturally reduced to ambient conditions, and the vessel was removed from the muffle furnace. The resulting product consisted of a mixture containing β-ZnTe$(en)_{0.5}$, byproduct (black color), and liquid. Separation of the solid components was achieved by pouring the mixture onto a filter and applying a vacuum to remove the liquid. β-ZnTe$(en)_{0.5}$ was then purified through sequential rinses with distilled water, 95 % ethanol (Koptec, CAS 64-17-5), and ethyl ether (VWR International, LLC., CAS 60-29-7), followed by air drying. The final product, β-ZnTe$(en)_{0.5}$, presented as colorless flake-like crystals.

4.2. Device Fabrication of β-ZnTe$(en)_{0.5}$

This overview aims to discuss UV photolithography, electron beam lithography (EBL), shadow mask, and stencil lithography, specifically in the context of device fabrication of β-ZnTe$(en)_{0.5}$. Initially, it is important to note that UV photolithography and EBL, while powerful, utilize chemicals like photoresists, developers, and solvents, which can lead to partial sample degradation and challenge lift-off processes due to adhesive chemical use. Furthermore, UV photolithography has been observed to induce cracks in β-ZnTe$(en)_{0.5}$, likely due to mask-sample contact within the mask aligner. To mitigate these issues, shadow masking and stencil lithography offer alternative fabrication approaches.

UV photolithography, a fundamental microchip fabrication technique that uses UV light and photomasks to pattern photoresist-coated substrates for precise microscale device creation, is also being adapted to pattern delicate 2D materials, enabling the fabrication of novel nanoscale electronic and optoelectronic devices [109, 194]. Although UV photolithography is a well-

established approach, fabrication processes still introduce minor defects in graphene and slight damage to MoS_2 and WSe_2 sheets; however, the good signal-to-noise ratio in their Raman spectra indicates minimal impact on material quality [109].

However, for applications requiring finer resolution, EBL is essential for nanoscale patterning in nanotechnology and semiconductor manufacturing, outperforming traditional photolithography's feature size limitations [110, 194]. For example, a novel three-level lithography technique combining statistical nanowire alignment with microscopic selection further surpasses traditional EBL limitations, achieving 1 nm nanoscale gaps, material flexibility, and high device functionality [31, 194].

In contrast to the high resolution of EBL, shadow mask, a basic patterning method, involves using a physical mask to block material deposition or etching [190]. However, a key limitation of both shadow masking and stencil lithography is the shadow effect [193]. This occurs when the deposition angle or the gap between the mask and substrate causes blurring or distortion of the patterned features, particularly affecting resolution and feature uniformity [137, 192, 193]. This effect is more pronounced with larger gaps or non-collimated deposition sources [159]. Figure 11 exhibits how the separation between the substrate and shadow mask influences the deposition area [159]. In shadow mask deposition, the spatial separation between the substrate and the mask critically influences the accuracy of the transferred pattern. As shown on the left side of Figure 11, when a non-negligible gap exists (separation $D \neq 0$), the deposited thin film exhibits a broadened profile characterized by reduced edge sharpness and overspray (smearing effect). This phenomenon arises from the divergence of the deposition flux, which allows material to deposit in regions nominally blocked by the mask. In contrast, achieving intimate contact between the substrate and the shadow mask effectively minimizes this divergence, resulting in a thin film

profile with sharp, well-defined edges, consistent with the intended pattern, as shown on the right side of Figure 11.

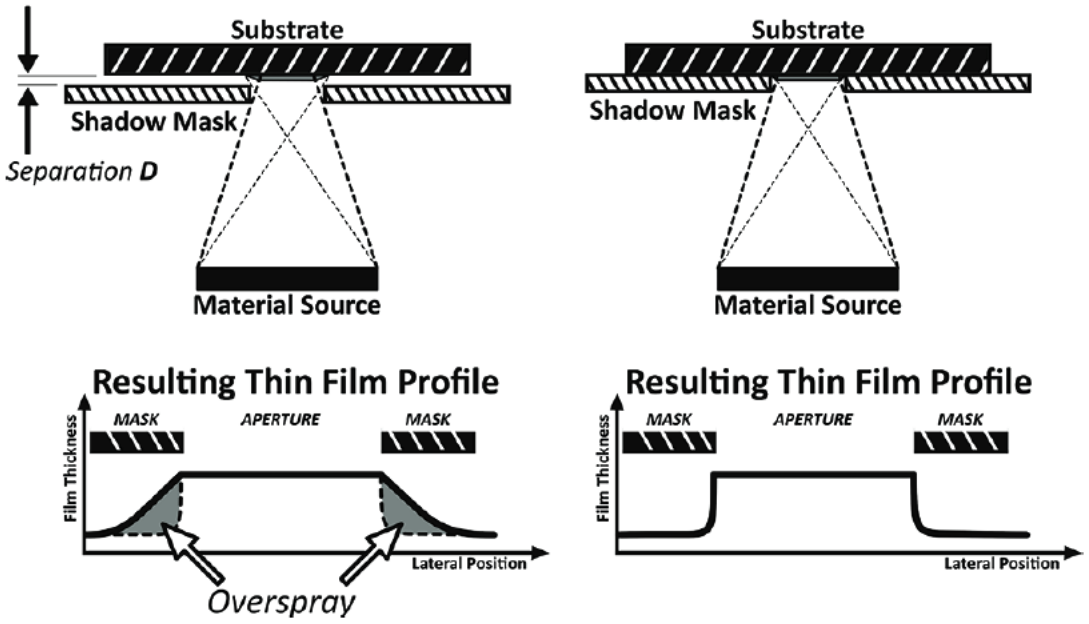

Figure 11: Schematic illustration of the influence of substrate-shadow mask separation (D) on thin film deposition profiles [159]. On the left, a non-negligible gap (separation $D \neq 0$) results in a broadened thin film profile with reduced edge sharpness and overspray, due to the divergence of the deposition flux (smearing effect). Material deposits in areas nominally blocked by the mask. On the right, intimate contact between the substrate and shadow mask minimizes this divergence, leading to a sharp, well-defined thin film profile consistent with the intended pattern.

The shadow mask approach, for instance, can create 5μm features, bridging integrated circuit (IC) and printed circuit board (PCB) fabrication, although thermal expansion necessitates precise control [159]. Shadow mask deposition is also employed for fabricating nonplanar microlenses for optoelectronic devices, with microlens curvature and deposition rates being influenced by

mask geometry, material, and deposition method [191]. To overcome the resolution limits of traditional shadow masks, such as Invar fine metal masks, silicon-based magnetic metal hard masks have been developed, incorporating magnetic films to reduce bending by gravity and improve pattern uniformity [193]. Spin-coated polystyrene spheres serve as a shadow mask with random apertures, including submicron openings [36]. A silicon shadow mask, fabricated via deep silicon etching, further demonstrates precise material deposition, including complex patterns and alignment structures [187]. Moreover, shadow mask evaporation is used to fabricate nanoscale metal contacts on delicate molecular devices, avoiding damage from conventional lithography [189]. Double shadow mask technique was employed to create submicron interelectrode gaps with asymmetric electrodes for studying space-charge-limited current (SCLC) behavior in organic single-nanofiber devices [38]. While organic crystal surfaces are inherently susceptible to contamination and defects, metal deposition via e-beam evaporation further exacerbates this issue by inducing localized states and increasing trap densities, which degrades device performance, a phenomenon highlighted by the stark difference in injection efficiency between e-beam evaporated and laminated contacts; thus, alternative methods like flip-chip lamination are crucial for maintaining crystal integrity [58].

Stencil lithography, an evolution of shadow masking, targets high-resolution nanopatterning [190]. It offers resist-free processing and versatility, enabling deposition, etching, and ion implantation on diverse materials [137, 188, 191]. Advancements in stencil lithography have addressed challenges like blurring and clogging, expanding its applications in plasmonic, 2D material contacts, biosensing, flexible devices, and biological patterning [137, 188, 190, 191]. Stencil lithography using suspended silicon nitride membranes enables resist-free fabrication of 15 nm metal dots and 15-20 nm lines, with resolution influenced by beam divergence and surface

diffusion [188]. Furthermore, a novel stencil lithography technique utilizing suspended PMMA membranes enables solvent-free fabrication of pentacene FETs with sub-micron resolution, achieving stable contacts and revealing SCLC dominated transport in short channels [192]. Beyond shadow mask and stencil lithography, microsoldering has been employed in the fabrication of 2D material devices, offering an alternative that eliminates the need for chemical processing and specialized metal deposition instrumentation; however, this technique is technically demanding, necessitates a degree of practical expertise, and carries the risk of potential sample damage due to excessive heat [108].

Although UV photolithography and EBL offer high resolution, they present challenges related to chemical use, which leads to the degradation of β-ZnTe(en)$_{0.5}$. The shadow mask approach provides viable, reusable alternatives, offering a resist-free, versatile patterning technique for device fabrication. Unlike UV photolithography and EBL, the shadow mask approach avoids UV photon and high-energy electron exposure, preserving the integrity of the materials. Moreover, it involves fewer steps, simplifying the fabrication process and reducing potential errors, which further contributes to its efficiency and cost-effectiveness.

While space-charge-limited current (SCLC) measurements can be performed on devices with either vertical (photovoltaics, LEDs) or lateral (FETs) structures, vertical devices are more commonly used for SCLC analysis [16, 25, 28, 30, 34, 36, 41, 44, 49, 115-117, 157]. The lateral dimension (a- and c-axis) of β-ZnTe(en)$_{0.5}$ ranges from tens to hundreds of micrometers, while their thickness (b-axis) is approximately 6-10 μm, enabling precise shadow mask alignment for metal deposition without specialized tools. The precise thickness of β-ZnTe(en)$_{0.5}$ was measured by Scanning Electron Microscopy (SEM) (JEOL JSM 6460 LV) and profilometer (KLA-Tencor P7 Profilometer). Both vertical and lateral device configurations are used in β-ZnTe(en)$_{0.5}$ for

SCLC measurement to investigate anisotropic transport properties along different crystal axes. Three electrode patterning techniques (photolithography, Electron-beam lithography, and shadow mask) were considered, with a shadow mask (Micron Laser Technology, Inc.) approach was ultimately chosen for metal deposition on β-$ZnTe(en)_{0.5}$ to minimize potential degradations by chemical exposures like photoresist and developer.

While SCLC analysis is commonly performed on single charge carrier devices, two charge carriers SCLC can be achieved under specific conditions. These conditions include: 1) the electrodes are symmetrical, and the metal work functions are closely matched to the semiconductor's electron affinity (for electron) and ionization energy (for holes), enabling efficient and equal injection of electrons and holes; 2) the semiconductor exhibits low or no trap states, minimizing carrier trapping; 3) electron-hole recombination is minimized, maintaining charge carrier concentrations; 4) the ratio of electron to hole mobility is close to 1, facilitating balanced carrier transport; and 5) diffusion current is neglected [20, 56, 124]. Two charge carrier devices typically exhibit higher current flow than single charge carrier devices because both electrons and holes contribute to conduction and partially neutralize space charge regions [124]. For accurate SCLC analysis, it is important to design electrodes so that the transverse dimension of electrodes should be much greater than the interelectrode spacing, as electrodes significantly influence carrier injection, transport barriers, and the onset of SCLC regimes (V_{Tr}) [25, 47]. Charge carrier transport in lateral metal-perovskite-metal structures, particularly the influence of the metal-perovskite interface, reveals distinct ohmic and SCLC regimes controlled by inter-electrode length and applied bias; shorter inter-electrode spacing increases the electric field, resulting in higher current densities and a faster transition from ohmic to SCLC behavior (lower V_{Tr}) [157]. Proper electrode design is crucial for accurately determining charge carrier mobility

and trap density from SCLC measurements, especially in complex materials like metal halide perovskites, where ion accumulation at electrodes can alter charge injection, necessitating advanced techniques (e.g., pulsed I-V measurement instead of steady-state) to minimize artifacts [16, 60, 91, 158].

Optimizing shadow mask thickness is crucial in device fabrication, as it must be thick enough to maintain structural integrity during metal deposition yet thin enough to prevent blocking deposition areas on the β-ZnTe$(en)_{0.5}$ due to line-of-sight limitations, while also minimizing the smearing effect caused by the separation between the mask and substrate, which is particularly problematic in small-feature structures [159].

Prior to device fabrication, a rigorous cleaning protocol was employed on substrates (Si/SiO_2). Initially, the substrates underwent a solvent-based cleaning regimen, designed to remove organic contaminants from the surface. This process typically involves sequential immersion in solvents such as acetone, isopropyl alcohol, and deionized water, each chosen for its specific solvency properties. Following the solvent cleaning, an RCA (Radio Corporate of America) cleaning procedure was performed. This method, comprising a series of chemical treatments, is specifically effective in removing both organic residues and ionic contaminants, including heavy metals [68, 69]. The RCA cleaning is crucial for achieving a pristine substrate surface, which is essential for ensuring high-quality thin film deposition and device performance. The sequential application of solvent and RCA cleaning procedures ensures the removal of a broad spectrum of surface contaminants, thereby optimizing the substrate for subsequent fabrication steps.

Figure 12 shows a schematic diagram of the vertical device preparation flow. Prior to device fabrication, the sample's condition was assessed using Confocal Raman Spectroscopy (Horiba LabRAM HR800, λ=532 nm). First, β-ZnTe$(en)_{0.5}$ is carefully placed onto a substrate using a

vacuum pen (Virtual Industries, INC., Pen-Vac™ Pro Series), with manual alignment achieved using a shadow mask under a microscope (Olympus, MX51). Heat-resistance tape (Kapton® tape) is used to secure the shadow mask on the substrate. Second, the aligned substrate with β-$ZnTe(en)_{0.5}$ is mounted on a sample holder (substrate holder) and loaded into a vacuum chamber (Kurt J. Lesker, PVD 75™) for the metal deposition. The PVD system is operated with the desired parameters, including material and thickness. To minimize heating effects, the metal electrodes were deposited in two layers, each 150 nm thick [91]. Unload the sample holder from the vacuum chamber after the metal deposition. Third, after the metal deposition on one side of the β-$ZnTe(en)_{0.5}$, the shadow mask is removed, and the sample is detached from the substrate using the vacuum pen. β-$ZnTe(en)_{0.5}$, with the metal electrodes side facing the substrate, is carefully placed onto the substrate using a vacuum pen. A shadow mask is then aligned on the opposite side, not previously deposited surface of the β-$ZnTe(en)_{0.5}$, under a microscope, following the same alignment procedure as described earlier. Precise alignment of the two electrodes along the stacking axis (b-axis) is crucial. Similarly, heat-resistance tape is used to secure a shadow mask on a substrate. Fourth, the aligned substrate with β-$ZnTe(en)_{0.5}$ is mounted on a sample holder and then loaded into the vacuum chamber for the metal deposition on the other side of β-$ZnTe(en)_{0.5}$. To avoid asymmetric electrode effects, the same material (and thickness) is used in the PVD process [157]. To reduce heat-related impacts, a dual-layer metal electrode, with each layer measuring 150 nm in thickness, was deposited [91]. Unload the sample holder from the vacuum chamber after the metal deposition. Fifth, a shadow mask and heat-resistance tapes are removed after unloading β-$ZnTe(en)_{0.5}$ from the vacuum chamber. While no chemicals are involved in the process, β-$ZnTe(en)_{0.5}$ is exposed to heat during the metal deposition process, necessitating Raman spectroscopy to monitor for possible degradation.

For two-probe vertical electrical measurements, β-ZnTe(en)$_{0.5}$ has two electrodes on both sides, aligned along the b-axis.

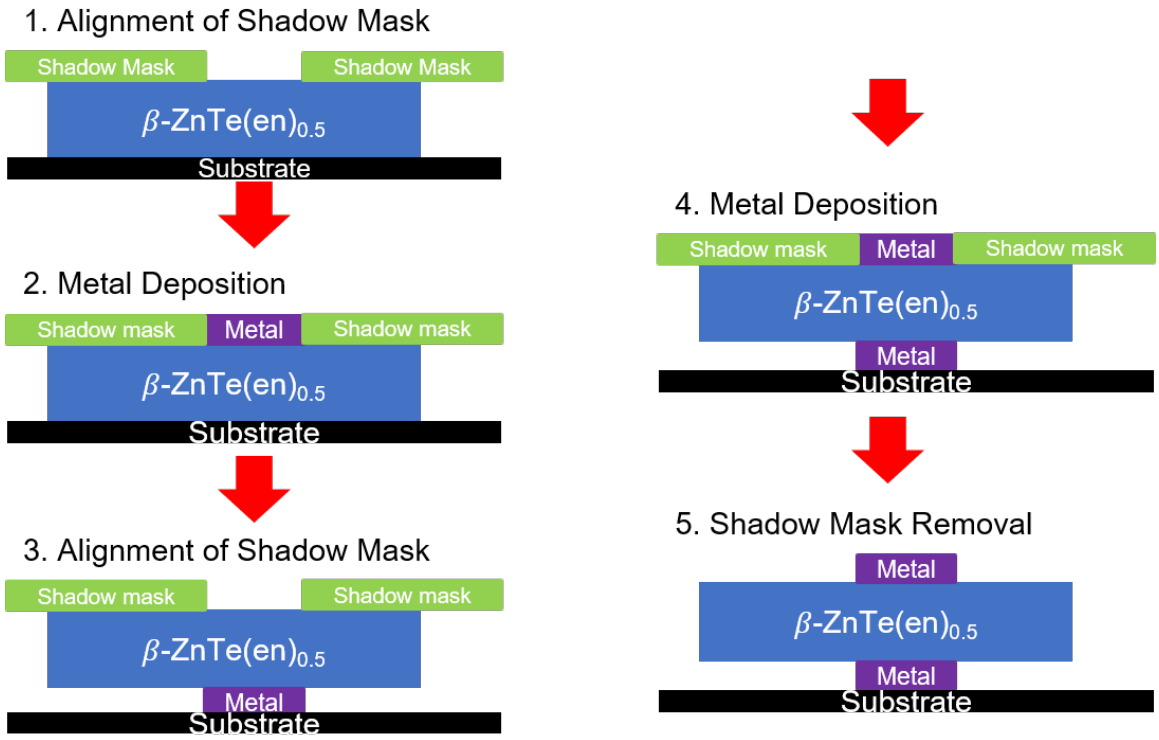

Figure 12: Cross-Section View of Schematic Diagram of Vertical Device Preparation Flow

Confocal Raman Spectroscopy (Horiba LabRAM HR800, λ = 532 nm excitation) was employed to determine the sample's condition prior to lateral device fabrication. Furthermore, polarization Raman spectroscopy was utilized to definitively confirm the crystal axis orientation [178]. Although empirical experience suggested the c-axis was along the longer edge of the crystal and the a-axis along the shorter edge, polarization Raman spectroscopy was employed to definitively confirm the crystal axis orientation, leveraging the unique Raman peak patterns characteristic of specific crystallographic directions [139, 178].

Figure 13 presents polarization Raman spectroscopy spectra acquired along the crystallographic a-axis and c-axis, with observed vibrational frequencies annotated. Notably, discrepancies were observed between the experimentally determined and computationally predicted frequencies [178]. The measured frequencies, derived from these polarization Raman spectra, were utilized for crystal axis identification. Three common vibrational modes were identified in both the a-axis and c-axis spectra, exhibiting frequencies of 23.64 cm^{-1}, 95.81 cm^{-1}, and 132.55 cm^{-1}, which deviate from the reported values of 23.8 cm^{-1}, 96.3 cm^{-1}, and 132.8 cm^{-1}, respectively. A reported vibrational mode frequency of 175.8 cm^{-1} was observed as 176.52 cm^{-1} along the crystal a-axis and 174.08 cm^{-1} along the crystal c-axis, indicating a slight frequency shift between the two crystal axes. Additionally, the a-axis spectra revealed frequencies at 1052.17 cm^{-1} and 1169.35 cm^{-1}, with corresponding deviations from reported values of 1054.1 cm^{-1} and 1171.2 cm^{-1}, respectively. Similarly, the c-axis spectra revealed modes at 284.56 cm^{-1}, 540.01 cm^{-1}, and 989.10 cm^{-1}, deviating from reported values of 285.0 cm^{-1}, 540.2 cm^{-1}, and 990.8 cm^{-1}, respectively.

While occasional deviations between observed and reported Raman frequencies are noted, understanding their origins is essential. In the context of β-$ZnTe(en)_{0.5}$'s exceptional crystallinity, characterized by a sub-1 cm^{-1} Raman linewidth (< 1 cm^{-1}) comparable to high-quality binary semiconductors (GaAs, CdTe, ZnO, and GaN), a 0.5 cm^{-1} frequency shift is considered within acceptable experimental limits [10, 178]. This minor deviation aligns with the inherent precision of Raman spectroscopy measurements on such highly ordered materials. A 1 cm^{-1} frequency shift, despite near-perfect structural order of β-$ZnTe(en)_{0.5}$, evidenced by narrow Raman linewidths and sharp X-ray diffraction rocking curves, effectively minimizes deviations arising from defects or disorder, is largely attributable to subtle intrinsic vibrational properties, such as

phonon interactions [10, 178]. Given the inherent crystallinity of β-ZnTe(en)$_{0.5}$, a 2 cm^{-1} Raman frequency shift, significantly exceeding expected precision, strongly indicates the influence of external factors like sample degradation, rather than intrinsic material properties.

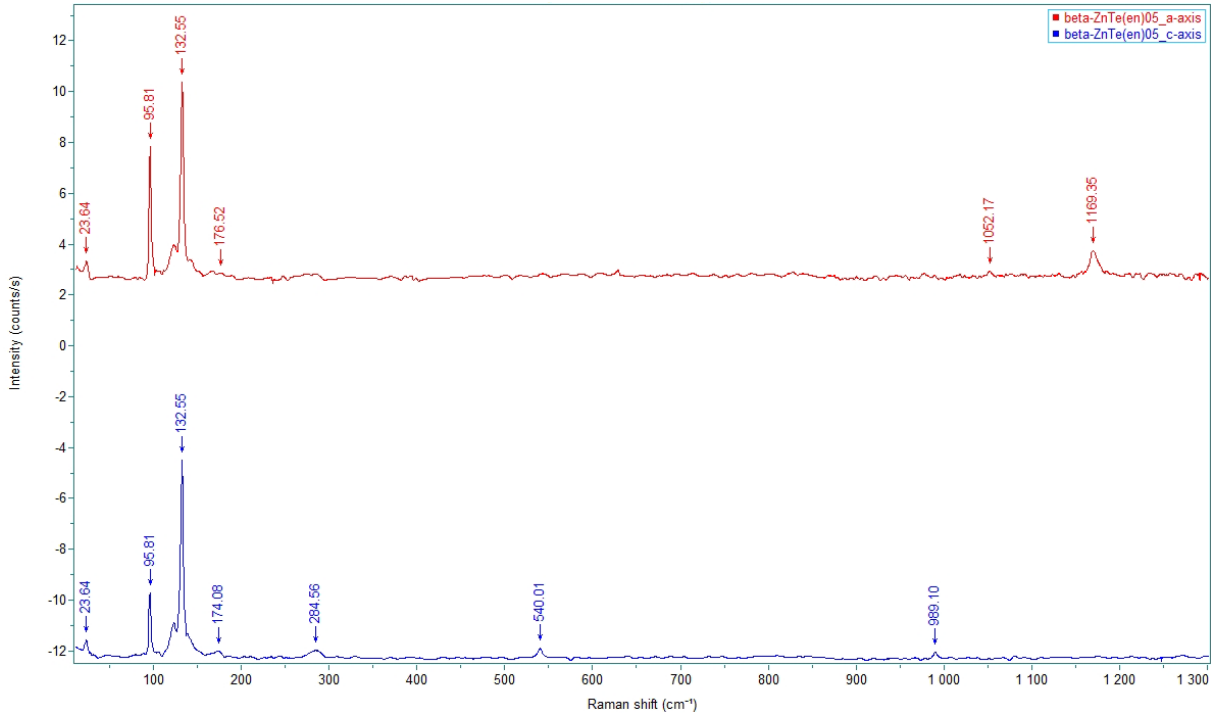

Figure 13: Polarization Raman spectroscopy spectra of β-ZnTe(en)$_{0.5}$ acquired along the crystallographic a-axis (red color) and c-axis (blue color) by Confocal Raman Spectroscopy (Horiba LabRAM HR800, λ = 532 nm excitation). Raw spectra, with observed vibrational mode frequencies annotated using LabSpec 6 Spectroscopy Suite Software, are presented without further analysis.

For lateral devices, β-ZnTe(en)$_{0.5}$ is placed on top of the substrate, and a shadow mask is aligned and placed over it. Under ideal conditions, electrostatic forces can secure the sample to the

substrate. However, under non-ideal conditions such as vibrations or airflow, the electrostatic force may be insufficient to secure the sample to the substrate, potentially leading to dislocation or detachment of β-$ZnTe(en)_{0.5}$ from its original location. Heat-resistant tape is then used to secure both the shadow mask and the substrate to the sample holder before loading them into the vacuum chamber for electrode deposition via the PVD process. After the initial process, it was observed that the samples were not secured in their original location but had shifted to an unintended position during transport to the vacuum chamber. This occurred because the sample holder needed to be flipped to be secured on the rotation stage in the vacuum chamber, causing misalignment of the samples. Thus, several adhesives compatible with β-$ZnTe(en)_{0.5}$, including cement glue, negative epoxy photoresist, and planarizing coating, are used. The condition of β-$ZnTe(en)_{0.5}$ is inspected using Raman spectroscopy prior to each starting device fabrication. After conducting controlled experiments, two approaches are used to fabricate lateral devices. Figure 14 illustrates a schematic diagram of the first approach for lateral device preparation. First, a 1.5 μm thick layer of SU-8 2 (Microchem), a permanent negative epoxy photoresist, was spin-coated onto the substrate (Si/SiO_2) using a Brewer Science, Inc., CEE200 spin coater with a two-step process: 500 rpm for 5 seconds, followed by 3000 rpm for 30 seconds. Second, β-$ZnTe(en)_{0.5}$ is then carefully placed onto the spin-coated negative epoxy photoresist using a vacuum pen under a microscope. Third, β-$ZnTe(en)_{0.5}$/substrate is then placed on a hot plate (Brewer Science, Inc., CEE 1100FX) and subjected to a two-step pre-bake process: 1 minute at 65 ℃, followed by 1 minute at 95 ℃. Fourth, β-$ZnTe(en)_{0.5}$/substrate is placed on the chuck of a mask alignment system (Quintel, Q4000-6TL) and exposed to i-line (365 nm) for 20 seconds. The exposure time varies depending on the optical power and the thickness of the negative epoxy photoresist, and the reference parameter can be obtained from the fact sheet. Fifth, β-

$ZnTe(en)_{0.5}$/substrate undergoes a post-bake process on the hot plate, with sequential heating for 1 minute at 65 ℃ and then 1 minute at 95 ℃. These processes are implemented to secure β-$ZnTe(en)_{0.5}$ onto the substrate. Sixth, a 1.5 μm thick layer of positive photoresist (SHIPLEY®, MICRODEPOSIT™ S1813™) is spin-coated onto β-$ZnTe(en)_{0.5}$/substrate using a spin coater with a two-step process: 500 rpm for 5 seconds, followed by 3000 rpm for 30 seconds. Seventh, β-$ZnTe(en)_{0.5}$/substrate is placed on the hot plate for a pre-bake process for 1 minute at 115 ℃. Eighth, β-$ZnTe(en)_{0.5}$/substrate is placed on the chuck of a mask alignment system, and a photomask (Photo Science, Inc.) is used for the electrode design, ensuring that the two electrodes will be parallel to the a- or c-axis of β-$ZnTe(en)_{0.5}$. Ninth, following the photomask alignment, β-$ZnTe(en)_{0.5}$ is exposed to the i-line (λ = 365 nm) for 20 seconds. A post-bake process is not required in this process. Tenth, β-$ZnTe(en)_{0.5}$/substrate is submerged in developer (AZ Electronic Materials USA Corp., AZ® 300MIF Developer) for 20 seconds, rinsed thoroughly with deionized water, and dry with a direct nitrogen gas (N_2). Eleventh, β-$ZnTe(en)_{0.5}$/substrate is secured on a sample holder and loaded into the vacuum chamber for the metal deposition. The PVD system is operated with the desired parameters, including material and thickness. Metal electrodes, each 150 nm thick and applied in two layers, were fabricated to minimize thermal effects [91]. The sample holder was unloaded from the vacuum chamber after metal deposition. Twelfth, after unloading the sample from a vacuum chamber, β-$ZnTe(en)_{0.5}$/substrate is submerged in acetone to remove undesired areas of positive photoresist and metal areas via a lift-off process. Carefully sink β-$ZnTe(en)_{0.5}$/substrate in acetone, watching the structure under the microscope. Extend the sinking time if unwanted areas are not removed. Ensure the sample is completely submerged in acetone during this process. Once the undesired areas are removed, rinse with IPA and dry with nitrogen gas.

Following these procedures, β-ZnTe(en)$_{0.5}$ will have two electrodes, ideally parallel to the a- or c-axis, enabling two-probe lateral electrical measurement.

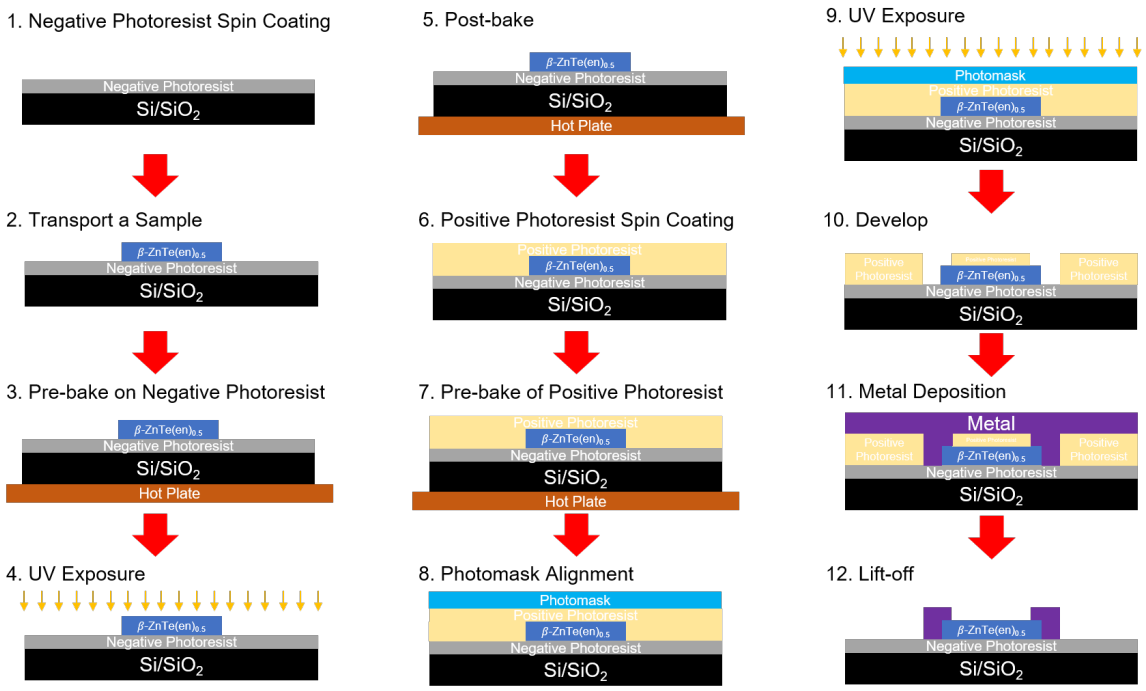

Figure 14: Cross-Section View of Schematic Diagram of 1st Lateral Device Preparation.

Following the fabrication of the device, it is observed that the hybrid Raman peaks weakened or disappeared, while two Tellurium Raman peaks emerged [10, 178]. This suggests that the extended chemical exposure, coupled with heat and UV exposure during processing, may have accelerated degradation. Therefore, an alternative device fabrication approach is warranted. Figure 15 illustrates the second approach for lateral device preparation, a simplified process involving fewer chemicals compared to the first approach shown in Figure 14. Using planarizing coating (Futurrex, Inc., PC3-1500) as a temporary adhesive layer, instead of negative epoxy photoresist, avoids the use of chemicals that potentially accelerate the degradation process, such as SU-8 2, S1813, MIF developer, and acetone, as well as UV exposures during β-ZnTe(en)$_{0.5}$

device fabrication process. First, a planarizing coating is spin-coated onto the substrate at 1000 rpm for 30 seconds. Here, the surface morphology of planarizing coating is a key factor in this process, whereas its exact thickness is less important, as the primary function of the coating is to secure β-ZnTe(en)$_{0.5}$ on the substrate. Second, β-ZnTe(en)$_{0.5}$ is then carefully placed onto the planarizing coating using a vacuum pen under a microscope. Third, β-ZnTe(en)$_{0.5}$/substrate is placed on the hot plate for 1 minute pre-bake at 115 ℃. Fourth, a shadow mask is aligned under a microscope to ensure the two electrodes are parallel to the a- or c-axis of β-ZnTe(en)$_{0.5}$. The heat-resistance tape is used to secure the shadow mask to the substrate. Fifth, the aligned substrate, now with the attached β-ZnTe(en)$_{0.5}$, is mounted on a sample holder and then loaded into the vacuum chamber for the metal deposition. The PVD system is operated with the desired parameters, including material and thickness. Heating effects were minimized by depositing metal electrodes in two 150 nm layers [91]. The sample holder was unloaded from the vacuum chamber after metal deposition. Sixth, after unloading the sample from a vacuum chamber, the shadow mask and heat-resistance tapes are removed.

Following these procedures, β-ZnTe(en)$_{0.5}$ will have two electrodes, ideally parallel to the a- or c-axis, enabling two-probe lateral electrical measurement. Three-probe electrical measurements are possible using a back gate, for which a heavily doped Si substrate would be a suitable choice.

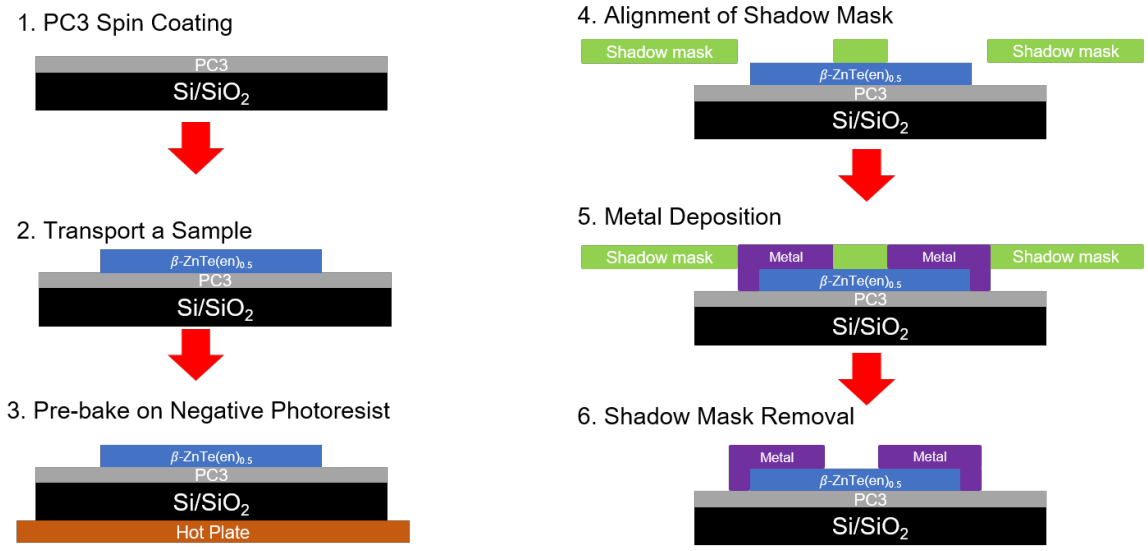

Figure 15: Cross-Section View of Schematic Diagram of 2nd Lateral Device Preparation.

Figure 11 highlights the critical requirement for intimate contact between the shadow mask and the sample (D = 0) to mitigate smearing effects during deposition [159]. Figure 16 schematically depicts that ideal conditions with no separation (D = 0) and the presence of any separation between the shadow mask and β-ZnTe(en)$_{0.5}$ (D ≠ 0) can lead to undesirable consequences, specifically broadening the electrode profile with reduced sharpness and electrode connection [159]. Ideally, with zero separation (D = 0), as shown in Figure 16 (a), well-defined two-terminal devices are achievable for lateral configurations. However, the presence of even a small separation between the shadow mask and β-ZnTe(en)$_{0.5}$ (D ≠ 0) can induce smearing, resulting in unintended electrical connections between the electrodes, as illustrated in Figure 16 (b). While electron-beam evaporation is known for its high directionality, stemming from the line-of-sight trajectory of evaporated atoms or molecules within a high-vacuum environment, the existence of separation can still contribute to smearing [194]. The observed smearing is likely attributable to

thermal deformation of the shadow mask during the deposition process. Despite secure adherence of β-ZnTe(en)$_{0.5}$ and the shadow mask to the sample holder, smearing occurred. To mitigate this metal electrode smearing issue, magnetic bars, which retain their properties under elevated temperatures, were employed. By positioning β-ZnTe(en)$_{0.5}$ between the magnetic bars and the shadow mask, optimal device fabrication was achieved.

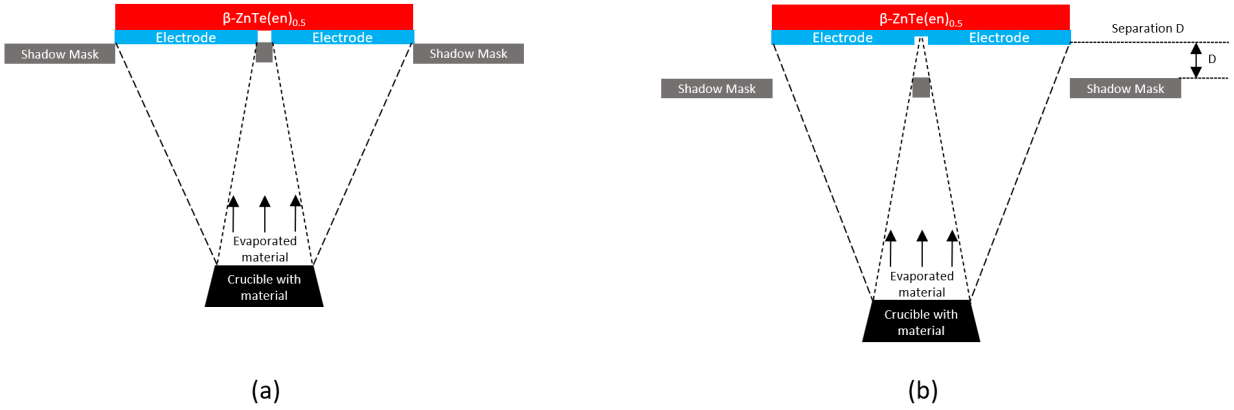

Figure 16: Cross-sectional view of schematic illustrations showing the impact of shadow mask separation (D) on electrode deposition. (a) Ideal conditions with no separation (D = 0) result in well-defined two-terminal devices for lateral configurations. (b) The presence of separation (D ≠ 0) between the shadow mask and β-ZnTe(en)$_{0.5}$ induces smearing, leading to unintended electrical connection between the two electrodes.

Although surface oxidation is common in ambient conditions, and not an absolute certainty, both bulk ZnTe and β-ZnTe(en)$_{0.5}$ surfaces might exhibit an inherent oxidation layer. This phenomenon is attributed to atmospheric exposure prior to metal deposition, leading to the formation of surface oxides. Furthermore, the sample is stored in ambient conditions, which can further contribute to the growth of the oxidation layer. Time-of-Flight Secondary Ion Mass

Spectrometry (ToF-SIMS) analysis, utilizing comparative sputtering rates between bulk ZnTe and β-ZnTe$(en)_{0.5}$, revealed the oxide layer thickness to be approximately 5 nm (e.g., TeOx, unpublished data by Mr. Yizhou Wang). This thickness is considered sufficiently thin to facilitate charge carrier tunneling, thereby minimizing contact resistance. However, the presence of this interfacial oxide layer also induces interface states between the deposited metal and the β-ZnTe$(en)_{0.5}$ material, as previously observed [90, 114, 121]. While surface oxidation can be intentionally implemented in certain device architectures, its uncontrolled formation, particularly in novel materials such as β-ZnTe$(en)_{0.5}$, introduces potential variability and may compromise sample integrity. Although the surface oxidation layer can be removed through appropriate treatments, such removal may not be advantageous if the layer's thickness does not impede charge carrier transport. Nonetheless, regardless of whether it's removed, awareness of the oxidation layer's existence is crucial during both device preparation and data analysis to ensure accurate interpretation of device performance.

CHAPTER 5: EXPERIMENTAL PROCEDURES WITH DATA AND RESULTS

Two-probe measurements are performed on β-ZnTe(en)$_{0.5}$ devices using a Keithley source meter unit (SMU) 2401 (Tektronix, Inc.). Data acquisition is controlled using Kickstart software (Tektronix, Inc.) running on a computer connected to the SMU via a GPIB-USB-HS instrument control device (National Instruments Corp.).

Initial vertical measurements were conducted without metal electrodes, with β-ZnTe(en)$_{0.5}$ placed directly on a conductive substrate (Global Chip Materials, LLC., Ceramic packages, LCC8447002). Electrical probes (The Micromanipulator Company, 7B Tungsten Probe Tip, 0.5 μm radius) were installed on manipulators (The Micromanipulator company, model 110 & 350) for precise controls. One probe contacted β-ZnTe(en)$_{0.5}$, while the other contacted the conductive substrate. Figure 17 shows the experimental setup used for the vertical electrical measurement of β-ZnTe(en)$_{0.5}$ [10]. Measurements were performed on two pristine β-ZnTe(en)$_{0.5}$ synthesized in different years: one synthesized in 2007 (S07-p) and one newly synthesized in 2019 measured in 2020 (S19-p).

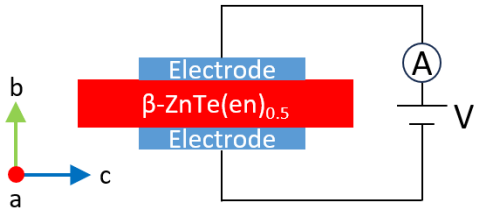

Figure 17: Experimental Setup for vertical electrical measurement [10].

The thicknesses of β-ZnTe(en)$_{0.5}$ were ascertained through Scanning Electron Microscopy (SEM) utilizing a JOEL JSM-6460LV instrument, as depicted in Figure 18. To ensure accurate

measurement, three distinct samples were analyzed, each imaged at two different magnifications. The first sample, presented in Figure 18 (a) (×1000 magnification) and Figure 18 (b) (×3000 magnification), measured 5.42 μm in thickness. The second sample, shown in Figure 18 (c) (×1000 magnification) and Figure 18 (d) (×3000 magnification), had a thickness of 7.17 μm. Finally, the third sample, displayed in Figure 18 (e) (×1500 magnification) and Figure 18 (f) (×3000 magnification)at magnifications of x1500 and x3000, was determined to be 9.17 μm thick. These measurements revealed a notable variation in thickness across the three samples.

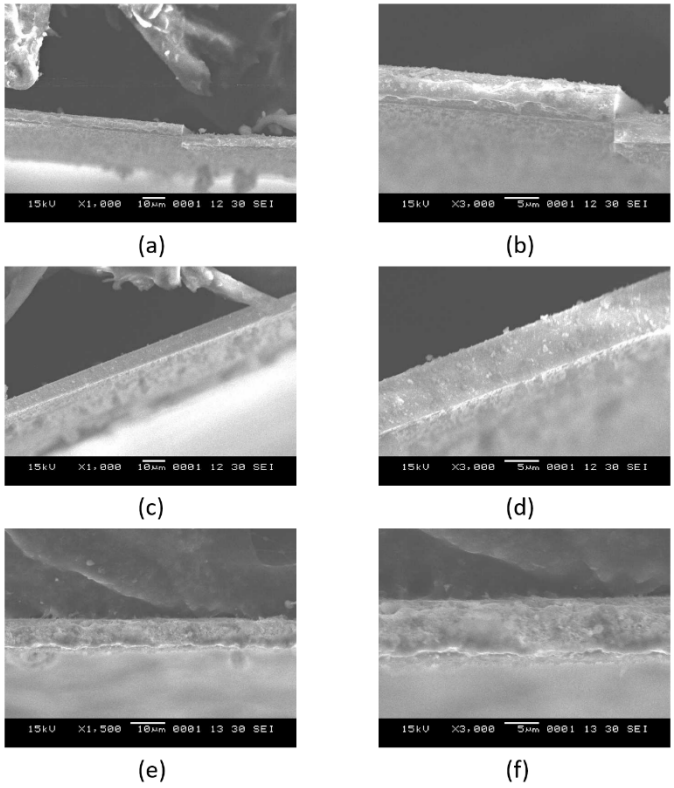

Figure 18: Scanning Electron Microscopy (SEM) images of β-ZnTe$(en)_{0.5}$ showing thickness measurements at varying magnifications. (a), (b) First sample, at ×1000 and ×3000 magnification respectively, thickness = 5.42 μm. (c), (d) Second sample, at ×1000 and ×3000 magnification

respectively, thickness = 7.17 μm. (e), (f) Third sample, at ×1500 and ×3000 magnification respectively, thickness = 9.17 μm.

Figure 19 shows the J-V characteristic of β-$ZnTe(en)_{0.5}$ vertical device in a linear scale. As shown in Figure 19, fitting the data to the Mott-Gurney law (Eq. 18, using $\varepsilon = 6$, $L_{S19\text{-}p} = 6$ μm, and $L_{S07\text{-}p} = 10$ μm with approximately 10% accuracy) yielded mobilities of $\mu_{S07\text{-}p} = 8.8 \times 10^{-3}$ $cm^2/(Vs)$ for S07-p and $\mu_{S19\text{-}p} = 2.5 \times 10^{-3}$ $cm^2/(Vs)$ for S19-p, representing the best achieved results for the respective batches of the samples [10]. The sample designation 'S07-p' indicates that the sample was synthesized in 2007 and was in pristine condition when measured. Similarly, the designation 'S19-p' indicates a sample synthesized in 2019, also in pristine condition. As expected for the transport along the inorganic-organic stacking direction, both mobility values are smaller than good quality inorganic semiconductors, but still higher than those of most organic semiconductors [10, 30].

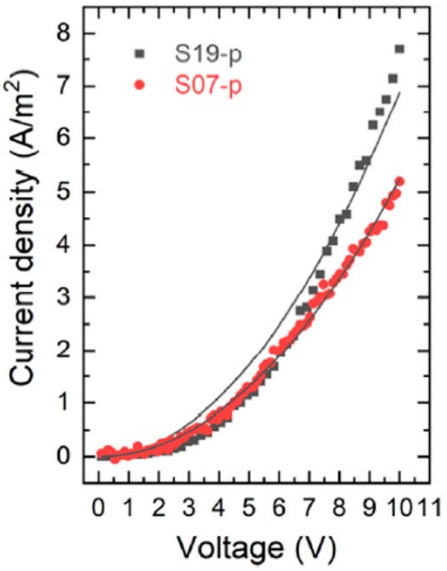

Figure 19: The J-V characteristics of β-ZnTe(en)$_{0.5}$ vertical devices are presented on a linear scale S07-p and S19-p [10]. The dots represent experimental data, and the lines show the fitted curves using the Mott-Gurney law (Eq. 18). S07-p and S19-p denote pristine samples synthesized in 2007 and 2019, respectively.

Figure 20 shows the J-V characteristic of β-ZnTe(en)$_{0.5}$ vertical device in a double logarithmic scale. A double logarithmic plot of the J-V curve effectively distinguishes distinct transport regimes, such as the ohmic ($J \propto V$), space-charge-limited ($J \propto V^n$, $n > 2$), and trap-influenced regions, each exhibiting a characteristic linear slope that facilitates the analysis, with deviations from the ideal SCLC behavior ($J \propto V^2$), revealing insights into the trap distribution, energy levels, and complex charge carrier transport mechanisms [17, 18, 160]. In a double logarithmic plot, the ideal ohmic regime exhibits a slope of 1 ($J \propto V$); however, as shown in Figure 20 (a), the slope of the S07-p sample in the ohmic regime deviates significantly from the ideal value. While this has not yet been explored in detail, plausible explanations exist to account for the

observed behaviors. Trap states within the material, particularly deep-level defects, can influence current-voltage behaviors, potentially leading to a slow current increase before the characteristic sharp rise associated with SCLC behavior [42]. The SCLC behavior in low-dimensional nanostructures such as nanowires and thin films differs significantly from ideal models due to a range of factors encompassing both classical effects like device geometry, contact asymmetries, and reduced dielectric properties, as well as quantum effects, dimensional constraints, and transient dynamics, thereby demanding advanced models to precisely characterize the observed deviations in voltage scaling and current densities [48, 60]. The dielectric constant's dependence on both frequency and field suggests that incorporating a field-dependent dielectric constant can improve the accuracy of current-voltage behavior interpretations, implying that the material's dielectric properties may vary with the applied field and potentially contribute to deviations from ideal ohmic behavior [53, 160]. Therefore, accurate SCLC analysis of organic semiconductors requires consideration of a field-dependent dielectric constant, as this field dependence directly influences field-dependent charge carrier mobility by modifying Coulomb interactions, trap effects, and dipole reorientation, which in turn alters charge transport and mobility extraction accuracy [30]. As shown in Figure 20 (a), the slope of the S07-p sample in the SCLC regime, $m_{SCLC} = 2.081$ is very close to the ideal value of 2 ($J \propto V^2$) in a double logarithmic plot. Fitting this regime alone yielded $\mu_{S07\text{-}p} = 8.8 \times 10^{-3}$ cm^2/(Vs), only slightly different from that from the full-range fitting.

In a double logarithmic plot for the S19-p, as shown in Figure 20 (b), in the low voltage regime, the S19-p sample's slope closely approximates the ideal value of 1 ($J \propto V$). However, as shown in Figure 20 (b), the slope in the high-voltage regime, $m_{SCLC} = 2.655$, deviates significantly from the ideal value of 2 ($J \propto V^2$). While a slope of approximately 2 is typically expected in the SCLC

regime, some studies have reported higher slopes. Deviations from the theoretical slope of 2 were noted in the SCLC regime, with reported values including 2.4, 2.5, 2.8, and 3.1, probably due to the presence of traps, where the power-law ($J \propto V^n$) is considered to be used instead of square-law ($J \propto V^2$) dependence, but the ideal Mott-Gurney is used for analysis [14, 17, 121, 155, 161]. The presence of traps, specifically in the form of exponential tail states within the bandgap, causes the slope of the current-voltage characteristic to deviate from the ideal value of 2 [121]. Deviations from the ideal slope, potentially due to trap filling or other material/device non-idealities as supported by related findings, including slopes exceeding 2 in SCLC measurements, can specifically indicate trap filling within the SCLC regime [14, 131, 158]. The spatial distribution of equilibrium and injected charge carriers can significantly influence the Schottky barrier height at metal-semiconductor junctions; consequently, the presence of this barrier height, which must be accurately determined for mobility calculations, suggests its significant impact on SCLC measurements [42, 162].

Figure 20 (c) presents the data for both S07-p and S19-p samples on a double logarithmic scale, which is useful for visualizing and comparing data spanning several orders of magnitude. Raman spectroscopy confirmed the pristine condition of β-ZnTe(en)$_{0.5}$ used in the electrical measurements, even after 13 years post-synthesis (S07-p). These samples, whose pristine condition was confirmed by Raman spectroscopy as shown in Figure 5, were also measured more than 15 years after their initial synthesis [10].

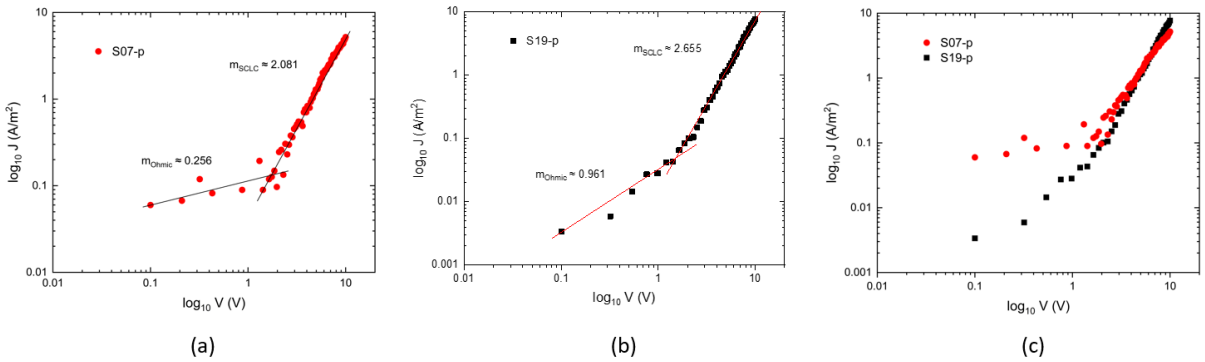

Figure 20: The J-V characteristics of β-ZnTe(en)$_{0.5}$ vertical devices are presented on a double logarithmic scale for (a) S07-p and (b) S19-p, respectively. (c) presents a comparative plot of the two datasets, revealing similar current densities. The dots represent experimental data, while the lines indicate the slope. S07-p and S19-p denote pristine samples synthesized in 2007 and 2019, respectively.

As demonstrated in Figure 19, S07-p and S19-p exhibit the superior performance characteristics among the vertical device configurations examined [10]. To further investigate these configurations, Figure 21 presents the linear J-V characteristics of β-ZnTe(en)$_{0.5}$ vertical devices for (a) S07-p_1, (b) S07-p_2, (c) S19-p_1, and (d) S19-p_2. The designations S07-p_1 and S07-p_2 denote pristine samples: S07-p_1 and S07-p_2 were synthesized in 2007, while S19-p_1 and S19-p_2 were synthesized in 2019. The numbered subscripts (e.g., _1, _2) distinguish individual devices within each sample batch. Experimental data, shown as dots, were fitted to the Mott-Gurney law (Eq. 18). Consistent with the fitting parameters used for Figure 19, the permittivity ($\varepsilon = 6$) and sample thickness ($L_{S19\text{-}p} = 6$ μm, and $L_{S07\text{-}p} = 10$ μm) were employed [10]. The resulting mobility values were: $\mu_{S07\text{-}p\_1} = 4.2 \times 10^{-3}$ cm^2/(Vs), $\mu_{S07\text{-}p\_2} = 4.5 \times 10^{-3}$ cm^2/(Vs), $\mu_{S19\text{-}p\_1} = 6.1 \times 10^{-4}$ cm^2/(Vs), and $\mu_{S19\text{-}p\_1} = 7.5 \times 10^{-4}$ cm^2/(Vs). Notably, these values are slightly

lower than the optimal mobilities previously reported for the respective sample batches ($\mu_{S07\text{-}p}$ = 8.8×10^{-3} $cm^2/(Vs)$ and $\mu_{S19\text{-}p} = 2.5 \times 10^{-3}$ $cm^2/(Vs)$), potentially due to minor variations in fabrication or measurement conditions [10].

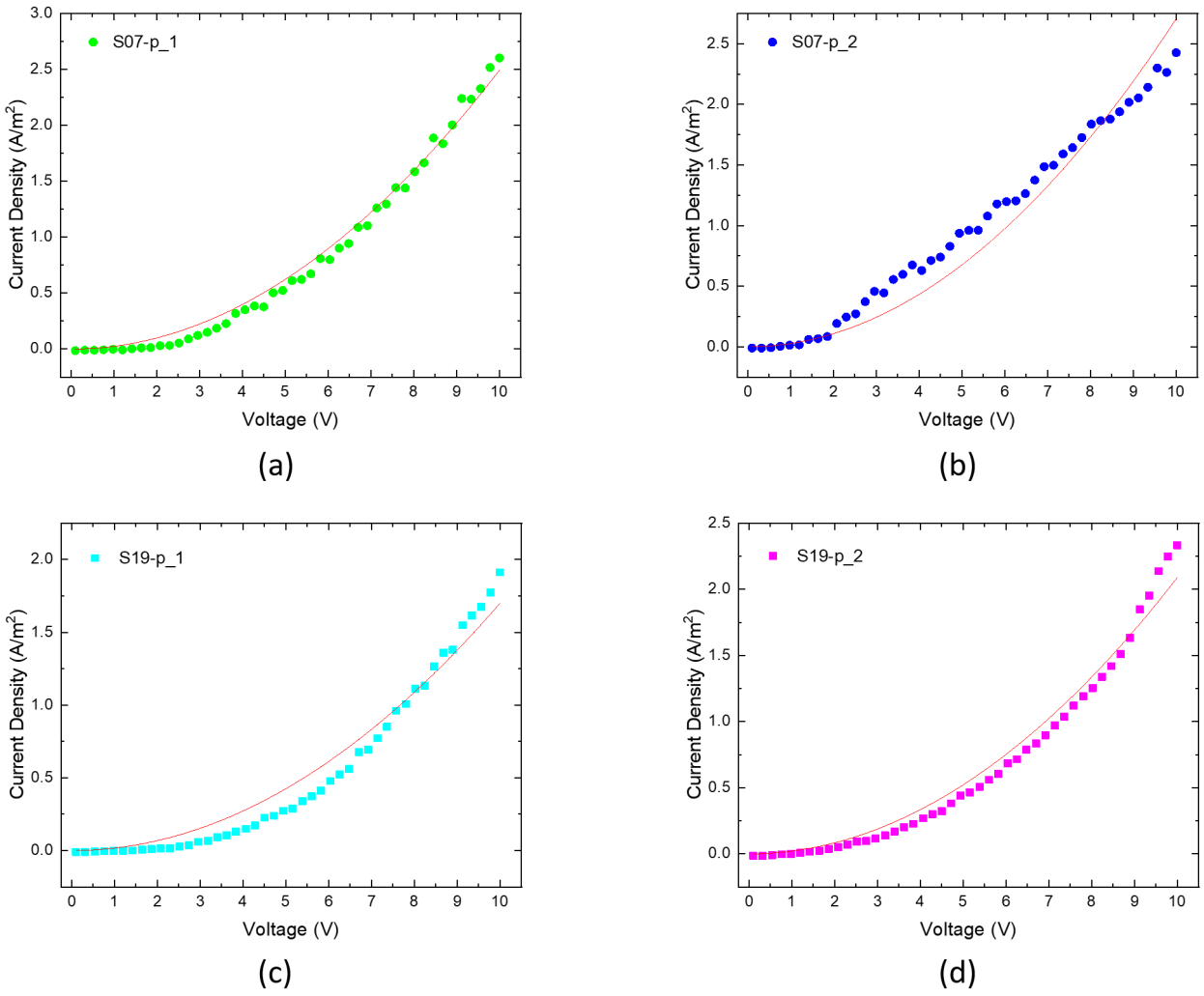

Figure 21: Linear J-V characteristics of β-$ZnTe(en)_{0.5}$ vertical devices: (a) S07-p_1, (b) S07-p_2, (c) S19-p_1, and (d) S19-p_2. Dots represent experimental data, and lines show Mott-Gurney law fits (Eq. 18). S07-p_1 and S19-p_1 are pristine samples from 2007 and 2019, respectively. The subscripts (e.g., _1, _2) denote individual devices within each sample batch.

In contrast to the ideal SCLC behavior observed in Figure 20, where optimized vertical devices (S07-p and S19-p) exhibited double logarithmic J-V characteristics with slopes of 2.081 and 2.655, respectively, the four devices analyzed herein, as shown in Figure 22, present significant deviations. While linear J-V characteristics enabled successful mobility determination using the Mott-Gurney law (Eq. 18), the corresponding double logarithmic plots revealed non-ideal features, characterized by slopes deviating from the theoretical value of 2.

In the previously reported optimal results (Figure 20), two distinct slope regions were identified: an ohmic region (slopes of 0.2081 and 0.961) transitioning to a trap-limited SCLC regime (slopes of 2.081 and 2.655), with a higher slope value indicating a trap-filled SCLC regime (slope = 2.655) [10]. However, Figure 22 reveals significantly different slope values for each device: 4.599 and 2.198 for S07-p_1 (Figure 22 (a)), 3.105 and 1.589 for S07-p_2 (Figure 22 (b)), 3.835 and 1.862 for S19-p_1 (Figure 22 (c)), and 10.817 and 2.390 for S07-p_1 (Figure 22 (d)). Notably, the absence of data in the low voltage regime prevented the identification of an ohmic region. Instead, the data suggests a transition from either trap-limited SCLC or trap-filled (steeper slopes) SCLC to a possible progression towards trap-free SCLC, a phenomenon not observed in the optimal results (Figure 20) [10].

While both optimal devices (S07-p and S19-p) showed a transition voltage (V_{Tr}), neither reached a trap-filled limit (V_{TFL}) in Figure 19. The slope observed for S07-p suggests a trend towards ideal trap-free SCLC, while the slope of S19-p ($J \propto V^n$, n > 2) indicates a clear trap-limited SCLC behavior (Figure 20) [10]. In contrast, Figure 22 shows no noticeable transition voltage (V_{Tr}). Instead, the low voltage regions exhibit elevated slopes ($J \propto V^n$, n > 2), consistent with a trap-filled limit (V_{TFL}), suggesting the influence of trap states on charge transport [58, 119-120].

Eq. 55 demonstrates a direct proportionality between V_{TFL} and trap density (N_t), implying samples with fewer trap states will generally show a lower V_{TFL}, and those with more traps, a higher V_{TFL} [33, 39, 46, 56]. The near-ideal SCLC behavior in S07-p suggests a minimal trap state concentration. However, S19-p, showing only V_{Tr}, and the prediction from Figure 10 and Eq. 55, suggest a higher V_{TFL} is anticipated at higher voltage regions and has a greater trap density relative to S07-p_1, S07-p_2, S19-p_1, and S19-p_2. Furthermore, both N_t and the capture cross-section of traps (σ_n) in Eq. 1, which are intrinsic to the material's defect structure, directly impact both the transition voltage (V_{Tr}) and the trap-filled limit voltage (V_{TFL}) [16, 27, 33, 57].

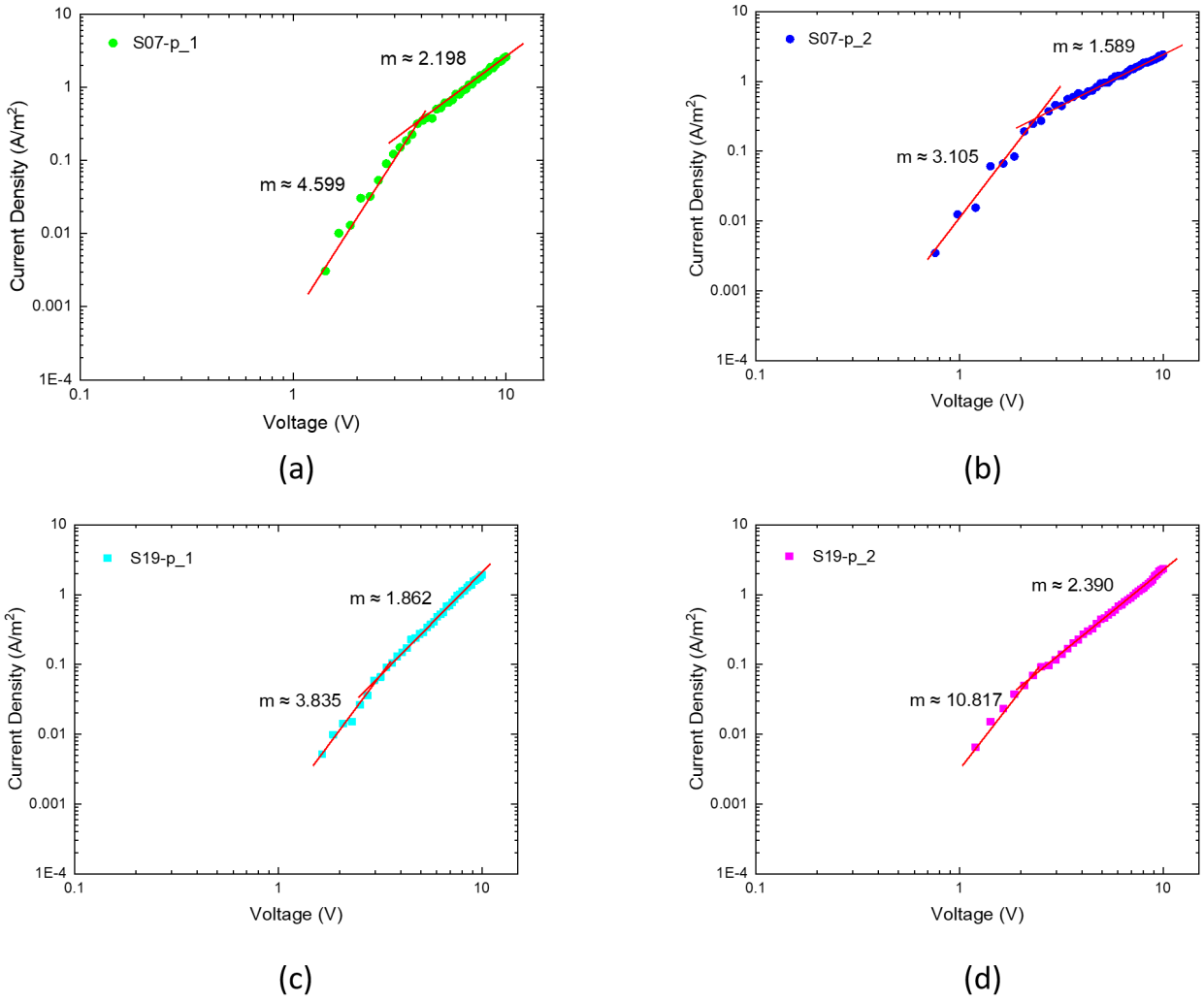

Figure 22: The J-V characteristics of β-ZnTe(en)$_{0.5}$ vertical devices are presented on a double logarithmic scale, showing different slope values: (a) S07-p_1: 4.599 and 2.198; (b) S07-p_2: 3.105 and 1.589; (c) S19-p_1: 3.835 and 1.862; (d) S19-p_2: 10.817 and 2.390.

In contrast to the vertical measurement, the lateral measurement utilized a probe system (Instec, Inc., HCP621GP) with tungsten-rhenium alloy probe tips (25 μm radius) and probe jigs, instead of the electrical probes and manipulators (The Micromanipulator company) used for the vertical measurement.

Figure 23 illustrates the experimental setup used for the lateral electrical measurement of β-$ZnTe(en)_{0.5}$ and provides a schematic representation of the devices along two distinct crystallographic axes. Specifically, Figure 23 (a) shows the measurement setup for the a-axis lateral device, and Figure 23 (b) shows the setup for the c-axis lateral device. Electrical measurements were conducted on two pristine β-$ZnTe(en)_{0.5}$ samples, both synthesized in the same year (S23). The sample thickness (W), determined by SEM, ranged from approximately 6 to 10 μm (Figure 18). The crystallographic c-axis was empirically observed to align with the longer edge, and the a-axis with the shorter edge, a determination subsequently confirmed by polarized Raman spectroscopy (Figure 13) [178].

For accurate SCLC analysis, optimal electrode configuration requires the transverse dimension of the electrodes to be substantially larger than the interelectrode spacing [25, 47]. A shadow mask with a 20 μm interelectrode spacing and centimeter-range transverse dimensions fulfilled this requirement. Figure 23 (c) schematically illustrates the lateral device configuration along the a-axis, where a consistent sample thickness (W) of 6 μm was used, and the device length (L) varied, reaching several hundred micrometers, as confirmed by optical microscopy. Figure 23 (d) schematically depicts the c-axis device configuration, also utilizing a 6 μm sample thickness (W), with a variable length (L) typically up to 100 μm, as determined by optical microscopy. Following current-voltage (I-V) measurements, the cross-sectional area ($A = L \times W$) was used to normalize current to current density for SCLC analysis. Importantly, the effective device area for in-plane charge carrier transport analysis (a-axis or c-axis) is the cross-sectional area, not the in-plane electrode dimensions. As previously illustrated in Figure 7, injected charge carriers traverse both vertically and laterally, exhibiting distinct mobilities due to material anisotropy transport property [117]. Therefore, the lateral devices described are specifically designed to

study the transport properties along the lateral dimensions (a-axis or c-axis). Due to the inherently complex nature of charge transport and potential material anisotropy, isolating pure lateral mobility in a standard lateral device configuration is challenging, as measurements inevitably include contributions from both lateral and vertical carrier movement.

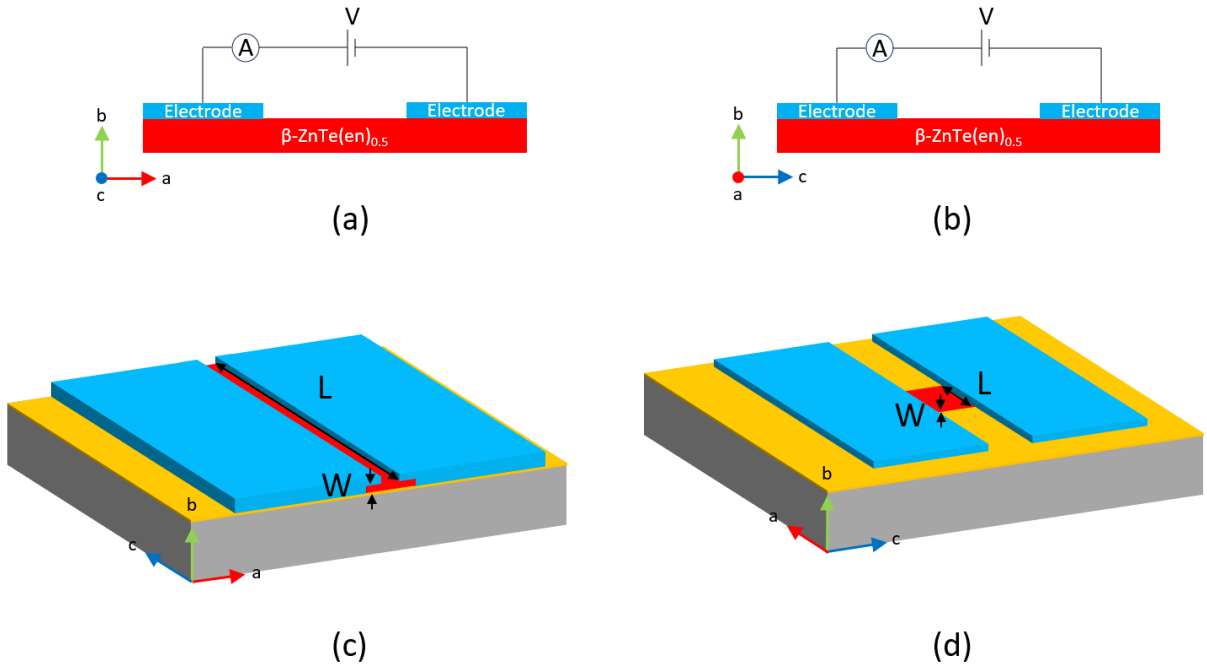

Figure 23: Experimental Setup for lateral electrical measurements of β-ZnTe(en)$_{0.5}$ and device schematic along two different crystal axes. (a), (c) a-axis device. (b), (d) c-axis device.

For SCLC analysis, current density was calculated by dividing the measured current by the cross-sectional area (A = L × W), determined from I-V measurements. Figure 24 shows the J-V characteristic of β-ZnTe(en)$_{0.5}$ lateral devices in a linear scale. As shown in Figure 24, fitting the data to the Mott-Gurney law (Eq. 18, using ε = 6, $L_{S23\text{-}p\_a\text{-}axis}$ = $L_{S23\text{-}p\_c\text{-}axis}$ = 20 μm) yielded

mobilities of $\mu_{S23\text{-}p\_a\text{-}axis} = 1.787 \times 10^2$ cm^2/(Vs) for the a-axis and $\mu_{S23\text{-}p\_c\text{-}axis} = 1.696 \times 10^1$ cm^2/(Vs) for the c-axis, representing the best achieved results from the same batches of the samples synthesized in 2023 (S23-p). The mobility value along the a-axis, as determined by the Mott-Gurney law (Eq. 18), is an order of magnitude greater than that along the c-axis.

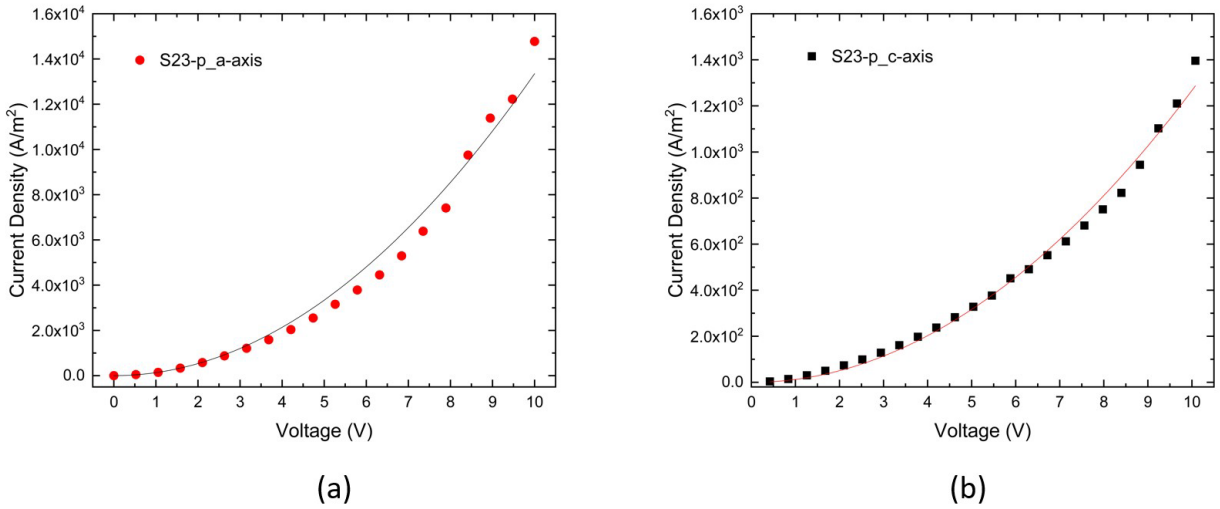

Figure 24: The J-V characteristics of β-ZnTe(en)$_{0.5}$ lateral devices are presented on a linear scale for (a) S23-p_a-axis and (b) S23-p_c-axis, respectively. The dots represent experimental data, while the lines show the fitted curves using the Mott-Gurney law (Eq. 18).

Figure 25 illustrates the J-V characteristic of β-ZnTe(en)$_{0.5}$ lateral devices, plotted on a double logarithmic scale to effectively display the wide range of current and voltage values. Ideally, the ohmic regime is characterized by a slope of 1 ($J \propto V$) at lower voltages, transitioning to a slope of slope of 2 ($J \propto V^2$) in the SCLC regime at intermediate voltages on a double logarithmic plot. However, only the SCLC regime was observed in both the S23-p_a-axis and S23-p_c-axis samples, without a clear ohmic regime. Although not shown in Figure 25, the transition voltage

(V_{Tr}) occurred at a lower voltage in the lateral devices than in the vertical devices, as illustrated in Figure 20.

The absence of a clear ohmic region, despite the observed SCLC behavior, is likely due to the limited number of data points acquired at lower voltages. Furthermore, the observations indicate that a high-resolution voltage scan (achieved through a faster scan rate or finer voltage steps) can reveal lower current values compared to a lower-resolution scan (slower scan rate or coarser voltage steps). While further investigation is required, potential explanations for the observed behaviors include contact instability, heat effects, or trap dynamics.

Figure 25 (c) presents the data for both S23-p_a-axis and S23-p_c-axis samples on a double logarithmic scale, which is useful for visualizing and comparing data spanning several orders of magnitude. The current density of S23-p along the a-axis is approximately an order of magnitude higher than that along the c-axis at the same voltage.

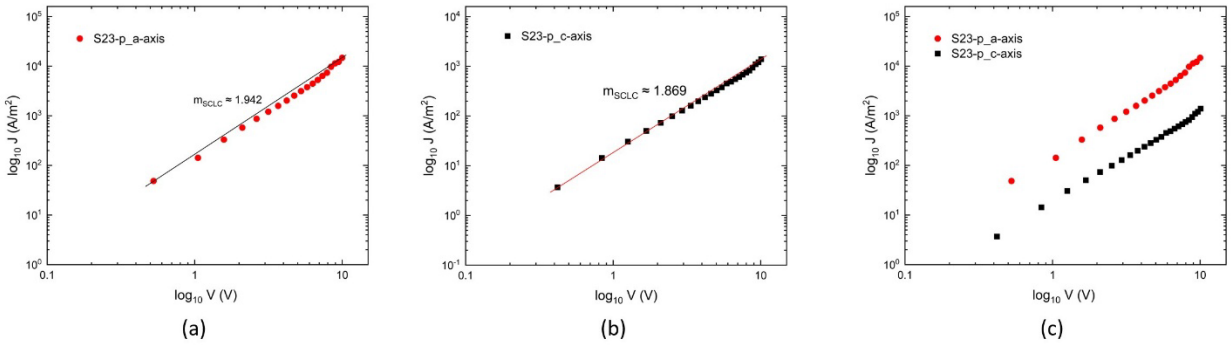

Figure 25: The J-V characteristics of β-ZnTe(en)$_{0.5}$ lateral devices are presented on a double logarithmic scale for (a) S23-p_a-axis and (b) S23-p_c-axis, respectively. (c) directly compares the two datasets, revealing one order of magnitude difference in current density. The dots represent experimental data, while the lines indicate the slope.

Among the examined lateral device configurations, S23-p_a-axis and S23-p_c-axis demonstrated superior performance characteristics, as illustrated in Figure 24. To further analyze the electrical transport in these configurations, Figure 26 presents the J-V characteristics of the β-ZnTe(en)$_{0.5}$ lateral device on both linear and double logarithmic scales.

The linear plots in Figure 26 (a) and Figure 26 (b), based on the Mott-Gurney law (Eq. 18), result in charge carrier mobilities of $\mu_{S23\text{-}p\_a\text{-}axis\_1} = 1.261 \times 10^1$ cm^2/(Vs) and $\mu_{S23\text{-}p\_c\text{-}axis\_1} = 5.247 \times 10^0$ cm^2/(Vs). Ideally, the ohmic regime in a double logarithmic plot shows a slope of 1 ($J \propto V$). However, as shown in Figure 26 (c), the S23-p_a-axis_1 sample exhibits a significantly lower slope (m = 0.332) in the ohmic regime, a behavior similar to the vertical device from the S07-p sample (m = 0.256) in Figure 20 (a). Furthermore, the slope in the SCLC regime for S23-p_a-axis_1 (m = 3.297) also deviates considerably from the ideal value of 2 ($J \propto V^2$), with a larger deviation compared to the vertical device from the S19-p sample (m = 2.655) in Figure 20 (b). While an SCLC slope around 2 is generally expected, higher slopes (e.g., 2.4, 2.5, 2.8, and 3.1) have been reported in literature, likely due to the presence of traps, necessitating the use of a power-law dependence ($J \propto V^n$, n >2) instead of the ideal square law ($J \propto V^2$), even when the Mott-Gurney equation is used for analysis [14, 17, 121, 155, 161]. In contrast, the double logarithmic plot for S23-p_c-axis_1 in Figure 26 (d) reveals a slope closely approximating the ideal value of 1 ($J \propto V$) in the ohmic regime and a slope near the ideal value of 2 ($J \propto V^2$) in the SCLC regime. Notably, the previously reported optimal devices (Figure 25) exhibited only an SCLC region with slopes close to 2 (1.942 and 1.869), showing a slight deviation from the ideal. Additionally, unlike the optimal devices, both S23-p_a-axis_1 and S23-p_c-axis_1 displayed a transition voltage (V_{Tr}).

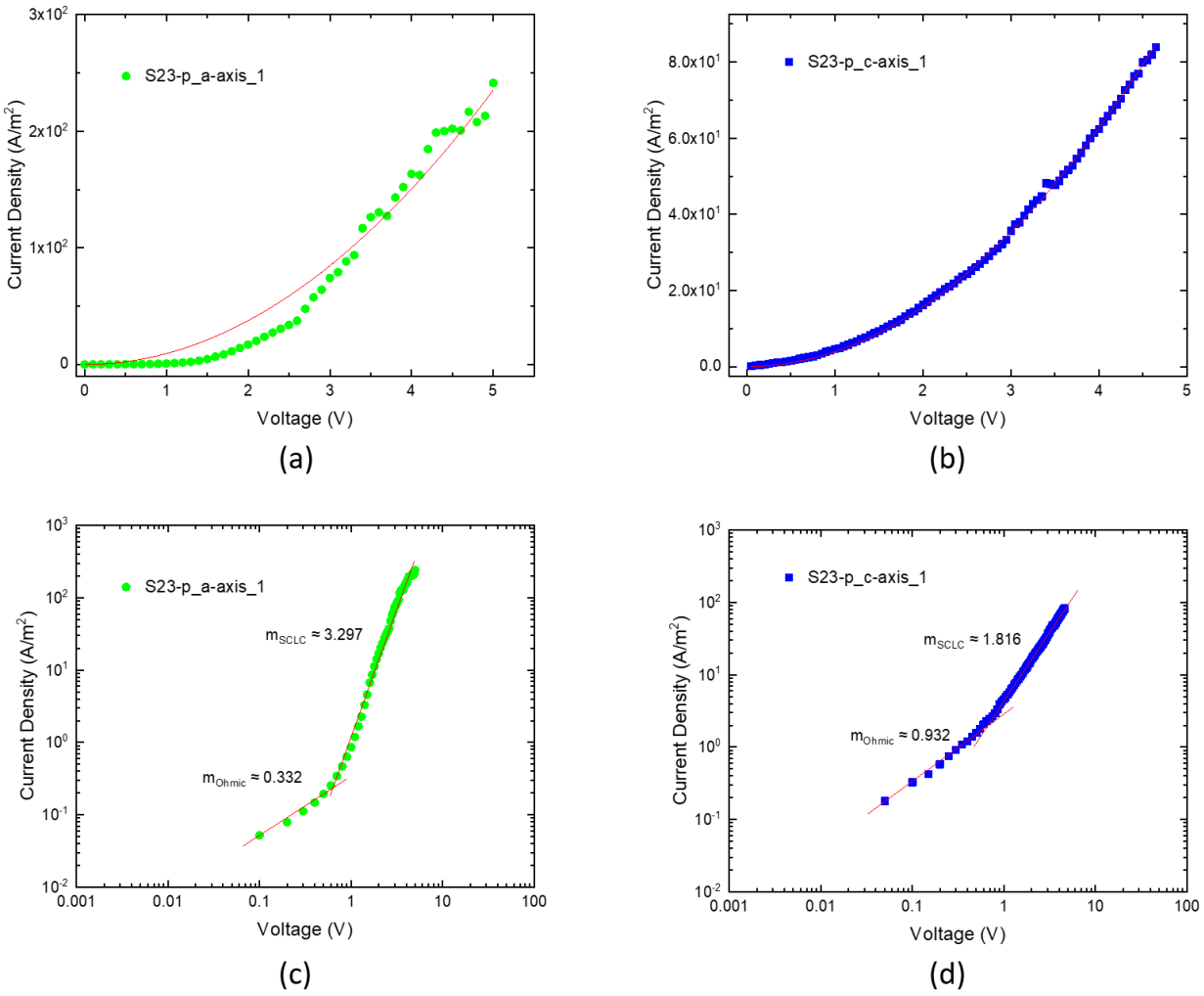

Figure 26: The J-V characteristics of the β-ZnTe(en)$_{0.5}$ lateral devices are presented on both linear and double logarithmic scales. (a) S23-p_a-axis_1 and (b) S23-p_c-axis_1 are shown on a linear scale. (c) S23-p_a-axis_1 and (d) S23-p_c-axis_1 are displayed on a double logarithmic scale.

In contrast to the four lateral devices (S23-p_a-axis, S23-p_c-axis, S23-p_a-axis_1, and S23-p_c-axis_1), where polarization Raman spectroscopy was implemented before device fabrication, an empirical approach was used to differentiate the crystallographic axes for S23-p_a-axis_2 and S23-p_c-axis_2 [178]. Figure 27 illustrates the J-V characteristics of the β-ZnTe(en)$_{0.5}$ lateral

device, displayed on both linear and double logarithmic scales. Analysis of the linear plots in Figure 27 (a) and Figure 27 (b), using the Mott-Gurney law (Eq. 18), yielded charge carrier mobilities of $\mu_{S23\text{-}p\_a\text{-}axis\_2} = 6.864 \times 10^1$ cm^2/(Vs) and $\mu_{S23\text{-}p\_c\text{-}axis\_2} = 5.992 \times 10^1$ cm^2/(Vs). Consistent with the best achieved devices in Figure 25, the double logarithmic plot for the S23-p_a-axis_2 sample in Figure 27 (c) reveals a power-law relationship ($J \propto V^n$, $n > 2$) instead of the expected square law ($J \propto V^2$), indicating the presence of traps. In contrast, the double logarithmic plot for S23-p_c-axis_2 in Figure 27 (d) shows distinct ohmic (m = 1.305) and SCLC (m = 2.644) regimes with some deviations, the SCLC slope being comparable to that of the vertical device from the S19-p sample (m = 2.655) in Figure 20 (b). The similar mobility values obtained for both devices (S23-p_a-axis_2 and S23-p_c-axis_2), which were fabricated by examining crystallographic axes without polarization Raman spectroscopy, suggest the need for incorporating polarization Raman spectroscopy alongside empirical observation [178].

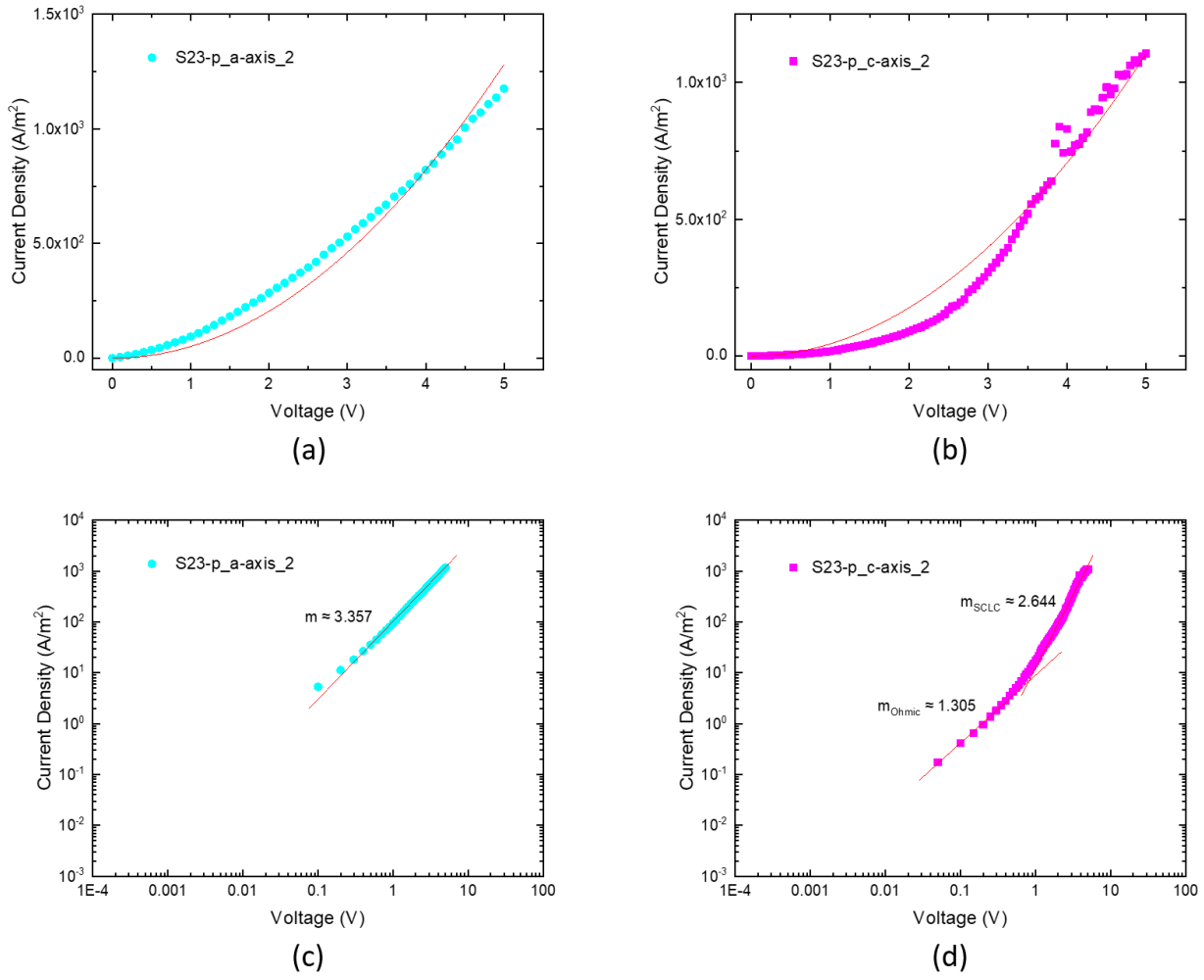

Figure 27: The J-V characteristics of the β-ZnTe(en)$_{0.5}$ lateral devices are presented on both linear and double logarithmic scales. (a) S23-p_a-axis_2 and (b) S23-p_c-axis_2 are presented on a linear scale. (c) S23-p_a-axis_2 and (d) S23-p_c-axis_2 are illustrated on a double logarithmic scale.

To contextualize these β-ZnTe(en)$_{0.5}$ mobility values, it is useful to compare them with reported mobilities for other 2D and 3D materials. Graphene exhibits a wide range of carrier mobilities. Electron mobility of monolayer graphene is also observed to be 10^4 cm²/(Vs) [103]. The mobility

of n-type graphene is 10^6 $cm^2/(Vs)$, and that of p-type graphene is 10^4 $cm^2/(Vs)$ [89]. For few-layer graphene (FLG), the mobility ranges from 3×10^3 to 10^4 $cm^2/(Vs)$ [101]. Multilayer graphene achieves mobilities up to 15×10^3 $cm^2/(Vs)$ at 300 K and approximately 6×10^4 $cm^2/(Vs)$ at 4 K [101, 109]. Graphene nanoribbons exhibit mobilities of 100-200 $cm^2/(Vs)$ [102], while engineered graphene with a 150 meV band gap achieves 200 $cm^2/(Vs)$ [102]. Field-effect hole mobility is 1010 $cm^2/(Vs)$, and electron mobility is 3550 $cm^2/(Vs)$ [109]. Molybdenum disulfide (MoS_2) also shows varying mobilities. Experimental mobility without a high-K dielectric gate material is 1 $cm^2/(Vs)$ [102]. With a hafnium oxide (HfO_2) top gate layer at 300 K, it reaches 150 $cm^2/(Vs)$ [102]. Theoretical electron mobility of MoS_2 is reported as 410 $cm^2/(Vs)$ [103]. Trilayer MoS_2 exhibits mobilities of 1.3 and 3.3 $cm^2/(Vs)$ [108], and field-effect carrier mobility is 0.06 $cm^2/(Vs)$ [109]. Black phosphorus (phosphorene) exhibits mobilities of 10^3 $cm^2/(Vs)$ for monolayers [102-103]. Tungsten diselenide (WSe_2) shows a field-effect carrier mobility of 0.03 $cm^2/(Vs)$ [109].

In contrast to these 2D materials, 3D semiconductors exhibit different mobility ranges. At room temperature, mobility values are: 540 $cm^2/(Vs)$ for electrons and 28 $cm^2/(Vs)$ for holes in ZnSe; 340 $cm^2/(Vs)$ for electrons and 100 $cm^2/(Vs)$ for holes in ZnTe; 1200 $cm^2/(Vs)$ for electrons and 50 $cm^2/(Vs)$ for holes in CdTe; 8800 $cm^2/(Vs)$ for electrons and 400 $cm^2/(Vs)$ for holes in GaAs [89]; and 1245 $cm^2/(Vs)$ [198], 1200 $cm^2/(Vs)$ [199], and 1350 $cm^2/(Vs)$ [200] for electron mobility in GaN.

The best achieved mobility for β-$ZnTe(en)_{0.5}$ along the a-axis ($\mu_{S23\text{-}p\_a\text{-}axis} = 1.787 \times 10^2$ $cm^2/(Vs)$) is notably comparable to the reported mobilities of certain 2D materials like graphene nanoribbons (100-200 $cm^2/(Vs)$) [102] and engineered graphene with a band gap (200 $cm^2/(Vs)$) [102], as well as the hole mobility in the 3D semiconductor ZnTe (100 $cm^2/(Vs)$) [89]. The

mobility achieved along the c-axis in β-ZnTe(en)$_{0.5}$ ($\mu_{S23\text{-}p\_c\text{-}axis}$ = 1.696 × 10^1 cm^2/(Vs)) is comparable to the hole mobility in the 3D semiconductor ZnSe (28 cm^2/(Vs)) and CdTe (50 cm^2/(Vs)) [89]. This value is on the lower end of the spectrum when compared to the 2D materials listed, being approximately one order of magnitude higher than certain experimental MoS_2 without a high-K dielectric gate material (1 cm^2/(Vs)) [102] and trilayer MoS_2 (1.3 and 3.3 cm^2/(Vs)) [108].

In summary, electrical transport measurements were conducted on β-ZnTe(en)$_{0.5}$ devices in both vertical and lateral configurations. Vertical measurements on pristine samples (S07-p and S19-p) yielded mobilities of 8.8 × 10^{-3} cm^2/(Vs) and 2.5 × 10^{-3} cm^2/(Vs), respectively, consistent with weaker transport along the inorganic-organic stacking direction. J-V characteristics in double logarithmic plots revealed deviations from ideal ohmic behavior, potentially due to trap states, device geometry, or field-dependent dielectric constants. However, the SCLC regime exhibited slopes close to the ideal value of 2 ($J \propto V^2$) for S07-p but showed significant deviation for S19-p ($J \propto V^n$, $n > 2$), possibly indicating trap filling and a deviation from the ideal slope of 2. Further investigation of specific vertical devices (S07-p_1, S07-p_2, S19-p_1, and S19-p_2) using linear J-V characteristics and the Mott-Gurney law yielded slightly lower mobility values compared to the optimal devices (S07-p and S19-p). Double logarithmic J-V plots for these devices showed significant deviations from ideal SCLC behavior, with elevated slopes suggesting a transition from trap-limited or trap-filled SCLC, and an absence of a clear ohmic region. The data indicate a stronger influence of trap states on charge transport in these specific devices, with no observable transition voltage (V_{Tr}) observed. Instead, the double logarithmic J-V characteristics suggest a transition from trap-limited or trap-filled SCLC to a possible progression towards trap-free SCLC, with evidence of reaching a trap-filled limit (V_{TFL}). It suggests a higher trap density

compared to the S07-p device, which shows near-ideal SCLC. However, these devices exhibit a lower trap density compared to the optimal S19-p sample, where only the transition voltage is observed, and not the trap-filled limit voltage. Thus, the analysis of specific vertical devices suggests a higher density of trap states compared to the optimal S07-p sample, and a different trap distribution compared to the optimal S19-p sample.

Lateral measurements on pristine samples (S23-p_a-axis and S23-p_c-axis) showed much higher mobilities, with 1.787×10^2 $cm^2/(Vs)$ along the a-axis and 1.696×10^1 $cm^2/(Vs)$ along the c-axis, demonstrating a multiple orders of magnitude difference. Only the SCLC regime was observed in lateral devices, with the transition voltage (V_{Tr}) occurring at lower values compared to vertical devices. The absence of a clear ohmic regime may be attributed to limited data points at low voltages and potential contact instability, heat effects, or trap dynamics, possibly related to lower trap states. The current density along the a-axis was approximately an order of magnitude higher than along the c-axis at the same voltage. To gain further insight into the lateral transport mechanisms, linear fits applied to the J-V characteristics of devices S23-p_a-axis_1 and S23-p_c-axis_1 yielded mobilities of 1.261×10^1 $cm^2/(Vs)$ and 5.247×10^0 $cm^2/(Vs)$, respectively. Both devices showed deviations from ideal ohmic and SCLC slopes, with S23-p_a-axis_1 exhibiting a particularly low ohmic slope and a high SCLC slope. In contrast, S23-p_c-axis_1 showed near-ideal slopes. Both displayed a transition voltage, unlike the previously reported optimal lateral devices (S23-p_a-axis and S23-p_c-axis), which exhibited only an SCLC region with near-ideal slopes and no observable transition voltage, potentially indicating lower trap density that require filling before the onset of SCLC in the optimal lateral devices. Moving on to devices S23-p_a-axis_2, with a mobility of 6.864×10^1 $cm^2/(Vs)$), and S23-p_c-axis_2, showing a mobility of 5.992×10^1 $cm^2/(Vs)$), these demonstrated similar mobility values despite being

fabricated without implementing polarization Raman spectroscopy. This suggests the importance of utilizing polarization Raman spectroscopy in conjunction with the empirical observation for accurate crystallographic axis identification. S23-p_a-axis_2 exhibited a power-law dependence ($J \propto V^n$, $n > 2$) indicative of traps, while S23-p_c-axis_2 showed distinct ohmic ($J \propto V$) and SCLC ($J \propto V^2$) regimes with some deviations.

Given the observed structural anisotropy along the three crystallographic axes (Figure 2), anisotropic electrical behavior is anticipated. SCLC measurements offer valuable insights for characterizing the anisotropic electrical behavior of semiconductors possessing anisotropic crystal structures. This technique allows for the determination of charge carrier mobility along distinct crystallographic axes, enabling a quantitative assessment of the anisotropy in charge transport such as mobility using the Mott-Gurney law. In fact, the successful application of SCLC measurements to a range of semiconductors has revealed substantial variations in mobility as a function of crystallographic orientation [165, 166].

CHAPTER 6: PHOTOELECTRON SPECTROSCOPY

Photoelectron spectroscopy (PES), also termed photoemission spectroscopy, has evolved from the foundational discovery of the photoelectric effect. In 1887, Heinrich Rudolf Hertz documented the emission of electrons from a material's surface upon illumination, though a comprehensive explanation remained unclear to him [111]. Albert Einstein explained this phenomenon in 1905, introducing the existence of photons and the quantization of their energy; this contribution, for which he received the 1921 Nobel Prize in Physics, provided the theoretical framework for the photoelectric effect [112]. Subsequent investigations employing X-rays to induce electron emission paved the way for X-ray photoelectron spectroscopy (XPS), and the development of high-resolution spectrometers enabled the acquisition of the first high-energy-resolution XPS spectrum, demonstrating its potential for chemical analysis; this advancement, recognized by the 1981 Nobel Prize in Physics awarded for Electron Spectroscopy for Chemical Analysis (ESCA), established PES as a powerful tool in chemical characterization [95, 113]. Photoemission (PE) experiments, while conceptually similar to their early counterparts of nearly a century ago, have undergone significant advancements in instrumentation and techniques [111]. Figure 28 illustrates the fundamental principle of the PE process, the main components of which are the photon source, analyzer, and detector [112].

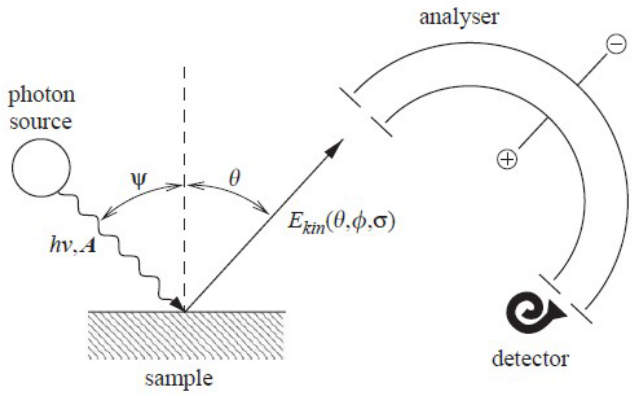

Figure 28: Sketch of simplified PES [112].

An electrostatic analyzer measures emitted photoelectrons, revealing information about their initial electronic states (kinetic energy, E_{kin}, and momentum, $p=\sqrt{2mE_{kin}}$), while the polarization of incident light with a well-defined vector potential (A) adds further valuable data, especially in angle-resolved photoelectron spectroscopy (ARPES) experiments [111]. Although the simplified sketch (Figure 28) provides a basic understanding, photoelectron excitation is a complex process than it illustrates [112].

When the photon energy exceeds the sample's work function ($\emptyset$), electrons are emitted from the surface via the photoelectric effect, which is governed by Einstein's equation below,

$$E_{kin}^{max} = h\nu - \emptyset \qquad \text{Eq. 76}$$

where E_{kin}^{max} is the maximum kinetic energy of the emitted photoelectrons, $h\nu$ is the photon energy, and $\emptyset$ is the work function of the sample (a characteristic constant of the sample surface) [111, 112]. Eq. 76 still forms the basis for the interpretation of modern PES experiments [112]. The inherent surface-sensitivity of PES arises from the strong scattering and inelastic losses experienced by emitted electrons, primarily through electron-electron and electron-phonon

collisions, which limit the escape depth of elastically scattered electrons to the near-surface region; this depth is governed by the electron mean free path, which varies strongly with the electron's kinetic energy, thus confining the probing depth of PES to the surface region and making it a highly surface-sensitive technique [111, 113]. Furthermore, the inherent surface-sensitivity necessitates ultra-high vacuum (UHV) conditions during PES measurements, as even minor surface contamination or the surface layer can significantly influence the detected signal and compromise data interpretation [111, 112]. While PES provides valuable insights into surface properties like electronic surface states, adsorbate structures, or ultra-thin films, its limited information depth can hinder the study of bulk properties in solids [112].

As illustrated in Figure 29, the three-step model simplifies the PE process by dividing it into three distinct, sequential steps: first, photoionization is initiated when an electron absorbs a photon of sufficient energy to surpass the ionization energy, leading to its transition to a higher, unbound energy level; second, this excited electron, possessing sufficient kinetic energy, is transported to the surface, enabling its escape from the material; and third, upon traversing the surface and entering the vacuum, the electron is detected [111]. While the schematic primarily illustrates valence band excitation, it encompasses all energy levels, including core levels, for general explanatory purposes.

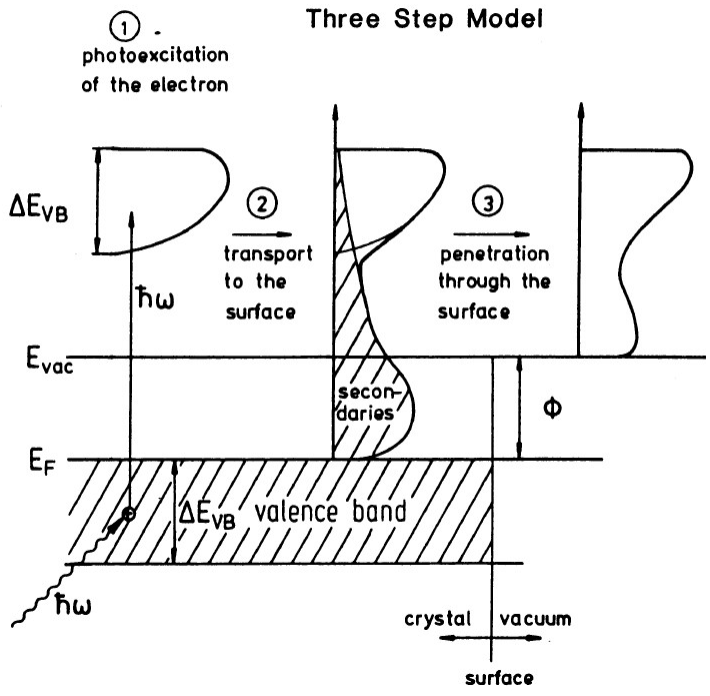

Figure 29: The three-step model for interpreting PE experiments: ① photoionization occurs through the absorption of a photon, which excites an electron; ② this excited electron is transported to the surface; ③ the electron travels through the surface into the vacuum where it is detected; [111].

The three-step model, while a somewhat artificial separation of the unified photoexcitation, transport, and escape process, has proven invaluable for interpreting PE experiments due to its significant conceptual simplification [95, 111].

Analysis of the emitted photoelectron distribution in energy and momentum space provides insights into several key material properties, including chemical composition and bonding, electronic band structure, and the characteristics of surface states and molecular orbitals [111, 112]. So, PES has broad applicability across diverse scientific disciplines, including surface

chemistry and materials science, and has been instrumental in understanding the fundamental principles of solid-state physics [112]. This analysis relies on a light source, a critical component that defines the energy and flux of photons incident on the sample; electron ejection and subsequent detection by the instrument occur when the photon energy of the light source exceeds the binding energy of an electron within the sample. [111]. PES uses light sources like gas discharge lamps, X-ray sources, and synchrotron radiation, with X-ray Photoelectron Spectroscopy (XPS) probing core-level states at higher binding energies and Ultraviolet Photoelectron Spectroscopy (UPS) primarily investigating valence band states [112]. While several monochromatic light sources are commercially available because narrower linewidths provide higher resolution, Al Kα ($h\nu$ = 1486.6 eV) and Ag Kα ($h\nu$ = 2984.4 eV) radiation sources are predominantly used for XPS, whereas He I ($h\nu$ = 21.2 eV) and He II ($h\nu$ = 40.8 eV) sources are more commonly employed for UPS [95].

PES techniques, including surface-sensitive and complementary UPS and XPS, differ primarily in their radiation source, utilizing low-energy ultraviolet photons and higher-energy X-rays, respectively, to induce electron emission and provide insights into a material's electronic structure. XPS yields core-level binding energies, enabling elemental identification and chemical state analysis, while UPS probes the valence band, revealing information about the work function (∅), ionization energy, and valence band density of states [94, 95, 140]. This distinction arises from the fact that XPS photoelectrons originate from core-level electron excitations, whereas UPS photoelectrons originate from valence-level electron excitations, as illustrated in Figure 30 [111].

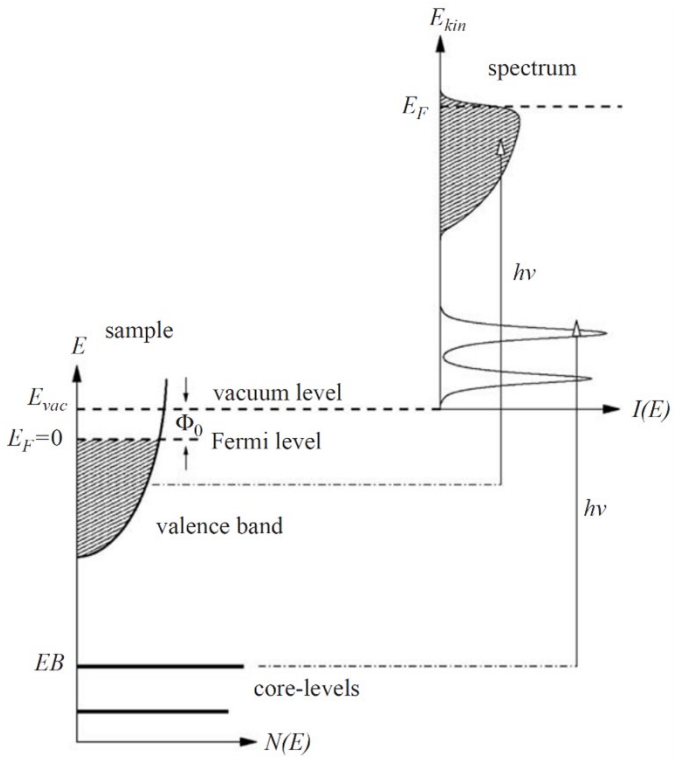

Figure 30: A simplified schematic energy diagram illustrating XPS and UPS photoelectron emission for a metal, where XPS probes core-level electron excitations and UPS probes valence-level electron excitations [111].

Modern XPS instrumentation can often integrate ultraviolet sources, such as the commonly employed He I source ($h\nu$ =21.2 eV) and/or He II source ($h\nu$ = 40.8 eV), allowing for the acquisition of UPS data within the same experimental setup. This combined approach facilitates a comprehensive understanding of both core and valence electronic states, proving especially valuable for studying surface modifications, thin films, and interfacial phenomena [111]. Specifically, UPS exhibits enhanced surface sensitivity compared to XPS due to the lower excitation energy of ultraviolet photons, approximately probing the top 1–3 nm of the material (sampling depth of 3λ) [95, 129]. This increased sensitivity, however, makes UPS measurements

more susceptible to surface contamination. Furthermore, while UPS provides superior energy resolution and is generally less destructive to organic layers than XPS, it is unsuitable for insulating surfaces due to charging effects [129].

While the simplified picture provides a basic understanding, photoelectron excitation is a complex process best described by Fermi's Golden Rule, derived from first-order perturbation theory, as detailed in the referenced citation [112]. In addition, a brief overview of PES's evolution beyond conventional surface analysis, encompassing advanced applications such as operando studies, interface analysis, and time-resolved measurements, along with its future directions, is presented in the cited reference [113].

Most PES, including XPS and UPS, can incorporate Monatomic Ion Beam Sputtering (IBS) and/or Gas Cluster Ion Beam (GCIB) techniques for surface cleaning or depth profiling. A simulation study compared Ga IBS and C_{60} GCIS surface interactions, revealing that the deeper penetration and cylindrical damage profile of Ga IBS ejects sample atoms, suggesting a more aggressive technique prone to defect formation and electronic structure alteration, potentially affecting surface states, while the shallower, crater-like material removal of C_{60} GCIB offers a gentler approach that may be advantageous for surface cleaning by minimizing electronic property changes and deep-level defect introduction [145]. Furthermore, the tunable energy per atom of GCIB is a critical parameter for optimizing and minimizing surface damage; both simulation and experimental results suggest that larger cluster sizes reduce the energy per atom, which contributes to less aggressive conditions, establishing GCIB as a versatile tool for cleaning and depth profiling complex materials [145, 170]. While GCIB encompasses various ion beam technologies, (Gas Cluster Ion Sputtering) GCIS is specifically designed for XPS/UPS, employing lower energies for a gentle sputtering approach to preserve chemical integrity during

analysis, whereas GCIB can utilize higher energies for more aggressive surface processing and diverse modifications [95].

6.1. X-ray Photoelectron Spectroscopy (XPS)

6.1.1. Fundamentals of XPS

XPS is a widely used surface-sensitive technique providing a comprehensive picture of a material's surface composition and chemistry by analyzing the binding energies and intensities of emitted photoelectrons, revealing elemental composition, chemical states, electronic structure, and bonding information at surfaces, films, and interfaces [95, 111].

While Figure 28 and Figure 29 offer a concise overview of PES principles and PE process interpretation, Figure 31 provides a more detailed illustration of the energetic processes occurring after X-ray incidence on the sample [95]. X-ray interaction with an atom can result in the transfer of energy to an inner-shell electron, leading to its ejection as a photoelectron with kinetic energy directly related to the incident X-ray's energy ($h\nu$), initiating a cascade of events including X-ray fluorescence (XRF) or Auger electron emission due to the creation of an inner-shell vacancy [132]. Although the most intense photoelectron lines are generally symmetrical and narrow, pure metals may exhibit asymmetry due to conduction electron coupling; less intense lines at higher binding energies typically broaden by 1-4 eV compared to those at lower binding energies, and insulating solids exhibit a general broadening of approximately 0.5 eV relative to conductors [132]. XRF is a process initiated by the ejection of an inner-shell electron following sufficient incident X-ray energy, causing ionization, and competes with Auger effects [132]. Following photoelectron emission and the creation of an excited atomic state, relaxation can occur via an electron transition from a higher energy level to fill the inner-shell vacancy; this

transition releases energy that may subsequently lead to the emission of an Auger electron, a process occurring within an extremely short timeframe of a few femtoseconds (10^{-15} seconds) following the initial photoelectric effect [111, 132]. While the photoelectron lines are the primary focus in XPS, other spectral features are also crucial for accurate data interpretation, as detailed in the literature [132].

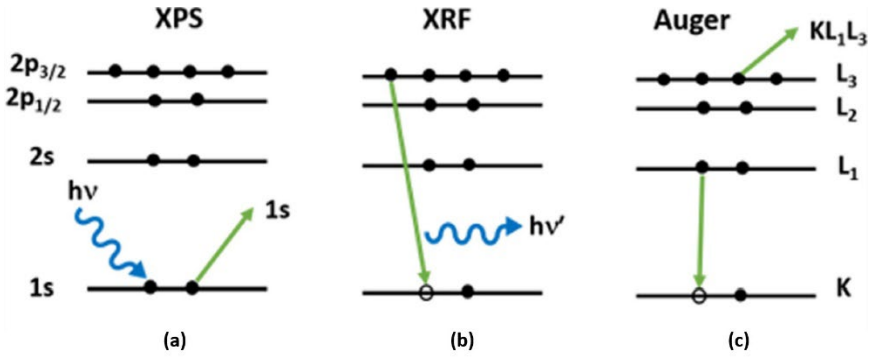

Figure 31: Schematic energy diagram of electron transitions of (a) photoelectron emission for XPS, (b) X-ray Fluorescence (XRF), and (c) Auger electron emission [95].

The fundamental principles of PES are also applicable to XPS, which operates on the same principles of photoelectron generation and detection, whereby core-level photoelectrons are ejected upon incidence of an X-ray photon on the sample surface, accelerated by an electric field toward a detector, and subsequently measured by an electron energy analyzer, as shown in Figure 32 [95, 111, 112]. The energy analyzer resolves photoelectrons based on their kinetic energy, and the intensity of the resulting XPS spectra is proportional to the number of detected photoelectrons at each specific energy. Modern XPS instruments predominantly utilize monochromatic X-ray sources to enhance spectral clarity by eliminating satellite peaks, thereby simplifying interpretation and improving energy resolution, yielding sharper, more well-defined

peaks with reduced linewidth and smaller FWHM [95, 132]. Observed XPS peak widths are a convolution of the natural linewidth (related to the core-hole lifetime as a consequence of the photoionization process), the X-ray source linewidth, and the instrument's contribution to the measured linewidth [132].

Some advanced spectrometers incorporate switchable-mode electron guns, enabling a single system to perform both charge neutralizer in XPS and focused beam applications such as LEED/Auger spectroscopy. The charge neutralizer in XPS minimizes analytical errors in insulating or poorly conductive samples by counteracting surface charge buildup that occurs during measurement; without this compensation, positive charge accumulation can occur due to photoelectron emission. Integrated cameras and ion sputtering sources (e.g., GCIS) are commonly employed for sample imaging and cleaning.

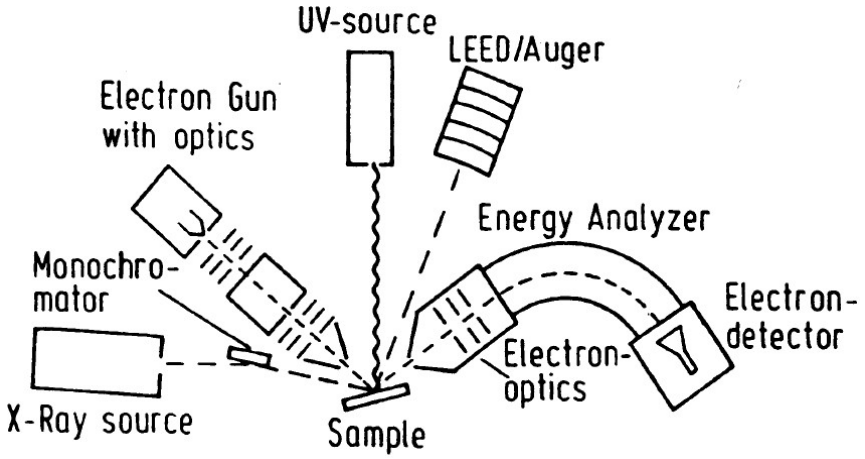

Figure 32: Schematic Diagram of PES equipped with Electron Gun, LEED (Low-Energy Electron Diffraction)/Auger, Analyzer, Detector, and X-ray and UV sources [111]. If a monochromatic X-ray source is available, a monochromator is not required.

Although XPS measures the kinetic energy of emitted photoelectrons, most available data represent XPS spectra with respect to the binding energy (E_B) using the following equation below,

$$E_B = h\nu - E_{kin} - \emptyset_{spec} \quad \text{Eq. 77}$$

where E_B is the binding energy, $h\nu$ is the X-ray photon energy, E_{kin} is the kinetic energy, and $\emptyset_{spec}$ is the work function of the spectrometer [111, 132]. The inclusion of $\emptyset_{spec}$ in Eq. 77 arises from the fact that photoelectron binding energy is measured relative to the sample Fermi level, not the vacuum level, as shown in Figure 33 [95]. For easier interpretation, a binding energy scale is employed, typically with 0 eV corresponding to the Fermi level (the highest occupied electron energy level if the metal at absolute zero temperature (0 K)), and increasing from right to left, reflecting the greater energy required to remove more tightly bound electrons [132].

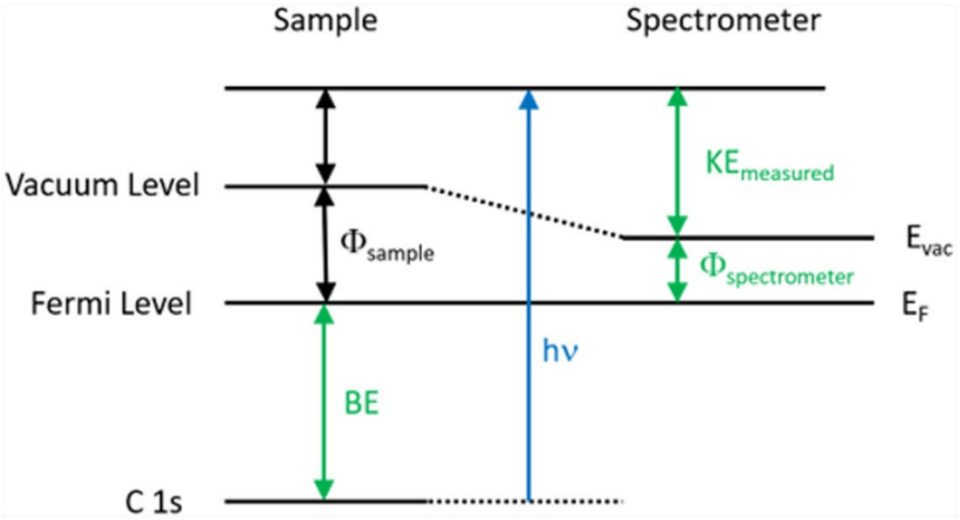

Figure 33: An energy level diagram illustrates the basic XPS equation, which includes the following components: the X-ray source energy ($h\nu$), the binding energy (BE = E_B) of the ejected electron (with C1s used as a well-defined and stable XPS reference), the kinetic energy of the

electron as measured by the spectrometer ($KE_{measured} = E_{kin}$), and the work function of the spectrometer ($\emptyset_{spectrometer}$) [95].

Although the spectrometer work function is a fundamental parameter in binding energy calculations, it is generally handled through instrument software and calibrations, thus typically not requiring direct user input; however, its influence on absolute binding energy accuracy, particularly when comparing data across different instruments or with theoretical values, necessitates consideration, and minimizing the sample's contact potential, often using a built-in charge neutralizer, is essential for optimal accuracy [95].

In this study, binding energies obtained from XPS and UPS were calibrated using the Fermi level of copper (Cu) in Eq. 77. As a result, all reported binding energies are referenced to the calibrated Fermi level at 0 eV.

The elemental and chemical composition, and chemical states of the atoms in a sample can be determined from the binding energy, which is independent of the x-ray source but material property, except for hydrogen (H) and helium (He) elements; however, the chemical environment, such as nearest neighbors and the oxidation state of the element, affects the binding energy [95, 111, 112]. While the elemental composition reveals the types and relative quantities of constituent elements (irrespective of bonding or arrangement), the chemical composition further describes bonding and arrangement, providing structure information. The chemical state specifies the various configurations atoms or molecules adopt based on their chemical, physical, and electronic properties, reflecting the nature of their chemical bonds.

For example, XPS spectra of tellurium and its various oxidation states show a clear trend of increasing binding energy with increasing oxidation state, with binding energy ranges of 572.70 -

573.50 eV for Te, 575.60 - 576.50 eV for TeO_2, and 576.60 - 577.30 eV for TeO_3 [132, 177]. This shift in binding energy (chemical shifts) is a direct result of the changing chemical environment around the tellurium atom as it loses electrons and forms bonds with more electronegative elements like oxygen (due to changes in chemical potential and polarizability), and these chemical shifts indicate the chemical state; similar trends are also observed in Titanium oxide states (TiO_x) [95, 132]. The NIST X-ray Photoelectron Spectroscopy Database is an invaluable resource for the scientific community, providing comprehensive reference data that greatly facilitates XPS analysis and serves as an excellent starting point for researchers identifying and analyzing core-level binding energies [177].

In XPS analysis, carbon correction, specifically referencing the C 1s peak at 284.60 eV (characteristic of C-C bonding), is a standard post-measurement procedure used to adjust binding energies in most analyses. Following the application of the C 1s correction at 284.60 eV, the binding energy values for all other elements within the XPS spectrum are considered accurate. However, while widely employed, the reliability of this correction is contingent upon the sample's characteristics and the presence of adventitious carbon; therefore, careful consideration of the sample, instrument, and experimental conditions is essential for proper data analysis.

Figure 34 shows the XPS high-resolution C 1s spectrum of β-$ZnTe(en)_{0.5}$ after Ar_{1000}^{+} GCIS with an energy of 10 KeV for 45 mins under UHV at room temperature using Al Kα radiation (1486.6 eV). As illustrated in the inset table within Figure 34, the lowest binding energy observed in the raw XPS spectra is fitted to C-C/C-H bonding at 284.60 eV, serving as the reference point for determining the binding energies of the other two spectral features. This lowest binding energy peak, attributed to C-C/C-H bonding, exhibits the highest intensity, indicative of the greatest atomic concentration because the unique set of binding energies associated with each element

enables XPS to identify and quantify the elemental composition of the sample [132]. The peak at the intermediate binding energy is most likely associated with C-N/C-OH bonding (286.17 eV), while the peak at the highest binding energy corresponds to C-O/C=O bonding (288.09 eV). Because XPS peak shapes and measured binding energies can be influenced by multiple final states and related processes (multiplet splitting, shakeup, shakeoff), which complicate interpretation beyond simple oxidation state and neighboring atom electronegativity effects, it is crucial to check existing literature before assigning unexpected peaks as novel chemical states, even though the initial state primarily dictates measured binding energies when only one final state is accessible [95, 111, 132]. Furthermore, the varying probabilities, or cross-sections, associated with each final state further complicate the accurate interpretation of the observed phenomena [132].

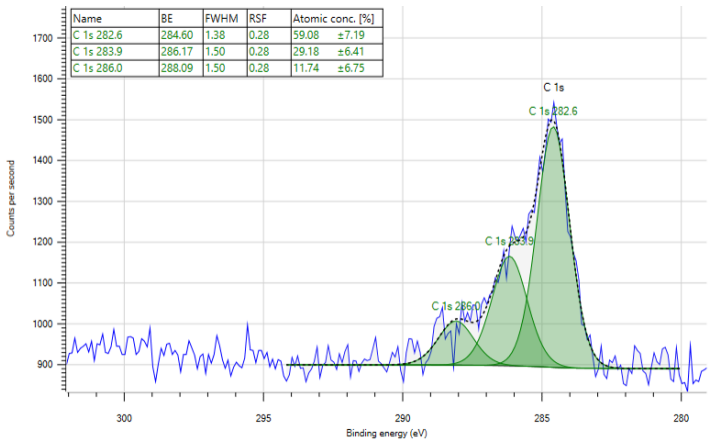

Figure 34: The XPS high-resolution C 1s spectrum of β-ZnTe(en)$_{0.5}$ acquired after Ar_{1000}^{+} GCIS process at 10 KeV for 45 minutes under UHV at room temperature using Al Kα radiation (1486.6 eV), was processed using ESCApe software. The blue line represents the acquired XPS spectrum, and the three green graphical features represent the fitted XPS spectrum after carbon correction (C 1s, C-C at 284.60 eV). The inset table shows the raw and fitted XPS C 1s spectra

(using a carbon correction of C 1s, C-C at 284.60 eV), along with the FWHM of each binding energy, the relative sensitivity factor (RSF), and the atomic concentration of each chemical state.

While incident X-rays penetrate a few micrometers deep, only electrons generated within approximately 10 nm of the surface, particularly those escaping without inelastic scattering, contribute to the characteristic photoelectron peaks used for analysis, with deeper electrons undergoing energy loss and contributing only to background signal [95, 132]. Although the y-axis typically represents intensity in arbitrary units (a.u.) rather than absolute values, the non-zero background values (around 900 cps) observed in Figure 34 are used to explain contributions from inelastically scattered electrons, secondary electrons, detector noise, and other background effects. The continuous background observed in XPS spectra is mainly attributed to inelastic scattering of emitted photoelectrons as they travel through the sample; these random, multiple scattering events result in a distribution of energy losses, where each photoelectron loses a varying amount of energy, contributing to a continuous background signal at lower kinetic energies (corresponding to higher binding energies) relative to the primary photoelectron peak [132].

When the sample thickness is significantly less than the XPS probing depth, valence band spectra may exhibit superimposed signals from both the sample and substrate, necessitating substrate spectrum analysis (e.g., via spectral subtraction) to ensure accurate interpretation. However, angle-resolved XPS (ARXPS) allows for the analysis of thinner surface layers than traditional XPS by providing information on elemental depth distribution through varying detection angles, although the exact depth probed is influenced by experimental parameters, material properties, and measurement conditions [95, 146].

While XPS is primarily known for its ability to provide information about the chemical state of materials, it also offers valuable insights into band structure studies, such as the valence band maximum (E_v), by analyzing the low binding energy region of the spectrum, where the E_v is typically located at the onset of the valence band emission [64, 138, 146, 171-175]. A refined procedure has been developed to precisely determine semiconductor core level to valence band maximum binding energy differences by analyzing simultaneously acquired core level and valence band XPS spectra, wherein the valence band maximum position is theoretically derived from the experimental XPS data [77, 78].

6.1.2. Sample Preparation and Experiment Procedures for XPS

XPS samples must be vacuum-compatible and handled with care to prevent contamination (using gloves and clean containers) and mounted appropriately to minimize charging; further sample preparation and mounting details are available in the cited references [95, 132].

Several mounting methods were attempted using conductive substrates since metallic behaviors are observed in UPS. First, β-$ZnTe(en)_{0.5}$ was attached to the Cupper conductive tape as a substrate. Second, gold conductive paste (Electron Microscopy Sciences, EMS Conductive Gold-Paste, SKU: 12642) was applied to the edge of β-$ZnTe(en)_{0.5}$ for attachment to the substrate (Au/Si) and allowed to fully cure for 24 hours at room temperature before XPS measurement. Third, a cleaned spatula was used to gently press β-$ZnTe(en)_{0.5}$ onto indium foil (Thermo Fisher Scientific, CAS: 7440-74-6, EINECS: 231-180-0) without breaking the samples. Fourth, methanol was initially used to secure the sample to the substrate (Au/Si and Pd/Si), but the sample detached during the GCIS process. If the monochromatic X-ray source and UV source

are not already activated, it is recommended that they be turned on and allowed to stabilize before sample preparation.

Figure 35 shows β-ZnTe(en)$_{0.5}$ mounted on the sample holder after being secured to the substrate. Copper plates and screws were used to secure the substrates for XPS measurement. A bulk ZnTe crystal was also prepared as a reference; it was easily mounted by placing it under the copper plate and securing it with two bolts on each side.

Figure 35: β-ZnTe(en)$_{0.5}$ is mounted on the sample holder after being secured to (a) Indium foil and (b) conductive substrate (Pd/Si).

Prior to XPS analysis at CHANL (Chapel Hill Analytical and Nanofabrication Laboratory), the condition of all β-ZnTe(en)$_{0.5}$ was verified using confocal Raman spectroscopy (Horiba LabRAM HR800, λ=532 nm) by acquiring spectra at multiple locations on each β-ZnTe(en)$_{0.5}$. Sample preparations and XPS measurements were carried out in CHANL using the Kratos Axis+ Supra XPS system. This system is equipped with a monochromatic Al Kα radiation source

(1486.6 eV), argon ion gas cluster ion sputtering (Ar_n^+ GCIS) for the cleaning process, and a helium lamp to enable UPS capability on the same samples without breaking vacuum.

The sample holder was loaded into a load-lock chamber and then transferred to the main analysis chamber, which was maintained at UHV condition (~10^{-8} to 10^{-9} Torr), after the pressure in the load-lock chamber reached an appropriate vacuum level (~10^{-6} to 10^{-7} Torr). Nitrogen (N_2) is used to purge the load-lock chamber to create a controlled environment, minimizing surface contamination during sample transfer and analysis, which ultimately led to more accurate and reliable results. This two-chamber system is commonly employed to maintain UHV conditions and minimize contaminations by preventing direct atmospheric exposure of the main analysis chamber. Once UHV is achieved, PES (XPS/UPS) measurement can proceed.

Due to the surface-sensitive nature of photoelectron spectroscopy (PES), sample cleanliness is crucial. As the current study did not include a control experiment with Ar_n^+ GCIS, previous data were referenced. It reported an etch rate of 0.72 (nm/min) on Tantalum pentoxide (Ta_2O_5) under Ar_{1000}^+ GCIS at 20 KeV(internal data obtained by Dr. Carrie Donley from CHANL). The experimental conditions employed, Ar_{1000}^+ GCIS at 10 KeV for 45 minutes, represent a less aggressive condition. Given that each argon ion (Ar^+) within the 10 KeV Ar_{1000}^+ cluster possesses approximately 10 eV of energy, a reduced etch rate is expected compared to the 20 keV experiment. Following Ar_{1000}^+ GCIS, the analysis vacuum chamber was purged with nitrogen (N_2) to remove residual argon ions (Ar^+). Once ultra-high vacuum (UHV) conditions were re-established, ultraviolet photoelectron spectroscopy (UPS) measurements were performed before X-ray photoelectron spectroscopy (XPS). This sequence was chosen because UPS requires less acquisition time (approximately 10 minutes per spot) than XPS. Performing UPS

first minimized the need for additional Ar^+ GCIS treatments between measurements while maintaining UHV conditions.

Prior to UPS measurements, the sample's position was carefully adjusted to prevent collisions with the optic elements for collecting photoelectrons. Real-time camera monitoring was utilized for this purpose. For Z-axis height optimization, a prominent peak, typically carbon or oxygen, is employed. In this specific instance, the zinc peak was selected for optimal Z-axis height determination. The sample height was incrementally adjusted with a small step size, either increased or decreased, until the maximum Zn peak intensity was achieved. Subsequently, a survey scan was performed to verify the optimal height.

Following Z-axis optimization, XPS was employed to optimize the iris (aperture) size. This optimization ensured that no substrate information was detected, isolating the signal from the sample surface. It was determined that an iris diameter of 55 μm achieved this condition. Once substrate interference was eliminated, UPS measurements proceeded.

UPS measurements were conducted using a He I ($h\nu$ = 21.2 eV) radiation source. Initially, a wide scan was performed with a step size of 0.025 eV and a dwell time of 0.1 seconds. Subsequently, high-resolution scans were acquired for both the low binding energy region (-1.22 eV to 5.22 eV) and the high binding energy region (15.22 eV to 19.22 eV), each with a step size of 0.01 eV. The dwell time for the high binding energy region scans was 0.1 seconds, while the dwell time for the low binding energy region scans was 0.6 seconds.

To enhance the accuracy of work function (∅) calculations, particularly in the determination of the secondary electron cutoff, a 9V bias was applied during the UPS measurements. However, it is important to note that the optimal bias potential is contingent upon the specific spectrometer configuration and the inherent properties of the sample.

Given the conductive nature of β-ZnTe$(en)_{0.5}$ under investigation, a charge neutralizer was not employed. This decision aligns with the standard practice of avoiding charge neutralizers for conductive samples, as they are generally recommended only for insulating materials. Furthermore, this intentional exclusion aimed to prevent potential interference and maximize the precision of work function (Ø) and valence band edge determination.

For XPS measurement, a survey scan is typically acquired initially to determine the basic elemental composition of the sample and identify any unexpected elements, thus guiding subsequent high-resolution scans for more detailed analysis of specific elements. While survey scans readily provide elemental composition, high-resolution scans require careful selection of photoelectron lines; typically, the most intense peak for an element is chosen for ease of detection and comparison with reference data, but potential peak interferences or limited chemical shifts may necessitate using less intense peaks or acquiring data from multiple photoelectron and Auger lines for accurate chemical state interpretation [95].

XPS scan parameters were optimized through iterative testing, resulting in the following settings: 80 eV pass energy, 1 eV step size, and 0.1 second dwell time for survey scans; and 20 eV pass energy, 0.1 eV step size, and 0.4 second dwell time for high-resolution scans. The binding energies of core levels and the valence band regions can be determined with an accuracy of 1 eV for survey scans and 0.1 eV for high-resolution scans. Generally, XPS scan parameters (pass energy, step size, and dwell time) are user-defined and must be optimized for quality data acquisition, varying between survey and high-resolution spectra, as well as across instruments; survey scans prioritize electron throughput (using larger pass energies, step sizes, and shorter dwell times), while high-resolution scans prioritize spectral resolution (using smaller pass

energies and step sizes, along with longer dwell times) to resolve subtle peak shape changes [95, 111, 132].

An iris is positioned at the entrance to the collection path. An iris (slot) size of 700 μm x 300 μm was selected to achieve high throughput and minimize charging effects.

A charge neutralizer, operating with a filament current of 0.39 A, a filament bias of 1.1 V, and a charge balance of 4.3 V, was employed during both survey and high-resolution XPS scans. Insulating samples are prone to charging, causing peak shifts and distortions, requiring charge neutralization (e.g., low-energy electron/ion beams) to mitigate the positive charge accumulation that shifts binding energies and can induce differential charging; even with optimized neutralization, residual shifts often necessitate energy calibration using an internal standard (carbon C 1s), though its variable binding energy limits its reliability [95, 111, 132].

6.1.3. Experimental Results of XPS on bulk ZnTe and β-ZnTe$(en)_{0.5}$

6.1.3.1. Chemical States of bulk ZnTe and β-ZnTe$(en)_{0.5}$ by XPS

Each element exhibits a unique XPS spectrum based on its characteristic energy levels. All transitions having binding energies below the X-ray source energy are theoretically observable, and photoelectron peaks are identified by the element and orbital from which the corresponding electrons are ejected [95, 111]. Therefore, XPS spectral interpretation typically proceeds by first identifying the most prominent C and O lines, followed by major and associated minor lines. Subsequently, interpretations are verified via spin-orbit doublet analysis, and finally, any remaining weak peaks are identified [132]. Following this, chemical state analysis, along with quantitative and qualitative assessments, are performed, with detailed steps and analytical considerations provided in the referenced literature [95, 132].

Regarding the nature of XPS photoelectron lines, all XPS lines, except those from *s* orbitals (*l=0*), are doublets due to spin-orbit coupling (denoted using the *j* quantum number as a subscript) [95]. This splitting is observed in core-level spectra of elements with non-zero orbital angular momentum (*l≠0*), arising from spin-orbit interaction and resulting in two peaks whose calculable intensity ratio (based on *j*) reflects the distinct quantum states [64, 92, 95, 132].

For accurate analysis, it is important to check XPS references, as these resources not only provide energies for expected photoelectron peaks (including chemical shifts, peak splitting, and shapes) but also often indicate when elemental peak shapes deviate from simple doublet/singlet patterns, making them an essential starting point for XPS analysis [95, 132, 177].

Bulk ZnTe was mounted directly on the sample holder by copper plate and screws. XPS analysis of bulk ZnTe is based on the binding energies of photoelectron peaks.

Bulk ZnTe sample, with approximate dimensions of 2mm x 2mm x 2mm, was utilized as a reference material to facilitate analysis and enhance the understanding of the properties of β-$ZnTe(en)_{0.5}$.

Figure 36 shows the XPS survey and high-resolution scans (Zn 2p and Te 3d) acquired from bulk ZnTe. As shown in Figure 36 (a), the bulk ZnTe surface appears severely contaminated, evidenced by the strong C 1s (87.45 at. %) and O 1s (9.44 at. %) peaks. However, after Ar_{1000}^{+} GCIS, the oxygen signal is eliminated, although a C 1s peak (11.50 at. %) persists, as shown in Figure 36 (b). Oxygen was observed in the previous analysis, but carbon was not reported [10]. While ideal ZnTe crystals are carbon-free, the observed presence of carbon could be attributed to either contamination during synthesis or redeposition from Ar_{1000}^{+} GCIS [145].

As expected, the Zn $2p_{3/2}$ peak exhibits a higher intensity than the Zn $2p_{1/2}$ peak, consistent with the Zn $2p_{3/2}$ peak being the most prominent feature in the Zn 2p region, as shown in Figure 36 (c)

and (d). The Zn 2p photoelectron lines are nearly coincident, regardless of Ar_{1000}^+ GCIS. This observation can be explained by the fact that the Zn photoelectron lines are observed at slightly lower binding energies than those characteristic of ZnO or ZnO_x, yet the binding energy ranges associated with ZnO and ZnO_x significantly overlap with the ZnTe lines [132, 177].

Obvious differences are observed in the Te 3d photoelectron lines before and after Ar_{1000}^+ GCIS, as shown in Figure 36 (e) and (f). The Te $3d_{5/2}$ peak also exhibits a higher intensity than the Te $3d_{3/2}$, consistent with it being the most prominent feature in the Te 3d region [132, 177]. To ensure reproducibility, four independent data sets were collected from different regions of the sample using Ar_{1000}^+ GCIS (denoted as c, d, e, f). A standard carbon correction procedure was applied by aligning the carbon C-C peak to a binding energy of 284.60 eV.

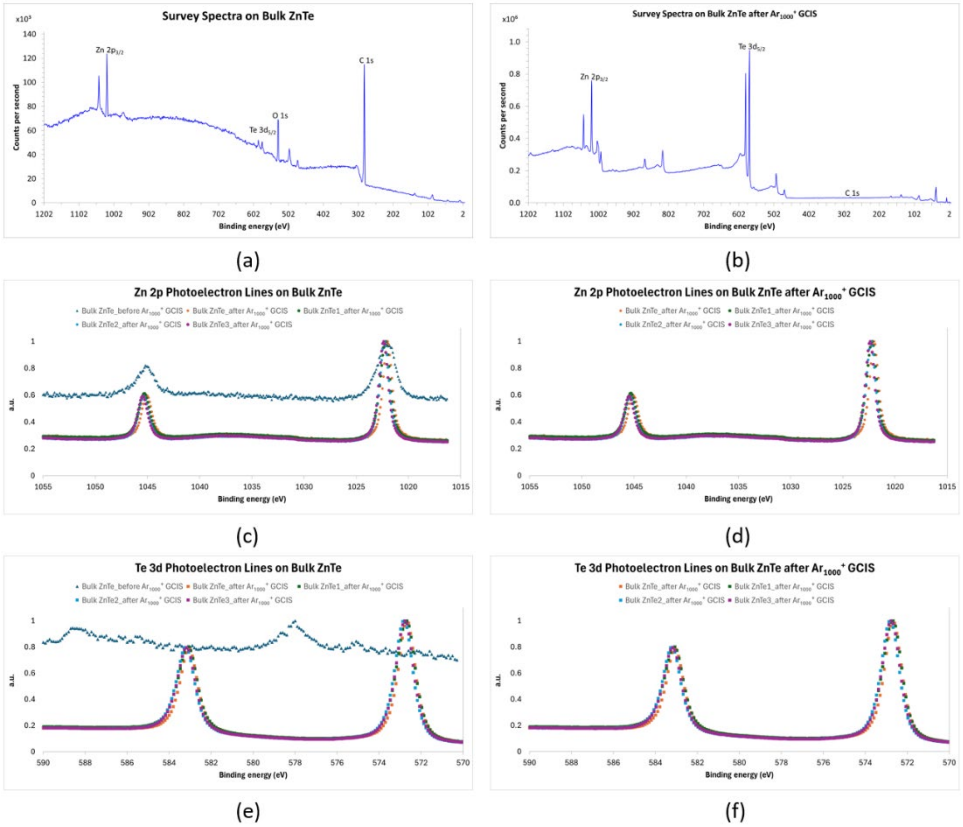

Figure 36: Survey XPS scan on bulk ZnTe (a) before Ar_{1000}^+ GCIS and (b) after Ar_{1000}^+ GCIS. High-resolution XPS scan on bulk ZnTe (c) Zn 2p before and after Ar_{1000}^+ GCIS, (d) Zn 2p after Ar_{1000}^+ GCIS, (e) Te 3d before and after Ar_{1000}^+ GCIS, (f) Te 3d after Ar_{1000}^+ GCIS. To demonstrate reproducibility, four data sets were acquired after Ar_{1000}^+ GCIS (c, d, e, f) from different locations on the sample. Carbon correction was applied to the XPS spectra by aligning the lowest binding energy peak to 284.60 eV (C-C).

Table 1 shows the photoelectron lines on bulk ZnTe before and after Ar_{1000}^+ GCIS. Carbon correction, as previously mentioned, was applied to the XPS spectra by aligning the lowest binding energy peak to 284.60 eV, corresponding to the C-C bond. While this is a useful initial step, it requires careful consideration, as comprehensive spectral analysis is essential for reliable results. This C 1s binding energy of 284.60 eV ± 0.1 eV is generally accepted for XPS calibration, though minor deviations can occur due to instrumental resolution and surface charging effects.

The Zn $2p_{3/2}$ photoelectron lines likely correspond to either ZnTe or ZnO_x on both before and after Ar_{1000}^+ GCIS, with the maximum binding energy difference of 0.37 eV. The binding energy regions for Zn, ZnTe, ZnO, and ZnO_x overlap, with the binding energy of Zn $2p_{3/2}$ within approximately 1.3 eV, complicating chemical state interpretation based on XPS alone [132, 177]. TeO_2 or TeO_3 is observed in the Te $3d_{5/2}$ photoelectron line before Ar_{1000}^+ GCIS, but the Te $3d_{5/2}$ photoelectron line indicates the presence of Te after Ar_{1000}^+ GCIS [132, 177].

Table 1: Photoelectron Lines on Bulk ZnTe before and after Ar_{1000}^{+} GCIS

Photoelectron Lines on Bulk ZnTe						
		Zn 2p		Te 3d		C 1s
		$2p_{1/2}$ (1045 eV)	$2p_{3/2}$ (1022 eV)	$3d_{3/2}$ (583 eV)	$3d_{5/2}$ (573 eV)	1S (284.60 eV)
ZnTe	Before Ar+ GCIS	1045.20	1022.10	588.40	578.00	284.61
	After Ar+ GCIS	1045.10	1022.00	583.10	572.70	284.60
ZnTe1	After Ar+ GCIS	1045.27	1022.17	583.07	572.67	284.65
ZnTe2	After Ar+ GCIS	1045.37	1022.27	583.17	572.77	284.60
ZnTe3	After Ar+ GCIS	1045.47	1022.37	583.17	572.77	284.62

Table 2 presents the elemental ratios on bulk ZnTe before and after Ar_{1000}^{+} GCIS. The ideal elemental Te:Zn ratio for bulk ZnTe is 1, but its value varies. The current O:Zn ratio is significantly lower than the previous measurement of 0.16 [10]. Elemental ratios provide valuable insight into the material's composition, they should be considered qualitative rather than strictly quantitative. This is because, during GCIS, lighter atoms are preferentially sputtered due to their higher sputtering yields, resulting from their lower mass and greater ease of ejection from the sample surface [176].

Table 2: Elemental Ratios on bulk ZnTe before and after Ar_{1000}^{+} GCIS

Elemental Ratio on Bulk ZnTe							
		Te:Zn	C:Zn	O:Zn	C:Te	O:Te	C:O
Bulk ZnTe	Before Ar^+ GCIS	0.20	33.63	3.63	169.66	18.31	9.27
	After Ar^+ GCIS	1.31	0.30	0.00	0.23	0.00	0.00
Bulk ZnTe1	After Ar^+ GCIS	1.11	0.16	0.02	0.15	0.02	7.68
Bulk ZnTe2	After Ar^+ GCIS	1.13	0.16	0.01	0.14	0.01	11.31
Bulk ZnTe3	After Ar^+ GCIS	1.13	0.20	0.03	0.18	0.02	7.56

1. Copper (Cu) conductive tape substrate

β-$ZnTe(en)_{0.5}$ was placed on a copper (Cu) substrate and mounted using a copper plate and screws for XPS measurement. XPS analysis of β-$ZnTe(en)_{0.5}$ is based on the binding energies of

photoelectron peaks and Auger electron lines. Although Auger Electron Spectroscopy (AES) was attempted, the data obtained was not suitable for analysis. Therefore, the analysis presented herein is exclusively based on binding energy measurements.

Figure 37 presents the XPS survey and high-resolution scans (Zn 2p and Te 3d) on β-$ZnTe(en)_{0.5}$. The survey scan indicated the presence of Zn, Te, C, N, and O; however, the atomic concentrations of C, N, and O were significantly reduced following Ar_{1000}^{+} GCIS, as shown in Figure 37 (a) and (b). Although not intentionally incorporated during synthesis, oxygen was observed in these results, consistent with prior findings [66, 93].

Figure 37 (c) shows the Zn photoelectron lines before and after Ar_{1000}^{+} GCIS. Notably, the Zn peaks before Ar_{1000}^{+} GCIS appear at lower binding energies compared to those observed after Ar_{1000}^{+} GCIS. As anticipated, the Zn $2p_{3/2}$ peak is the most dominant feature in the Zn 2p region, exhibiting a higher intensity than the Zn $2p_{1/2}$ peak. While the binding energy ranges for the Zn $2p_{3/2}$ photoelectron line overlap for Zn, ZnTe, ZnO, and ZnO_x, the Zn peak is known to occur at slightly lower binding energies than those of ZnTe, ZnO, or ZnOx [132, 177].

As depicted in Figure 37 (e), distinct differences in the Te 3d photoelectron lines are obvious before and after Ar_{1000}^{+} GCIS, consistent with the observations for bulk ZnTe (Figure 36 (e)). Figure 37 (f) shows a slight peak shift is observed between the two spectra, with the Te $3d_{5/2}$ peak being the most prominent feature in the Te 3d region and displaying a greater intensity than the Te $3d_{3/2}$ peak [132, 177].

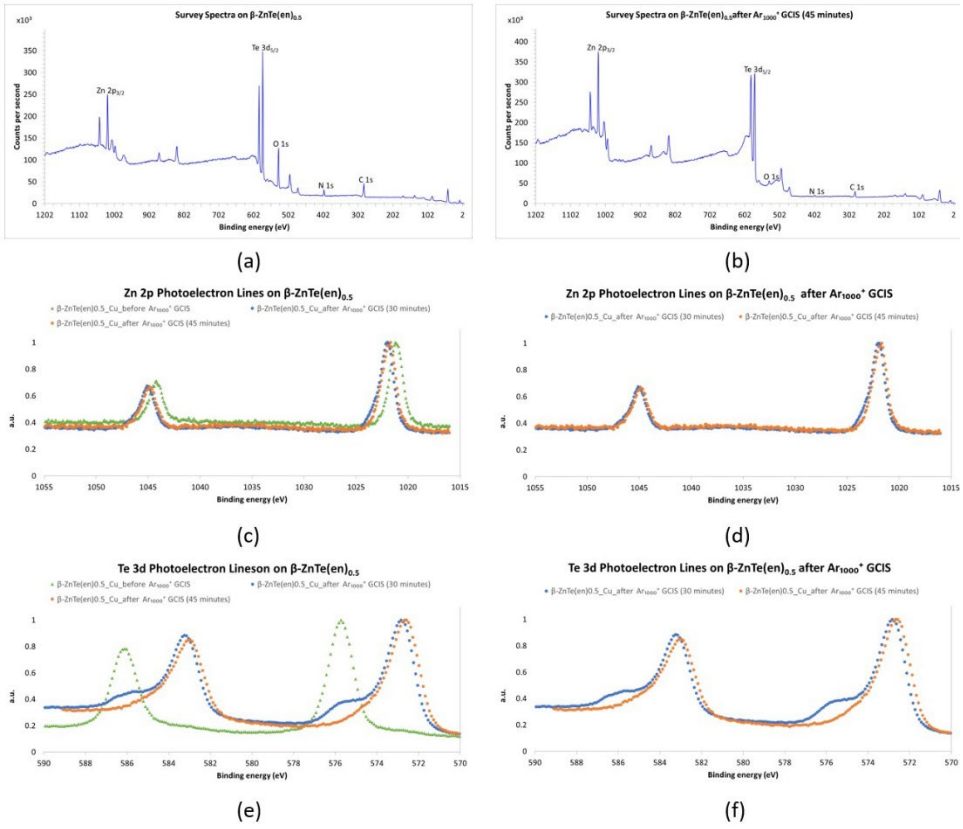

Figure 37: Survey XPS scan of β-ZnTe(en)$_{0.5}$ on Cu substrate (a) before Ar_{1000}^{+} GCIS and (b) after Ar_{1000}^{+} GCIS. High-resolution XPS scan on β-ZnTe(en)$_{0.5}$ (c) Zn 2p before and after Ar_{1000}^{+} GCIS, (d) Zn 2p after Ar_{1000}^{+} GCIS, (e) Te 3d before and after Ar_{1000}^{+} GCIS, (f) Te 3d after Ar_{1000}^{+} GCIS. Carbon correction was applied to the XPS spectra by aligning the lowest binding energy peak to 284.60 eV (C-C).

Table 3 exhibits the photoelectron lines on β-ZnTe(en)$_{0.5}$ before and after Ar_{1000}^{+} GCIS. As previously noted, carbon correction was performed by aligning the lowest binding energy peak to 284.60 eV (C-C bond).

The Zn 2p$_{3/2}$ peak, a Zn peak, was identified solely through binding energy analysis (the conventional XPS method), not Auger Electron Spectroscopy (AES). After 30 minutes of Ar_{1000}^{+}

GCIS, the Zn $2p_{3/2}$ peak exhibited binding energies consistent with either ZnTe or ZnO_x; however, AES analysis confirmed the presence of ZnO_x. The Zn $2p_{3/2}$ peak's binding energy, after an additional 15 minutes of Ar_{1000}^+ GCIS (total 45 minutes), could not distinguish between ZnTe and ZnO_x; however, AES analysis confirmed the presence of ZnO.

Prior to Ar_{1000}^+ GCIS, the Te $3d_{5/2}$ peak was consistent with TeO_2. Following Ar_{1000}^+ GCIS, a slight shift in the Te 3d photoelectron lines was observed; however, both post Ar_{1000}^+ GCIS Te $3d_{5/2}$ peaks remained within the binding energy range characteristic of Te, as determined solely by XPS binding energy analysis, without AES. The binding energy (ΔE_B) shifts observed in the current XPS data are consistent with previous findings, where the Te $3d_{3/2}$ and $3d_{5/2}$ photoelectron lines in β-$ZnTe(en)_{0.5}$ exhibit a shift of approximately -2.7 eV after in situ Ar etching, which removes approximately 150 nm of the top surface [10]. The current data, which shows a shift to lower binding energies after Ar_{1000}^+ GCIS, corroborates this trend, but with slightly larger shifts of -3.05 eV for the $3d_{3/2}$ line and -3.15 eV for the $3d_{5/2}$ line. These shifts are indicative of a change in the chemical state of Te 3d, specifically the reduction of TeO_x to Te. Slight deviations are typically expected, and both the N and O peaks fall within their respective photoelectron line ranges [132, 177]. It is important to note that definitive chemical state identification, especially for light elements such as N and O, often requires complementary analysis techniques such as AES. However, this is beyond the scope of the present study and is left for future investigation.

Table 3: Photoelectron Lines of β-$ZnTe(en)_{0.5}$ on Cu substrate before and after Ar_{1000}^{+} GCIS

Photoelectron Lines on β-$ZnTe(en)_{0.5}$							
	Zn		Te		C	N	O
	$2p_{1/2}$ (1045 eV)	$2p_{3/2}$ (1022 eV)	$3d_{3/2}$ (583 eV)	$3d_{5/2}$ (573 eV)	1S (284.60 eV)	1S (398 eV)	1S (531 eV)
Before Ar^{+} GCIS	1044.23	1021.23	586.03	575.73	284.59	399.53	530.13
After Ar^{+} GCIS (30 minutes)	1045.14	1021.94	583.14	572.84	284.61	399.94	530.44
After Ar^{+} GCIS (45 minutes)	1044.88	1021.68	582.98	572.58	284.60	399.88	530.68

Table 4 shows the ideal and measured elemental ratios of β-$ZnTe(en)_{0.5}$ on Cu substrate before and after Ar_{1000}^{+} GCIS, revealing several notable trends. The measured elemental ratios deviate from the ideal, and two explanations are provided to support this observation. First, preferential sputtering of lighter elements over heavier elements is observed following Ar_{1000}^{+} GCIS, as evidenced by the decreased atomic concentration of the organic elements C, N, and O. Furthermore, preferential sputtering of the lighter element Zn relative to Te is observed between 30 minutes and 45 minutes of Ar_{1000}^{+} GCIS. While Ar_n^{+} GCIS is effective for surface cleaning under vacuum conditions, the inherent redeposition associated with the technique can influence elemental analysis accuracy [145]. This redeposition effect, even under the relatively mild conditions (Ar_{1000}^{+}) employed, where smaller cluster numbers (e.g., Ar_{10}^{+}) can have a disproportionately stronger influence than larger ones (e.g., Ar_{1000}^{+}), may still contribute to the observed results.

While the surface sensitivity of XPS (typically the top 1–10 nm) makes it ideal for analyzing the surface composition, it's important to recognize that this same sensitivity can also be misleading when studying layered structures (e.g., superlattice heterogeneous structures). β-$ZnTe(en)_{0.5}$ can be seen as a superlattice heterogeneous structure since two monolayers of ZnTe are connected to ethylenediamine ($C_2H_8N_2$), and this sequence is repeated. Thus, its atomic concentration is strongly dependent on the probing depth. However, ARXPS can be used for detailed depth

information since this technique offers a non-destructive method for depth profiling by varying the photoelectron detection angle, thus avoiding the need for ion sputtering, which is typically used to remove the surface of the sample.

Thermal degradation significantly increased the O:Zn ratio from 0.05 (S19-p) and 0.41 (S07-p) in pristine samples to 0.71 (S19-th) and 1.08 (S03-th) after the thermal degradation process, measured by energy-dispersive X-ray (EDX), indicating a relative increase in oxygen content compared to zinc as the samples degraded [10]. After Ar_{1000}^+ GCIS, the sample exhibited O:Zn ratio of 0.27 after 30 minutes and 0.32 after 45 minutes, suggesting a pristine condition was retained for XPS analysis.

While elemental ratios offer valuable qualitative insights into material composition, they should not be considered strictly quantitative due to the preferential sputtering of lighter atoms during Ar_n^+ GCIS, a consequence of their higher sputtering yields resulting from lower mass and easier ejection [176]. Organic materials generally exhibit higher sputter rates than inorganic materials under Ar_n^+ GCIS, a trend also observed in the data [197].

Table 4: Ideal and measured elemental ratios of β-$ZnTe(en)_{0.5}$ on Cu substrate before and after Ar_{1000}^+ GCIS

Elemental Ratio on β-$ZnTe(en)_{0.5}$										
	Te:Zn	C:Zn	N:Zn	C:Te	N:Te	N:C	O:Te	O:Zn	N:O	C:O
Ideal Condition	1.00	1.00	1.00	1.00	1.00	1.00	0.00	0.00	0.00	0.00
Before Ar_{1000}^+ GCIS	1.43	3.48	0.91	2.43	0.63	0.26	2.53	3.62	0.25	0.96
After Ar_{1000}^+ GCIS (30 minutes)	1.09	0.44	0.14	0.40	0.13	0.32	0.25	0.27	0.52	1.63
After Ar_{1000}^+ GCIS (45 minutes)	1.32	1.07	0.21	0.81	0.16	0.19	0.24	0.32	0.64	3.34

In addition to the copper (Cu) tape as a substrate, other conductive substrates such as Au/Si (with gold conductive paste) and indium (In) foil, were used. β-$ZnTe(en)_{0.5}$ was positioned on an Au/Si substrate, with gold conductive paste applied to its edge, and then secured onto the sample holder

using a copper plate and screws. XPS analysis of β-$ZnTe(en)_{0.5}$ was based on the binding energies of photoelectron peaks exclusively, as AES yielded no interpretable data.

2. Au/Si substrate

β-$ZnTe(en)_{0.5}$ was gently placed onto the Au/Si substrate, and a small amount of gold conductive paste was applied to adhere the sample to the substrate. The assembled sample was subsequently secured to the sample holder using a copper plate and screws. The chemical states analysis of β-$ZnTe(en)_{0.5}$, presented herein, relies exclusively on precise binding energy measurements associated with photoelectron peaks.

Figure 38 shows the XPS survey and high-resolution scans of β-$ZnTe(en)_{0.5}$ on the Au/Si substrate, including the Zn 2p and Te 3d regions. Figure 38 (a) and (b) present survey scans showing the presence of Zn, Te, C, N, and O before and after Ar_{1000}^{+} GCIS, respectively. The intensity of C, N, and O was significantly diminished following Ar_{1000}^{+} GCIS, with similar patterns observed in Figure 37 (a) and (b). In addition to the expected elements, gold was observed in the XPS spectra, likely due to smearing from the gold conductive paste. Despite several attempts to mitigate this, gold persists. One potential solution to eliminate the gold signal is to reduce the iris size from the current 700 μm x 300 μm to a smaller aperture, enabling spot analysis down to 15 μm in diameter. An optimal iris diameter of 55 μm was found to eliminate the gold signal. However, this comes with the trade-off of increased charging risk and lower throughput, which, while potentially manageable for XPS, could be detrimental for techniques like UPS.

The Zn $2p_{3/2}$ peak is the dominant peak in the Zn 2p photoelectron lines, exhibiting greater intensity than the Zn $2p_{1/2}$ peak. This is illustrated in Figure 38 (c) and (d), which demonstrate the near coincidence of the Zn 2p photoelectron lines, irrespective of Ar_{1000}^{+} GCIS. This near

coincidence is further complicated by the significant overlap in binding energy ranges observed for the Zn $2p_{3/2}$ photoelectron lines of Zn, ZnTe, ZnO, and ZnO_x [132, 177].

Noticeable differences in the Te 3d photoelectron lines are evident before and after Ar_{1000}^+ GCIS, as illustrated in Figure 38 (e) and (f). The Te $3d_{5/2}$ peak exhibits greater intensity than the Te $3d_{3/2}$, consistent with its prominence with the Te 3d photoelectron lines region [132, 177].

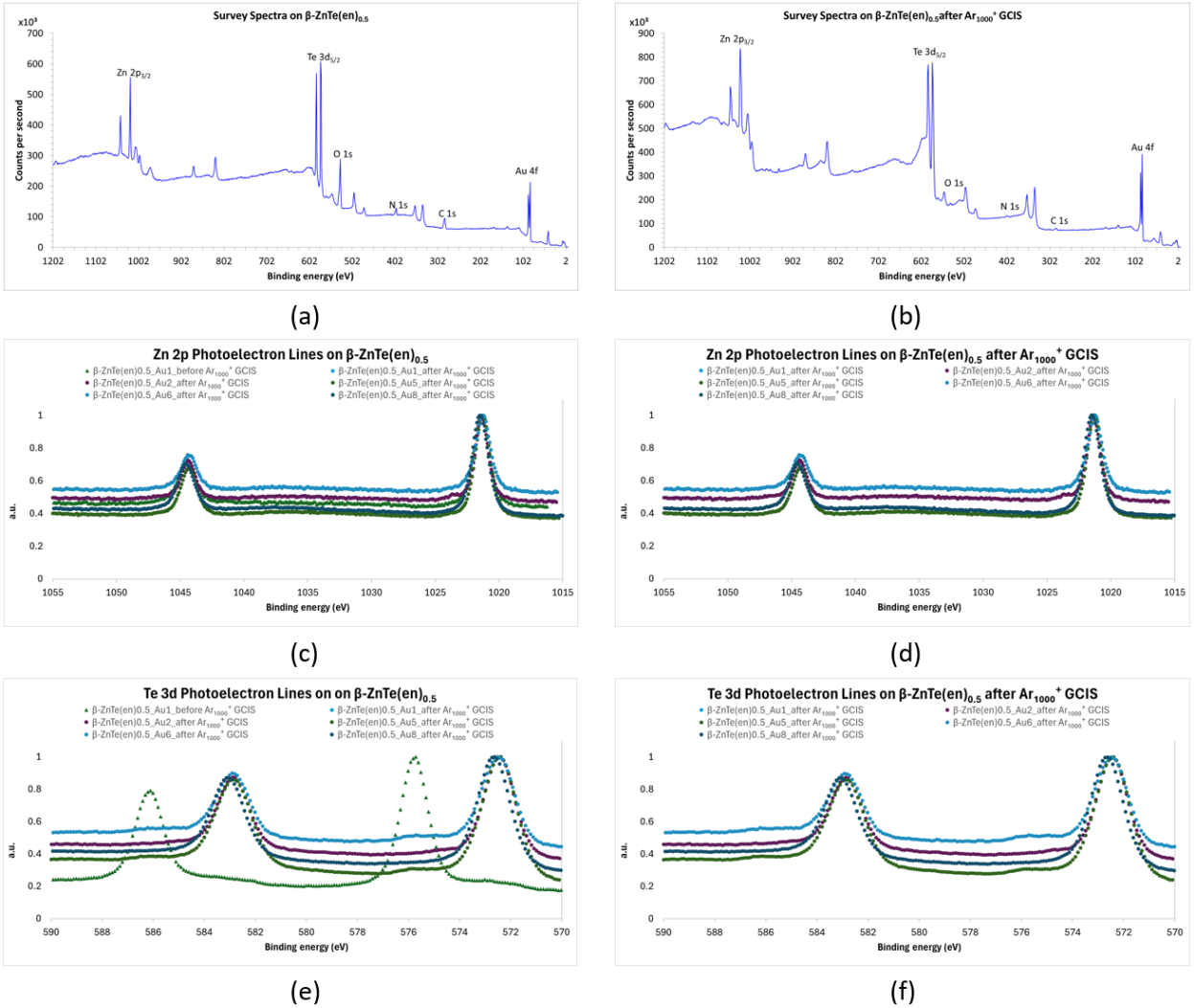

Figure 38: Survey XPS scan of β-$ZnTe(en)_{0.5}$ on the Au/Si substrate (with gold conductive paste) for Au1 (a) before Ar_{1000}^+ GCIS and (b) after Ar_{1000}^+ GCIS. High-resolution XPS scan on β-

$ZnTe(en)_{0.5}$ (c) Zn 2p before and after Ar_{1000}^+ GCIS, (d) Zn 2p after Ar_{1000}^+ GCIS, (e) Te 3d before and after Ar_{1000}^+ GCIS, (f) Te 3d after Ar_{1000}^+ GCIS. Carbon correction was applied to the XPS spectra by aligning the lowest binding energy peak to 284.60 eV (C-C).

Table 5 presents photoelectron Lines of β-$ZnTe(en)_{0.5}$ before and after Ar_{1000}^+ GCIS, with carbon correction performed by aligning the lowest binding energy peak to 284.60 eV (C-C bond). Before Ar_{1000}^+ GCIS, the observed Zn $2p_{3/2}$ peak displayed binding energies corresponding to either Zn or ZnO. Following Ar_{1000}^+ GCIS, the Zn $2p_{3/2}$ peak's binding energies were confined within a 0.4 eV range. This narrow range made it impossible to distinguish between Zn, ZnTe, ZnO, and ZnO_x, as their reported binding energies not only exceed 0.4 eV, but also exhibit significant overlap, particularly between ZnTe, ZnO, and ZnO_x [132, 177].

Before Ar_{1000}^+ GCIS, the Te $3d_{5/2}$ peak was consistent with TeO_2, and after Ar_{1000}^+ GCIS, it remained within the binding energy range characteristic of Te. The shift in the Te $3d_{3/2}$ and $3d_{5/2}$ photoelectron lines to lower binding energies after Ar_{1000}^+ GCIS, with shifts of -3.35 eV, confirms the reduction of TeO_x to Te. This observation is consistent with the prior work, which reported a -2.7 eV shift after in situ Ar etching [10].

Although high-resolution spectra of nitrogen was absent from certain datasets (Au2, Au5, and Au6), the presence of both N and O was confirmed within their established photoelectron line ranges, with allowances made for minor deviations [132, 177].

Table 5: Photoelectron Lines of β-ZnTe(en)$_{0.5}$ on Au/Si substrate before and after Ar_{1000}^{+} GCIS

Photoelectron Lines on β-ZnTe(en)$_{0.5}$								
		Zn		Te		C	N	O
		$2p_{1/2}$ (1045 eV)	$2p_{3/2}$ (1022 eV)	$3d_{3/2}$ (583 eV)	$3d_{5/2}$ (573 eV)	1S (284.60 eV)	1S (398 eV)	1S (531 eV)
Au1	Before Ar^{+} GCIS	1044.42	1021.42	586.12	575.72	284.60	399.32	530.22
	After Ar^{+} GCIS	1044.67	1021.67	582.77	572.37	284.62	399.57	532.77
Au2	After Ar^{+} GCIS	1044.39	1021.39	582.89	572.39	284.59	-	530.29
Au5	After Ar^{+} GCIS	1044.29	1021.29	582.79	572.39	284.59	-	529.99
Au6	After Ar^{+} GCIS	1044.42	1021.22	582.92	572.52	284.61	-	530.22
Au8	After Ar^{+} GCIS	1044.63	1021.43	583.03	572.63	284.58	399.83	530.03

Noticeable trends, relative to the ideal elemental ratios, are evident in the measured elemental ratios of β-ZnTe(en)$_{0.5}$ before and after Ar_{1000}^{+} GCIS, as presented in Table 6. Following Ar_{1000}^{+} GCIS, preferential sputtering is observed, with lighter elements like C, N, and O decreasing in atomic concentration, and further preferential sputtering of Zn relative to Te occurring between 30 and 45 minutes of Ar_{1000}^{+} GCIS. Although nitrogen was unexpectedly absent in Au2 and Au6, a generally low (< 6 at. %) or undetectable nitrogen concentration was observed in the samples after Ar_{1000}^{+} GCIS, possibly due to several factors. Preferential sputtering during even gentle Ar_n^{+} GCIS can lead to the more efficient removal or redistribution of lighter elements like nitrogen compared to heavier inorganic elements. Therefore, while elemental ratios provide valuable qualitative insights into material composition, they should be interpreted qualitatively rather than quantitatively due to this preferential sputtering of lighter atoms during Ar_n^{+} GCIS, which arises from their higher sputtering yields due to lower mass and easier ejection [176]. Furthermore, the potential for redeposition, particularly of heavier elements under high vacuum conditions due to sputtering yield differences, is crucial to consider when analyzing samples containing both heavy and light elements after Ar_n^{+} GCIS [145, 176]. Because β-ZnTe(en)$_{0.5}$, which is a superlattice nanostructure alternating organic and inorganic elements, these

differential redeposition rates can significantly influence observed elemental ratios, potentially leading to misinterpretations of sample compositions if not properly accounted for.

The O:Zn ratio of β-$ZnTe(en)_{0.5}$, reported to be less than 0.41 in its pristine condition, remained below 0.42 after Ar_{1000}^{+} GCIS, suggesting that the sample maintained a pristine condition for XPS analysis [10].

Table 6: Ideal and measured elemental ratios of β-$ZnTe(en)_{0.5}$ on the Au/Si substrate before and after Ar_{1000}^{+} GCIS

Elemental Ratio on β-$ZnTe(en)_{0.5}$											
		Te:Zn	C:Zn	N:Zn	C:Te	N:Te	N:C	O:Te	O:Zn	N:O	C:O
	Ideal Condition	1.00	1.00	1.00	1.00	1.00	1.00	0.00	0.00	0.00	0.00
Au1	Before Ar^+ GCIS	1.51	4.07	1.03	2.70	0.68	0.25	2.73	4.12	0.25	0.99
	After Ar^+ GCIS	1.16	0.57	0.14	0.49	0.12	0.25	0.14	0.16	0.89	3.64
Au2	After Ar^+ GCIS	1.04	0.90	0.00	0.87	0.00	0.00	0.09	0.09	0.00	9.74
Au5	After Ar^+ GCIS	1.00	0.59	0.22	0.59	0.22	0.37	0.24	0.24	0.92	2.49
Au6	After Ar^+ GCIS	0.92	1.64	0.00	1.78	0.00	0.00	0.46	0.42	0.00	3.88
Au8	After Ar^+ GCIS	0.79	0.96	0.23	1.22	0.29	0.24	0.36	0.29	0.81	3.36

3. Indium (In) foil substrate

β-$ZnTe(en)_{0.5}$ was carefully placed on an indium (In) foil substrate. Gentle pressure was applied with a clean spatula to ensure uniform contact between the sample and substrate, avoiding any structural damage. The assembled sample was then affixed to the sample holder using a copper plate and screws. The chemical states of β-$ZnTe(en)_{0.5}$ are determined exclusively using precise binding energy measurements of photoelectron peaks, consistent with previous data sets obtained from Cu and Au substrates.

Figure 39 (a) and (b) show XPS survey scans of β-$ZnTe(en)_{0.5}$ before and after Ar_{1000}^{+} GCIS, respectively, revealing the presence of Zn, Te, C, N, and O. Following Ar_{1000}^{+} GCIS, the intensities of the C, N, and O peaks were significantly reduced, a similar trend observed in previous data using different substrates (Figure 37 and Figure 38). The persistent presence of

indium signal in the XPS spectra, despite mitigation efforts, can be addressed by reducing the iris diameter to 55 μm. This approach eliminates the indium signal but introduces a trade-off of increased charging risk and lower throughput.

As seen in Figure 39 (c) and (d), the Zn $2p_{3/2}$ peak, which is the most intense in the Zn 2p spectrum, remains nearly coincident regardless of Ar_{1000}^{+} GCIS. The overlapping binding energies of the Zn $2p_{3/2}$ lines for Zn, ZnTe, ZnO, and ZnO_x create challenges in distinguishing between zinc-containing elements [132, 177].

The Te 3d photoelectron spectra, presented in Figure 39 (e) and (f), demonstrate observable variations following Ar1000+ GCIS. Especially, the Te $3d_{5/2}$ component exhibits a greater intensity than the Te $3d_{3/2}$, in accordance with its established prominence in the Te 3d spectral region [132, 177].

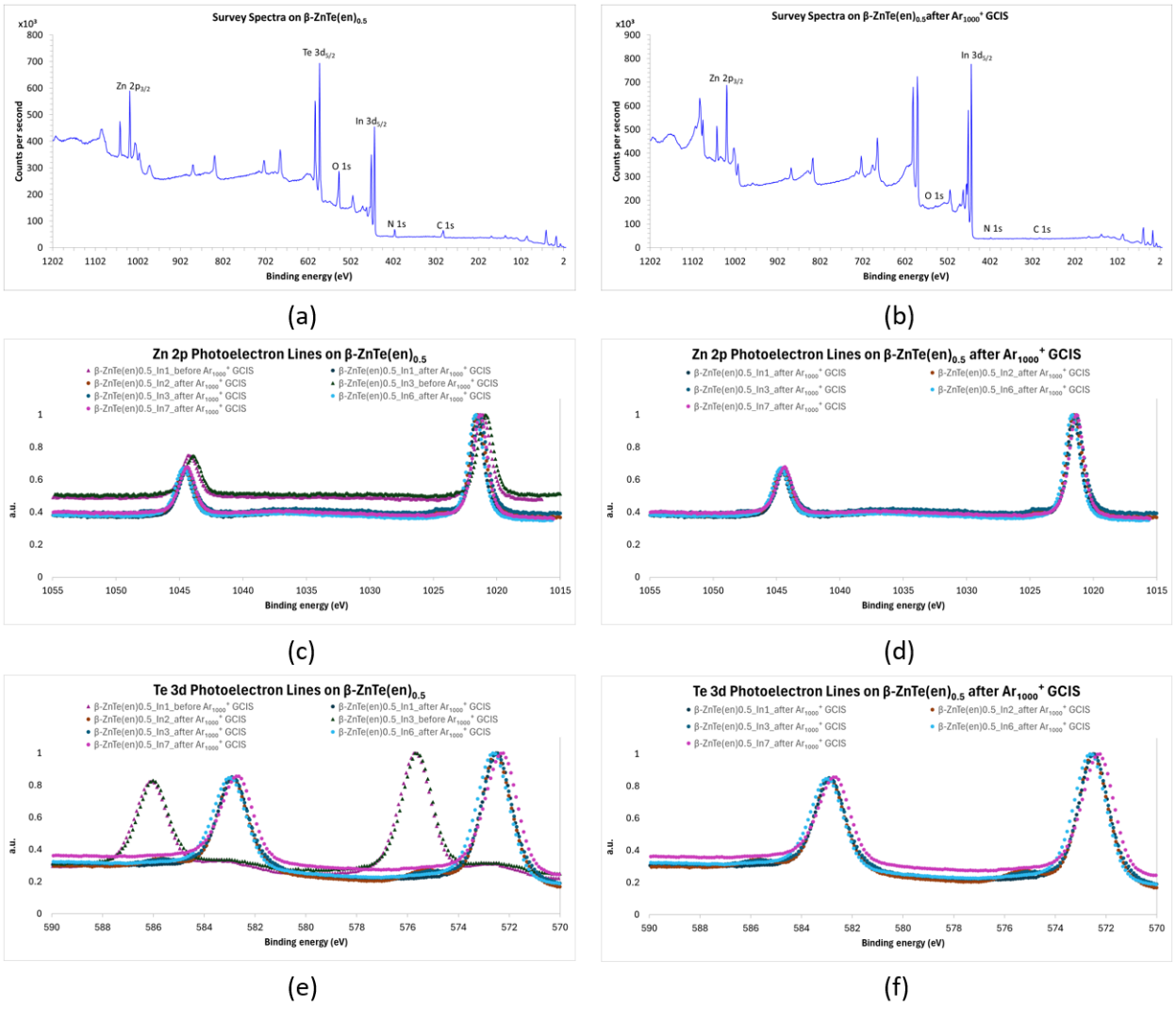

Figure 39: Survey XPS scan of β-ZnTe(en)$_{0.5}$ on In foil substrate for In1 (a) before Ar_{1000}^{+} GCIS and (b) after Ar_{1000}^{+} GCIS. High-resolution XPS scan on β-ZnTe(en)$_{0.5}$ (c) Zn 2p before and after Ar_{1000}^{+} GCIS, (d) Zn 2p after Ar_{1000}^{+} GCIS, (e) Te 3d before and after Ar_{1000}^{+} GCIS, (f) Te 3d after Ar_{1000}^{+} GCIS. Carbon correction was applied to the XPS spectra by aligning the lowest binding energy peak to 284.60 eV (C-C).

Figure 39 exhibits the photoelectron lines of β-ZnTe(en)$_{0.5}$ before and after Ar_{1000}^{+} GCIS, with carbon correction applied (C-C at 284.60 eV). Prior to Ar_{1000}^{+} GCIS, the Zn 2p$_{3/2}$ photoelectron

line indicated the chemical states of Zn. Post Ar_{1000}^{+} GCIS, the photoelectron line of the Zn $2p_{3/2}$ was inconclusive, overlapping with Zn, ZnTe, ZnO, and ZnOx due to a narrow 0.73 eV range, which aligns with both reported values and observed data from the previous two data sets [132, 177].

The Te $3d_{5/2}$ peak, initially indicative of TeO_2, shifts to a range consistent with elemental Te after Ar_{1000}^{+} GCIS. A -3.2 eV shift in Te $3d_{3/2}$ and $3d_{5/2}$ lines confirm TeO_x reduction, aligning with previous reports [10].

Both nitrogen and oxygen were detected within established binding energy ranges, accounting for minor deviations [132, 177].

Table 7: Photoelectron Lines of β-$ZnTe(en)_{0.5}$ on In foil substrate before and after Ar_{1000}^{+} GCIS

Photoelectron Lines on β-$ZnTe(en)_{0.5}$								
		Zn		Te		C	N	O
		$2p_{1/2}$ (1045 eV)	$2p_{3/2}$ (1022 eV)	$3d_{3/2}$ (583 eV)	$3d_{5/2}$ (573 eV)	1S (284.60 eV)	1S (398 eV)	1S (531 eV)
In1	Before Ar^+ GCIS	1044.36	1021.16	586.06	575.66	284.60	399.46	530.16
	After Ar^+ GCIS	1044.56	1021.56	582.86	572.46	284.62	399.76	531.16
In2	After Ar^+ GCIS	1044.51	1021.51	582.91	572.51	284.59	399.81	529.91
In3	Before Ar^+ GCIS	1043.91	1020.91	586.01	575.71	284.62	399.11	530.01
	After Ar^+ GCIS	1044.41	1021.31	582.91	572.51	284.60	399.61	530.31
In6	After Ar^+ GCIS	1044.64	1021.64	582.94	572.64	284.60	399.24	530.14
In7	After Ar^+ GCIS	1044.34	1021.34	582.64	572.24	284.59	398.64	530.14

Table 8 reveals the ideal and observable trends in the elemental ratios of β-$ZnTe(en)_{0.5}$ before and after Ar_{1000}^{+} GCIS. As expected, the preferential sputtering resulted in decreased atomic concentrations of lighter elements (C, N, O) relative to inorganic elements (Zn, Te) after Ar_{1000}^{+} GCIS. Therefore, elemental ratios should be interpreted qualitatively, not quantitatively because lighter elements exhibit higher sputtering yields due to their lower mass, leading to their more efficient removal or redistribution [145, 176]. Adding to the complexity, redeposition, especially of heavier elements, can distort results, especially in superlattice nanostructures like β-

$ZnTe(en)_{0.5}$, which feature alternating organic and inorganic layers [145]. Nevertheless, despite these analytical challenges, the O:Zn ratio remained below 0.30 after Ar_{1000}^{+} GCIS, confirming a pristine state, consistent with the previous report [10].

Table 8: Ideal and measured elemental ratios of β-$ZnTe(en)_{0.5}$ on In foil substrate before and after Ar_{1000}^{+} GCIS

Elemental Ratio on β-$ZnTe(en)_{0.5}$											
		Te:Zn	C:Zn	N:Zn	C:Te	N:Te	N:C	O:Te	O:Zn	N:O	C:O
	Ideal Condition	1.00	1.00	1.00	1.00	1.00	1.00	0.00	0.00	0.00	0.00
In1	Before Ar^+ GCIS	1.39	2.55	0.87	1.83	0.63	0.34	2.59	3.60	0.24	0.71
	After Ar^+ GCIS	1.16	0.27	0.15	0.23	0.13	0.57	0.09	0.11	1.40	2.48
In2	After Ar^+ GCIS	1.05	0.25	0.15	0.24	0.14	0.60	0.22	0.23	0.65	1.08
In3	Before Ar^+ GCIS	1.40	2.31	0.92	1.65	0.66	0.40	3.00	4.21	0.22	0.55
	After Ar^+ GCIS	1.16	0.32	0.18	0.28	0.16	0.57	0.14	0.16	1.15	2.02
In6	After Ar^+ GCIS	0.97	0.65	0.30	0.67	0.31	0.46	0.23	0.23	1.33	2.88
In7	After Ar^+ GCIS	0.90	0.84	0.32	0.93	0.35	0.38	0.34	0.30	1.05	2.75

6.1.3.2. Electronic Structure of β-$ZnTe(en)_{0.5}$ by XPS

XPS is primarily known for its efficacy in core-level chemical state analysis. However, it also serves as a powerful technique for band structure investigations. Specifically, the valence band maximum (E_v) can be accurately determined by analyzing the low binding energy region corresponding to the onset of valence band emission [64, 138, 146, 171-175].

In this study, XPS analysis was conducted to elucidate the electronic properties of β-$ZnTe(en)_{0.5}$. Prior UPS measurements exhibited metallic-like behavior (6.2.2), suggesting possible substrate interference. To mitigate this, a diameter of 55 μm iris was employed, and XPS confirmed the successful removal of substrate contributions. Nevertheless, metallic characteristics persisted in the UPS spectra, suggesting an alternative approach for the valence band maximum analysis. Figure 40 presents the XPS spectra of β-$ZnTe(en)_{0.5}$, spanning from the core level regions to the valence band maximum. To accurately determine the E_v position, a linear extrapolation of the

background signal and a separate linear extrapolation of the steep leading edge of the valence band emission were performed. The intersection of these two extrapolated lines, as depicted in Figure 40 (c) and (d), defines the location of the E_v. This method, though less accurate than the first derivative technique, provides reliable results [95].

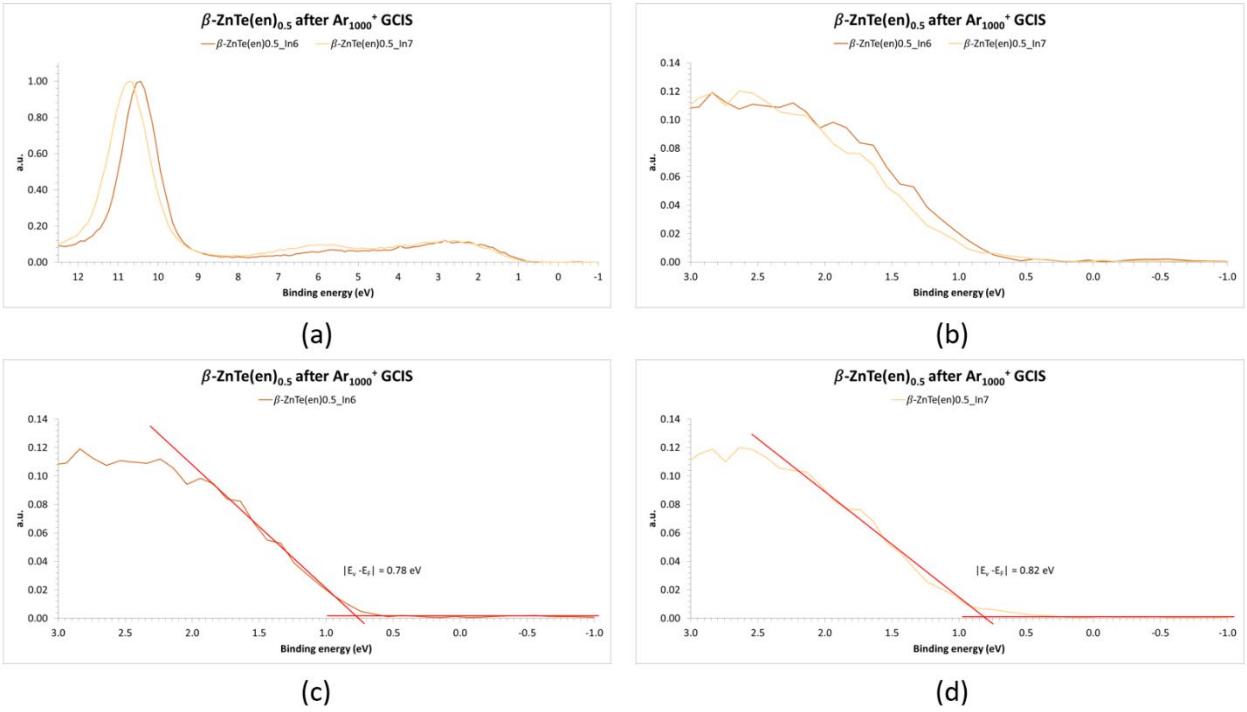

Figure 40: XPS spectra of core levels relative to the valence band maximum (E_v) of β-$ZnTe(en)_{0.5}$. (a) High-resolution XPS spectrum illustrating the overall core level features. (b) XPS spectra in the lower binding energy region, focusing on the valence band maximum (E_v) region. (c) $E_v \approx 0.78$ eV; (d) $E_v \approx 0.82$ eV: XPS spectrum detailing the E_v region for work function determination using the extrapolation approach.

The experimental determination of E_v resulted in values of 0.78 eV and 0.82 eV, indicating a 0.04 eV deviation. This deviation is considered within the acceptable range, considering the

measurement step of 0.1 eV. It is important to note that the E_v values were obtained using the aforementioned extrapolation method, which inherently carries a degree of uncertainty compared to the first derivative technique. However, the derived E_v values are deemed trustworthy. Under the XPS measurement conditions utilized, no substrate interference was detected.

The E_v was determined to be approximately 0.80 eV below the Fermi level. This placement indicates that the highest occupied electronic state resides 0.80 eV from the Fermi level. Complementary photoluminescence (PL) measurements conducted at room temperature revealed a bandgap energy of 3.55 eV for β-$ZnTe(en)_{0.5}$. Consequently, the position of the Fermi level is significantly closer to the valence band (0.80 eV) than to the conduction band (2.75 eV), calculated by subtracting the E_v energy from the bandgap energy. This disparity in energy level placement suggests p-type conductivity of β-$ZnTe(en)_{0.5}$. The proximity of the Fermi level to the valence band signifies a higher concentration of holes as majority carriers, a characteristic feature of a p-type semiconductor.

In summary, X-ray photoelectron spectroscopy (XPS) analysis was conducted on both bulk ZnTe and β-$ZnTe(en)_{0.5}$ to investigate their chemical states and electronic properties. Initially, surface contamination, primarily carbon and oxygen, was observed in both samples before Ar_{1000}^+ GCIS (Gas Cluster Ion Sputtering). Subsequently, after Ar_{1000}^+ GCIS, oxygen was largely eliminated, while residual carbon persisted.

Furthermore, the core-level spectra of Zn 2p and Te 3d revealed characteristic spin-orbit doublets. However, distinguishing between Zn, ZnTe, ZnO, and ZnO_x chemical states based solely on Zn 2p binding energies proved challenging due to overlapping energy ranges. In contrast, Te 3d spectra showed a clear reduction of TeO_x to Te involved non-oxide structures

after Ar_{1000}^{+} GCIS, evidenced by shifts to lower binding energies, changing from oxidized to reduced state.

Moreover, elemental ratios were affected by preferential sputtering of lighter elements (C, N, O) over heavier elements (Zn, Te) during Ar_{1000}^{+} GCIS. Additionally, redeposition effects, particularly in the superlattice structure of β-$ZnTe(en)_{0.5}$, further complicated quantitative analysis. Therefore, elemental ratios were interpreted qualitatively.

Finally, valence band maximum (E_v) analysis using XPS revealed an E_v of approximately 0.80 eV below the Fermi level, calculated as the average of 0.78 eV and 0.82 eV, thus confirming p-type conductivity. This finding was further supported by photoluminescence (PL) measurements, which determined a bandgap of 3.55 eV, placing the Fermi level closer to the valence band maximum.

6.2. Ultraviolet Photoelectron Spectroscopy (UPS)

6.2.1. Fundamentals of UPS

To understand the UPS spectrum generation, Figure 41 illustrates an energy-level diagram depicting the sequence of events generating a UPS spectrum for metal, with the process outlined as follows: (a) Ultraviolet photons (*hv*) excite valence band electrons above E_{VAC}, creating an approximate reflection of the valence band's energy distribution; (b) Excited electrons (photoelectrons) must first be transported to the surface before escaping, where a fraction arrive elastically, retaining their initial valence band position, while others lose kinetic energy (dependent on their transport path), leading to the formation of secondary electrons that extend from the Fermi level (E_F) to above the vacuum level; (c) The spectrometer detects photoelectrons escaping into the vacuum with kinetic energy E_{kin}, provided they possess energies above the

vacuum level, yielding an observed UPS spectrum composed of both directly emitted valence band electrons and secondary electrons [129, 147].

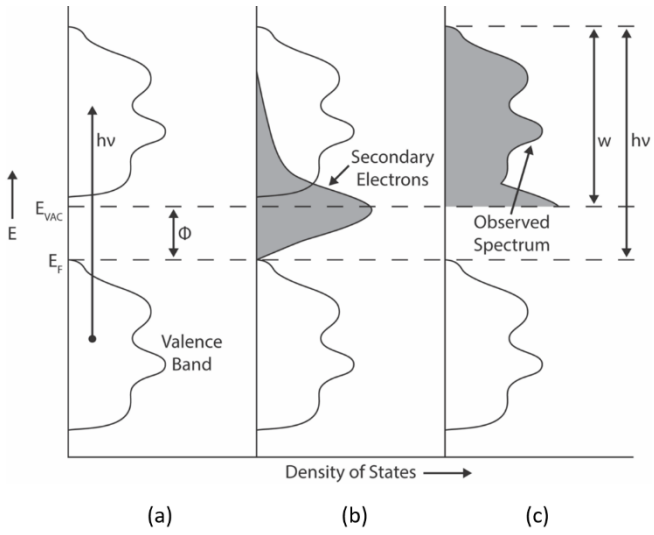

Figure 41: An energy-level diagram illustrating the sequence of events generating a UPS spectrum: (a) Incident ultraviolet photons of energy (*hv*) induce valence band electron excitation, promoting them to energy levels exceeding the vacuum level (E_{vac}); (b) In the process of transport from the bulk to the surface-vacuum interface, a portion of the excited electrons lose kinetic energy via inelastic scattering, producing secondary electrons; (c) The observed UPS spectrum is composed of both elastically emitted photoelectrons and secondary electrons with kinetic energies exceeding the vacuum level (E_{vac}) [129].

It is important to note that UPS spectra are conventionally presented with binding energy (E_B) on the x-axis, rather than kinetic energy in reverse order. This convention arises from the fact that binding energy is an intrinsic material property, remaining invariant with respect to the incident

photon energy (hv). In contrast, the kinetic energy of emitted photoelectrons is directly dependent on the photon energy of the excitation source. Moreover, while Figure 41 shares similarities with the preceding Figure 29, it provides a detailed representation of UPS spectrum construction, whereas the previous figure offered a generalized overview of PES principles. When analyzing the UPS spectrum, as shown in Figure 42, a secondary electron cutoff spectrum (E_{SECO}), measured on the higher binding energy side, corresponds to detected secondary electrons emitted from the sample surface, while the valence band maximum (E_v), measured on the lower binding energy side relative to the aligned Fermi level, provides information on the valence band electronic structure [95, 129]. Although electrical equilibrium aligns the Fermi levels of the spectrometer and sample, the resulting vacuum level offset is directly dependent on the work function (∅) difference. Modern UPS instruments mitigate this by employing automatic Fermi level alignment features, ensuring proper alignment prior to measurement. Especially, in the UPS spectrum, the lower binding energy region provides more reliable information than the higher binding energy region due to the dominance of elastically emitted photoelectrons at E_v, whereas inelastically scattered secondary electrons prevail at E_{SECO}, particularly within the spectral region extending to the vacuum level [129].

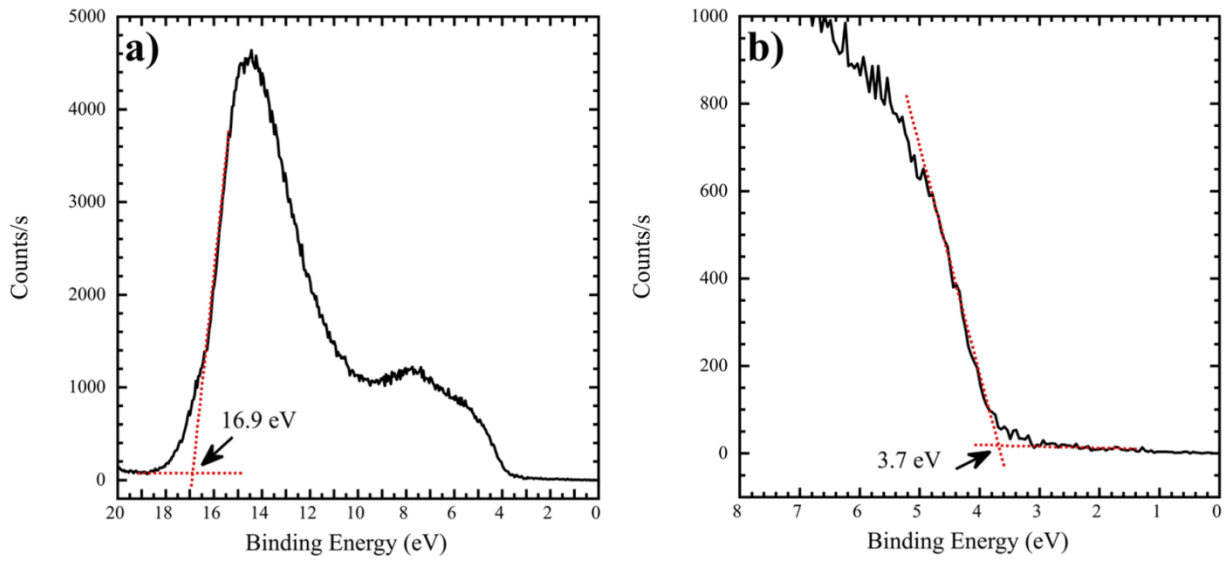

Figure 42: UPS measurements of sputter-cleaned TiO_2 (110) at room temperature using He I (hv = 21.2 eV): a) E_{SECO} determination relative to the Fermi level (E_F); b) expanded view near the E_F for valence band maximum (E_v) determination [129].

It is worth noting that UPS is a preferred technique for work function determination, primarily attributed to its high energy resolution in the valence band region, which enables precise measurement of emitted electron kinetic energies following photon absorption [140, 146, 147]. For quantitative analysis, in UPS analysis, the valence band maximum binding energy, $|E_F - E_V|$, and the secondary electron cutoff can be determined by finding the intersection of extrapolations of the parallel background extrapolation and two steep extrapolations (one from the lower and the other from the higher binding energy side), with the region between these steep extrapolations representing the actual density of states of the sample [64, 94, 95, 138, 140, 146]. Moreover, the minimum absolute work function, an intrinsic property of the surface, is determined by this technique, which is independent of all experimental parameters except the

ultraviolet photon energy [180]. Although this approach has lower accuracy compared to the first derivative method, it is commonly employed in the literature and provides dependable results [95,126-130, 135, 138, 140, 147]. Furthermore, to simplify E_{SECO} determination in UPS, the midpoint of the high binding energy side's steep line, provided its width is below 0.2 eV, can be used, eliminating the necessity for a parallel baseline and differing by only 0.1 eV from other established methodologies [138].

The work function of metals or semiconductors can be determined by,

$$\emptyset = h\nu - (E_{SECO} - E_F) \quad \text{Eq. 78}$$

where $h\nu$ is the photon energy, h is Planck's constant (6.626×10^{-34} J·s), ν is the frequency of incident photons, and E_F is mostly aligned to the binding energy of 0 eV [95, 129].

In non-metallic samples such as semiconductors, the ionization energy can be calculated by using the following equation [95].

$$IE = h\nu - (E_{SECO} - E_v) \quad \text{Eq. 79}$$

Although UPS measurements are generally reliable for homogeneous samples (e.g., clean metal surface) and published work functions are often macroscopically averaged, it is recognized that variations in work function arise from differing crystal orientations. However, the analysis of heterogeneous samples, inhomogeneous surfaces, and nanostructured materials presents significant challenges due to existing uncertainty in the fundamental understanding of work function determination [94, 147]. Moreover, work function variations are commonly observed, with deviations often arising when using different measurement techniques [146, 167].

In addition to crystal orientation and sample homogeneity, altering the surface conditions influences the work function, independent of the orientations and polymorph; while the Fermi level and the vacuum level can be independently adjusted through doping, surface space-charge

layers, or the surface dipole, these adjustments do not affect the ionization energy (± 0.15 eV) [94, 138].

Despite both UPS and XPS providing valence band spectra, UPS excels in surface defect detection due to its enhanced surface sensitivity, resulting from lower photon energies and yielding higher signal intensities in the valence band [138, 140].

6.2.2. Experimental Results of UPS on bulk ZnTe and β-ZnTe(en)$_{0.5}$

As a reference material to facilitate analysis and enhance the understanding of the properties of β-ZnTe(en)$_{0.5}$, bulk ZnTe was mounted on the sample holder and secured with copper plates and screws to ensure good electrical conduction. Figure 43 illustrates the wide UPS spectrum of bulk ZnTe, which clearly exhibits key spectral features, including the secondary electron cutoff (E_{SECO}), the valence band maximum (E_v), and the Fermi level (E_F) of bulk ZnTe, providing a comprehensive overview of its electronic structure. Additionally, the plot includes the individual UPS spectra of bulk ZnTe 2 and bulk ZnTe 3, along with their average spectrum.

As depicted in Figure 43, E_{SECO} is located in the higher binding energy region, whereas E_v is situated in the lower binding energy regions relative to the E_F, which is aligned to a binding energy of 0 eV. Furthermore, the E_v region yields more reliable data compared to the E_{SECO} region due to the predominance of elastically emitted photoelectrons in the vicinity of E_v, while inelastically scattered secondary electrons dominate proximate to E_{SECO}, especially near the vacuum level [129].

The presence of a minor feature in the E_{SECO} region of the UPS spectrum may indicate inhomogeneous conductivity, which introduces complications. This hypothesis is strengthened by the effective surface cleaning achieved using Ar_{1000}^+ GCIS. However, while alternative

factors could contribute to this observation, they do not appear to significantly impact the determination of the E_{SECO}.

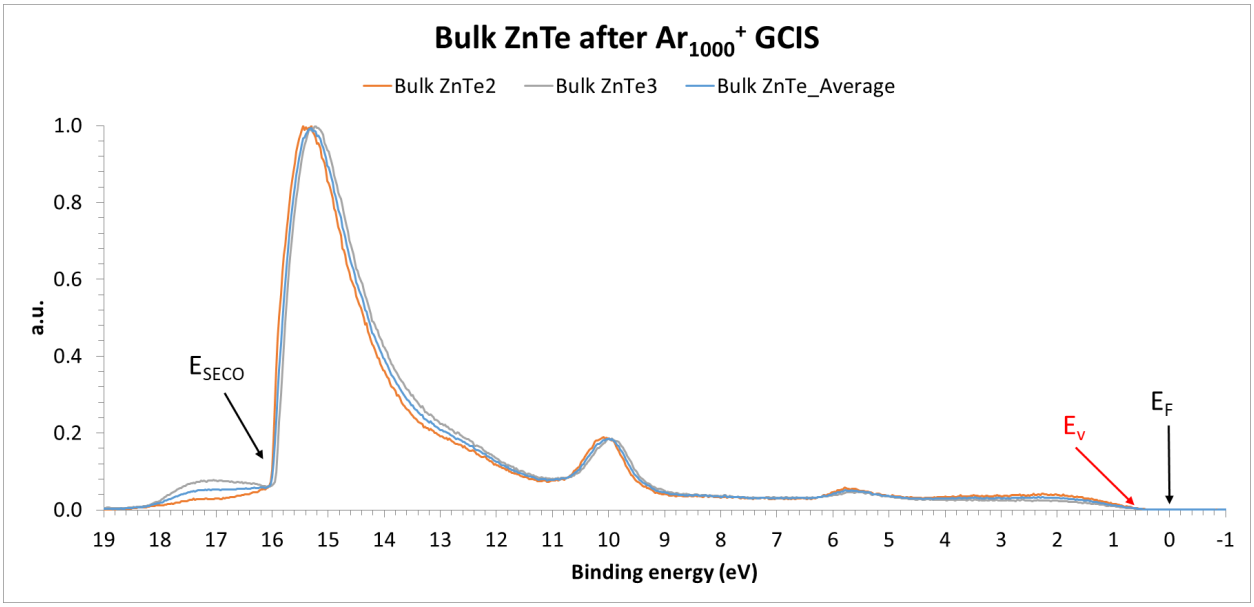

Figure 43: Wide UPS spectrum of bulk ZnTe, showing the second electron cutoff (E_{SECO}), the valence band maximum (E_v), and the Fermi level (E_F), with an average spectrum.

Figure 44 presents high-resolution UPS spectra of bulk ZnTe, illustrating the determination of the E_{SECO} and E_v locations using extrapolation approach: (a) Lower binding energy region of bulk ZnTe spectra from two locations and their average; (b) Higher binding energy region of bulk ZnTe spectra from two locations and their average; (c) Lower binding energy region of bulk ZnTe2 spectrum; (d) Higher binding energy region of bulk ZnTe2 spectrum; (e) Lower binding energy region of bulk ZnTe3 spectrum; (f) Higher binding energy region of bulk ZnTe3 spectrum.

To establish the electronic properties of these samples, the valence band maximum (E_v), secondary electron cutoff (E_{SECO}), and work function (∅) were determined. For bulk ZnTe2, the

E_v was determined to be 0.50 ± 0.05 eV below the E_F, E_{SECO} was measured at 16.00 ± 0.05 eV, and the work function was calculated to be 5.20 eV using Eq. 78. Similarly, for bulk ZnTe3, E_v was also located 0.50 ± 0.05 eV below the E_F, E_{SECO} measured at 16.05 ± 0.05 eV, and a work function was calculated to be 5.15 eV using Eq. 78. Both E_{SECO} and E_v values will have a combined standard deviation of 0.05 eV, which is reasonable for both E_{SECO} and E_v, considering instrument resolution, extrapolation fitting uncertainty, and human judgment. The work function of bulk ZnTe was determined to be approximately 5.175 ± 0.035 eV using simple arithmetic. The spectra used to generate the average in Figure 44 (a) and (b) were acquired from two distinct locations on an identical bulk ZnTe sample, revealing highly similar results. However, a minor deviation of 0.05 eV was observed in the E_{SECO} values between these two locations, which is considered relatively small and likely attributable to inhomogeneous conductivity or measurement uncertainties. Importantly, both spectra exhibited identical E_v values, indicating no significant sample inconsistency. Furthermore, while the 0.05 eV deviation in E_{SECO} may arise from the employed extrapolation method, known for its lower accuracy compared to the first derivative technique, it does not substantially affect the determination of the work function (Ø), remaining within the range of experimental uncertainty.

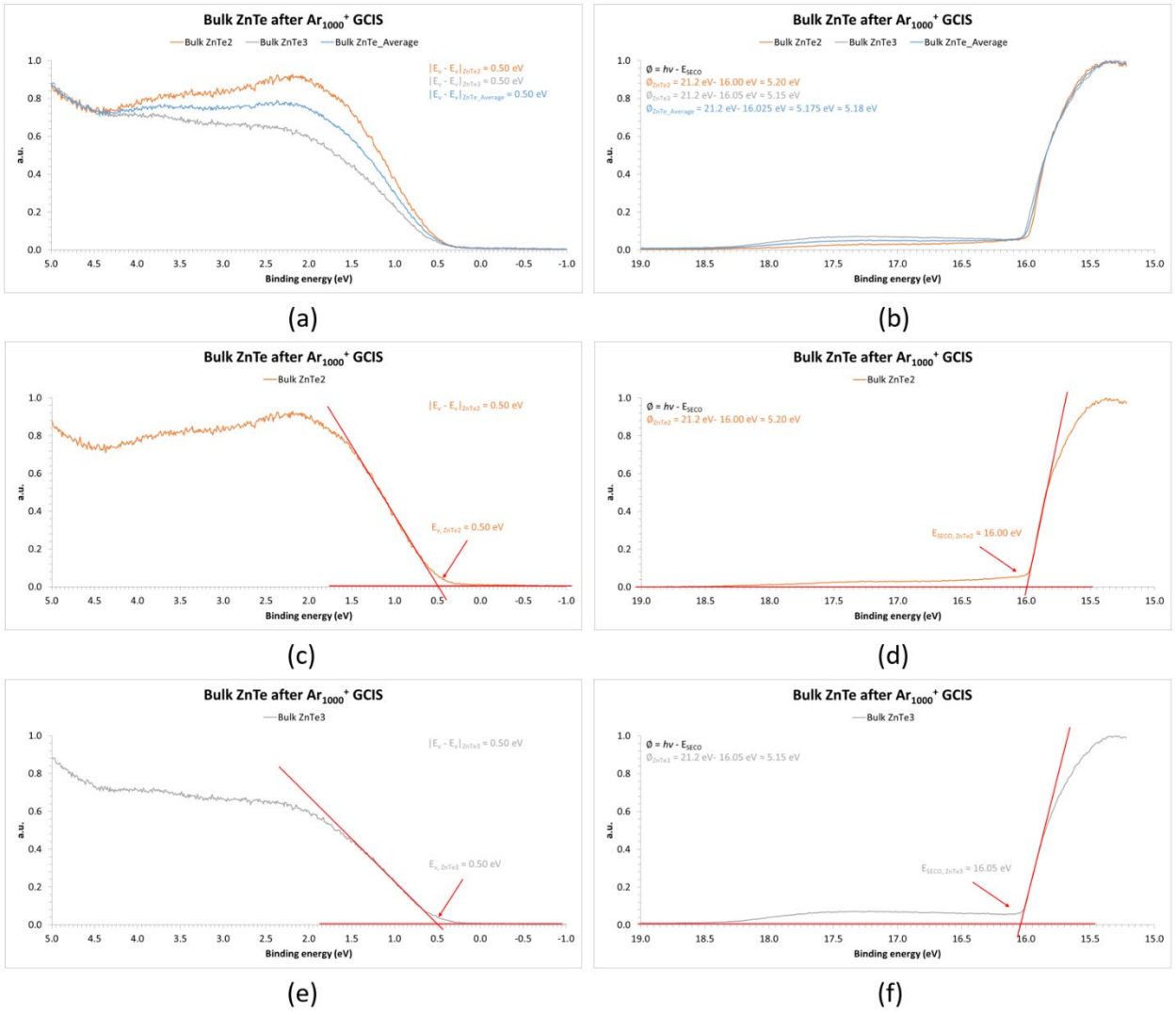

Figure 44: High-resolution UPS spectra of bulk ZnTe, illustrating the determination of the second electron cutoff (E_{SECO}) and the valence band maximum (E_v) locations via extrapolation approach. (a) lower binding energy region of bulk ZnTe2, bulk ZnTe3, and their average, (b) higher binding energy region of bulk ZnTe2, bulk ZnTe3, and their average, (c) lower binding energy region of bulk ZnTe2, (d) higher binding energy region of bulk ZnTe2, (e) lower binding energy region of bulk ZnTe3, (f) higher binding energy region of bulk ZnTe3.

Figure 45 illustrates the wide UPS spectra of β-ZnTe(en)$_{0.5}$ on two different substrates: (a) gold thin film on silicon (Au/Si) and (b) indium (In) substrate. While these spectra successfully exhibit the secondary electron cutoff (E_{SECO}) and the Fermi level (E_F), a significant challenge arises from the absence of an observable valence band maximum (E_v). This absence created a problem, as it prevented a complete assessment of β-ZnTe(en)$_{0.5}$'s electronic properties. Without the E_v, there is a risk of incorrectly interpreting ZnTe(en)$_{0.5}$ as metallic, rather than semiconducting.

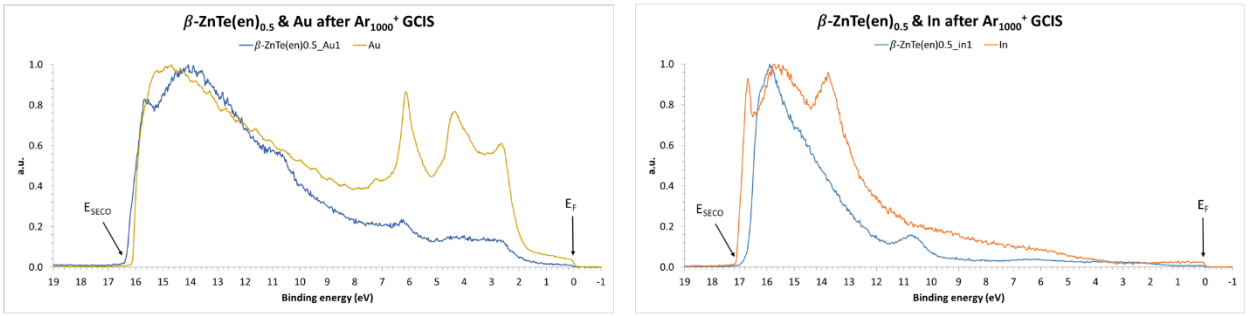

(a) (b)

Figure 45: Wide UPS spectra of β-ZnTe(en)$_{0.5}$ on two different substrates: (a) gold thin film on silicon (Au/Si) and (b) indium (In) substrate. The spectra show the second electron cutoff (E_{SECO}) and the Fermi level (E_F), along with individual UPS spectra of the (a)Au and (b) In.

Figure 46 shows high-resolution UPS spectra of β-ZnTe(en)$_{0.5}$ on an Au/Si substrate and gold substrates, demonstrating the determination of the secondary electron cutoff (E_{SECO}) using the extrapolation approach. This method allows for the precise identification of the E_{SECO}, a key feature used to derive the work function and understand the surface electronic behavior of β-ZnTe(en)$_{0.5}$.

Figure 46 (a) presents a comprehensive compilation of UPS data. It includes five distinct UPS spectra of β-ZnTe(en)$_{0.5}$ on an Au/Si substrate, their arithmetically calculated average, and the UPS spectrum of the bare gold substrate. This configuration allows for a direct comparison between individual measurements and their average, thus enabling a rigorous evaluation of experimental reproducibility. The work function values, derived from the E_{SECO} positions, are as follows: (b) β-ZnTe(en)$_{0.5}$_Au1: approximately 4.72 eV, (c) β-ZnTe(en)$_{0.5}$_Au2: approximately 4.70 eV, (d) β-ZnTe(en)$_{0.5}$_Au3: approximately 4.73 eV, (e) β-ZnTe(en)$_{0.5}$_Au4: approximately 4.68 eV, (f) Gold substrate (Au): approximately 5.08 eV. The work function of β-ZnTe(en)$_{0.5}$ was determined to be approximately 4.71 ± 0.022 eV through simple arithmetic.

The observed work function of gold, 5.08 eV, is in excellent agreement with the reported values [38, 95, 167, 180]. However, while the work function of gold can be significantly varied by surface conditions, a reported value of 4.82 eV lacks context owing to the absence of information regarding surface treatment [181].

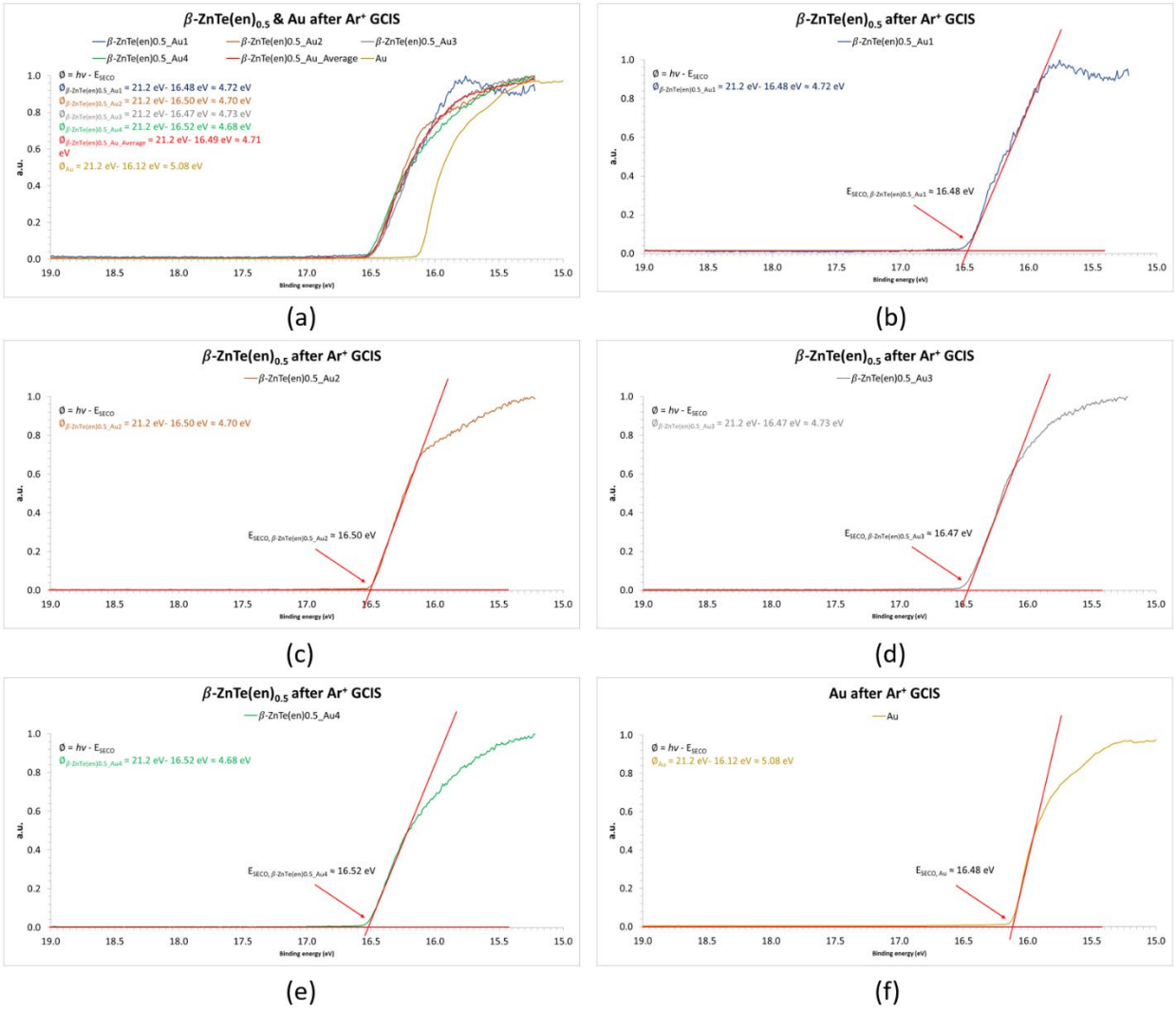

Figure 46: High-resolution UPS spectra of β-ZnTe(en)$_{0.5}$ on Au/Si substrate and gold (Au) substrate, illustrating the determination of the second electron cutoff (E_{SECO}) using the extrapolation approach. (a) Combined UPS spectra of β-ZnTe(en)0.5 on Au/Si substrate, including all five individual datasets, the calculated average, and the gold substrate spectrum. The work function derived from the E_{SECO} are: (b) $\emptyset_{\beta\text{-ZnTe(en)0.5\_Au1}} \approx 4.72$ eV, (c) $\emptyset_{\beta\text{-ZnTe(en)0.5\_Au2}} \approx 4.70$ eV, (d) $\emptyset_{\beta\text{-ZnTe(en)0.5\_Au3}} \approx 4.73$ eV, (e) $\emptyset_{\beta\text{-ZnTe(en)0.5\_Au4}} \approx 4.68$ eV, (f) $\emptyset_{Au} \approx 5.08$ eV.

Figure 47 presents high-resolution UPS spectra of β-ZnTe(en)$_{0.5}$ on indium (In) substrate and In foil substrate, demonstrating the determination of the secondary electron cutoff (E_{SECO}) using the extrapolation approach. Through this method, accurate determination of the E_{SECO} is achieved, a crucial step in deriving the work function and thus revealing the surface electronic properties of β-ZnTe(en)$_{0.5}$.

Figure 47 (a) provides a combined UPS spectra of two distinct UPS spectra of β-ZnTe(en)$_{0.5}$ on In foil substrate, their average, and the bare indium foil substrate. This arrangement allows for a direct comparison between individual measurements and their average, thereby enabling an evaluation of experimental reliability. Derived from the E_{SECO} positions, the work function values are: (b) $\emptyset_{\beta\text{-ZnTe(en)0.5\_In1}} \approx 4.52$ eV, (c) $\emptyset_{\beta\text{-ZnTe(en)0.5\_In3}} \approx 4.45$ eV, (d) $\emptyset_{In} \approx 4.10$ eV. The observed work function of indium is in excellent agreement with the reported value, 4.09 eV [89].

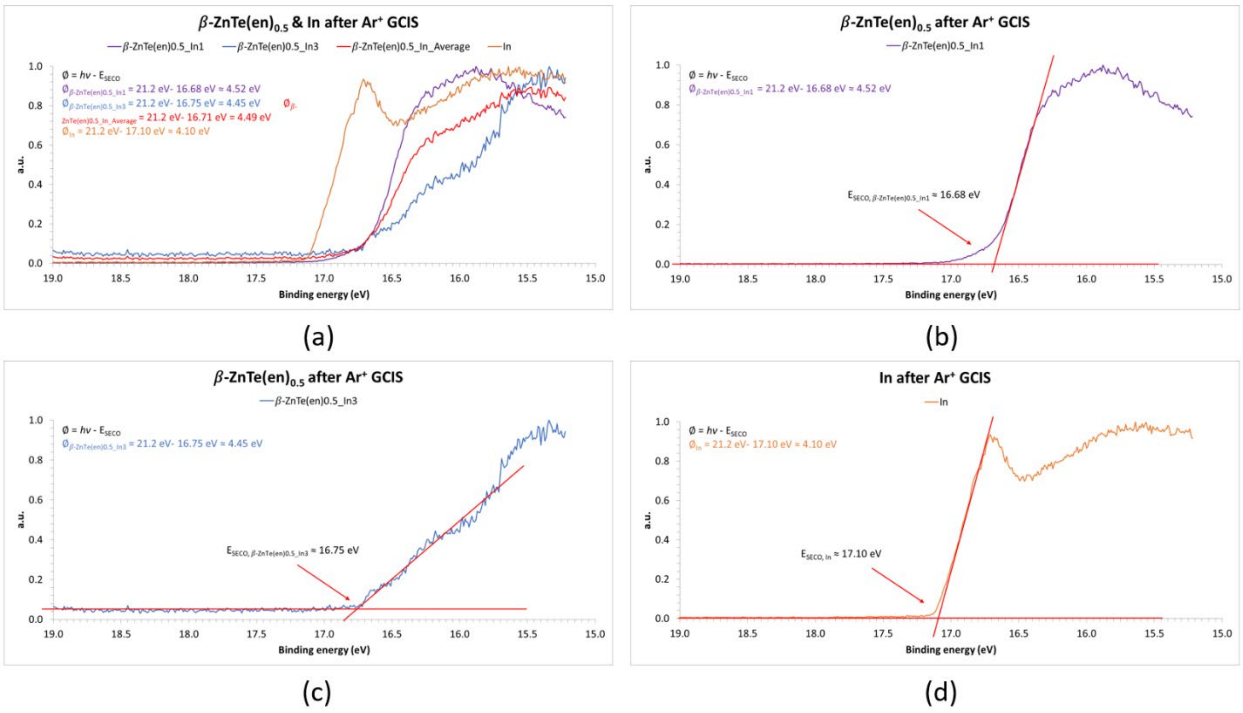

Figure 47: High-resolution UPS spectrum of β-ZnTe(en)$_{0.5}$ on indium (In) substrate and In foil substrate, illustrating the determination of the second electron cutoff (E_{SECO}) using the extrapolation approach. (a) Combined UPS spectra of β-ZnTe(en)0.5 on In foil substrate, including two individual datasets, the calculated average, and the indium foil substrate spectrum. The work function derived from the E_{SECO} are: (b) $\emptyset_{\beta\text{-ZnTe(en)0.5\_In1}} \approx 4.52$ eV, (c) $\emptyset_{\beta\text{-ZnTe(en)0.5\_In3}} \approx 4.45$ eV, (d) $\emptyset_{In} \approx 4.10$ eV.

The electronic properties of β-ZnTe(en)$_{0.5}$ present a complex picture, demanding careful analysis of both UPS and XPS data. Initially, UPS spectra suggested metallic-like behavior, with the valence band edge (E_v) appearing near the Fermi level (E_F). However, a distinct E_v is clearly observed in the XPS spectrum of Figure 40, contradicting this initial interpretation and necessitating further investigation.

To understand this discrepancy, it is crucial to recognize the fundamental differences between UPS and XPS. UPS, utilizing 21.2 eV photons, probes valence electrons and is highly surface-sensitive (1-3 nm). In contrast, XPS, employing 1486.6 eV photons, excites core electrons and probes deeper (1-10 nm). Furthermore, β-ZnTe(en)$_{0.5}$ is a superlattice nanostructure with a thickness of 6-10 μm and approximate macroscopic lateral dimensions (500 μm x 100 μm), significantly exceeding the probing depths of both techniques.

Interestingly, the work function of β-ZnTe(en)$_{0.5}$ measured by UPS varies with the substrate's work function, indicating substrate influence. Specifically, UPS spectra show that when the substrate has a higher work function, the sample's apparent work function increases, and vice versa. In contrast, XPS shows no such substrate signature.

To examine the substrate interference in the UPS data, the individual UPS spectra of the Au/Si and In foil substrates were included for comparison in Figure 45. Indeed, no substrate features are observed in the lower binding energy region. However, it is noteworthy that certain wide UPS spectra exhibited almost identical features in this region. Moreover, upon close examination of Figure 45 (a), it shows that the E_{SECO} of β-ZnTe(en)$_{0.5}$ is located at a higher binding energy than that of gold. On the other hand, in Figure 45 (b), the E_{SECO} of β-ZnTe(en)$_{0.5}$ is situated at a lower binding energy relative to indium. Based on this data, it can be hypothesized that the work function of β-ZnTe(en)$_{0.5}$ is in between the work functions of the gold and indium foil substrates. The substrate influence observed in UPS, despite the significant thickness of β-ZnTe(en)$_{0.5}$, indicates a need for further explanation. One potential explanation is that the X-ray and UV radiation sources are not perfectly aligned with the collection path, as shown in Figure 48. For accurate detection, both sources must illuminate the same area on the sample. Therefore, even a small misalignment can produce detrimental results, challenging data interpretation. Given that

no substrate information is observed with XPS under identical experimental conditions, source alignment becomes a critical factor. Additionally, high-resolution XPS valence spectra reveal clear valence band maximum values in Figure 40.

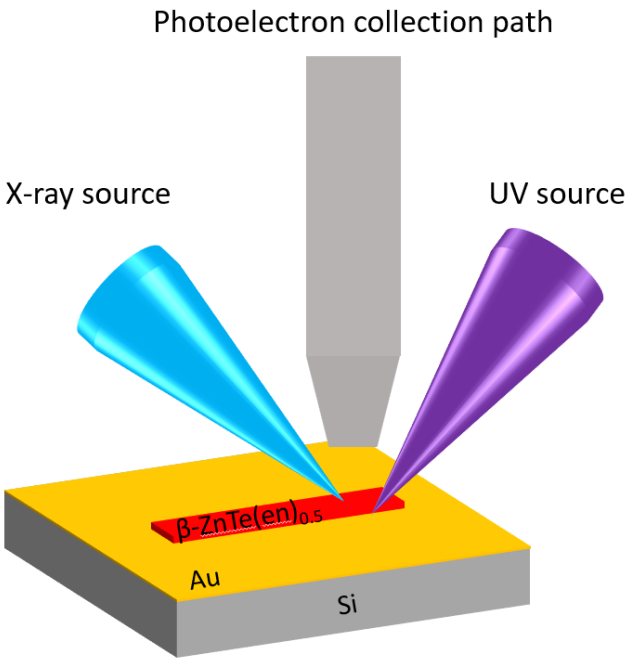

Figure 48: Schematic diagram depicting the arrangement of X-ray and UV radiation sources in an XPS/UPS instrument, with the sources deliberately misaligned with the photoelectron collection path to highlight the critical role of source alignment and collection optics in capturing and redirecting emitted photoelectrons to the detector.

It is well-established that the E_v region typically provides more reliable data than the E_{SECO} region. This is due to the predominance of elastically emitted photoelectrons near E_v, while inelastically scattered secondary electrons dominate near E_{SECO}, especially near the vacuum level [129]. Thus, the E_v region is crucial for accurately determining the bandgap energy and valence band features.

Furthermore, given that the electron mean free path at these low kinetic energies (He I at 21.2 eV) is very short, substrate photoelectrons should not reach the detector unless there are cracks in β-ZnTe(en)$_{0.5}$. Consequently, the data suggests a convolution of signals in the UPS spectrum, potentially reflecting a weighted average of bulk and surface contributions.

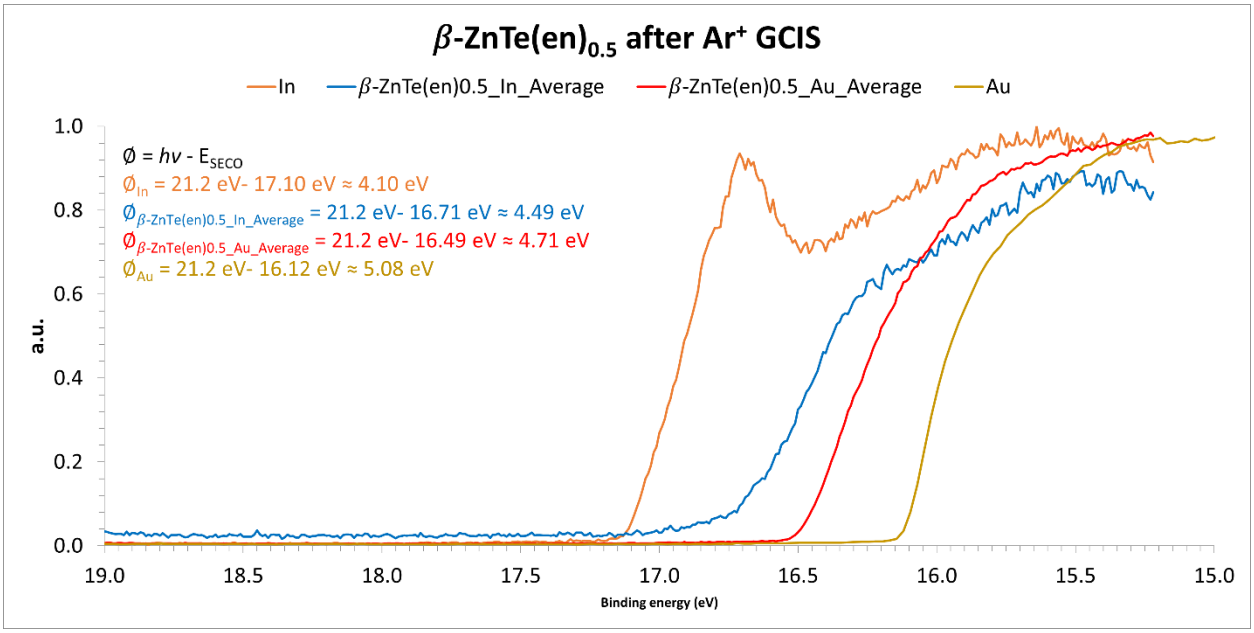

Figure 49: Substrate-dependent work function of β-ZnTe(en)$_{0.5}$. Measured values range from 4.49 eV (on In foil substrate) to 4.71 eV (on Au/Si substrate), indicating the actual work function lies within this range.

In summary, Ultraviolet Photoelectron Spectroscopy (UPS) was used to determine the valence band maximum (E_v), secondary electron cutoff (E_{SECO}), and work function (Ø) of bulk ZnTe. Two measurements yielded highly consistent results, with Ev at 0.50 eV below the Fermi level (E_F) (determined by the work function of the instrument Au) and work functions of 5.20 eV and 5.15 eV, averaging to 5.175 ± 0.025 eV. A minor 0.05 eV deviation in E_{SECO}, likely attributable to sample inhomogeneity or measurement uncertainty, did not significantly affect the work

function determination. Although work function ($\emptyset$) values are not directly provided, the work function of ZnTe can be calculated using the reported electron affinity (χ), bandgap energy (E_g), and ionization energy (IE). The bandgap energy values were identical, but the electron affinity and ionization energy values differed by approximately 0.1 eV, resulting in a 0.1 eV difference in the calculated work function [84-87]. Moreover, a literature value deviates from the observed data by approximately 0.05 eV [88]. The consistency of the observed data with literature values, despite the component value variations, indicates the reliability of the observed data.

UPS of β-ZnTe(en)$_{0.5}$ showed no clear valence band maximum, hindering accurate electronic property determination. This contrasts with XPS, which revealed a distinct E_v (Figure 40). The discrepancy stems from UPS's surface sensitivity and potential signal convolution, while XPS probes deeper and offers more reliable E_v data.

Furthermore, the work function of β-ZnTe(en)$_{0.5}$ exhibited substrate-dependent variations, with the average work function on the Au/Si substrate determined to be 4.71 eV, and on the In foil substrate, 4.49 eV. Therefore, the presence of substrate-related features within the UPS spectra strongly suggests that the actual work function of β-ZnTe(en)$_{0.5}$ resides within the range of 4.49 eV to 4.71 eV, as shown in Figure 49. However, this conclusion is not definitive and requires further investigation. To address this unresolved question and provide conclusive evidence, it is recommended that complementary experimental techniques be employed.

CHAPTER 7: KELVIN PROBE FORCE MICROSCOPY (KPFM)

7.1. Fundamentals of KPFM

Kelvin probe force microscopy (KPFM) is a highly sensitive technique used to quantify the local contact potential difference (CPD) between a conductive atomic force microscopy (AFM) tip and a sample surface [94, 98, 99, 179, 180, 181, 182]. Specifically, KPFM enables the acquisition of high spatial resolution maps of morphology, work function, and surface potential [58, 179]. Indeed, KPFM has evolved from a specialized method for characterizing nanoscale electronic/electrical properties of metal/semiconductor surfaces and devices to a versatile technique capable of imaging potential distributions on organic and biological materials with sub-nanometer resolution, establishing it as a premier tool for electrical characterization of nanostructures [179, 182]. By leveraging the modification of local contact potential by trapped charge carriers, Kelvin probe force microscopy (KPFM) has proven invaluable in determining trap origins and their spatial distributions, especially in examining the impact of grain boundaries on charge carrier trapping in organic thin films [58].

Several factors, including work function, adsorption layers, oxide layers, doping concentration, and temperature fluctuations, influence the CPD quantified by KPFM [98]. In particular, the fundamental principle of KPFM relies on the electrostatic interaction arising from the difference in work functions ($\Delta\emptyset_{\text{tip \& sample}} \neq 0$) between the AFM tip ($\emptyset_{\text{tip}}$) and the sample ($\emptyset_{\text{sample}}$) [99, 179]. This work function difference leads to the CPD, the primary output from KPFM measurement, used to generate surface potential maps or determine local work functions, and this CPD is [179, 180].

To understand this process, consider the following: When the AFM tip and sample are electrically connected via the KPFM circuit, their Fermi levels equilibrate through electron

transfer from the material with the lower work function to that with the higher work function [99, 180]. This charge transfer establishes a potential difference, the CPD, which can be determined using the following equation [179],

$$V_{CPD} = \frac{\emptyset_{tip} - \emptyset_{sample}}{-e} \quad \text{Eq. 80}$$

where e is an elementary charge [99].

Figure 50 shows a schematic representation of electronic energy levels, demonstrating three cases of AFM tip and sample interactions, illustrating the principles of contact potential difference: (a) The AFM tip and the sample surface are physically separated by a finite distance, denoted as d, ensuring no direct electron transfer pathway and maintaining electrical discontinuity, while the vacuum levels are aligned but the Fermi levels remain misaligned due to the work function difference between the sample and the AFM tip; (b) Upon electrical contact, the CPD, generated by the work function difference between the AFM tip and the sample, initiates electron transfer from the sample with a lower work function to the AFM tip with a higher work function, resulting in Fermi level alignment through uniform electron redistribution while simultaneously creating a misalignment of vacuum levels; (c) The CPD between the AFM tip and the sample is nullified by introducing an external bias ($|V_{DC}| = |\Delta\emptyset_{tip\ \&\ sample}| = |V_{CPD}|$), thereby creating an opposing potential that forces the vacuum levels of the tip and sample to align, effectively eliminating the CPD-induced potential offset; accordingly, the work function of the sample ($\emptyset_{sample}$) can be determined if the AFM tip work function ($\emptyset_{tip}$) is known [99, 179].

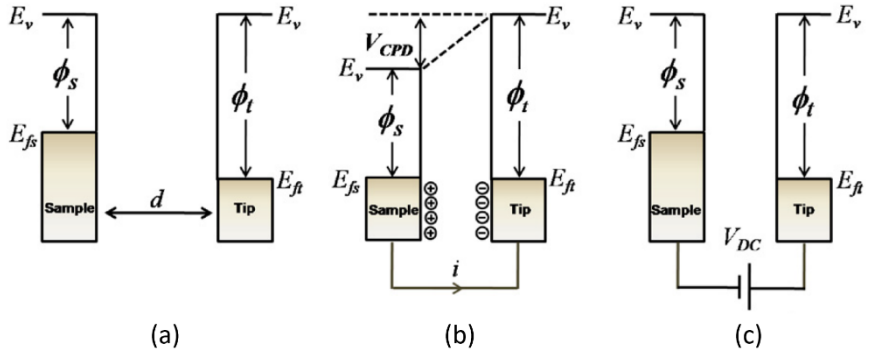

Figure 50: Schematic representation of electronic energy levels illustrating the contact potential difference (CPD) [179]. E_v represents the vacuum level, E_{fs} is the Fermi level of the sample, E_{ft} is the Fermi level of the AFM tip. (a) The AFM tip and sample are spatially separated by a distance d, maintaining electrical discontinuity. (b) A contact potential difference, resulting from the work function difference between the AFM tip and sample, is generated upon electrical contact. (c) An external bias ($|V_{DC}| = |\Delta\emptyset_{tip\ \&\ sample}| = |V_{CPD}|$) is applied between the AFM tip and sample to counteract the CPD, resulting in the alignment of their respective vacuum levels.

Given a known AFM tip work function, the sample's work function can be determined through the rearrangement of Eq. 80 [180].

$$\emptyset_{sample} = \emptyset_{tip} - e \cdot V_{CPD} \qquad \text{Eq. 81}$$

As a result, the magnitude of the applied voltage (V_{DC}), specifically the bucking voltage, plays a pivotal role in the accurate determination of the sample's work function [99]. Furthermore, the work function exhibits exceptional sensitivity to surface characteristics, thereby making it a valuable probe of environmental influences, given that surface contaminants can induce substantial variations in the energy necessary to extract an electron from the Fermi level [180].

In practice, KPFM employs AFM principles, which include contact, amplitude modulation (AM), and frequency modulation (FM) modes, for surface potential measurements [179, 182]. While contact-mode KPFM measures surface topography via direct tip contact, AM-KPFM (tapping mode) and FM-KPFM (non-contact mode) use cantilever oscillation and detect amplitude or frequency changes, respectively [179]. Generally, AM-KPFM provides higher energy resolution (~5 meV) compared to FM-KPFM (~10–20 meV) due to its signal-to-noise ratio [179, 182]. In contrast, FM-KPFM offers superior accuracy in surface potential measurements compared to AM-KPFM, primarily due to FM-KPFM's enhanced sensitivity to the electrostatic force gradient directly beneath the probe tip (while maintaining a constant amplitude of cantilever oscillation), which minimizes spatial averaging and improves spatial resolution, thereby mitigating the incorrect surface potential values associated with AM-KPFM's cantilever contribution [179]. Despite this, AM-KPFM can still achieve atomic-scale resolution, though both modes are limited at sub-nanometer scales [179, 181].

For optimal performance, high-resolution KPFM demands atomically sharp and conductive AFM tips, with tip selection dictating resolution, stability, and preparation complexity, thereby necessitating optimization based on specific experimental parameters [179]. Moreover, the accuracy of the sample work function determination via KPFM directly relies upon the precision of the reference work function value ($\emptyset_{tip}$); any uncertainty in the reference adversely affects the measured sample work function [180].

However, KPFM has limitations: it requires probe work function calibration, compromising measurement accuracy due to sample exchange; it averages surface potential, unable to distinguish contributions from band bending and surface dipoles; topographic height changes can disrupt measurements because of capacitance gradient effects; and it's slow due to simultaneous

topography and potential mapping, risking cross-talk [98, 179]. Additionally, the combined substantial influence of the substrate, charge carrier concentration changes, and other contributing effects on charge transfer to 2D materials, which alters the surface potential, causes KPFM to encounter significant challenges in accurately quantifying surface potential differences between layers in 2D material, particularly between monolayer and bilayer graphene, making layer-to-layer comparisons unreliable [181].

Despite these limitations, the ability to perform CPD measurements via KPFM in dark conditions provides a distinct advantage over PES for the evaluation of semiconductor surfaces where band bending is susceptible to surface photovoltage effects [94]. Furthermore, while KPFM enables the determination of work function, the combined use of PES and IPES provides a comprehensive analysis of the electronic structure [94, 128]. Nevertheless, PES, unlike KPFM, provides full spectral distribution, allowing separate determination of band bending and surface dipoles, and is not affected by tip-sample distance [179].

While KPFM typically yields higher work function values than UPS due to its averaging of the work function difference under the probe, as opposed to UPS's measurement of the lowest work function, an exception arises in the presence of polar adsorbates, where under ambient conditions, the gold work function can be reduced by up to 0.4 eV due to the physisorption of surface adsorbates, especially polar molecules [180, 182]. In terms of spatial resolution, KPFM exhibits a significant advantage over PES, while demonstrating comparable sensitivity [179, 182]. Moreover, UPS work function measurements are limited to a macroscopic lateral resolution, whereas KPFM enables work function mapping with sub-nanometer precision [182]. Unlike UPS, which is typically conducted under ultra-high vacuum (UHV) conditions to minimize surface contamination and ensure accurate electron detection, thus mitigating

atmospheric gas interference, KPFM is frequently employed in ambient environments, where surface adsorbates and humidity exert a substantial influence on the measured surface potential, thereby impacting work function determination [180, 182].

7.2. Experimental Results

Determining the work function of a sample using Eq. 81 is simplified when the work function of the atomic force microscopy (AFM) tip is known. However, AFM tip manufacturers typically do not provide this information. Therefore, it is common practice to use well-defined work function materials, such as gold or highly oriented pyrolytic graphite (HOPG) because of their stability, flatness, and established work function values [99, 180-182, 184, 185]. Despite their widespread use, the reported work function of HOPG exhibits variability [185]. A reliable work function value for HOPG in ambient conditions is 4.475 ± 0.005 eV [182, 184]. This variability is attributed to spatial heterogeneity and temporal evolution of the HOPG work function, as observed by Kelvin probe force microscopy (KPFM) [185].

While gold or HOPG are frequently employed as reference substrates, muscovite mica (Highest Grade Mica Sheets, Prod# 56-15, Ted Pella, INC) is also a suitable substrate for KPFM. For sample preparation, a mica sheet was placed onto a circular metal sample holder, a puck with a diameter of approximately 15 mm. Pristine β-$ZnTe(en)_{0.5}$ was then carefully positioned onto the mica surface using a vacuum pen. Methanol was used as a temporary adhesive to secure the sample to the mica sheet, ensuring stability during the measurement. The sample holder was subsequently transported to the KPFM stage of an Innova KPFM system (Bruker). The KPFM analysis was then conducted in ambient atmospheric conditions, reflecting typical laboratory settings.

KPFM enables the concurrent acquisition of topographical and surface potential data [98, 179]. Data collection was performed using a raster scanning technique, capturing information during both forward and reverse line movements. Topographical data, obtained from the forward scan, was acquired in tapping mode, where tip-sample interactions are dominated by atomic forces. Subsequently, surface potential data was acquired during the reverse scan in non-contact mode. In this mode, the AFM tip was lifted to a predetermined distance, determined by an inter-atomic force vs. distance curve, ensuring that electrostatic forces, rather than atomic forces, primarily governed the tip-sample interaction [179]. Thus, this dual-scan approach enabled the concurrent acquisition of topographical and surface potential information.

Figure 51 presents the results of KPFM measurements conducted in the absence of light. It shows: (a) an optical image, (b) a topographical spatial map, and (c) a work function spatial map of β-ZnTe(en)$_{0.5}$, both acquired from the same location. The measurement area was initially set to 5 μm x 5 μm; however, instabilities in the data, likely due to the heterogeneous topography of β-ZnTe(en)$_{0.5}$, required the left side of the topographical (b) and work function maps (c) to be cropped to ensure reliable data, leaving a final measurement area of 4 μm x 5 μm.

Prior to measurement, an optically clean region was selected based on visual inspection. To quantify the overall work function of β-ZnTe(en)$_{0.5}$, an average value, 4.59 ± 0.03 eV, was computed by summing the work function values of each data pixel in the image and dividing by the total number of pixels.

Before presenting the detailed results, it is crucial to acknowledge that UPS and KPFM utilize different measurement principles, leading to potentially non-identical work function values, with UPS measuring the minimum and KPFM an area average. [89, 180]. UPS measurements, as presented in Figure 49 indicate that the work function of β-ZnTe(en)$_{0.5}$ falls within the range of

4.49 eV to 4.71 eV. This finding is corroborated by KPFM data, which determined the work function of β-ZnTe(en)$_{0.5}$ to be 4.59 ± 0.03 eV, confirming its value within the UPS-derived range. Therefore, this shows that even with the differences in measurement techniques, both techniques show very similar results.

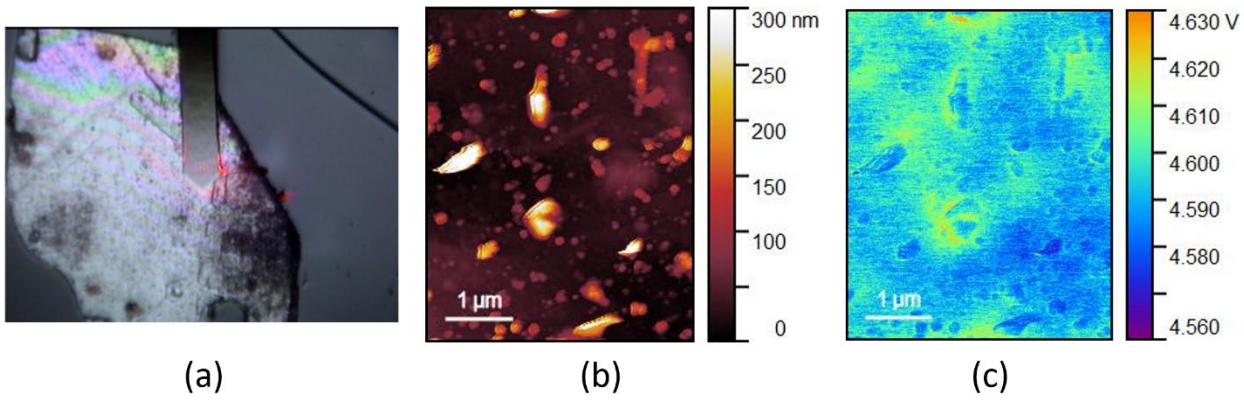

Figure 51: KPFM data of β-ZnTe(en)$_{0.5}$ in dark conditions. (a) Optical image, (b) topography map (4 µm x 5 µm), (c) work function map (4 µm x 5 µm). Cropping was necessary due to topographic instabilities.

Figure 52 presents two topographical spatial maps obtained through sequential scans of the same location of β-ZnTe(en)$_{0.5}$, revealing significant surface heterogeneity. Figure 52 (a) shows the topography map of the first scan, while Figure 52 (b) displays the topography map from the follow-up scan. A comparative analysis of these scans highlights topographical variations, with specific instances circled for clarity. These variations suggest that the AFM tip may displace surface debris during contact mode, the method used for topography acquisition. Furthermore, given the absence of any prior cleaning procedures, it is highly probable that the bright colorations observed within the circled regions are attributable to surface debris, rather than the intrinsic heterogeneity of β-ZnTe(en)$_{0.5}$.

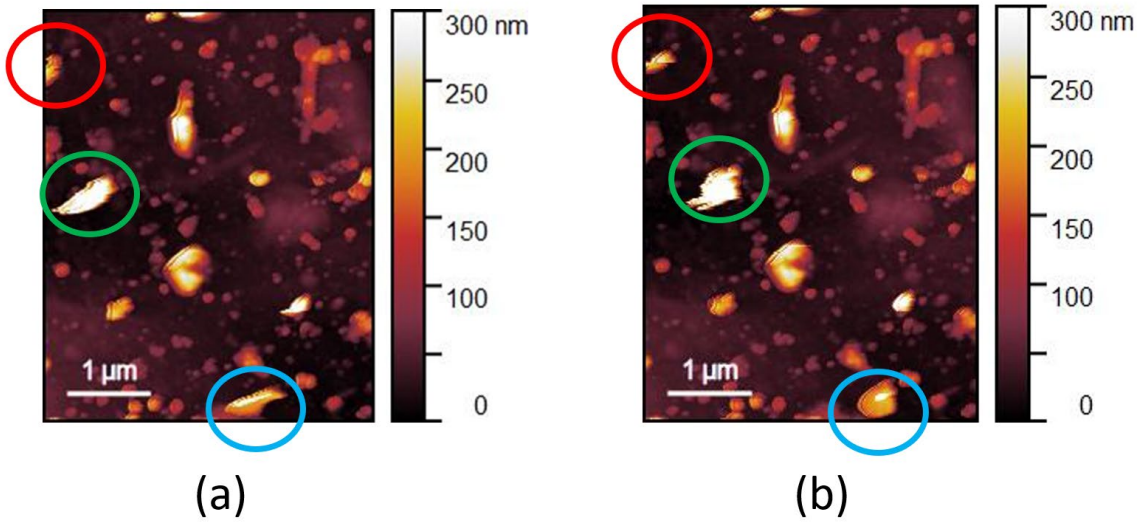

Figure 52: Sequential topographical spatial maps of the same β-ZnTe(en)$_{0.5}$ location, illustrating significant surface heterogeneity. (a) Topography map from the initial scan. (b) Topography map from the subsequent scan. Observed differences suggest the AFM tip may be displacing surface debris during contact mode scanning.

In summary, Kelvin Probe Force Microscopy (KPFM) was employed to characterize the surface properties of β-ZnTe(en)$_{0.5}$ on a mica substrate under ambient and dark conditions. The KPFM measurements revealed an average work function of 4.59 ± 0.03 eV for β-ZnTe(en)$_{0.5}$, which is consistent with the work function range of 4.49 eV to 4.71 eV obtained from UPS measurements. Topographical analysis indicated significant surface heterogeneity, and sequential scans highlighted potential tip-induced displacement of surface debris. To ensure data reliability, cropping of the topographical and work function maps was performed due to instabilities caused by either the heterogeneous topography or debris. The presence of bright colorations in topographical maps suggested surface debris artifacts, emphasizing the importance of surface

cleaning in KPFM measurements. This study successfully demonstrated the concurrent acquisition of topographical and work function data using KPFM, highlighting the importance of careful sample preparation and data analysis for accurate results.

CHAPTER 8: HOT PROBE MEASUREMENTS

8.1. Fundamentals of Hot-Probe Method

In contrast to conventional techniques for doping type determination, such as spectroscopic methods and Hall measurements, which often face limitations including high complexity or limited accessibility, particularly when applied to low-dimensional structures, due to their development for bulk materials, the hot probe method offers a simpler alternative [149, 150, 151]. The hot probe method, a standard technique for semiconductor conductivity type determination, leverages the thermoelectric effect to differentiate between n-type and p-type materials [148, 151].

Upon application of heat to one probe (hot probe), a voltage arises instantaneously, reaches a steady state within a few seconds, and subsequently maintains that steady state as long as the circuit remains connected [150]. However, intermittent contact with the hot probe results in observed voltage fluctuations. Furthermore, moisture-assisted hot probe analysis, which replaces the traditional heated source, successfully identifies the doping type in low-dimensional inorganic semiconductors, including thin films, nanowires, and nanotubes [149].

Figure 53 depicts the schematic diagram of the hot probe measurement. Thermally excited charge carriers diffuse outward from the hot probe, following Fick's law and resembling a drive-in diffusion process with a Gaussian distribution, creating a depletion region as they leave the heated zone [148, 150]. This procedure involves the application of a thermally elevated probe (hot probe), often heated with a soldering iron, and an ambient temperature probe (cold probe) to the semiconductor surface [148, 151]. These probes are electrically connected to a sensitive electrometer or multimeter, with the heated probe configured as the positive terminal and the

unheated probe as the negative terminal; although the specific polarity assignment is arbitrary, consistent application is crucial for accurate interpretation [150].

As a result, measurement of the potential difference resulting from the thermally induced diffusion of majority charge carriers, driven by a localized temperature gradient creating a carrier concentration gradient from the heated probe, facilitates conductivity type identification [148, 151]. Indeed, thermally-induced diffusion of majority charge carriers, illustrated by electron diffusion resulting in a positive voltage for n-type semiconductors (Figure 53 (a)) and hole diffusion resulting in a negative voltage for p-type semiconductors (Figure 53 (b), directly correlates voltage polarity to the majority carrier species, thereby enabling accurate conductivity type classification [150, 151].

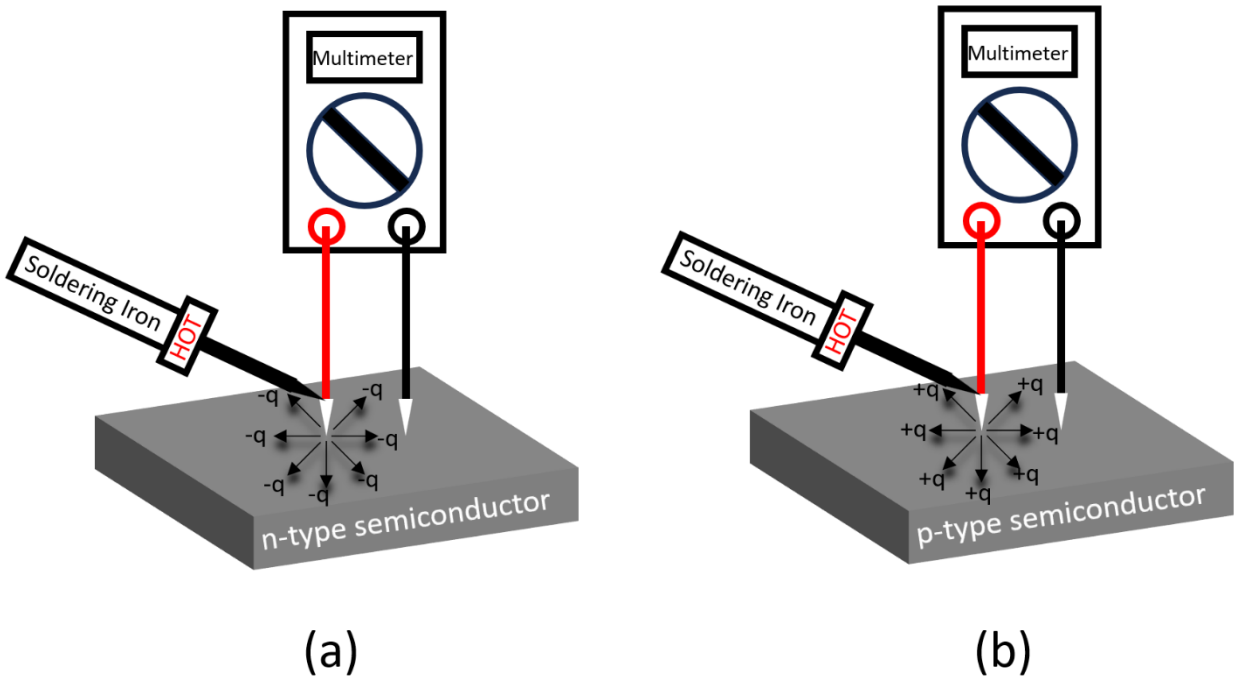

Figure 53: Schematic diagram of hot probe method for conductivity type determination in (a) n-type and (b) p-type semiconductors, constructed based on references [150, 151]. A soldering iron

heats the positive probe, inducing thermal excitation and diffusion of majority charge carriers. (a) In n-type semiconductors, electron diffusion from the heated probe results in a positive voltage reading. (b) In p-type semiconductors, hole diffusion from the heated probe results in a negative voltage reading.

It is important to note that an observed positive correlation exists between temperature and measured voltage; however, excessive thermal application can compromise the reliability of measurement results, particularly in thin film samples [148, 151]. Building upon this technique, an advanced hot probe methodology has been developed, extending beyond conventional conductivity type determination to include the estimation of majority charge carrier concentration in semiconductors, utilizing a theoretical model derived from the continuity and Poisson equations to characterize the process [148, 150]. Experimental validation of the advanced hot probe technique, which approximates majority carrier concentration by quantifying excess charge induced by the heated probe, was performed using bulk Si and Ge, along with Ge thin film semiconductor samples, demonstrating a significant contribution to semiconductor characterization and device development by enabling a more comprehensive assessment of material properties [148].

In addition to the advancement of hot probe method capability, moisture-assisted hot probe method provides a practical, effective, and rapid technique for determining doping types in thin films and inorganic nanowires, showcasing its broad potential for advancing semiconductor-based devices in materials science and device engineering [149].

8.2. Experimental Results

The primary objective of the hot probe method in this study was to ascertain the conductivity type of β-$ZnTe(en)_{0.5}$ to support the results of XPS spectra confirming the valence band maximum location relative to the Fermi level from Figure 40. Initially, a direct lateral measurement approach was attempted, wherein two probes were manually positioned on the pristine β-$ZnTe(en)_{0.5}$ placed on a substrate (Si/SiO_2). However, the inherent fragility of β-$ZnTe(en)_{0.5}$ resulted in frequent fracturing during the application of the heat to one probe by a soldering iron. Alternative contact enhancement strategies, including the use of conductive tape and paste, proved successful in device preparation but yielded no observable electrical results. Consequently, a refined measurement methodology was implemented, implementing electrode deposition using e-beam evaporation, as depicted in Figure 15. Two distinct device configurations, corresponding to crystallographic a-axis and c-axis orientations, were fabricated for the hot probe method, as shown in Figure 54. Upon application of heat to the designated positive terminal probe, both device configurations exhibited a negative voltage potential, indicative of p-type semiconductor behavior. This consistent observation across both crystallographic orientations confirms the p-type conductivity of β-$ZnTe(en)_{0.5}$, aligning with the XPS results.

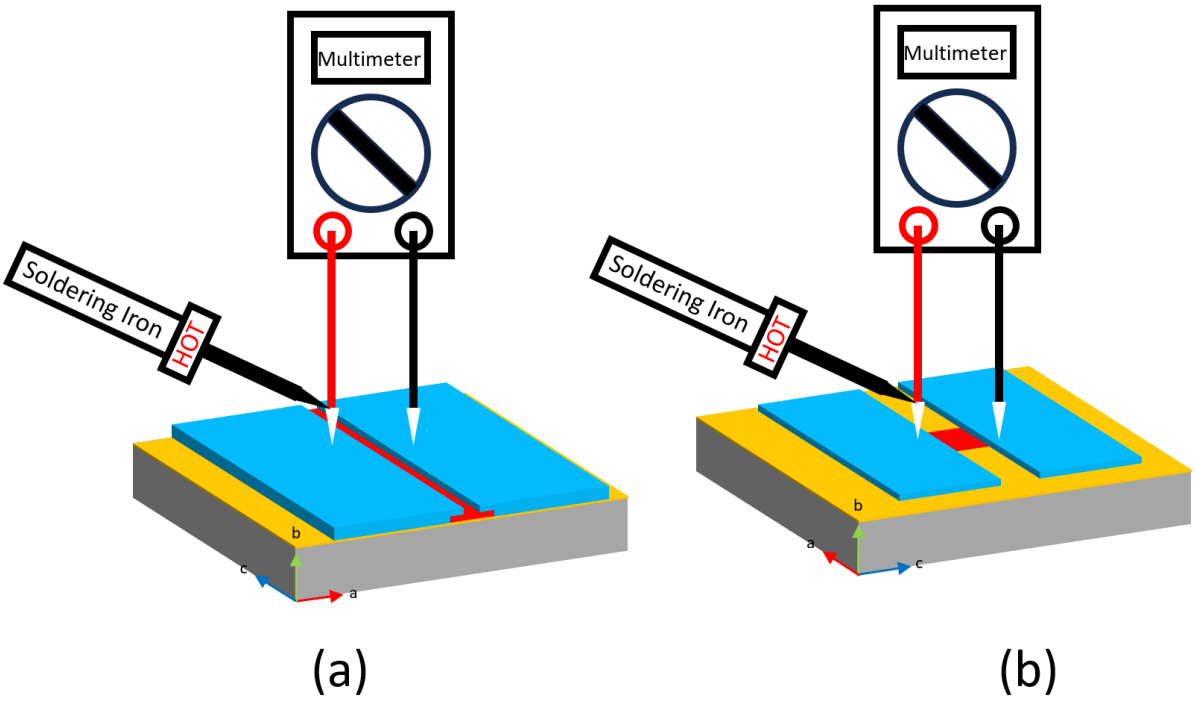

Figure 54: Hot probe measurement device configurations fabricated along crystallographic axes: (a) a-axis device, (b) c-axis device.

In summary, the hot probe method, as demonstrated in this study, offers several key advantages for semiconductor characterization, particularly for fragile and low-dimensional materials. Its simplicity, rapid measurement capability, and adaptability (including moisture-assisted variations) make it a valuable tool for determining conductivity type. Furthermore, advancements in the technique, such as the ability to estimate majority carrier concentration, extend its utility for comprehensive material analysis. This study showcases the method's effectiveness in confirming the p-type conductivity of β-ZnTe(en)$_{0.5}$, highlighting its robustness and reliability in challenging experimental scenarios.

CHAPTER 9: ELECTRONIC STRUCTURE FROM XPS, UPS, KPFM, AND HOT PROBE MEASUREMENTS

9.1. Electronic Structure of bulk ZnTe

To construct the energy band diagram of bulk ZnTe, Ultraviolet Photoelectron Spectroscopy (UPS) data was utilized to determine key electronic properties. Figure 43 presents the wide UPS spectrum of bulk ZnTe, showcasing the secondary electron cutoff (E_{SECO}), the valence band maximum (E_v), and the Fermi level (E_F), thereby providing a comprehensive overview of its electronic structure. A minor feature observed within the ESECO region may indicate inhomogeneous conductivity, although this does not significantly impact the determination of E_{SECO}.

However, it is important to acknowledge that reported bandgap energy (E_g) values in the literature exhibit a range from 2.1 eV to 2.39 eV. These deviations can be attributed to several factors, including temperature variations, surface oxidation, and differences in measurement techniques [1, 2, 5, 6, 76, 79-82, 84-89, 138]. Similarly, reported work function (∅) and electron affinity (χ) values also vary, which can be due to differences in doping levels and measurement techniques [75, 83-88, 167].

High-resolution UPS spectra of bulk ZnTe, as depicted in Figure 44 were employed to determine the E_{SECO} and E_v locations using the extrapolation approach. For bulk ZnTe2, the E_v was determined to be 0.50 eV below the E_F, the E_{SECO} was measured at 16 eV, and the work function was calculated to be 5.20 eV using Eq. 78. Similarly, for bulk ZnTe3, E_v was also located 0.50 eV below the E_F, the E_{SECO} measured at 16.05 eV, and a work function was calculated to be 5.15 eV using Eq. 78. Furthermore, the electron affinity values are 5.70 eV for bulk ZnTe2 and 5.65

eV for bulk ZnTe3. The spectra used to generate the average in Figure 44 (a) and (b) were acquired from two distinct locations on an identical bulk ZnTe sample, revealing highly similar results. A minor deviation of 0.05 eV was observed in the E_{SECO} values between these two locations, likely attributable to inhomogeneous conductivity or measurement uncertainties, but both spectra exhibited identical E_v values, indicating no significant sample inconsistency. Although the 0.05 eV deviation in E_{SECO} may arise from the employed extrapolation method, known for its lower accuracy compared to the first derivative technique, it does not substantially affect the determination of the work function, remaining within the range of experimental uncertainty.

To complete the energy band diagram, the bandgap energy of bulk ZnTe from photoluminescence (PL) measurements is used in conjunction with the UPS-derived E_v and work function values to construct the energy band diagram. The electronic properties of bulk ZnTe can be fully characterized by combining the E_v value (0.50 eV), the work function (5.20 eV and 5.15 eV), and the bandgap energy (2.26 eV), enabling the construction of a reliable energy band diagram, as shown in Figure 55 [79-81, 84-89].

Figure 55 exhibits an energy diagram depicting for bulk ZnTe with flat bands to the surface, incorporating the bandgap energy (E_g), and illustrates the relationship between electron affinity (χ), work function ($\emptyset$), ionization energy (IE), and the Fermi level (E_F) relative to the vacuum level. This characteristic alignment of E_v relative to E_F serves as a definitive indicator of p-type conductivity in bulk ZnTe. The observed energy level alignment suggests that the Fermi level resides closer to the valence band, implying an abundance of holes as majority charge carriers within the bulk ZnTe. A discrepancy of approximately 0.1 eV was observed in the ionization

energy values [84-87]. Furthermore, a literature value either deviates from or is identical to the observed data, with a maximum difference of 0.05 eV [88].

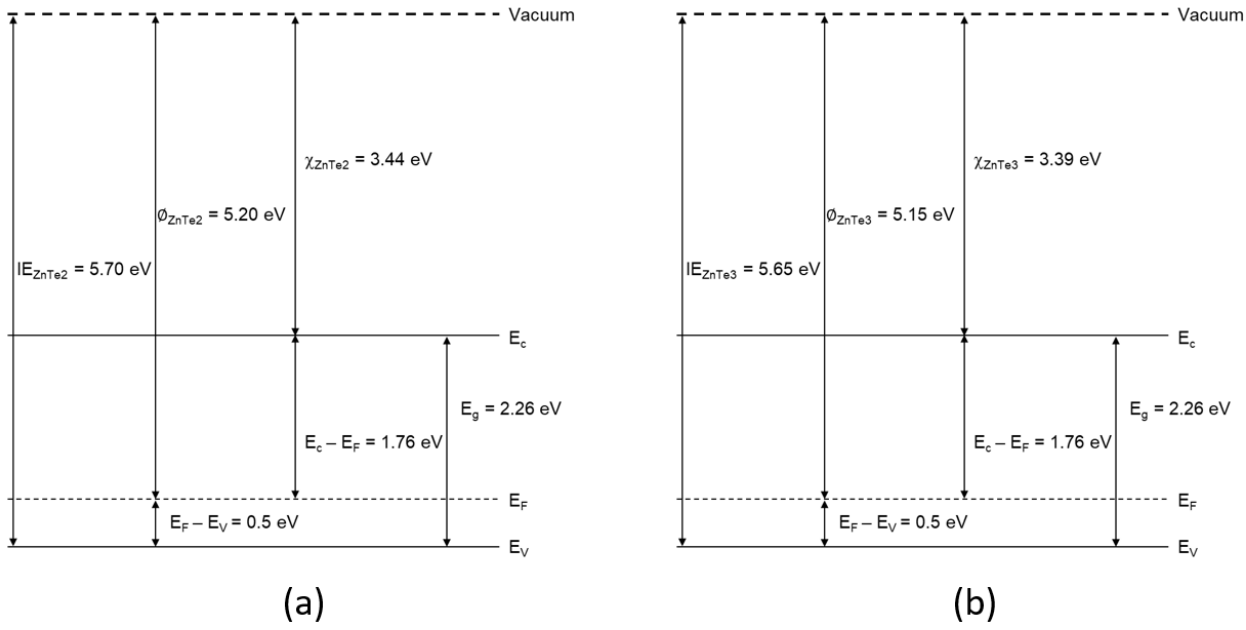

Figure 55: Energy diagram of bulk ZnTe with flat bands to the surface, showing the relationships between bandgap energy (E_g), electron affinity (χ), work function ($\emptyset$), ionization energy (IE), and the Fermi level (E_F) relative to the vacuum level, based on a simplified model from the cited reference [94].

9.2. Electronic Structure of β-ZnTe(en)$_{0.5}$

The construction of a comprehensive energy band diagram for β-ZnTe(en)$_{0.5}$, was achieved through the implementation of a multi-technique methodology, utilizing data acquired from X-ray Photoelectron Spectroscopy (XPS), Ultraviolet Photoelectron Spectroscopy (UPS), Kelvin Probe Force Microscopy (KPFM), and the hot probe method.

XPS was utilized to determine the valence band maximum (E_v) relative to the Fermi level (E_F). The UPS measurements exhibited metallic-like behavior, potentially due to substrate interference. To mitigate this, a 55 μm iris was used during XPS, effectively eliminating substrate contributions. Figure 40 presents the XPS spectra, illustrating the determination of the valence band maximum using linear extrapolation of the background signal and the steep leading edge of valence band emission. The intersection of these extrapolated lines defined E_v, a method considered reliable, albeit less accurate than the first derivative technique [95]. The experimental E_v values were 0.78 eV and 0.82 eV, with a 0.04 eV deviation, deemed acceptable given the 0.1 eV measurement step. As a result, the E_v was determined to be approximately 0.80 eV below E_F using simple arithmetic. Room-temperature photoluminescence (PL) measurements revealed a bandgap energy of 3.55 eV. Therefore, the Fermi level was found to be significantly closer to the valence band (0.8 eV) than the conduction band (2.75 eV), confirming the p-type conductivity of β-ZnTe(en)$_{0.5}$.

UPS spectra were acquired on Au/Si and In foil substrates (Figure 45). While the secondary electron cutoff (E_{SECO}) and E_F were observed, a distinct E_v was absent, potentially leading to the misinterpretation of β-ZnTe(en)$_{0.5}$ as metallic. High-resolution UPS spectra (Figure 46 and Figure 47) facilitated E_{SECO} determination using the extrapolation approach, enabling work function derivation. Substrate-dependent variations in the β-ZnTe(en)$_{0.5}$ work function were observed. The average work function was 4.71 eV on Au/Si substrate and 4.49 eV on In foil substrate, suggesting the actual work function lies within this range (Figure 49). It is hypothesized that the substrate interference in the UPS data, despite the significant thickness of the sample, is likely due to the misalignment of the X-ray and UV radiation sources (Figure 48).

Nevertheless, the work function of gold and indium was found to be in good agreement with reported values [89, 95, 167, 180].

To corroborate the UPS data, KPFM was employed to characterize surface properties under ambient conditions (Figure 51). The average work function of β-ZnTe(en)$_{0.5}$ was determined to be 4.59 ± 0.03 eV, consistent with the 4.49 eV to 4.71 eV range obtained from UPS. This consistency supports the reliability of the work function values obtained from UPS.

Additionally, the hot probe method was implemented to confirm the p-type conductivity indicated by XPS (Figure 40). Both a-axis and c-axis device configurations (Figure 54) exhibited negative voltage potentials upon heating the positive probe, confirming p-type behavior, consistent with XPS findings.

Comprehensive characterization of the electronic properties of β-ZnTe(en)$_{0.5}$ was achieved by integrating the valence band maximum (E_v) value from XPS (0.80 eV), the bandgap energy (E_g) from PL (3.55 eV), and the work function (∅) from KPFM (4.59 ± 0.03 eV), which aligns with the UPS range of 4.49 eV to 4.71 eV. Furthermore, the electron affinity (χ) value and the ionization energy (IE) were calculated to be 1.84 eV and 5.39 eV, respectively. The observed consistency between UPS and KPFM work function values, despite differing measurement principles, reinforces the reliability of the obtained work function value. Moreover, the hot probe method's confirmation of p-type conductivity validates the XPS-derived E_v placement. Therefore, a reliable energy band diagram of β-ZnTe(en)$_{0.5}$ can be constructed based on the obtained information, as shown in Figure 56.

Figure 56 presents the energy diagram of β-ZnTe(en)$_{0.5}$, illustrating the flat band approximation at the surface and the relationships between the electron affinity (χ), work function (∅), and ionization energy (IE) relative to the vacuum level. The position of the valence band maximum

relative to the Fermi level (E_F) confirms p-type conductivity in β-ZnTe(en)$_{0.5}$, with holes as the majority carriers.

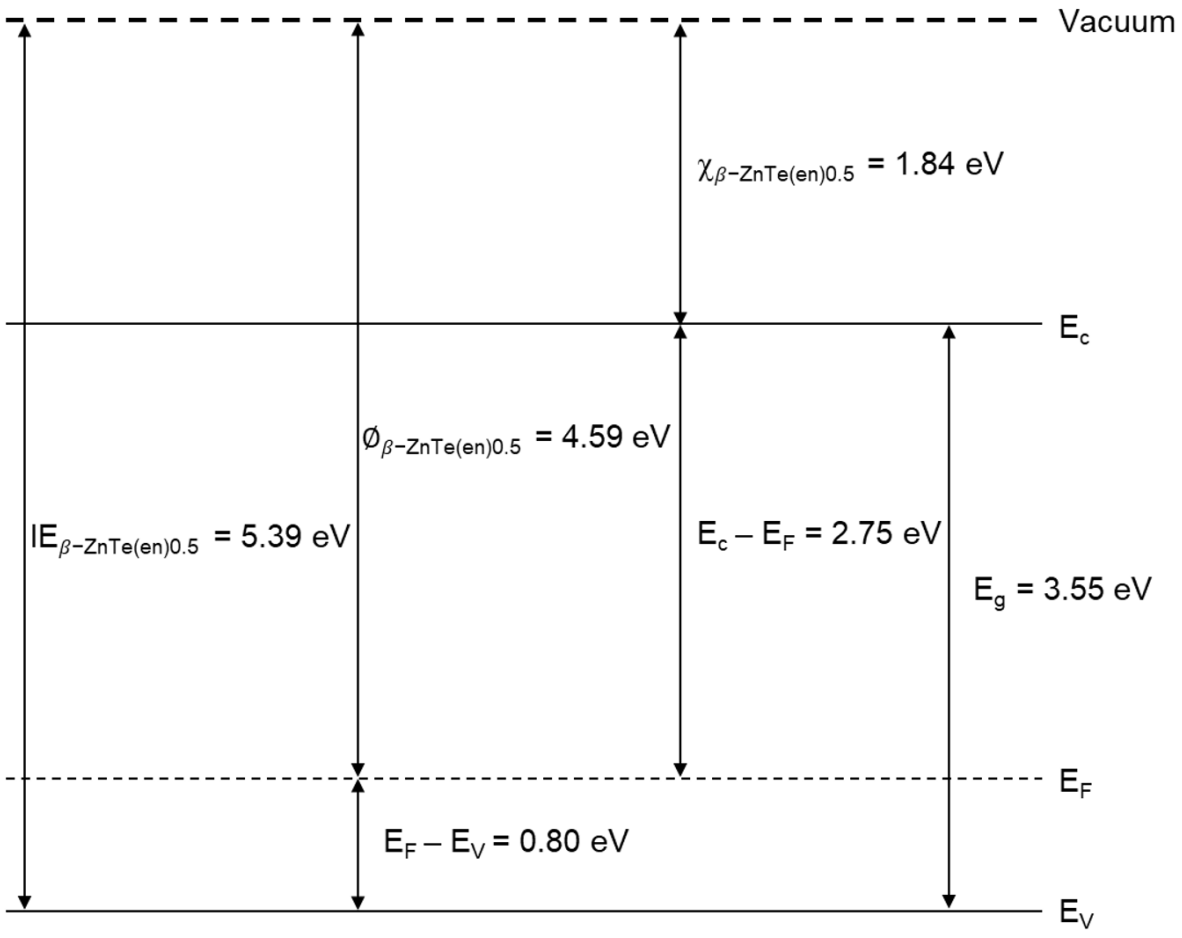

Figure 56: Energy diagram of β-ZnTe(en)$_{0.5}$, illustrating the flat band approximation at the surface and the relationship between electron affinity (χ), work function (∅), and ionization energy (*IE*) with respect to the vacuum level.

Figure 57 presents the energy diagram comparing β-ZnTe(en)$_{0.5}$ and ZnTe. Specifically, Figure 57 (a) depicts the energy band diagram constructed by aligning the Fermi levels (E_F) of β-ZnTe(en)$_{0.5}$ and ZnTe, using data from Figure 55 and Figure 56. This alignment, performed

using room-temperature band gap energies ($E_{g\_\beta\text{-}ZnTe(en)0.5}$ = 3.55 eV, E_{g_ZnTe} = 2.26 eV), resulted in a conduction band maximum offset (E_c) of 0.99 eV and a valence band maximum offset (E_v) of 0.30 eV. In contrast, previously calculated data, as shown in Figure 57 (b), revealed the conduction band offset and valence band offset of 0.71 eV and 0.62 eV, respectively, based on low-temperature band gap energies ($E_{g\_\beta\text{-}ZnTe(en)0.5}$ = 3.72 eV, E_{g_ZnTe} = 2.39 eV) [5-6]. The observed discrepancies between these two sets of offset values, specifically 0.28 eV for ΔEc and 0.32 eV for ΔEv, likely arise from the use of differing band gap energies.

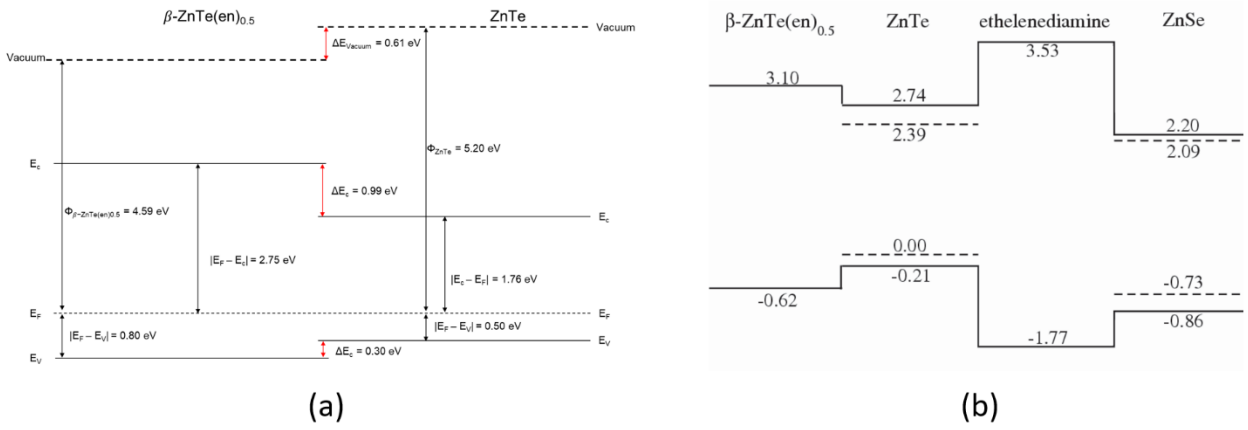

Figure 57: Energy band diagram comparison of β-ZnTe(en)$_{0.5}$ and ZnTe. (a) Energy band alignment based on room-temperature band gap energies ($E_{g\_\beta\text{-}ZnTe(en)0.5}$ = 3.55 eV, E_{g_ZnTe} = 2.26 eV), yielding a conduction band offset (ΔEc) of 0.99 eV and a valence band offset (ΔEv) of 0.30 eV. (b) Previously calculated energy band alignment using low-temperature band gap energies ($E_{g\_\beta\text{-}ZnTe(en)0.5}$ = 3.72 eV, E_{g_ZnTe} = 2.39 eV), resulting in ΔE_c = 0.71 eV and ΔE_v = 0.62 eV [6].

CHAPTER 10: Conclusion and Future Works

10.1. Conclusion

This study has demonstrated the exceptional properties and potential of β-ZnTe(en)$_{0.5}$, an organic-inorganic hybrid material with remarkable long-term stability and unique structural characteristics. The solvothermal synthesis approach, coupled with shadow mask lithography, enabled the fabrication of high-quality devices, facilitating a detailed investigation of the material's charge transport and electronic properties.

Space-Charge-Limited Current (SCLC) analysis revealed significant anisotropic charge transport in β-ZnTe(en)$_{0.5}$, with notably higher mobilities along the a- and c-axes compared to the b-axis. This anisotropy, directly linked to the material's layered crystal structure, underscores the importance of SCLC measurements in characterizing such hybrid nanostructures. The observed deviations from ideal Mott-Gurney behavior at low voltages suggest the presence of trap states or device geometry effects, necessitating further investigation.

A comprehensive electronic structure investigation, utilizing XPS, UPS, KPFM, and hot probe measurements, confirmed the p-type conductivity of β-ZnTe(en)$_{0.5}$ and established its work function and band alignment. The consistency between the results obtained from different techniques highlights the effectiveness of a multi-technique approach for accurately determining the electronic properties of complex materials.

The exceptional stability, anisotropic transport, and well-defined electronic structure of β-ZnTe(en)$_{0.5}$ make it a promising candidate for optoelectronic applications. The successful synthesis and fabrication methods developed in this study provide a foundation for future

research aimed at optimizing device performance and exploring novel applications of this intriguing material.

10.2. Future Works

Future research on β-ZnTe$(en)_{0.5}$ should focus on several key areas to deepen the understanding of its electronic properties and optimize its potential for optoelectronic applications. Firstly, device fabrication techniques must be refined to create single charge carrier devices, specifically electron-only and hole-only devices. This requires the selection of appropriate electrode materials with low or high work functions, respectively, to form ohmic contacts that satisfy the Space-Charge-Limited Current (SCLC) conditions. Rigorous electronic structure characterization is essential to guide this process, ensuring reliable data acquisition. In the lateral device configuration, two pristine samples with different cross-sectional areas were used due to variations in sample geometry. To minimize potential contributions from variations in contact geometry, a maskless alignment approach was employed. A systematic process was initiated to create identical electrode geometries within one pristine sample. Two electrodes were aligned along each crystallographic axis (a-axis and c-axis) using a Heidelberg μMLA maskless aligner. This new device fabrication approach allows for lateral measurements to be performed on a single device, reducing deviations that could arise from sample-to-sample variations. Additionally, future device fabrication should explore varying interelectrode widths on the same lateral device to confirm the extracted mobility and the consistent application of electrodes for vertical devices.

Secondly, SCLC measurements must be expanded to include temperature-dependent and pulsed I-V techniques. When a continuous (DC) voltage (steady-state) is applied, self-heating can alter

electrical properties, whereas pulsed I-V measurements, using short voltage pulses with low duty cycles, minimize this effect, providing more accurate intrinsic characteristics [16, 54, 60, 91, 158]. Temperature-dependent SCLC measurements are crucial for determining trap energy levels (E_t), trap density of states (N_t), and barrier heights, enabling comparison with analytical analyses and simulations for validation [24, 27, 30, 33]. Furthermore, future SCLC studies should incorporate surface trap effects to improve material parameter estimations, explain I-V curve asymmetries, optimize contact fabrication, and explore novel device functionalities through surface trap engineering, utilizing sophisticated models and simulations [34]. Incorporating non-idealities into SCLC analysis, such as surface trap effects and device geometry influences, is also vital for a more accurate representation of charge transport.

Thirdly, a full electronic structure investigation requires further exploration using techniques such as Inverse Photoelectron Spectroscopy (IPES) and Scanning Tunneling Microscopy/Spectroscopy (STM/STS). While XPS and UPS provide valuable information about core-level and valence electrons, IPES complements these by probing unoccupied electronic states, such as the conduction band structure [128]. STM/STS is highly surface-sensitive, necessitating operation under ultra-high vacuum conditions to avoid erroneous data interpretation [134]. These techniques can provide detailed spatial variations in spectroscopy, aiding in the extraction of electronic structure and properties through curve-fitting and comparison with theoretical models.

Surface information is critical for understanding metal electrode deposition on β-$ZnTe(en)_{0.5}$, particularly along the stacking axis (b-axis), where oxidation layers may form. Auger electron spectroscopy can provide a more in-depth analysis of chemical states than XPS. Proper ohmic contacts are essential for barrier-free charge transport, and the Schottky-Mott Rule, while widely

used, overlooks surface information like interface dipoles [90, 97]. Sufficient n-type doping in a device with electron-injecting contacts leads to an ohmic current-voltage characteristic within a specific voltage range, where the electron concentration is dominated by dopants rather than injected charges, and conductivity is determined by electron mobility and doping level [43]. Investigating methods to minimize surface states without damaging the sample, such as argon gas sputtering, is crucial, and the effects of such treatments on Fermi level pinning and sample condition should be thoroughly assessed [10].

Experimental determination of ohmic contacts for electron-only and hole-only devices, coupled with systematic device preparation and Raman spectroscopy analysis before each fabrication and measurement step, will enhance data reliability. Further verification of β-$ZnTe(en)_{0.5}$'s undoped nature can be achieved through Hall effect, capacitance-voltage (C-V) measurement, and Scanning Spreading Resistance Microscopy (SSRM) measurements. Techniques to analyze trap states (shallow and deep) and proper analysis approaches will further satisfy ideal conditions for Mott-Gurney law analysis.

Finally, electrical pulse measurements, alongside DC measurements, should be conducted to investigate frequency-dependent permittivity, which impacts mobility values in Mott-Gurney law analysis and hysteresis in I-V characteristics [53-54, 60]. Ellipsometry and impedance spectroscopy can be employed to study permittivity values and their frequency dependence, respectively [53].

REFERENCES

[1] Huang, X., Li, J., & Fu, H. (2000). The first covalent organic− inorganic networks of hybrid chalcogenides: structures that may lead to a new type of quantum wells. *Journal of the American Chemical Society*, *122*(36), 8789-8790.

[2] Huang, X., Li, J., Zhang, Y., & Mascarenhas, A. (2003). From 1D chain to 3D network: tuning hybrid II-VI nanostructures and their optical properties. *Journal of the American Chemical Society*, *125*(23), 7049-7055.

[3] Li, J. H., Moss, S. C., Zhang, Y., Mascarenhas, A., Pfeiffer, L. N., West, K. W., ... & Bai, J. (2003). Layer Ordering and Faulting in (GaAs)n/(AlAs)n Ultrashort-Period Superlattices. *Physical review letters*, *91*(10), 106103.

[4] Fu, H., & Li, J. (2004). Density-functional study of organic–inorganic hybrid single crystal ZnSe (C 2 H 8 N 2) 1/2. *The Journal of chemical physics*, *120*(14), 6721-6725.

[5] Fluegel, B., Zhang, Y., Mascarenhas, A., Huang, X., & Li, J. (2004). Electronic properties of hybrid organic–inorganic semiconductors. *Physical Review B*, *70*(20), 205308.

[6] Zhang, Y., Dalpian, G. M., Fluegel, B., Wei, S. H., Mascarenhas, A., Huang, X. Y., ... & Wang, L. W. (2006). Novel approach to tuning the physical properties of organic-inorganic hybrid semiconductors. Physical review letters, 96(2), 026405.

[7] Moon, C. Y., Dalpian, G. M., Zhang, Y., Wei, S. H., Huang, X. Y., & Li, J. (2006). Study of Phase Selectivity of Organic− Inorganic Hybrid Semiconductors. *Chemistry of materials*, *18*(12), 2805-2809.

[8] Zhang, Y., Islam, Z., Ren, Y., Parilla, P. A., Ahrenkiel, S. P., Lee, P. L., ... & Li, J. (2007). Zero thermal expansion in a nanostructured inorganic-organic hybrid crystal. *Physical review letters*, *99*(21), 215901.

[9] Qian, X., Gu, X., & Yang, R. (2017). Thermal conductivity modeling of hybrid organic-inorganic crystals and superlattices. *Nano Energy*, *41*, 394-407.

[10] Ye, T., Kocherga, M., Sun, Y. Y., Nesmelov, A., Zhang, F., Oh, W., ... & Zhang, Y. (2021). II–VI Organic–Inorganic Hybrid Nanostructures with Greatly Enhanced Optoelectronic Properties, Perfectly Ordered Structures, and Shelf Stability of Over 15 Years. *ACS nano*, *15*(6), 10565-10576.

[11] Mott, N. F., & Gurney, R. W. (1964). Electronic Processes in Ionic Crystals Oxford.

[12] Chandra, W., Ang, L. K., Pey, K. L., & Ng, C. M. (2007). Two-dimensional analytical Mott-Gurney law for a trap-filled solid. *Applied physics letters*, *90*(15).

[13] Smith, W. (1873). Effect of Light on Selenium. *Nature*, *7*, 303.

[14] Gupta, G., Banerjee, S., Dutta, S., Aarnink, A. A., Schmitz, J., Kovalgin, A. Y., & Hueting, R. J. (2018). Charge carrier transport and electroluminescence in atomic layer deposited poly-GaN/c-Si heterojunction diodes. *Journal of Applied Physics*, *124*(8).

[15] Rose, A. (1951). An Outline of Some Photoconductive Processes. *RCA Rev*, *12*(3), 362.

[16] Smith, R. W., & Rose, A. (1955). Space-charge-limited currents in single crystals of cadmium sulfide. *Physical Review*, *97*(6), 1531.

[17] Rose, A. (1955). Space-charge-limited currents in solids. *Physical Review*, *97*(6), 1538.

[18] Lampert, M. A. (1956). Simplified theory of space-charge-limited currents in an insulator with traps. *Physical Review*, *103*(6), 1648.

[19] Wright, G. T. (1958). Space-charge limited currents in insulating materials. *Nature*, *182*(4645), 1296-1297.

[20] Parmenter, R. H., & Ruppel, W. (1959). Two-Carrier Space-Charge-Limited Current in a Trap-Free Insulator. *Journal of Applied Physics*, *30*(10), 1548-1558.

[21] Johnson, J. B. (1960). Contribution of Thomas A. Edison to thermionics. *American journal of physics*, *28*(9), 763-773.

[22] Wright, G. T. (1961). Mechanisms of space-charge-limited current in solids. *Solid-State Electronics*, *2*(2-3), 165-189.

[23] Mark, P., & Helfrich, W. (1962). Space-charge-limited currents in organic crystals. *Journal of Applied Physics*, *33*(1), 205-215.

[24] Bube, R. H. (1962). Trap density determination by space-charge-limited currents. *Journal of Applied Physics*, *33*(5), 1733-1737.

[25] Geurst, J. A. (1966). Theory of space-charge-limited currents in thin semiconductor layers. *physica status solidi (b)*, *15*(1), 107-118.

[26] Murgatroyd, P. N. (1970). Theory of space-charge-limited current enhanced by Frenkel effect. *Journal of Physics D: Applied Physics*, *3*(2), 151.

[27] Chiu, F. C. (2007). Electrical characterization and current transportation in metal⁄ Dy2O3⁄ Si structure. *Journal of Applied Physics*, *102*(4).

[28] Grinberg, A. A., Luryi, S., Pinto, M. R., & Schryer, N. L. (1989). Space-charge-limited current in a film. *IEEE Transactions on Electron Devices*, *36*(6), 1162-1170.

[29] Luginsland, J. W., Lau, Y. Y., Umstattd, R. J., & Watrous, J. J. (2002). Beyond the Child–Langmuir law: A review of recent results on multidimensional space-charge-limited flow. *Physics of Plasmas*, *9*(5), 2371-2376.

[30] Yasuda, T., Yamaguchi, Y., Zou, D. C., & Tsutsui, T. (2002). Carrier mobilities in organic electron transport materials determined from space charge limited current. *Japanese journal of applied physics*, *41*(9R), 5626.

[31] Steinmann, P., & Weaver, J. M. R. (2005). Nanometer-scale gaps between metallic electrodes fabricated using a statistical alignment technique. *Applied Physics Letters*, *86*(6), 063104.

[32] Shen, X. M., Zhao, D. G., Liu, Z. S., Hu, Z. F., Yang, H., & Liang, J. W. (2005). Space-charge-limited currents in GaN Schottky diodes. *Solid-state electronics*, *49*(5), 847-852.

[33] Chiu, F. C., Chou, H. W., & Lee, J. Y. M. (2005). Electrical conduction mechanisms of metal⁄ La2O3⁄ Si structure. *Journal of Applied Physics*, *97*(10).

[34] De Boer, R. W. I., & Morpurgo, A. F. (2005). Influence of surface traps on space-charge limited current. *Physical Review B*, *72*(7), 073207.

[35] Carbone, A., Kotowska, B. K., & Kotowski, D. (2005). Space-charge-limited current fluctuations in organic semiconductors. *Physical review letters*, *95*(23), 236601.

[36] Chao, Y. C., Meng, H. F., & Horng, S. F. (2006). Polymer space-charge-limited transistor. *Applied physics letters*, *88*(22), 223510.

[37] Xia, Y., He, W., Chen, L., Meng, X., & Liu, Z. (2007). Field-induced resistive switching based on space-charge-limited current. *Applied physics letters*, *90*(2), 022907.

[38] Henrichsen, H. H., Kjelstrup-Hansen, J., Engstrøm, D., Clausen, C. H., Bøggild, P., & Rubahn, H. G. (2007). Electrical conductivity of organic single-nanofiber devices with different contact materials. *Organic Electronics*, *8*(5), 540-544.

[39] Carbone, A., Pennetta, C., & Reggiani, L. (2009). Trapping-detrapping fluctuations in organic space-charge layers. *Applied Physics Letters*, *95*(23), 318.

[40] Torricelli, F., Zappa, D., & Colalongo, L. (2010). Space-charge-limited current in organic light emitting diodes. *Applied Physics Letters*, *96*(11), 51.

[41] Joung, D., Chunder, A., Zhai, L., & Khondaker, S. I. (2010). Space charge limited conduction with exponential trap distribution in reduced graphene oxide sheets. *Applied Physics Letters*, *97*(9), 093105.

[42] Zhang, X. G., & Pantelides, S. T. (2012). Theory of space charge limited currents. *Physical review letters*, *108*(26), 266602.

[43] Kirchartz, T. (2013). Influence of diffusion on space-charge-limited current measurements in organic semiconductors. *Beilstein journal of nanotechnology*, *4*(1), 180-188.

[44] Blakesley, J. C., Castro, F. A., Kylberg, W., Dibb, G. F., Arantes, C., Valaski, R., ... & Kim, J. S. (2014). Towards reliable charge-mobility benchmark measurements for organic semiconductors. *Organic Electronics*, *15*(6), 1263-1272.

[45] Fischer, J., Tress, W., Kleemann, H., Widmer, J., Leo, K., & Riede, M. (2014). Exploiting diffusion currents at Ohmic contacts for trap characterization in organic semiconductors. *Organic Electronics*, *15*(10), 2428-2432.

[46] Shi, D., Adinolfi, V., Comin, R., Yuan, M., Alarousu, E., Buin, A., ... & Bakr, O. M. (2015). Low trap-state density and long carrier diffusion in organolead trihalide perovskite single crystals. *Science*, *347*(6221), 519-522.

[47] González, G. (2015). Quantum theory of space charge limited current in solids. *Journal of Applied Physics*, *117*(8), 084306.

[48] Alagha, S., Shik, A., Ruda, H. E., Saveliev, I., Kavanagh, K. L., & Watkins, S. P. (2017). Space-charge-limited current in nanowires. *Journal of Applied Physics*, *121*(17), 174301.

[49] Röhr, J. A., Kirchartz, T., & Nelson, J. (2017). On the correct interpretation of the low voltage regime in intrinsic single-carrier devices. *Journal of Physics: Condensed Matter*, *29*(20), 205901.

[50] Röhr, J. A., Moia, D., Haque, S. A., Kirchartz, T., & Nelson, J. (2018). Exploring the validity and limitations of the Mott–Gurney law for charge carrier mobility determination of semiconducting thin-films. *Journal of Physics: Condensed Matter*, *30*(10), 105901.

[51] Kwan, C. P., Street, M., Mahmood, A., Echtenkamp, W., Randle, M., He, K., ... & Bird, J. P. (2019). Space-charge limited conduction in epitaxial chromia films grown on elemental and oxide-based metallic substrates. *AIP Advances*, *9*(5), 055018.

[52] Röhr, J. A. (2019). Direct determination of built-in voltages in asymmetric single-carrier devices. *Physical Review Applied*, *11*(5), 054079.

[53] Sajedi Alvar, M., Blom, P. W., & Wetzelaer, G. J. A. (2020). Space-charge-limited electron and hole currents in hybrid organic-inorganic perovskites. *Nature communications*, *11*(1), 1-9.

[54] Duijnstee, E. A., Ball, J. M., Le Corre, V. M., Koster, L. J. A., Snaith, H. J., & Lim, J. (2020). Toward understanding space-charge limited current measurements on metal halide perovskites. *ACS Energy Letters*, *5*(2), 376-384.

[55] Röhr, J. A., & MacKenzie, R. C. (2020). Analytical description of mixed ohmic and space-charge-limited conduction in single-carrier devices. *Journal of Applied Physics*, *128*(16), 165701.

[56] Lamb, D. R. (1967). *Electrical conduction mechanisms in thin insulating films*. Methuen.

[57] Colinge, J. P., & Colinge, C. A. (2005). *Physics of semiconductor devices*. Springer Science & Business Media.

[58] Haneef, H. F., Zeidell, A. M., & Jurchescu, O. D. (2020). Charge carrier traps in organic semiconductors: a review on the underlying physics and impact on electronic devices. *Journal of Materials Chemistry C*, *8*(3), 759-787.

[59] Chen, X., Cheng, S., Xiao, L., & Sun, H. (2020). Identifying, understanding and controlling defects and traps in halide perovskites for optoelectronic devices: a review. Journal of Physics D: Applied Physics, 53(37), 373001.

[60] Zhang, P., Ang, Y. S., Garner, A. L., Valfells, Á., Luginsland, J. W., & Ang, L. K. (2021). Space–charge limited current in nanodiodes: Ballistic, collisional, and dynamical effects. Journal of Applied Physics, 129(10), 100902.

[61] Vines, L., Monakhov, E., & Kuznetsov, A. (2022). Defects in semiconductors. Journal of Applied Physics, 132(15), 150401.

[62] Child, C. D. (1911). Discharge from hot CaO. *Physical Review (Series I)*, *32*(5), 492.

[63] Langmuir, I. (1913). The effect of space charge and residual gases on thermionic currents in high vacuum. *Physical Review*, *2*(6), 450.

[64] Kittel, C. (2021). Introduction to solid state physics, 8th ed. Wiley.

[65] Lundstrom, M. (2002). Fundamentals of carrier transport, 2nd ed. *Measurement Science and Technology*, *13*(2), 230-230.

[66] Zhang, Y. (2022). II-VI based organic-inorganic hybrid structures: Brief review and perspective. *Journal of Luminescence*, 118936.

[67] Zhang, Y. (2018). Electronic structures of impurities and point defects in semiconductors. *Chinese Physics B*, *27*(11), 117103.

[68] Kern, W. (1990). The evolution of silicon wafer cleaning technology. *Journal of the Electrochemical Society*, *137*(6), 1887.

[69] Kern, W. (2018). Overview and evolution of silicon wafer cleaning technology. In *Handbook of silicon wafer cleaning technology* (pp. 3-85). William Andrew Publishing.

[70] Van der Ziel, A. (1976). *Solid state physical electronics,* 3rd ed. Prentice-Hall Englewood Cliffs.

[71] Sze, S. M., Li, Y., & Ng, K. K. (2021). *Physics of semiconductor devices*. John wiley & sons.

[72] Demazeau, G. (2008). Solvothermal reactions: an original route for the synthesis of novel materials. *Journal of Materials Science*, *43*, 2104-2114.

[73] Huo, Y., Xiu, S., Meng, L. Y., & Quan, B. (2023). Solvothermal synthesis and applications of micro/nano carbons: A review. *Chemical Engineering Journal*, *451*, 138572.

[74] Feng, X., Tang, Q., Zhou, J., Fang, J., Ding, P., Sun, L., & Shi, L. (2013). Novel mixed–solvothermal synthesis of MoS2 nanosheets with controllable morphologies. *Crystal Research and Technology*, *48*(6), 363-368.

[75] Van de Walle, C. G., & Neugebauer, J. (2003). Universal alignment of hydrogen levels in semiconductors, insulators and solutions. *Nature*, *423*(6940), 626-628.

[76] Li, Y. H., Walsh, A., Chen, S., Yin, W. J., Yang, J. H., Li, J., ... & Wei, S. H. (2009). Revised ab initio natural band offsets of all group IV, II-VI, and III-V semiconductors. *Applied Physics Letters*, *94*(21), 212109.

[77] Kraut, E. A., Grant, R. W., Waldrop, J. R., & Kowalczyk, S. P. (1980). Precise determination of the valence-band edge in x-ray photoemission spectra: application to measurement of semiconductor interface potentials. *Physical Review Letters*, *44*(24), 1620.

[78] Kraut, E. A., Grant, R. W., Waldrop, J. R., & Kowalczyk, S. P. (1983). Semiconductor core-level to valence-band maximum binding-energy differences: Precise determination by x-ray photoelectron spectroscopy. *Physical Review B*, *28*(4), 1965.

[79] Rohatgi, A., Ringel, S. A., Sudharsanan, R., Meyers, P. V., Liu, C. H., & Ramanathan, V. (1989). Investigation of polycrystalline CdZnTe, CdMnTe, and CdTe films for photovoltaic applications. *Solar Cells*, *27*(1-4), 219-230.

[80] Olusola, O. I., Madugu, M. L., Abdul-Manaf, N. A., & Dharmadasa, I. M. (2016). Growth and characterisation of n-and p-type ZnTe thin films for applications in electronic devices. *Current Applied Physics*, *16*(2), 120-130.

[81] Ahamed, J. U., Begum, N. P., & Khan, M. N. I. (2017). Property elucidation of vacuum-evaporated zinc telluride thin film towards optoelectronic devices. *Sādhanā*, *42*, 1773-1781.

[82] Abazari, M., Ahmad, F. R., Raghavan, K. C., Cournoyer, J. R., Her, J. H., Davis, R., ... & Korevaar, B. A. (2013). Carrier density in p-type ZnTe with nitrogen and copper doping. *MRS Online Proceedings Library (OPL)*, *1538*, 383-389.

[83] Swank, R. K. (1967). Surface properties of II-VI compounds. *Physical Review*, *153*(3), 844.

[84] Dumont, H., Bourée, J. E., Marbeuf, A., & Gorochov, O. (1993). Photo-assisted growth of ZnTe by metalorganic chemical vapour deposition. *Journal of crystal growth*, *130*(3-4), 600-610.

[85] Alfaramawi, K., Sweyllam, A., Abboudy, S., Imam, N. G., & Motaweh, H. A. (2010). Interface states-induced-change in the energy band diagram and capacitance–voltage characteristics of isotype ZnTe/CdTe heterojunctions. *International Journal of Modern Physics B*, *24*(24), 4717-4725.

[86] Gullu, H. H., Surucu, O. B., Isik, M., Terlemezoglu, M., & Parlak, M. E. H. M. E. T. (2020). Material and Si-based diode analyses of sputtered ZnTe thin films. *Journal of Materials Science: Materials in Electronics*, *31*, 11390-11397.

[87] Tanaka, T., Tsutsumi, R., Yoshinaga, T., Sonoyama, T., Saito, K., Guo, Q., & Ikeda, S. (2023). Effect of heterojunction structures on photoelectrochemical properties of ZnTe-based photocathodes for water reduction. *RSC advances*, *13*(1), 575-580.

[88] Zakutayev, A., Tate, J., Platt, H. A., Keszler, D. A., Barati, A., Klein, A., & Jaegermann, W. (2010). Band alignment at the BaCuSeF/ZnTe interface. *Applied Physics Letters*, *96*(16), 162110.

[89] Haynes, W. M. (2016). *CRC handbook of chemistry and physics*. CRC press. 12-124

[90] Tung, R. T. (2014). The physics and chemistry of the Schottky barrier height. *Applied Physics Reviews*, *1*(1).

[91] Fisher, W. R., Calado, P., Röhr, J. A., Smith, J. A., Shi, X., Game, O., ... & Barnes, P. R. (2022). The Validity Window of Space-Charge-Limited Current Measurements of Metal Halide Perovskite Devices. *arXiv preprint arXiv:2204.00459*.

[92] Fox, M. (2002). Optical properties of solids.

[93] Ye, T., Sun, Y. Y., Kocherga, M., Nesmelov, A., Schmedake, T. A., & Zhang, Y. (2023). Degradation Kinetics of Organic–Inorganic Hybrid Materials from Micro-Raman Spectroscopy and Density-Functional Theory: The Case of β-ZnTe (en) 0.5. *Small*, 2302935.

[94] Kahn, A. (2016). Fermi level, work function and vacuum level. *Materials Horizons*, *3*(1), 7-10.

[95] Stevie, F. A., & Donley, C. L. (2020). Introduction to x-ray photoelectron spectroscopy. *Journal of Vacuum Science & Technology A*, *38*(6).

[96] Henisch, H. K. (1984). Semiconductor contacts: an approach to ideas and models. *Oxford Univ. press*

[97] Mönch, W. (2013). *Electronic properties of semiconductor interfaces* (Vol. 43). Springer Science & Business Media.

[98] Nonnenmacher, M., o'Boyle, M. P., & Wickramasinghe, H. K. (1991). Kelvin probe force microscopy. *Applied physics letters*, *58*(25), 2921-2923.

[99] Vilitis, O., Rutkis, M., Busenberg, J., & Merkulov, D. (2016). Determination of contact potential difference by the Kelvin Probe (Part I) I. Basic principles of measurements. *Latvian Journal of Physics and Technical Sciences*, *53*(2), 48.

[100] Zhang, Z., Liu, P., Song, Y., Hou, Y., Xu, B., Liao, T., ... & Sun, Z. (2022). Heterostructure engineering of 2D superlattice materials for electrocatalysis. *Advanced Science*, *9*(35), 2204297.

[101] Novoselov, K. S., Geim, A. K., Morozov, S. V., Jiang, D. E., Zhang, Y., Dubonos, S. V., ... & Firsov, A. A. (2004). Electric field effect in atomically thin carbon films. *science*, *306*(5696), 666-669.

[102] Mir, S. H., Yadav, V. K., & Singh, J. K. (2020). Recent advances in the carrier mobility of two-dimensional materials: a theoretical perspective. *ACS omega*, *5*(24), 14203-14211.

[103] Pei, K., & Zhai, T. (2020). Emerging 2D organic-inorganic heterojunctions. *Cell Reports Physical Science*, *1*(8).

[104] Lemme, M. C., Akinwande, D., Huyghebaert, C., & Stampfer, C. (2022). 2D materials for future heterogeneous electronics. *Nature communications*, *13*(1), 1392.

[105] Allain, A., Kang, J., Banerjee, K., & Kis, A. (2015). Electrical contacts to two-dimensional semiconductors. *Nature materials*, *14*(12), 1195-1205.

[106] Zheng, Y., Gao, J., Han, C., & Chen, W. (2021). Ohmic contact engineering for two-dimensional materials. *Cell Reports Physical Science*, *2*(1).

[107] Ouyang, B., Xiong, S., & Jing, Y. (2018). Tunable phase stability and contact resistance of monolayer transition metal dichalcogenides contacts with metal. *npj 2D Materials and Applications*, *2*(1), 13.

[108] Gant, P., Niu, Y., Svatek, S. A., Agraït, N., Munuera, C., García-Hernández, M., ... & Castellanos-Gomez, A. (2017). Lithography-free electrical transport measurements on 2D materials by direct microprobing. *Journal of Materials Chemistry C*, *5*(43), 11252-11258.

[109] Zhang, R., Chen, T., Bunting, A., & Cheung, R. (2016). Optical lithography technique for the fabrication of devices from mechanically exfoliated two-dimensional materials. *Microelectronic engineering*, *154*, 62-68.

[110] Mizuta, H., Kalhor, N., Hang, S., Boden, S., Moktadir, Z., Rutt, H., & Bagnall, D. (2013). Ultrafine graphene nanodevice fabrication. *SPIE Newsroom*.

[111] Hüfner, S. (2013). *Photoelectron spectroscopy: principles and applications*. Springer Science & Business Media.

[112] Hüfner, S., Schmidt, S., & Reinert, F. (2005). Photoelectron spectroscopy—An overview. *Nuclear Instruments and Methods in Physics Research Section A: Accelerators, Spectrometers, Detectors and Associated Equipment*, *547*(1), 8-23.

[113] Nilsson, A. (2022). Concluding remarks: Photoelectron spectroscopy and the future of surface analysis. *Faraday discussions*, *236*, 528-544.

[114] Belu, A. M., Graham, D. J., & Castner, D. G. (2003). Time-of-flight secondary ion mass spectrometry: techniques and applications for the characterization of biomaterial surfaces. *Biomaterials*, *24*(21), 3635-3653.

[115] Willardson, R. K., & Beer, A. C. (1977). *Semiconductors and semimetals*. Academic press.

[116] Jin, X., Wang, H., & Feng, C. (2019). Space Charge Effect and Resistance Switching in Doped Monocrystalline Silicones. *Applied Sciences*, *9*(3), 434.

[117] Trukhanov, V. A., Bruevich, V. V., & Paraschuk, D. Y. (2018). Effect of space charge limited current on performance of organic field-effect transistors. *Synthetic Metals*, *246*, 254-259.

[118] Henisch, H. K., Manifacier, J. C., Callarotti, R. C., & Schmidt, P. E. (1980). Space-charge controlled conduction in thick metal-insulator-metal barriers. *Journal of Applied Physics*, *51*(7), 3790-3793.

[119] Schmidt, P. E., Octavio, M., Callarotti, R. C., & Henisch, H. K. (1982). Single-carrier space-charge controlled conduction. *Journal of Applied Physics*, *53*(7), 4996-5005.

[120] Schmidt, P. E., & Henisch, H. K. (1982). Drift-diffusion theory of symmetrical double-junction diodes. *Solid-State Electronics*, *25*(11), 1129-1133.

[121] Röhr, J. A., Shi, X., Haque, S. A., Kirchartz, T., & Nelson, J. (2018). Charge transport in spiro-OMeTAD investigated through space-charge-limited current measurements. *Physical review applied*, *9*(4), 044017.

[122] Röhr, J. A. (2022). On Injection in Intrinsic Single-Carrier Devices. *arXiv preprint arXiv:2201.03436*.

[123] Lampert, M. A., & Schilling, R. B. (1970). Current injection in solids: The regional approximation method. In *Semiconductors and semimetals* (Vol. 6, pp. 1-96). Elsevier.

[124] Bube, R. H. (1992). *Photoelectronic properties of semiconductors*. Cambridge University Press.

[125] Vidor, F. F., Meyers, T., & Hilleringmann, U. (2015). Flexible electronics: integration processes for organic and inorganic semiconductor-based thin-film transistors. *Electronics*, *4*(3), 480-506.

[126] Lee, J. M., Baek, J. H., Gill, T. M., Shi, X., Lee, S., Cho, I. S., ... & Zheng, X. (2019). A Zn: BiVO 4/Mo: BiVO 4 homojunction as an efficient photoanode for photoelectrochemical water splitting. *Journal of Materials Chemistry A*, *7*(15), 9019-9024.

[127] Barajas-Aguilar, A. H., Irwin, J. C., Garay-Tapia, A. M., Schwarz, T., Paraguay Delgado, F., Brodersen, P. M., ... & Jiménez Sandoval, S. J. (2018). Crystalline structure, electronic and lattice-dynamics properties of NbTe2. *Scientific reports*, *8*(1), 1-14.

[128] Terashima, M., Miyayama, T., Shirao, T., Mo, H. W., Hatae, Y., Fujimoto, H., & Watanabe, K. (2020). The electronic band structure analysis of OLED device by means of in situ LEIPS and UPS combined with GCIB. *Surface and Interface Analysis*, *52*(12), 948-952.

[129] Whitten, J. E. (2023). Ultraviolet photoelectron spectroscopy: Practical aspects and best practices. *Applied Surface Science Advances*, *13*, 100384.

[130] Baddorf, A. P. (2023). Identifying the secondary electron cutoff in ultraviolet photoemission spectra for work function measurements of non-ideal surfaces. *Scientific Reports*, *13*(1), 13452.

[131] Van Mensfoort, S. L. M., & Coehoorn, R. (2008). Effect of Gaussian disorder on the voltage dependence of the current density in sandwich-type devices based on organic semiconductors. *Physical Review B*, *78*(8), 085207.

[132] Chastain, J., & King Jr, R. C. (1992). Handbook of X-ray photoelectron spectroscopy. *Perkin-Elmer Corporation*, *40*, 221.

[133] Neamen, D. A., & Biswas, D. (2011). *Semiconductor physics and devices*. United States: McGraw-Hill higher education.

[134] Al-Brithen, H. A., Smith, A. R., & Gall, D. (2004). Surface and bulk electronic structure of ScN (001) investigated by scanning tunneling microscopy/spectroscopy and optical absorption spectroscopy. *Physical Review B*, *70*(4), 045303.

[135] Ishii, H., & Seki, K. (1997). Energy level alignment at organic/metal interfaces studied by UV photoemission: breakdown of traditional assumption of a common vacuum level at the interface. IEEE Transactions on Electron Devices, 44(8), 1295-1301.

[136] Sze, S. M., Coleman Jr, D. J., & Loya, A. (1971). Current transport in metal-semiconductor-metal (MSM) structures. *Solid-State Electronics*, *14*(12), 1209-1218.

[137] Vazquez-Mena, O., Gross, L., Xie, S., Villanueva, L. G., & Brugger, J. (2015). Resistless nanofabrication by stencil lithography: A review. *Microelectronic Engineering*, *132*, 236-254.

[138] Kashiwaya, S., Morasch, J., Streibel, V., Toupance, T., Jaegermann, W., & Klein, A. (2018). The work function of TiO2. *Surfaces*, *1*(1), 73-89.

[139] Loudon, R. (1964). The Raman effect in crystals. *Advances in Physics*, *13*(52), 423-482.

[140] Shao, G. (2021). Work function and electron affinity of semiconductors: Doping effect and complication due to fermi level pinning. *Energy & Environmental Materials*, *4*(3), 273-276.

[141] Fan, H. Y. (1951). Temperature dependence of the energy gap in semiconductors. *Physical Review*, *82*(6), 900.

[142] O'donnell, K. P., & Chen, X. (1991). Temperature dependence of semiconductor band gaps. *Applied physics letters*, *58*(25), 2924-2926.

[143] Cardona, M., Meyer, T. A., & Thewalt, M. L. W. (2004). Temperature dependence of the energy gap of semiconductors in the low-temperature limit. *Physical review letters*, *92*(19), 196403.

[144] Yu, C., Chen, Z., J Wang, J., Pfenninger, W., Vockic, N., Kenney, J. T., & Shum, K. (2011). Temperature dependence of the band gap of perovskite semiconductor compound CsSnI3. *Journal of Applied Physics*, *110*(6).

[145] Postawa, Z., Czerwinski, B., Szewczyk, M., Smiley, E. J., Winograd, N., & Garrison, B. J. (2004). Microscopic insights into the sputtering of Ag {111} induced by C60 and Ga bombardment. *The Journal of Physical Chemistry B*, *108*(23), 7831-7838.

[146] Eda, Y., Manaka, T., Hanawa, T., Chen, P., Ashida, M., & Noda, K. (2022). X-ray photoelectron spectroscopy-based valence band spectra of passive films on titanium. *Surface and Interface Analysis*, *54*(8), 892-898.

[147] Schultz, T., Lenz, T., Kotadiya, N., Heimel, G., Glasser, G., Berger, R., ... & Koch, N. (2017). Reliable work function determination of multicomponent surfaces and interfaces: the role of electrostatic potentials in ultraviolet photoelectron spectroscopy. *Advanced Materials Interfaces*, *4*(19), 1700324.

[148] Golan, G., Axelevitch, A., Gorenstein, B., & Manevych, V. (2006). Hot-probe method for evaluation of impurities concentration in semiconductors. *Microelectronics journal*, *37*(9), 910-915.

[149] Han, J. W., Kim, B., Kobayashi, N. P., Li, J., & Meyyappan, M. (2012). A simple method for the determination of doping type in nanomaterials based on electrical response to humidity. *Applied Physics Letters*, *101*(14).

[150] Axelevitch, A., & Golan, G. (2013). Hot-probe method for evaluation of majority charged carriers concentration in semiconductor thin films. *Facta universitatis-series: Electronics and Energetics*, *26*(3), 187-195.

[151] Au, B. W. C., Chan, K. Y., Sin, Y. K., & Ng, Z. N. (2017). Hot-point probe measurements of N-type and P-type ZnO films. *Microelectronics International*, *34*(1), 30-34.

[152] Vaccaro, F. P., Pohl, K. R., Smith, S. J., Berg, L. V. D., DeVito, R. P., & Johnson, C. R. (2001). *Limitations of the Hecht Equation Encountered in Measuring μτ Products in Mercuric Iodide*. Technical report, Constellation Technology Corporation, 7887 Bryan Dairy Road Suite 100, Largo, FL, 33777

[153] Xiao, B., Calado, P., MacKenzie, R. C., Kirchartz, T., Yan, J., & Nelson, J. (2020). Relationship between fill factor and light intensity in solar cells based on organic disordered semiconductors: the role of tail states. *Physical Review Applied*, *14*(2), 024034.

[154] Izmailov, R., Strand, J., Ronchi, N., Shluger, A., & Afanas' ev, V. (2024). Electron emission from deep traps in HfO 2 under thermal and optical excitation. *Physical Review B*, *109*(13), 134109.

[155] Kim, J. K., Cho, K., Kim, T. Y., Pak, J., Jang, J., Song, Y., ... & Lee, T. (2016). Trap-mediated electronic transport properties of gate-tunable pentacene/MoS2 pn heterojunction diodes. *Scientific reports*, *6*(1), 1-8.

[156] Huang, Y., Gong, X., Meng, Y., Wang, Z., Chen, X., Li, J., ... & Hu, W. (2021). Effectively modulating thermal activated charge transport in organic semiconductors by precise potential barrier engineering. *Nature communications*, *12*(1), 21.

[157] Ganesh, N., Ashar, A. Z., Purohit, S., Narasimhan, K. L., & Narayan, K. S. (2022). Visualization of carrier transport in lateral metal-perovskite-metal structures and its influence on device operation. *Physical Review Applied*, *17*(2), 024060.

[158] Le Corre, V. M., Duijnstee, E. A., El Tambouli, O., Ball, J. M., Snaith, H. J., Lim, J., & Koster, L. J. A. (2021). Revealing charge carrier mobility and defect densities in metal halide perovskites via space-charge-limited current measurements. *ACS energy letters*, *6*(3), 1087-1094.

[159] Decker, W., Belan, R., Heydemann, V. D., Armstrong, S., & Fisher, T. (2016, May). Novel low pressure sputtering source and improved vacuum deposition of small patterned features using precision shadow masks. In *Proceedings of the Society of Vacuum Coaters 59th Annual Technical Conference, Indianapolis, IN, USA* (pp. 9-13).

[160] Liu, Y., Wang, H., Jin, X., & Zhang, M. (2018). The space charge limited current and huge linear magnetoresistance in silicon. *Scientific Reports*, *8*(1), 775.

[161] Son, D. I., Park, D. H., Choi, W. K., Cho, S. H., Kim, W. T., & Kim, T. W. (2009). Carrier transport in flexible organic bistable devices of ZnO nanoparticles embedded in an insulating poly (methyl methacrylate) polymer layer. *Nanotechnology*, *20*(19), 195203.

[162] Wetzelaer, G. A. H. (2020). Improved determination of the mobility and built-in voltage in asymmetric single-carrier devices. *Physical Review Applied*, *13*(3), 034069.

[163] Li, J., Bi, W., Ki, W., Huang, X., & Reddy, S. (2007). Nanostructured crystals: Unique hybrid semiconductors exhibiting nearly zero and tunable uniaxial thermal expansion behavior. *Journal of the American Chemical Society*, *129*(46), 14140-14141.

[164] Many, A. (1965). High-field effects in photoconducting cadmium sulphide. *Journal of Physics and Chemistry of Solids*, *26*(3), 575-578.

[165] Reese, C., & Bao, Z. (2007). High-resolution measurement of the anisotropy of charge transport in single crystals. *Advanced Materials*, *19*(24), 4535-4538.

[166] Hourani, W., Rahimi, K., Botiz, I., Koch, F. P. V., Reiter, G., Lienerth, P., ... & Simon, L. (2014). Anisotropic charge transport in large single crystals of π-conjugated organic molecules. *Nanoscale*, *6*(9), 4774-4780.

[167] Michaelson, H. B. (1977). The work function of the elements and its periodicity. *Journal of applied physics*, *48*(11), 4729-4733.

[168] Kraft, D., Thissen, A., Broetz, J., Flege, S., Campo, M., Klein, A., & Jaegermann, W. (2003). Characterization of tellurium layers for back contact formation on close to technology treated CdTe surfaces. *Journal of applied physics*, *94*(5), 3589-3598.

[169] Smyth, C. M., Zhou, G., Barton, A. T., Wallace, R. M., & Hinkle, C. L. (2021). Controlling the Pd Metal Contact Polarity to Trigonal Tellurium by Atomic Hydrogen-Removal of the Native Tellurium Oxide. *Advanced Materials Interfaces*, *8*(7), 2002050.

[170] Chang, H. Y., Lin, W. C., Chu, P. C., Wang, Y. K., Sogo, M., Iida, S. I., ... & Miyayama, T. (2022). X-ray photoelectron spectroscopy equipped with gas cluster ion beams for evaluation of the sputtering behavior of various nanomaterials. *ACS Applied Nano Materials*, *5*(3), 4260-4268.

[171] Zhang, Z., Li, B., Qian, Q., Tang, X., Hua, M., Huang, B., & Chen, K. J. (2017). Revealing the nitridation effects on gan surface by first-principles calculation and X-Ray/ultraviolet photoemission spectroscopy. *IEEE Transactions on Electron Devices*, *64*(10), 4036-4043.

[172] Zhang, T., Hossain, M. A., Lee, C. Y., Zakaria, Y., Abdallah, A. A., & Hoex, B. (2018). Atomic layer deposited ZnxNi1− xO: A thermally stable hole selective contact for silicon solar cells. *Applied Physics Letters*, *113*(26).

[173] Fares, C., Tadjer, M. J., Woodward, J., Nepal, N., Mastro, M. A., Eddy, C. R., ... & Pearton, S. J. (2019). Valence and conduction band offsets for InN and III-nitride ternary alloys on (− 201) bulk β-Ga2O3. *ECS Journal of Solid State Science and Technology*, *8*(7), Q3154.

[174] Ghobadi, T. G. U., Ghobadi, A., Soydan, M. C., Vishlaghi, M. B., Kaya, S., Karadas, F., & Ozbay, E. (2020). Strong light–matter interactions in Au plasmonic nanoantennas coupled with prussian blue catalyst on BiVO4 for photoelectrochemical water splitting. *ChemSusChem*, *13*(10), 2577-2588.

[175] Eda, Y., Manaka, T., Hanawa, T., Chen, P., Ashida, M., & Noda, K. (2022). X-ray photoelectron spectroscopy-based valence band spectra of passive films on titanium. *Surface and Interface Analysis*, *54*(8), 892-898.

[176] Okajima, Y. (1980). Estimation of sputtering rate by bombardment with argon gas ions. *Journal of Applied Physics*, *51*(1), 715-717.

[177] Powell, C. J., Jablonski, A., & Nakayama, K. (2022). *NIST X-ray Photoelectron Spectroscopy Database (Version 4.1)* [NIST Standard Reference Database 20]. National Institute of Standards and Technology.

[178] Ye, T. (2022). *Long-Term Stability, Vibrational and Optical Properties of β-ZnTe (En) 0.5 and Related Organic-Inorganic Hybrid Superlattices* (Doctoral dissertation, The University of North Carolina at Charlotte).

[179] Melitz, W., Shen, J., Kummel, A. C., & Lee, S. (2011). Kelvin probe force microscopy and its application. *Surface science reports*, *66*(1), 1-27.

[180] Kim, J. S., Lägel, B., Moons, E., Johansson, N., Baikie, I. D., Salaneck, W. R., ... & Cacialli, F. (2000). Kelvin probe and ultraviolet photoemission measurements of indium tin oxide work function: a comparison. *Synthetic metals*, *111*, 311-314.

[181] Panchal, V., Pearce, R., Yakimova, R., Tzalenchuk, A., & Kazakova, O. (2013). Standardization of surface potential measurements of graphene domains. *Scientific reports*, *3*(1), 2597.

[182] Wrana, D., Cieślik, K., Belza, W., Rodenbücher, C., Szot, K., & Krok, F. (2019). Kelvin probe force microscopy work function characterization of transition metal oxide crystals under ongoing reduction and oxidation. *Beilstein journal of nanotechnology*, *10*(1), 1596-1607.

[183] Varshni, Y. P. (1967). Temperature dependence of the energy gap in semiconductors. *physica*, *34*(1), 149-154.

[184] Hansen, W. N., & Hansen, G. J. (2001). Standard reference surfaces for work function measurements in air. *Surface science*, *481*(1-3), 172-184.

[185] Bai, R., Tolman, N. L., Peng, Z., & Liu, H. (2023). Influence of atmospheric contaminants on the work function of graphite. *Langmuir*, *39*(34), 12159-12165.

[186] Sivula, K. (2022). Improving charge carrier mobility estimations when using space-charge-limited current measurements. *ACS Energy Letters*, *7*(6), 2102-2104.

[187] Tixier, A., Mita, Y., Gouy, J. P., & Fujita, H. (2000). A silicon shadow mask for deposition on isolated areas. *Journal of Micromechanics and Microengineering*, *10*(2), 157.

[188] Deshmukh, M. M., Ralph, D. C., Thomas, M., & Silcox, J. (1999). Nanofabrication using a stencil mask. *Applied Physics Letters*, *75*(11), 1631-1633.

[189] Zhou, Y. X., Johnson, A. T., Hone, J., & Smith, W. F. (2003). Simple fabrication of molecular circuits by shadow mask evaporation. *Nano Letters*, *3*(10), 1371-1374.

[190] Egger, S., Ilie, A., Fu, Y., Chongsathien, J., Kang, D. J., & Welland, M. E. (2005). Dynamic shadow mask technique: A universal tool for nanoscience. *Nano letters*, *5*(1), 15-20.

[191] Blickenstaff, S. B., Sarangan, A. M., Nelson Jr, T. R., Leedy, K. D., & Agresta, D. L. (2005). Influence of shadow mask design and deposition methods on nonplanar dielectric material deposition. *Journal of Micro/Nanolithography, MEMS and MOEMS*, *4*(2), 023015-023015.

[192] Yun, H., Kim, S., Kim, H., Lee, J., McAllister, K., Kim, J., ... & Wook Lee, S. (2015). Stencil nano lithography based on a nanoscale polymer shadow mask: Towards organic nanoelectronics. *Scientific reports*, *5*(1), 10220.

[193] Chen, L., Wang, X., Wei, Y., & Zhou, C. (2022). A magnetic metal hard mask on silicon substrate for direct patterning ultra-high-resolution OLED displays. *Micromachines*, *13*(7), 997.

[194] Campbell, S. A. (2008). Fabrication engineering at the micro-and nanoscale (3rd ed.).

[195] Zhao, J. H., Schlesinger, T. E., & Milnes, A. G. (1987). Determination of carrier capture cross sections of traps by deep level transient spectroscopy of semiconductors. *Journal of applied physics*, *62*(7), 2865-2870.

[196] Zhang, P., Valfells, Á., Ang, L. K., Luginsland, J. W., & Lau, Y. Y. (2017). 100 years of the physics of diodes. *Applied Physics Reviews*, *4*(1).

[197] Seah, M. P., Havelund, R., Shard, A. G., & Gilmore, I. S. (2015). Sputtering yields for mixtures of organic materials using argon gas cluster ions. *The Journal of Physical Chemistry B*, *119*(42), 13433-13439.